11-28-2022

# BIOACTIVE SELF-FORMING HYDROGELS FOR BIOMEDICAL APPLICATIONS

Kirstene Arcuino Gultian Giddings
*Rowan University*

---

## Recommended Citation

Gultian Giddings, Kirstene Arcuino, "BIOACTIVE SELF-FORMING HYDROGELS FOR BIOMEDICAL APPLICATIONS" (2022). *Theses and Dissertations*. 3073.
https://rdw.rowan.edu/etd/3073

# BIOACTIVE SELF-FORMING HYDROGELS FOR BIOMEDICAL APPLICATIONS

by

Kirstene Arcuino Gultian Giddings

A Dissertation

Submitted to the
Department of Biomedical Engineering
Rowan-Virtua School of Translational Biomedical Engineering & Sciences
College of Engineering
In partial fulfillment of the requirement
For the degree of
Doctor of Philosophy
at
Rowan University
September 23, 2022

Dissertation Chair: Sebastián L. Vega, Ph.D., Assistant Professor, Department of Biomedical Engineering

Committee Members:
Amir Miri, Ph.D., Assistant Professor, Department of Biomedical Engineering, New Jersey Institute of Technology
Erik Brewer, Ph.D., External Partnerships Chair, Department of Biomedical Engineering
Rachel Riley, Ph.D., Assistant Professor, Department of Biomedical Engineering
Tae Won Kim, M.D, Assistant Professor, Department of Orthopaedic Surgery, Cooper Medical School of Rowan University

# Dedications

To my parents Severino (Jr.) and Rebecca, my brother Audrey, my husband Chaun, and my grandmother-in-law Christine without whom none of my success would be possible.

# Acknowledgments

I thank my advisor Dr. Sebastián L. Vega for his advice, support, and understanding throughout my professional pursuits. These past four years he has provided me with guidance and independence to conduct meaningful studies and overcome challenges that presented along the way. Dr. Vega’s mentoring approach has helped me develop the qualities needed to become a well-rounded researcher which I can apply to advance my career.

I thank my thesis committee members, Dr. Amir Miri from the Biomedical Engineering Department of New Jersey Institute of Technology, Dr. Erik Brewer and Dr. Rachel Riley from the Biomedical Engineering Department of Rowan University, and Dr. Tae Won Kim from the Orthopaedic Surgery Department of Cooper Medical School of Rowan University for supporting my research plans and for their valuable advice, knowledge, and assistance over the course of my research.

I would also like to thank all the students that I have mentored through Engineering Clinic, RISER Program, NSF REU Program, and BioEngineering And Me for teaching me how to be a good mentor.

My deepest gratitude to my family – Nanay, Tatay, Audrey, Chaun, and Christine for their endless support and encouragement and for being present throughout my journey. I would not be in the Ph.D. program at Rowan University without their sacrifices.

# Abstract

Kirstene Arcuino Gultian Giddings
BIOACTIVE SELF-FORMING HYDROGELS FOR BIOMEDICAL APPLICATIONS
2022-2023
Sebastián L. Vega, Ph.D.
Doctor of Philosophy in Biomedical Engineering

Hydrogels are soft biomaterials that feature a wide range of physical and biochemical properties. Although highly versatile, hydrogels typically require an exogeneous input (e.g., light, pH, temperature) to form, and this limits their use to conditions where a catalyst is present. The goal of this dissertation is to expand the use of catalyst-based hydrogels by developing hydrogels with independently tunable properties which gel *in situ* without external stimuli. This new class of hydrogels was developed by first modifying macromers with norbornene (Nor) or tetrazine (Tet) moieties. Macromers containing Nor or Tet remain liquid when dissolved, and upon mixing self-form into Nor-Tet hydrogels. Hydrogels with broad mechanical properties are obtained, and peptide functionalization has no effect on mechanics or gelation time. Nor-Tet hydrogels functionalized with adhesive RGD peptides exhibit exceptional cell-matrix interactions, and stem cells in Nor-Tet solutions are protected from shear forces cells experience during liquid cell injections. Nor-Tet hydrogels functionalized with peptides containing active motifs of bone morphogenetic protein 2 (BMP2) also induce 3D osteogenic differentiation, and BMP2 Nor-Tet hydrogel injections into medullary cavities result in nascent trabecular bone growth in femurs. Taken together, the self-forming Nor-Tet hydrogels developed can be used to safely deliver cells *in vivo* and can serve as a targeted therapeutic to locally treat degenerative musculoskeletal diseases including osteoporosis.

# Table of Contents

## Table of Contents (Continued)

## Table of Contents (Continued)

## Table of Contents (Continued)

# List of Figures

Figure Page

## List of Figures (Continued)

## List of Figures (Continued)

Figure Page

# List of Tables

# Chapter 1

# Introduction

## 1.1 Hydrogels and Methods of Formation

Hydrogels are three dimensional crosslinked hydrophilic polymer networks which can absorb and hold large amounts of water or aqueous fluids.[1–3] The term hydrogel was first used by J.M. van Bemmelen in 1894 to describe a colloidal gel.[4] Four decades later, DuPont scientists synthesized poly(2-hydroxyethyl methacrylate) (HEMA) which they described as a hard, brittle, and glassy polymer.[5] In 1960, Wichterle and Lim described the polymerization of HEMA with crosslinking agents in an aqueous environment and emphasized the use of HEMA hydrogels in contact lens fabrication and as a filler after enucleation of the eye.[6] This study of Wichterle and Lim is the first report of hydrogel application in the biomedical field.[6] Since this report and due to the highly-hydrated nature of hydrogels similar to the human body, hydrogels have been widely-studied and applied for numerous biomedical applications including drug delivery, tissue engineering, and regenerative medicine.[6–9]

The presence of hydrophilic functional groups in the polymer backbone including amino ($-NH_2$), hydroxyl (-OH), carboxyl (-COOH), sulphonic ($-SO_3H$), and amidic (-CONH and/or $-CONH_2$) groups allow hydrogels to retain large amounts of water.[10] Apart from high water absorption capability, hydrogels have the advantages of degradability, biocompatibility, tunability of biophysical and biochemical properties, and ability to maintain porous structures compared to other types of biomaterials.[8,10] The tunability of hydrogel properties make it a suitable scaffold material for cell growth by functionalization of bioactive molecules to mimic the properties of various tissues in the body.[11] For tissue engineering applications, appropriate cells are incorporated within the hydrogels, implanted into the body, and allowed to form new tissues. As the hydrogel degrades, healthy tissue is left behind.[11] The polymeric properties of hydrogels allow the encapsulation and protection of small molecules, proteins, and nucleic acids and the spatiotemporal control of drug release.[12–16] Thus, hydrogels have become an important class of materials used for local drug delivery.[17–19]

Polymers used for hydrogel formation can be natural (occur in nature) or synthetic (derived from petroleum oil).[20,21] Examples of natural polymers include HA, alginate, chitosan (CS), collagen, and gelatin.[20,21] While natural polymers have excellent biocompatibility, their use is limited due to low mechanical properties and poor stability.[22–24] Synthetic polymers used in hydrogel fabrication include poly(ethylene glycol) (PEG), poly(acrylic acid), poly(ethylene oxide), and poly(vinyl alcohol).[25] Unlike natural polymers, synthetic polymers can be molecularly tailored with block structures and with defined molecular weights which creates hydrogels with highly reproducible physical and chemical properties.[25–30] While synthetic polymers have excellent tunability and reproducibility, they form hydrogels that may not be degradable or biocompatible.[31,32] Thus, additional biofunctionalization is required to imbibe biomaterial properties.

The variety of polymers used in hydrogel fabrication brought about a number of crosslinking methods to form hydrogels effectively and efficiently (Figure 1). Hydrogel formation commonly begins with the preparation of a precursor solution, which is composed of polymer dissolved in an aqueous medium and other relevant components which may include an initiator (a chemical substance that leads continuous crosslinking).[10] Consequently, the precursor solution is exposed to an appropriate stimulus, e.g., light, change in temperature, or addition of ionic components, which activates the formation of crosslinks between the polymeric components (Figure 2). The formation of crosslinks drastically increases the viscosity of the solution until the sol to gel transition is completed or the stimulus is removed. The result is a highly-hydrated crosslinked hydrogel.[33,34]

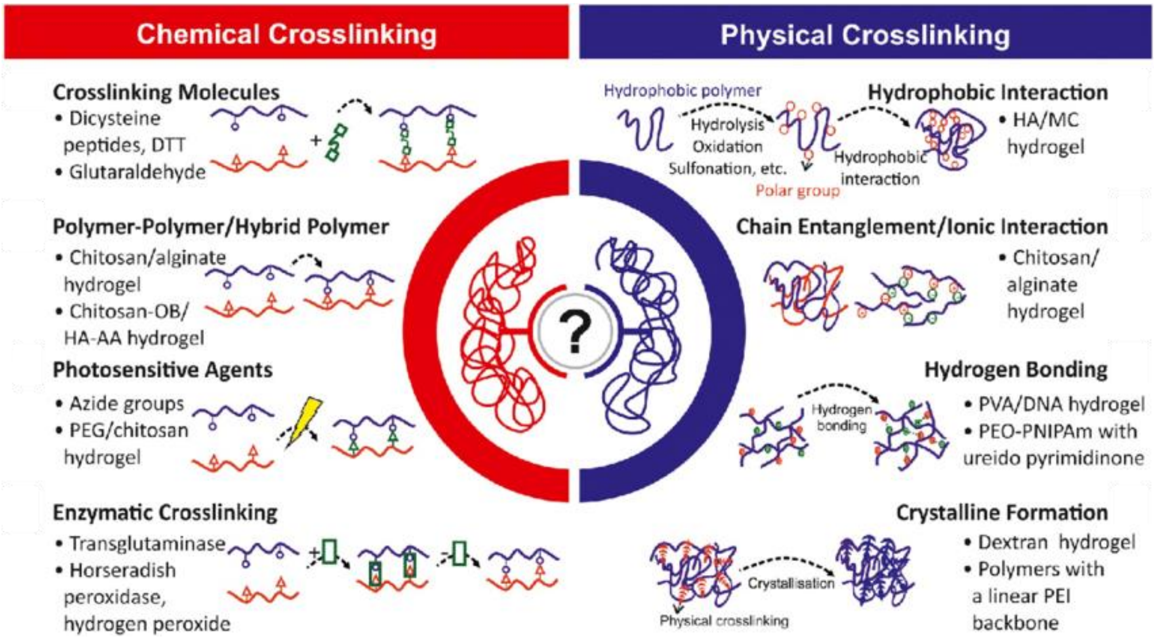

*Figure 1.* Methods of hydrogel synthesis.[35] Hydrogels can be formed through chemical crosslinking (covalent bonding) or physical crosslinking (weak interactions). Chemical crosslinks form by chemical reactions initiated by light heat, pressure, change in pH, or addition of enzyme. Physical crosslinks form between polymer chains typically through ionic bonds.

Synthesis of physically-crosslinked hydrogels involve catalysts including temperature, pH, and electrostatic or ionic reactions.[36] Depending on the polymer used, thermoresponsive hydrogels undergo sol to gel transition above a lower critical solution temperature (LCST) or below an upper critical solution temperature (UCST).[37,38] Many natural polymers exhibit a UCST. For example, gelatin has a concentration-dependent UCST of 25 to 30 °C.[39] Although not many synthetic polymers with physiological UCSTs exist, poly(N-acryloyl glycinamide) has been shown to form gels when cooled to 37 °C.[40] The Michael-addition reaction is an example of pH-catalyzed physical crosslinking. Michael-addition reactions between thiols and acrylates in polymers form hydrogels with tunable mechanical properties, and with gelation rates that vary with pH.[41,42] Some anionic polymers (e.g., alginate) form ionically crosslinked hydrogels upon mixing with divalent cations (e.g., $Ca^{2+}$, $Zn^{2+}$, $Mg^{2+}$).[3] While physically-crosslinked hydrogels are insoluble in aqueous media, the crosslinks formed are not permanent in nature. Thus, physically crosslinked hydrogels are reversible.

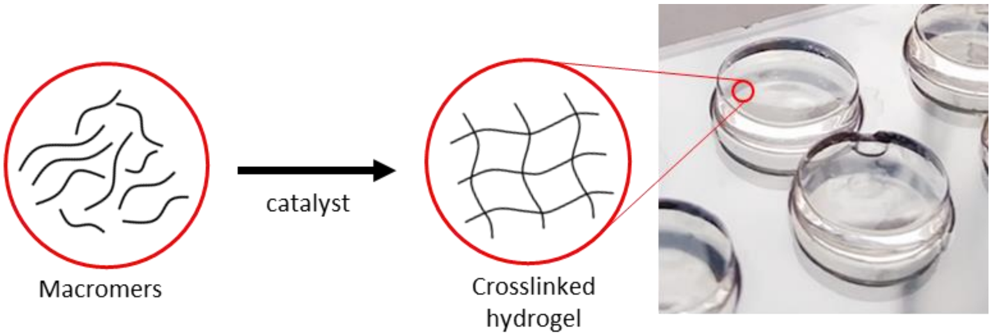

*Figure 2.* Schematic of hydrogel formation. Hydrogel formation begins with a precursor solution containing polymer chains or macromers. A catalyst is introduced and results in the formation of crosslinked hydrogel. Hydrogels take the form of the mold in which they are contained.

Covalent crosslinking or chemical crosslinking of polymers result in permanent hydrogels.[20] Free-radical photopolymerizations using visible or ultraviolet light as catalyst are the most commonly used method of hydrogel formation due to fast gelation under physiological conditions.[43] Free-radical chain-growth photopolymerization of acrylated macromers form hydrogels with polydisperse kinetic chains, while free-radical step-growth photopolymerization between thiol and vinyl groups result in one-to-one click reactions that form hydrogels with a homogenous network structure.[44–46]

Common methods of hydrogel formation rely on catalysts (e.g., temperature, cations, pH, light), which limits their use to conditions where catalysts are present. Alternatively, Diels Alder (DA) reactions, commonly used in polymer manufacturing, have been used to form hydrogels without requiring light or other stimuli.[47,48] For example, Furan-modified HA (HA-Fur) macromers begin form soft hydrogels upon mixing with maleimide-modified PEG (PEG-Mal) macromers and reach completion after several hours.[49] Alternatively, the Inverse Electron Demand Diels Alder Reaction (IEDDA) between Nor-and Tet-modified gelation macromers form soft hydrogels within 5 minutes after mixing.[50] While the DA reaction does not require an external input, DA self-forming hydrogels have poor mechanical properties which limits their application.

Despite the broad use of hydrogels, the weak mechanical properties and the fragile nature of hydrogels result in limited applications. Thus, novel hydrogels with improved and stable properties are needed and remain an important consideration for hydrogel biomaterial research.

## 1.2 Limitations of Current Hydrogel Formation Techniques

Despite the advancements in hydrogel formation techniques, some properties of hydrogels are short of expectations for biomedical applications (e.g., biocompatibility, mechanical properties, biofunctionality) thus, they require additional modifications.[51,52] For example, polymers used in thermogelation may have LCSTs or UCSTs that are not within the physiological range and therefore not suitable for *in vivo* applications.[39,53] High pH buffers are typically needed for pH-dependent reactions. While the Michael-addition reaction has been reported to be amenable to 3D cell culture, viability of encapsulated cells are typically compromised due to the need for high pH.[42] Ionically crosslinked hydrogels are biocompatible but have poor mechanical properties and are unstable due to the diffusion of divalent cations over time.[54]

Free-radical chain-growth photopolymerization form hydrogels with polydisperse kinetic chains, which result in non-homogenous crosslinking density within the hydrogel that could unpredictably influence the interactions between encapsulated cells and hydrogel [44,45] Free-radicals created during photopolymerization form reactive oxygen species that could damage the DNA of encapsulated cells.[55] Additionally, ultraviolet light can increase oxidative stress in encapsulated cells and lead to unwanted changes in cellular phenotype.[56]

While the DA reaction to form hydrogels does not require a catalyst, formation take several hours at neutral pH and require acidic conditions which is not suitable for 3D cell culture to speed up hydrogel formation.[49] Alternatively, addition of methyl groups on the Fur moieties results in hydrogel formation under 15 minutes.[57] However, DA reactions between furfural and Mal are reversible and prone to hydrolysis, which leads to changes in hydrogel properties including swelling, stiffness, and porosity.[57,58]. Although hydrogels formed using the IEDDA reactions are highly biocompatible, hydrogel mechanics are low and hydrogel polymerization is slow, which limits their clinical use and could cause non-homogenous cell distribution during gelation.[50,59] Additionally, hydrogels formed with the DA and IEDDA reactions cannot be peptide-functionalized without affecting crosslinking density or requiring a secondary reaction (e.g., photoreaction) post-hydrogel polymerization.[50,60]

Traditional methods of hydrogel formation generally rely on external input which may affect the biophysical and biochemical properties of formed hydrogels and are not suitable for cell culture. While alternative chemistries which do require any catalyst exist, hydrogels formed have poor mechanical properties and functionalization is tedious. Therefore, a novel method of creating hydrogels which can self-form and which allows ease of biofunctionalization will address the limitations of current methods of hydrogel formation.

## 1.3 Hypothesis and Aims of the Dissertation

Various strategies have been developed to form suitable hydrogel scaffolds for biomedical applications including free-radical photopolymerization [44–46,61], ionic or thermal crosslinking [62–65], pH-dependent crosslinking [41,42], and copper-catalyzed cycloaddition reactions [66]. Although these crosslinking strategies have been extensively applied, they are limited by their need for catalysts (e.g., light, temperature, pH), formation of unwanted radical species, and cytotoxic byproducts. The IEDDA reaction between Nor) and Tet has recently been used as an alternative approach to form stable covalently crosslinked hydrogels with tunable properties [50,59,60,67,68]. Although the IEDDA reaction does not require catalysts, to date the hydrogels formed using this technique have poor control over mechanics and gelation time. Moreover, hydrogels formed with a Diels-Alder Nor-Tet chemistry cannot be peptide-functionalized without either affecting crosslinking density or requiring a secondary photoreaction after the hydrogels are formed [50,60].

For tissue engineering applications, biophysical and biochemical signals within the hydrogel scaffold are essential to recapitulate the desired tissue construct [55,69]. Hydrogel elasticity, tissue-level stiffness, and stability are strong drivers of cellular mechanosensing and phenotypic commitment *in vitro* [70]. For example, human mesenchymal stem cells (MSCs) atop rigid substrates produce bone-tissue specific proteins secreted by osteoblasts while MSCs on soft hydrogels express neuronal biomarkers [70]. Moreover, MSCs encapsulated in HA hydrogels that permit or restrict cell-mediated degradation favored osteogenesis or adipogenesis, respectively [71]. Biochemical cues are also important towards engineering biomaterials that mimic native tissues. For example, hydrogels modified with a bone-morphogenetic protein (BMP-2) mimetic peptide promoted osteogenesis of MSCs [72]. Although tremendous advances have been made in the biomedical field, biochemical modifications or tethering bioactive signals to hydrogels remains challenging.

As such, the goal of this dissertation is to develop a hydrogel biomaterial system crosslinked via the IEDDA reaction which allows high control over the biophysical properties of the hydrogel while independently incorporating biochemical modifications for biomedical applications. This was achieved by pursing three specific aims: (1) to develop a peptide-biofunctionalized hydrogel system and to explore the parameters which control the mechanics and gelation kinetics of the hydrogel system, (2) to investigate the effects of the novel hydrogel system on cell-material interactions, particularly on cellular mechanosensing and stem cell lineage commitment, and (3) to evaluate the suitability of the novel hydrogel system for translational biomedical applications. **The hypotheses of Aim 1 are:** (i) modifying macromers with a higher degree if Nor and Tet substitution will enable greater control over mechanical properties and gelation time and (ii) macromers can be pre-functionalized with thiolated peptides without affecting Nor-Tet interactions. **The hypotheses for Aim 2 are:** (i) cultured stem cells will respond to signals from tethered bioactive peptides and (ii) changes in the biophysical properties of the hydrogel will result in cellular and molecular changes of cultured cells. Lastly, **the hypotheses for Aim 3 are:** (i) the physical properties of the Nor-Tet hydrogel can protect cells from shear stresses during extrusion, and (ii) bioactive Nor-Tet hydrogels can locally regenerate tissues *in vivo*.

**Chapter 2** is a review of the recent advances in self-forming hydrogels crosslinked via DA and IEDDA reactions for the use as carriers of therapeutic agents, scaffolds for tissue repair and regeneration, and to create multifunctional versatile hydrogels. **Chapter 2** lays the foundation and rationale for the studies in **Chapter 3**, where we developed HA macromers with a high degree of Nor and Tet substitution and formed HA Nor-Tet hydrogels without an external catalyst. We found that these hydrogels are mechanically stable, and gelation times and stiffness are tunable by changing the total HA macromer concentration and stoichiometric ratio between HANor and HATet macromers. The bioactivity of HAN Nor-Tet hydrogels was independently controlled by covalently tethering peptides to methacrylate groups in methacrylated HANor macromers. MSCs on two-dimensional HA Nor-Tet hydrogels functionalized with a peptide mimic of fibronectin (Arginine-Glycine-Aspartic Acid, RGD) adhered, proliferated, and were mechanically sensitive to changes in hydrogel stiffness. Further, HA Nor-Tet hydrogels supported three-dimensional cell encapsulation and influenced the preferential differentiation of encapsulated MSCs. Additionally, MSCs in the HA Nor-Tet hydrogel precursor solution are highly viable and protected from shear forces experienced while extruding from syringe needles during cellular injections. This showcases our ability to independently tune the properties of HA Nor-Tet hydrogels which have broad applicability in basic and translational research.

In **Chapter 4** we applied the techniques used in **Chapter 3** to develop injectable HA Nor-Tet hydrogels functionalized with a peptide mimic of bone morphogenetic protein 2 (Aspartic Acid-Tryptophan-Isoleucine-Valine-Alanine, DWIVA), a bone growth factor, that can be used as a biomaterial for local regeneration of bone tissue and for the potential local treatment of osteoporosis. Towards this, we demonstrated that this hydrogel system enhance osteogenic differentiation of MSCs *in vitro* and induced trabecular bone growth *in vivo*. We showed that the effective concentration of DWIVA peptide in self-forming hydrogels can be controlled by changing the amount of peptide added during coupling with methacrylated HANor macromers. Further, we confirmed that the bioactivity of the DWIVA peptide is preserved post-coupling by showing that expression of alkaline phosphatase (ALP), a bone biomarker, is enhanced in human MSCs seeded atop or encapsulated within HA Nor-Tet hydrogels functionalized with DWIVA. Additionally, we demonstrated that this hydrogel can regenerate trabecular bone in femurs, which can be used as a targeted therapeutic to improve bone density locally. In **Chapter 5** we improved trabecular bone growth in rat femurs by incorporating MSCs in the DWIVA-coupled HA Nor-Tet hydrogels injected into rat femurs. Increased trabecular bone growth was quantified through bone morphometry following microcomputed tomography imaging (microCT) and histomorphometry.

The results presented in these chapters show that highly tunable hydrogels formed using the IEDDA reaction can be used in various cellular and acellular biomedical applications, specifically as a medium for cell delivery in cell therapies and a biomaterial construct for bone tissue engineering. This work can help lay the foundation for a new generation of hydrogel biomaterials for biomedical applications. **Chapter 6** details future research directions to advance this body of work. For example, looking at the effects of interplay between macromer size and Nor and Tet modification and macromer pre-coupling on hydrogel kinetics and mechanics, simultaneous functionalization of Nor-Tet hydrogels with the wrist and knuckle epitopes of BMP-2 to evaluate synergistic effects in bone regeneration, the use of Nor-Tet hydrogels in restoration of soft tissues, and as a real-time dosimeter and spacer for radiation oncology.

# Chapter 2

# Injectable Diels-Alder Hydrogels for Biomedical Applications

## 2.1 Introduction

Biomaterials with enhanced properties are extensively studied and developed to address the growing need for effective targeted treatments of diseases and local repair of damaged or injured tissues. Hydrogels have become desirable biomaterials due to their biocompatibility, non-toxicity, biofunctionality, biodegradability, similarity of characteristics to native extracellular matrix (ECM), and tunability of properties for encapsulation and subsequent sustained or controlled release of therapeutic agents (cells, genes, drugs, proteins, etc.).[2,7–9,25]

Implantation of pre-formed hydrogels for targeted treatments or local tissue repair requires an invasive surgical procedure that may cause significant discomfort to patients and may need a longer time to heal.[73,74] In contrast, injectable hydrogels can be delivered to sites of need through a minimally-invasive procedure and can be applied to irregularly-shaped or hard-to-reach sites. [36,45,46] Injectable hydrogels are prepared with polymer materials approved by the Food and Drug Administration (FDA) to meet biocompatibility requirements. Natural polymers including alginate, chondroitin sulfate CS, gelatin, HA, fibrin and silk have been used. Synthetic polymers such as PEG, poly(vinyl alcohol) (PVA), polycaprolactone (PCL), poly(L-glutamic acid) (PLLA), and polyaniline have also been utilized for hydrogel formation. Besides biocompatibility, these polymers have the advantage of amenability to chemical modifications through their many functional groups. For example, HA has hydroxyl (-OH) and carboxyl (-COOH) functional groups[75], gelatin has -OH, -COOH, and amine (-$NH_2$) groups[59], while PEG has -OH groups[76]. To form injectable hydrogels, the aqueous precursor which is a mixture of polymeric components and relevant materials is loaded into a syringe (Figure 3A). The precursor solution is injected to the site of need while its viscosity is low (Figure 3B). The formation of crosslinks drastically increases the viscosity of the solution until the sol to gel transition is completed and a highly hydrated crosslinked polymer network (hydrogel) is formed over time (Figure 3C).[33,34] The crosslinks in the hydrogels can form via chemical or physical crosslinking reactions which may require catalysts such as visible or ultraviolet light, enzymes, pH, electrostatic interactions, or temperature.

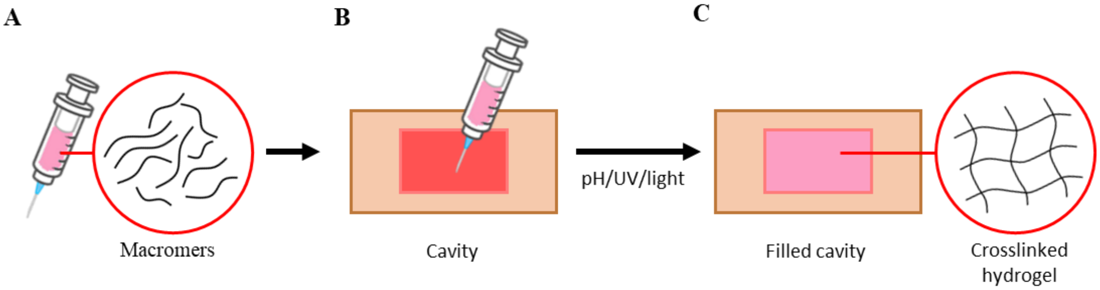

*Figure 3.* Mechanism of injectable hydrogel crosslinking. **(A)** The aqueous precursor solution with relevant components is loaded into a syringe and **(B)** injected into the site of need. **(C)** Formation of crosslinks drastically increases the viscosity of the solution until the sol to gel transition is completed and a highly hydrated crosslinked polymer network is formed over time.

Injectable hydrogels have been extensively used in many biomedical applications including the delivery of therapeutic agents and the repair of tissues such as bone, cartilage, muscle, and skin.[77] For applications in drug delivery, therapeutic agents are mixed with the hydrogel precursor solution and injected into the site of need where the therapeutic agents are entrapped.[74] In tissue engineering applications, the biophysical and biochemical features of the cell microenvironment are reproduced within the hydrogel structure to induce an expected cell fate.[78] Towards this, natural or synthetic polymeric macromers are synthesized and crosslinked to reach desired biophysical properties and functionalized with molecules that provide biochemical signals such as peptides, antibodies, and proteins.[72,79–81] For injectable hydrogels to successfully perform their functions, the sol-gel transition should occur without interfering with native biological processes, proceed under mild and physiologically-relevant environmental conditions, should not require or produce toxic chemicals, and the product must be obtained in high yields. These criteria are characteristics of hydrogels formed via click chemistry reactions.[82,83]

Click chemistry is generally defined as a group of modular reactions that proceed under mild conditions, with high yields, and generate non-harmful by-products.[84–86] Click chemistry has emerged as an efficient crosslinking method for the formation of hydrogels for biomedical applications.[87,88] For example, copper-catalyzed reactions have been extensively used for crosslinking hydrogels for cell encapsulation and tissue engineering. However, oxidation of the copper catalyst led to low efficiency, and the accumulation of excess copper ions within the hydrogels resulted in cytotoxicity.[89,90] Alternatively, thiol group-based click chemistry between thiols and vinyl sulfone, acrylates, or Mals form hydrogels with tunable mechanical properties and gelation rates.[91,92] While some studies report that thiol group-based click reactions are amenable to 3D cell culture, the viability of encapsulated cells is typically compromised due to the need for high pH buffers, limiting their use to either acellular or 2D cell culture.[42] The catalyst-free DA reaction and IEDDA reaction between a diene, e.g., Fur and Tet, and dienophile, e.g., Mal and Nor, is an excellent example of click chemistry. DA reactions are highly robust, occur in an aqueous medium with high reaction rates, and do not yield toxic byproducts.[93] Early applications of the DA reaction to form hydrogels used macromers modified with Fur (diene) and macromers modified with Mal (dienophile) to create improved hydrogel microenvironments for cell encapsulation and potential applications for drug delivery and tissue engineering. For example, Nimmo et al. reported HA-Fur crosslinked with PEG-diMal to form hydrogels for soft tissue engineering.[49] Similarly, Owen et al. demonstrated the encapsulation of biomolecules, e.g., galactose, within HA-Fur and PEG-bis-Mal hydrogels to create 3D microenvironments that can direct the function of encapsulated cells.[94] Similarly, Kirchhoff et al. used PEG-Fur and PEG-Mal to form hydrogels that readily degrade at body temperature through the hydrolysis of Mal groups.[58] Although the hydrolysis of the Mal groups can be useful in some applications, e.g., drug delivery, a major limitation of DA hydrogels formed between Furs and Mals is that these reactions are reversible resulting in uncontrollable changes to hydrogel properties including swelling, stiffness, and porosity.[57,58] Alternatively, the IEDDA reaction between macromers modified with Tet (diene) and Nor (dienophile) is irreversible and offers alternative chemistry for creating injectable hydrogels. For example, Alge et al. utilized PEG-Tet macromer and diNor peptide to form hydrogels within minutes while encapsulating MSCs with high viability.[60]

Through the efforts of researchers in the past seven years, both the DA and IEDDA reactions have been implemented in more complex functions for biomedical applications. In this chapter, recent studies that utilized the DA and IEDDA reactions to form injectable hydrogels for use as carriers of therapeutic agents or scaffolds for tissue repair and regeneration and to create multifunctional versatile hydrogels are reviewed.

### ***2.1.1 Diels-Alder and Inverse Electron Demand Diels-Alder Chemistries***

The DA reaction was discovered by and named after scientists Otto Diels and Kurt Alder. Due to their discovery, they were awarded the Nobel Prize in Chemistry in 1950.[95] Since then, the DA reaction has been regarded as one of the most versatile reaction known in organic chemistry. The DA reaction is a [4+2] cycloaddition between a conjugated diene ($4\pi$-electrons) as the electron-donating group (EDG) and a substituted alkene dienophile ($2\pi$-electrons) as the electron-withdrawing group (EWG) which forms a cyclic, six-membered product (Figure 4A). The driving force of the DA reaction is the formation of new $\delta$-bonds which are energetically more stable than $\pi$-bonds. During the reaction, the highest occupied molecular orbital (HOMO) of the diene (1,4 carbon atoms of the diene) overlaps with the lowest unoccupied molecular orbital (LUMO) of the dienophile (carbon atoms of the dienophile) resulting in re-hybridization from $sp^2$ to $sp^3$ and formation of the new $\delta$-bonds (Figure 4B). The 2,3 carbon atoms of the diene remain in $sp^2$ hybridization to form the new double bond.[96–100] The normal DA reaction typically involves electron-rich dienes, e.g., cyclopentadiene or Fur, and electron-poor dienophiles, e.g., maleic anhydride or Mal.[101,102] Fur is the most common diene and Mal the most common dienophile used in injectable DA hydrogels for biomedical applications (Figure 5A).

An alternative reaction to DA involves reactants with reversed electron distribution. In the IEDDA reaction, dienes are relatively electron deficient (EWG) while the dienophiles are electron-rich (EDG) and contain one or more electron-donating groups, resulting in higher orbital energies (Figure 4C).[98,103] In IEDDA, the LUMO of the diene and the HOMO of the dienophile react very strongly and result in the most energetically favorable bond (Figure 4D). IEDDA is known to take place between Tets (diene) and alkenes (dienophiles), in which the reaction readily eliminates nitrogen and results in dihydropyridizines and ultimately to pyradizines after further oxidation.[103] Tet and Nor are the most commonly used diene and dienophile, respectively, to form injectable IEDDA hydrogels for biomedical applications (Figure 5B).

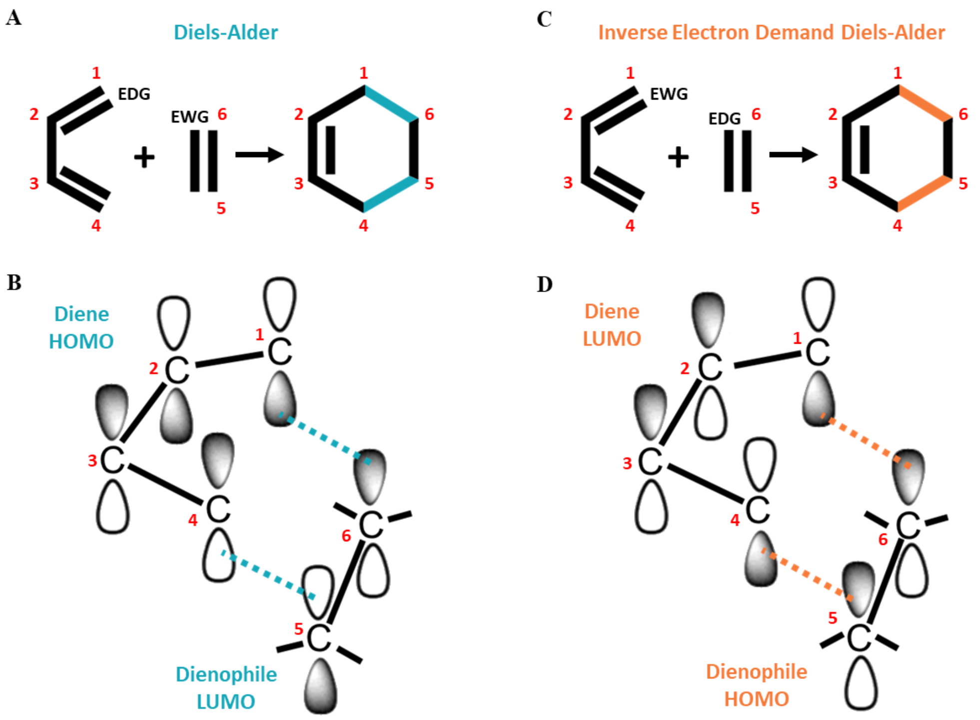

*Figure 4.* Overview of Diels Alder and Inverse Electron Demand Diels Alder reactions. **(A)** The DA reaction is a [4+2] cycloaddition between a conjugated diene ($4\pi$-electrons) (EDG) and a substituted alkene dienophile ($2\pi$-electrons) (EWG) which forms a cyclic, six-membered product. **(B)** the HOMO of the diene (1,4 carbon atoms of the diene) overlaps with the LUMO of the dienophile (carbon atoms of the dienophile) resulting in re-hybridization from $sp^2$ to $sp^3$ and formation of the new $\delta$-bonds. **(C)** In the IEDDA reaction, dienes are relatively electron deficient (EWG) while the dienophiles are electron rich (EDG) and contains one or more electron donating groups, resulting in higher orbital energies. **(D)** the LUMO of the diene and the HOMO of the dienophile react very strongly and result in the most energetically favorable bond.

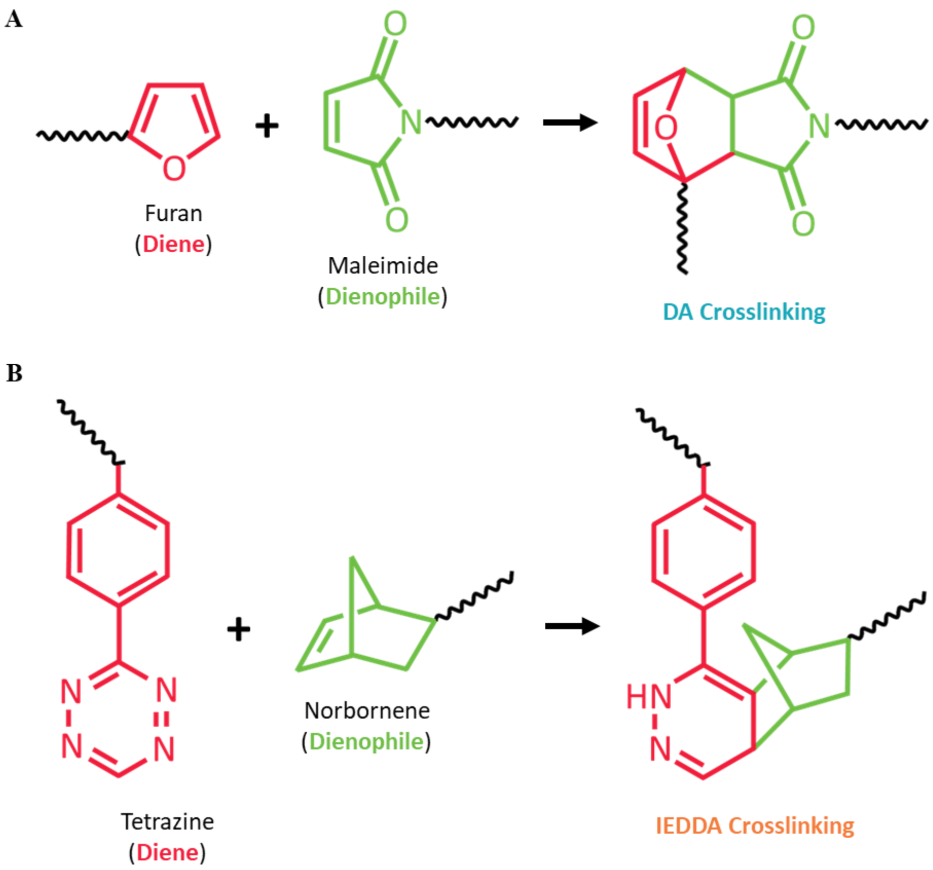

*Figure 5.* Overview of common dienes and dienophiles used in DA and IEDDA reactions. **(A)** Furan is the most common diene and Maleimide the most common dienophile used in injectable DA hydrogels. **(B)** Tetrazine is the most commonly used diene and Norbornene is the most commonly used dienophile used in injectable IEDDA hydrogels for biomedical applications.

## 2.2 Hydrogels for Drug Delivery and Sustained Release

The polymeric nature and porous network structure of hydrogels allow the encapsulation of drugs, proteins, and small molecules.[7,104] Injectable hydrogels are advantageous for local delivery because they provide protection from shear forces during extrusion, the potentially harsh environment conditions in the delivery site, and rapid clearance by the body. Subsequent release of the encapsulated components is achieved through diffusion of the components through the hydrogel network or via the degradation of the hydrogel.[7,104] Through this release mechanism, the rate of release of the encapsulated components can be controlled to maintain a therapeutic concentration in the surrounding tissue over an extended period.

Hydrogel microspheres are the most common type of materials used for controlled drug delivery due to the variety of drugs, small molecules, and proteins that can be loaded into the microspheres.[105] Hydrogel microspheres have a spherical geometry with particle size ranging from 0.1 to 200 μm.[105] The DA reaction in combination with spray drying technique is used in the formation of hydrogel microspheres.[106–108] Hydrogel microspheres formed with CS-Fur and bis-Mal was used to study the release methylene blue as a model substance.[106] In a similar study, the DA reaction between furfurylamine and N-maleoyl alanine were utilized to form hydrogel microspheres loaded with urea as a model substance.[107] Meanwhile, by modifying starch with succinic acid amide and N-maleoyl alanine, the anti-cancer drug 5-fluoroacil was loaded and released from hydrogel microspheres and showed high cytotoxicity to human breast cancer cells.[108] Alternatively, the IEDDA reaction between Tet and Nor was used to form gelation microspheres loaded with a strong alkaline substance to activate endogenous transforming growth factor beta 1 (TGFβ1) for *in situ* pulp-dentin tissue regeneration.[109]

Macromers modified with Fur and Mal have also been extensively used in forming DA hydrogels for drug delivery and sustained release.[110–113] Specifically, succesful encapsulation and release of dexamethasone (anti-inflammatory)[114], bevacizumab (chemotherapy)[115], vanillin (anti-epileptic)[116], and diclofenac potassium (pain reliever)[117] have been studied. Alternatively, the IEDDA reaction between Tet and Nor[118–120] has been used to form hydrogels with encapsulated drugs such as cisplatin (chemotherapy)[68], doxurubicin (chemotherapy)[121–123], and ketoprofin (anti-inflammatory)[124]. To add another later of controllable drug release, Tet crosslinkers containing a diselenide bridge have been used to form Nor-Tet hydrogels that degrade when irradiated with near-infrared light (NIR).[118,123] At physiological conditions, the loaded drugs show a suppresed release profile while NIR light triggers rapid release.[118,123]

The needle and syringe system is the primary means of protein or antibody delivery and comes with many challenges including permeability, stability, and pharmacokinetics and phamacodynamics of therapeutics.[125] To overcome these challenges, the DA reaction between Fur and Mal and IEDDA reaction between Tet and Nor have been utilized to form hydrogels for loading and controlled release of proteins and antibodies.[126–128] Specifically, the release profile of Fab1 protein[129] and bovine serum albumin[130] as model proteins were controlled by tuning the biophysical properties of the hydrogels.

The sustained release of cells and cellular components from hydrogels are also being explored.[131–133] For example, the DA reaction between Fur and Mal was utilized for the sustained release of MSC-deerived small extracellular vesicles for the treatment of osteoarthritis.[131] The reversible DA reaction between fulvene and Mal formed hydrogels that gradually released T-cells for the treatmnet of haematological cancers.[132] Alternatively, Nor- and Tet-modified methylcellulose hydrogels have been used for the co-delivery of neural stem cells and chondroitinase ABC, a potent enzyme that degrades glial scarring that forms after injury to the central nervous system.[133]

## 2.3 Hydrogels Scaffolds for Cell Culture and Tissue Engineering

Hydrogels are formulated to mimic the natural ECM of cells and thus promote their survival. Hence, hydrogels have become attractive materials for cell encapsulation for *in vitro* and *in vivo* applications.[10,20,25,134] DA and IEDDA reactions have been utilized to improve cellular hydrogel systems because these reactions do not require catalysts which could potentially be harmful for cells. For example, pre-formed hydrogels synthesized by reacting Fur-modified HA and bis-Mal PEG promote the neurite outgrowth of PC12 cells seeded atop pre-formed hydrogels.[135] The HA macromer was pre-functionalized with a thiol-containing peptide derived from laminin-1 to improve cell adhesion without disrupting the interactions between the Fur and Mal moieties.[135] While this system is useful in the synthesis of pre-formed hydrogels, it takes several hours to form at physiological pH and requires acidic conditions which are not suitable for 3D cultures.[49] By replacing Fur with methylFur, a more electron-rich diene, hydrogels were formed in under 15 minutes at a physiologic pH.[57] Reactions between Furs and Mals are reversible and are prone to hydrolysis.[57,58] While this may be helpful in some applications, it is a major limitation of hydrogels when mechanical integrity of the hydrogel is of importance. By replacing Fur with electron-rich cyclic fulvenes as dienes, more stable hydrogels that support 3D cell culture were formed.[136]

Although these DA reactions can create injectable and suitable hydrogel environments for 3D cell culture, hydrogel mechanics are low (storage modulus, $G' <$ 1,000 Pa) which limit its application to recapitulating soft tissues. Additionally, gelation times for DA reactions are high (upwards of 3 hours) which limit its practical applications. The IEDDA reactions between Tet- and Nor-modified macromers are irreversible and can form injectable hydrogels with high mechanical properties and gelation times. Hydrogels to improve wound closure and blood flow that gel within 4 – 7 mins were formed by reacting CS-Tet and PEG-Nor.[137] By reacting alginate biopolymer with Nor or Tet moieties, hydrogels with increased mechanical properties (elastic modulus of ~7 kPa and gelation time of ~20 mins for 3% w/v hydrogels) were formed.[50] Formed alginate hydrogels were functionalized with a peptide mimic of fibronectin to improve cell adhesion, spreading, and proliferation by coupling peptides to unreacted Nor through thiol-ene photochemistry.[50] Similarly, gelatin biopolymer modified with Nor and Tet moieties formed hydrogels suitable for cell culture.[59] By varying the degree of Nor- and Tet- modification and Nor/Tet ratio of the gelatin macromers, the elastic modulus of the hydrogels varied between 0.5 kPa to 5 kPa and gelation time varied from between 10 and 70 mins.[138] By using HA as polymer backbone, gelation times between 4 and 46 mins were achieved.[133] Besides demonstrating the tunability of the hydrogel properties, cells that were encapsulated within the IEDDA hydrogels or injected while suspended in the pre-hydrogel solution were highly viable and shows that these hydrogels provide a suitable environment for 3D cell culture.[50,59,133,138]

Biomaterials used in tissue engineering are composed of cells cultured in a biomaterial scaffold with appropriate biophysical and biochemical signals to recapitulate the desired tissue.[55] Besides suitability for 3D cell culture and the tunability of mechanics, injectable hydrogels must be functionalized with biochemical signals to effectively function as a biomaterial for tissue engineering applications. DA and IEDDA hydrogels have been shown to be amenable to chemical modifications such as peptide mimics of ECM components.[50,59,135] By physically loading recombinant human bone morphogenetic protein 2 (rhBMP-2), a potent inducer of osteogenesis, into Tet-modified

HA and trans-cyclooctene (TCO)-modified PEG, encapsulated MSCs showed increased expression of osteogenic biomarkers.[139] However, rhBMP-2 is a large and expensive growth factor, and high doses of untethered rhBMP-2 are associated with serious complications including ectopic bone formation and impaired neurological function.[140–142] Peptides that mimic the bioactivity of native growth factors are an inexpensive and potentially more efficacious substitute that can be immobilized into biomaterials. For example, HA modified with Tet and TCO were functionalized with a chondrogenic differentiation factor through chemical immobilization of a peptide mimics of cytomodulin-2 (CM) to the HA-Tet macromer.[143] In the same study, it was found that physically loaded CM peptide was rapidly released from the hydrogel and was not able to provide a stable source of biochemical signal for encapsulated cells. Indeed, increased expression of chondrogenic biomarkers was observed in cells encapsulated in hydrogels with immobilized CM peptide compared to physically loaded CM peptide. To promote the differentiation and viability of chondrocytes in 3D cell cultures, oxygen-generating polycaprolactone-Pluronic® F-127 microparticles were physically loaded into Tet-modified chondroitin sulfate and Nor-modified PEG hydrogels.[144] Indeed, encapsulated chondrocytes expressed increased amounts of chondrogenic biomarkers in the presence of oxygen-releasing microparticles.

## 2.4 Multifunctional Versatile Hydrogels

Advances in hydrogel formulations and formation techniques are constantly developed to effectively recapitulate the native properties of target tissues for tissue engineering and to efficiently deliver hydrogels to target sites in a non-invasive manner (e.g., injectable hydrogels).[145] Most formulations for forming injectable hydrogels form soft and weak hydrogels which easily break under fatigue or degrade at a fast rate due to irreversibility or susceptibility to hydrolysis.[146] Applications of these hydrogels are limited to *in vitro* studies or engineering of soft tissues. Thus, there is tremendous interest in forming tough or mechanically strong injectable hydrogels which can recover under cyclic loading and exhibit self-healing abilities upon fracture or the ability to recover crosslinking networks. One of the most common strategies to form tough hydrogels is to incorporate sacrificial weak and permanent strong crosslinks into polymer networks.[147] Under loading, the weak bonds break and dissipate energy to support the strong bonds that hold the strength and shape recovery of the hydrogel.[147] Reversible sacrificial bonds using weak physical interactions such as ionic bonding[148] or hydrogel bonding[149] have been incorporated with permanent covalent crosslinks to form hydrogels with recoverable mechanical properties. However, these techniques require low or high temperature, toxic reagents, or UV radiation which prevents injectability.[150] Additionally, conventional physicochemical tough hydrogels have inefficient self-healing and slow recovery of mechanical properties under cyclic loading.[151]

Alternative methods in forming tough hydrogels utilized the DA chemistry which provides the advantage of injectability for applications in bone and cartilage tissue engineering. To improve the mechanical strength of DA hydrogels for bone tissue engineering without reducing water content, dual crosslinking networks (DN) combining DA reaction with physical crosslinking was applied.[152,153] Physical crosslinking was achieved through the supramolecular interaction between cyclodextrin and adamantane and the sol to gel transition of poly(N-isopropyl acrylamide) (PNIPAM). The DA covalent crosslinking was achieved through the interactions between CS-Fur and PEG-

Mal.[152] Faster gelation was observed after replacing the physical crosslinking components with the non-covalent crosslinking of CS-Fa and Pluronic F127-Mal.[154]. To improve the cranial bone regeneration ability of the hydrogel, an additional crosslinking scheme was added resulting in a triple crosslinking network (TN).[155] The third crosslinking scheme involved the acylhydrazone bond crosslinking between alginate modified with hydrazide and aldehyde moieties which allowed the encapsulation and sustained release of bio-glass, a silicate-based inorganic biomaterial.[155]

The cartilage tissue has limited self-healing capacity due to limited blood supply and poor access to ECM secretions.[156] Thus, injectable functional hydrogels for cartilage tissue engineering must be able to bear and distribute loads to protect the subchondral bone and have the ability to self-heal or recover.[157] DN networks utilizing the DA chemistry have been used to produce injectable hydrogels that are fatigue-resistant, can immediately self-recover under cyclic loading, and can self-heal upon fracture.[93,158] Hydrogels formed upon mixing of HA macromers modified with Fur and adipic dihydrazide (HA-Fur-ADH) and HA modified with Fur and aldehyde (HA-Fur-CHO) via the covalent acylhydrazone reactions between ADH and CHO moieties which provides self-healing ability.[93] Simultaneously, the DA reactions between Fur moieties in the HA macromers and the Mals in the PEG-diMal crosslinker results in rapid hydrogel formation and provides the hydrogels with structural integrity and mechanical strength.[93] To overcome fast enzymatic degradation of HA hydrogels and improve tissue adhesion and injectability, the DA reaction was combined with phenyl boronate ester bonds created by crosslinking HA-Fur-3-aminophenylboronic acid with PEG-Mal crosslinker.[158]

Cells are an essential component in tissue engineering biomaterial constructs and must be encapsulated under gentle conditions to remain highly viable.[159–162] However, cell encapsulation and delivery using hydrogels with tunable and consistent composition remains a challenge.[163,164] DN networks utilizing the DA reaction in combination with enzymatic crosslinking have been used to improve cell encapsulation in hydrogels with improved mechanics and tunability.[108,153,165] For example, Poly(γ-glutamic acid) (PGA) modified with Fa and tyramine (PGA-Fa-Tyr) rapidly formed hydrogels after the addition of PEG-diMal crosslinker.[130] The mechanical properties of the hydrogel was controlled by varying the ratio between hydrogen peroxide ($H_2O_2$) and Tyr ($H_2O_2$/Tyr) and between Fa and Mal (Fa/Mal) in the hydrogel precursor solution.[130] Similarly, this technique was applied to the formation of 3D microgels with encapsulated cells which helped advance the understanding of cellular interactions with synthetic substrates.[165,166]

## 2.5 Summary and Future Perspectives

The DA and IEDDA reactions are two of the most interesting click reactions for conjugation of injectable hydrogels for biomedical applications. The reactions occur under physiological conditions and are suitable for encapsulation of cells which are an essential component of successful tissue-engineered constructs. The functional groups involved, a diene and a dienophile are not found in natural biopolymers thus modification of the polymer backbones is required. Commercially available crosslinkers such as diMal and diTet can crosslink diene-modified macromers. Different injectable hydrogels for drug delivery and sustained release and tissue engineering have been developed following the DA and IEDDA chemistries. Both chemistries allow tunability of mechanical properties which broadens the range of applications possible for injectable hydrogels. The reversibility of DA reactions have been utilized for specific functions and may be further modulated to improve DA hydrogel systems. There is increasing interest in developing highly efficient bioprinting protocols to generate tissue models and creating *in vitro* organoids for modeling diseases. This is an area where the potential of the DA and IEDDA chemistries can be exploited to allow more research groups to study and further improve injectable hydrogel biomaterials for biomedical applications.

# Chapter 3

# Self-Forming Norbornene-Tetrazine Hydrogels with Independently Tunable Properties

## 3.1 Abstract

Although photopolymerization reactions are commonly used to form hydrogels, these strategies rely on light and may not be suitable for delivering therapeutics in a minimally invasive manner. Here, hyaluronic acid (HA) macromers are modified with Nor or Tet and upon mixing click into covalently crosslinked Nor-Tet hydrogels via a Diels-Alder reaction. By incorporating a high degree of Nor and Tet substitution, Nor-Tet hydrogels with a broad range in elastic moduli (5 to 30 kPa) and fast gelation times (1 to 5 minutes) are achieved. By pre-coupling methacrylated HANor macromers with thiolated peptides via a Michael addition reaction, Nor-Tet hydrogels are peptide-functionalized without affecting their physical properties. Mesenchymal stem cells (MSCs) on RGD-functionalized Nor-Tet hydrogels adhere and exhibit stiffness-dependent differences in matrix mechanosensing. Fluid properties of Nor-Tet hydrogel solutions allow for injections through narrow syringe needles, and can locally deliver viable cells and peptides. Substituting HA with enzymatically degradable gelatin also results in cell-responsive Nor-Tet hydrogels, and MSCs encapsulated in Nor-Tet hydrogels preferentially differentiate into adipocytes or osteoblasts, based on 3D cellular spreading regulated by stable (HA) and degradable (gelatin) macromers.

## 3.2 Introduction

Hydrogels are three-dimensional and highly hydrated crosslinked polymer networks that are used in various biomedical applications including tissue engineering, drug delivery, and regenerative medicine.[2,7–9,25] To synthesize hydrogels, free-radical photopolymerization reactions using visible or ultraviolet light are commonly used due to fast gelation under physiological conditions.[43] Depending on the moities present, hydrogels can be formed via chain-growth or step-growth photopolymerization.[45,46] Free-radical chain-growth photopolymerization of acrylated macromers form hydrogels with polydisperse kinetic chains, resulting in local differences in crosslink density,[44,45] which introduces heterogeneity that could unpredictably influence cell-hydrogel interactions of encapsulated cells. In contrast, free-radical step-growth photopolymerization between molecules containing thiol and vinyl (ene) groups result in one-to-one click reactions that form hydrogels with a homogenous network structure.[45,46] Photopolymerized hydrogels have many advantages, including high biocompatibility and fast gelation times. Step-growth hydrogels also benefit from the potential for photopatterning which introduces heterogeneity to an otherwise homogeneous material.[167] Despite these advantages, free-radical photopolymerization reactions require light and thus are limited to applications where light is readily available.

Alternatives to hydrogel photopolymerization rely on other catalysts including pH, electrostatic interactions, and temperature.[36] For example, Michael-addition reactions between thiols and acrylates form hydrogels with tunable mechanical properties, and gelation rates can be decreased with increasing pH.[41,42] Michael-addition reactions are robust, and have been used to form hydrogels and have been used for static and dynamic 2D cell culture studies.[33] However, due to slow gelation times and the need for high pH buffers, these hydrogels are limited to either acellular or 2D cell culture. Alginate is an anionic biopolymer that forms ionically crosslinked hydrogels when mixed with divalent cations (e.g., $Ca^{2+}$ or $Zn^{2+}$).[3] Ionically crosslinked hydrogels form rapidly, and alginate hydrogels specifically have been extensively used for tissue engineering and cellular delivery applications.[54] Despite their high biocompatibility and ease of use, ionically crosslinked hydrogels generally feature low mechanical properties and are unstable due to the diffusion of divalent cations over time. Thermoresponsive hydrogels transition from liquid to hydrogel above a lower critical solution temperature (LCST) or below an upper critical solution temperature (UCST).[37,38] Sala et. al developed thermosensitive poly(N-vinylcaprolactam) (PNVCL) hydrogels that are liquid at room temperature and gel at a physiologic LCST.[168] Chondrocytes and mesenchymal stem cells encapsulated in these hydrogels exhibit high viability and cartilage extracellular matrix formation *in vitro* and *in vivo*. Gelatin is a thermoresponsive polymer that has a concentration-dependent UCST of ~25 to 30 °C,[39] which is not suitable for *in vivo* applications but could be leveraged for additive manufacturing processes. Although not many synthetic polymers with physiologic UCSTs exist,[53] Boustta and colleagues developed poly(N-acryloyl glycinamide) (PNAGA) hydrogels that gel when cooled to 37 °C as a potential injectable drug-releasing material.[40]

While catalyst-based hydrogel polymerization reactions can create hydrogels with myriad properties, these hydrogel techniques rely on an external input (e.g., light, pH, cations, temperature), which limits their use to conditions where a catalyst is present. Diels-Alder reactions are highly specific cycloadditions between dienes and dienophiles that do not require light or other stimuli in aqueous environments.[47,48] For example, hyaluronic acid (HA) macromers modified with furan (diene) were reacted with di-maleimide (dienophile) poly(ethylene glycol) (PEG) crosslinkers to create self-forming hydrogels.[49] Since furan-maleimide hydrogels take several hours to form at a neutral pH, these hydrogels are typically synthesized in acidic conditions not suitable for 3D cell culture. By adding an electron-donating methyl group to furan dienes, methylfuran-dialdehyde hydrogels can be synthesized in under 15 minutes at a physiologic pH.[57] However, a major limitation of Diels-Alder hydrogels formed between furans and maleimides is that these reactions are reversible and prone to hydrolysis, resulting in uncontrollable changes to hydrogel properties including swelling, stiffness, and porosity.[57,58] By using electron-rich cyclic fulvenes in lieu of furan dienes, Madl & Heilshorn formed more stable fulvene-maleimide hydrogels that support 3D cell culture.[136]

Although these Diels-Alder reactions can create biocompatible, self-forming hydrogels, hydrogel mechanics are low (storage modulus, $G' < 1{,}000$ Pa) and gelation times are high (upwards of 3 hours). Diels-Alder reactions between Tet (diene) and Nor (dienophile) are irreversible and offer an alternative chemistry for creating self-forming hydrogels with tunable properties.[50,59,60] Hydrogels that use this chemistry were first reported by Alge et. al, by reacting 4-arm PEG-Tet with di-Nor peptides.[60] By including Nor-modified RGD, biocompatible self-forming hydrogels with adhesive domains were created, with storage moduli ranging from 225 to 2,345 Pa by varying PEG-Tet concentration. In another study, by modifying alginate biopolymers with Nor or Tet moieties (5% Nor and Tet substitution), hydrogels with increased mechanical properties (elastic modulus ~15 kPa for 4% w/v hydrogels) were formed.[50] Although these hydrogels are structurally stable and support 3D cell culture, hydrogel polymerization is slow (> 1 hour), which limits their clinical use and could cause an inhomogeneous cell distribution during gelation. By using gelatin macromers with higher Nor (GelNor) and Tet (GelTet) substitution (~20%), Koshy et al. synthesized rapid self-forming hydrogels that gel as little as ~5 minutes with a G′ of ~4,000 Pa.[59]

We hypothesize that by increasing the degree of substitution of Nor and Tet moieties, self-forming hydrogels with fast gelation times and superior mechanics can be achieved. We also hypothesize that macromers pre-coupled with peptides can be used to incorporate bioactive motifs to Nor-Tet hydrogels without impacting mechanical properties or gelation rates. In this study, carboxyl groups of HA macromers were modified with Nor (HANor, 50% substitution) or Tet (HATet, 40% substitution) to create self-forming Nor-Tet hydrogels. Mechanical properties and gelation kinetics were controlled by tuning the total macromer concentration and the stoichiometric ratio between HANor and HATet macromers. By modifying HANor hydroxyl groups with methacrylates (HANorMe), thiol-containing peptides were pre-coupled to methacrylates in HANorMe macromers and used to form peptide-functionalized Nor-Tet hydrogels. Using this platform, we investigated matrix mechanosensing of MSCs on 2D RGD-functionalized Nor-Tet hydrogels and the protective effects of Nor-Tet hydrogel solutions on MSCs injected from needles of clinically relevant dimensions. Further, by substituting HA in HANor with enzymatically degradable gelatin (GelNor), we controlled MSC spreading and MSC differentiation into adipogenic (round, HANor) or osteogenic (spread, GelNor) lineages of encapsulated MSCs cultured in bipotential adipogenic/osteogenic (AD/OS) induction medium.

## 3.3 Results and Discussion

### *3.3.1 Macromer Synthesis and Nor-Tet Hydrogel Polymerization*

HANor macromers were synthesized by converting sodium hyaluronate (HA) to its tetrabutylammonium salt (HATBA), followed by an anhydrous benzotriazole-1-yl-oxy-tris(dimethylamino)-phosphonium hexafluorophosphate (BOP) reaction in dimethyl sulfoxide (DMSO) between carboxyl groups in HATBA and amines in norbornene amine (Nor-$NH_2$) (Figure 6A).[167] HATet macromers were synthesized by reacting carboxyl residues in HATBA with amines in tetrazine amine (Tet-$NH_2$) in the presence of 1-(3-dimethylaminopropyl)-3-ethylcarbodiimide (EDC) and N-hydroxysuccinimide (NHS) (Figure 6B).[50,59] Upon mixing, HANor and HATet macromers self-form into stable Nor-Tet hydrogels (Figure 6C). At 37 °C, the storage modulus (G´) of 2% w/v hydrogels after 60 (1,800 ± 100 Pa) and 180 (1,930 ± 120 Pa) minutes is not statistically significant (Figure 6D), demonstrating that Nor-Tet hydrogels self-form in under an hour. To evaluate the specificity of Diels-Alder reactions between HANor and HATet, two tests were performed. HANor or HATet were first mixed with unmodified HA, resulting in no hydrogel formation (Figure 7A). HANor and HATet were also mixed in the presence of either Nor-$NH_2$ or Tet-$NH_2$ molecules in excess (1,000x). Here, the unbound Nor and Tet molecules bind to their respective Diels-Alder partners, preventing hydrogels from forming (Figure 7B). These findings demonstrate that the Diels-Alder reactions between Nor and Tet are highly specific and necessary for Nor-Tet hydrogels to self-form.

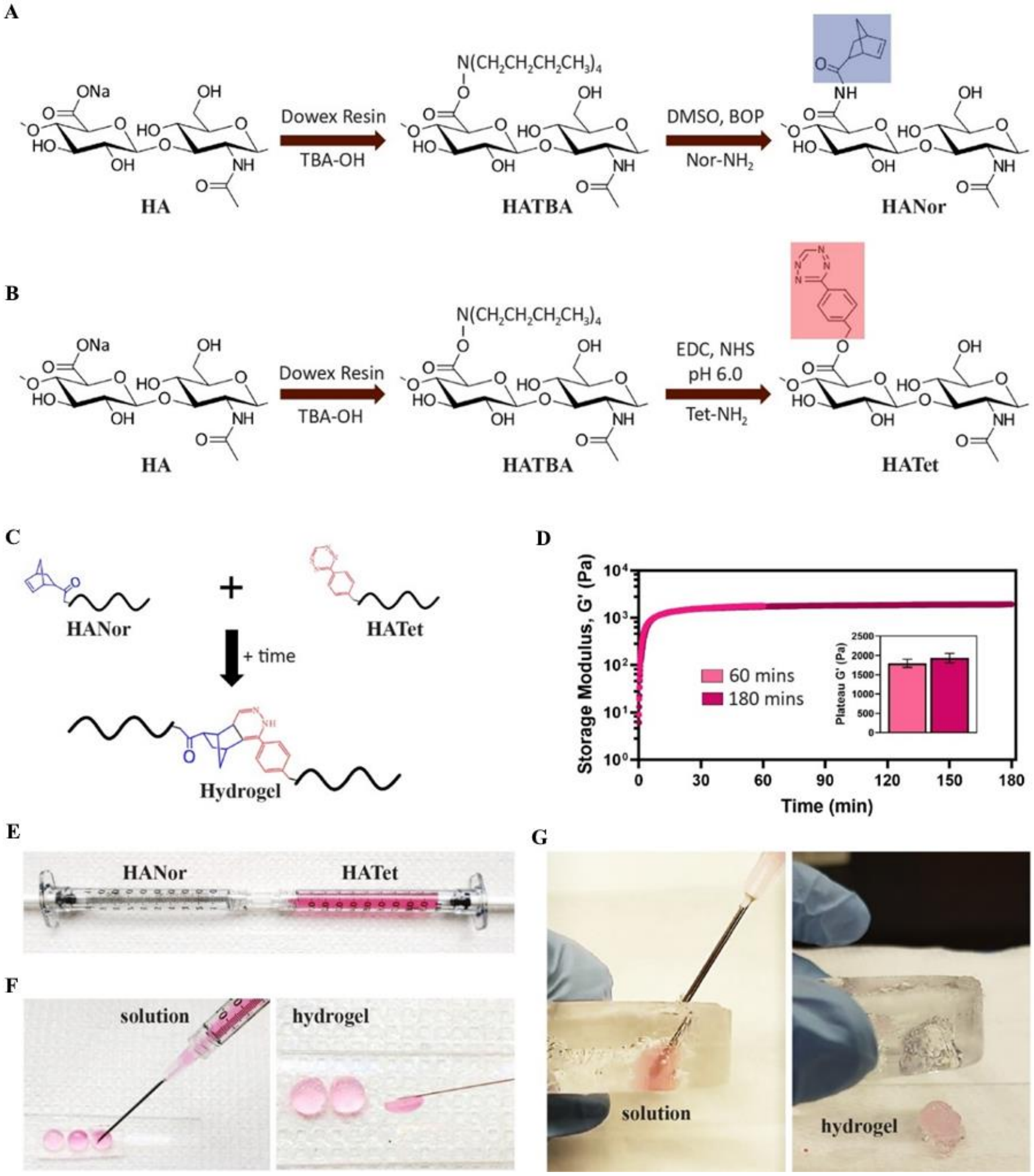

*Figure 6.* Macromer synthesis and Nor-Tet hydrogel polymerization. **(A)** HA macromers modified with Nor (HANor) or **(B)** Tet (HATet) **(C)** spontaneously from stable crosslinked hydrogels when combined. **(D)** Representative time sweep rheology plot of 2% w/v Nor-Tet hydrogels polymerizing at 37 ºC for 60 minutes and 180 minutes. **(E)** HANor and HATet macromers can be dissolved rapidly at room temperature and loaded into syringes for mixing through a Luer-Lock coupler. Mixed macromers remain in solution long enough for extrusion into **(F)** molds or **(G)** cavities, resulting in self-forming hydrogels that conform to the shape of space they occupy.

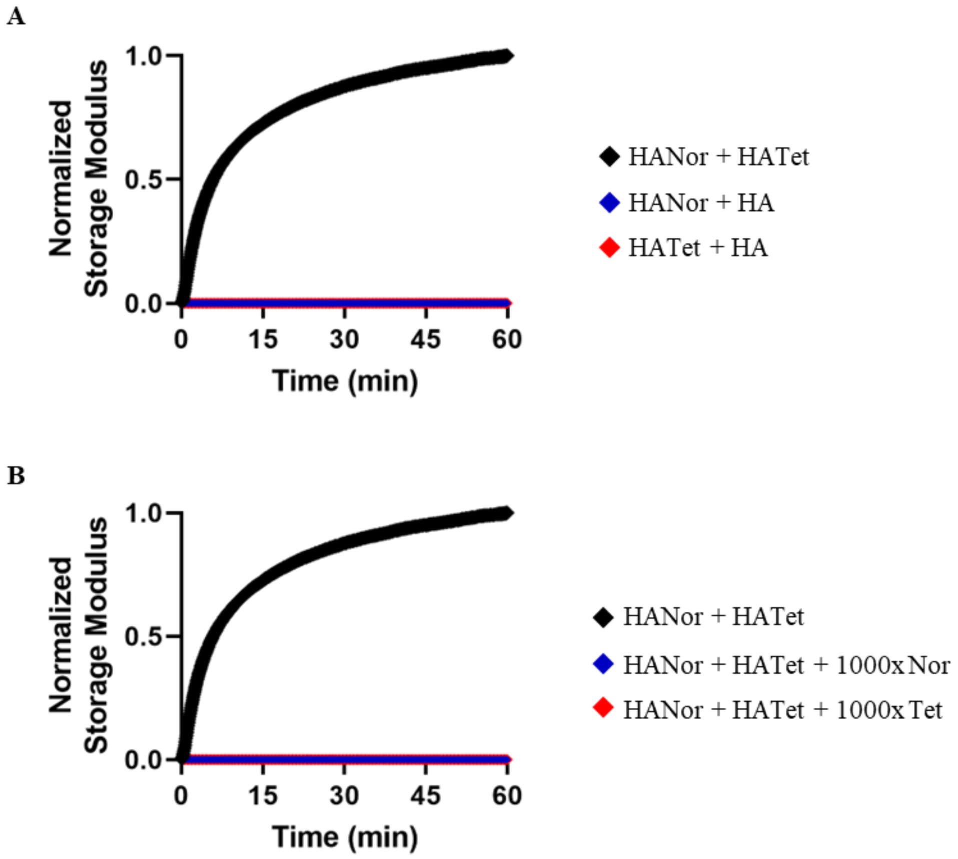

*Figure 7.* Storage modulus (G′) evolution through time sweep rheometry for **(A)** 2% w/v Nor-Tet hydrogels normalized to plateau G´ of the HANor + HATet group (black diamond). Mixing of HANor with unmodified HA (blue diamond) or HATet with unmodified HA (red diamond) does not result in crosslinking. **(B)** 2% w/v Nor-Tet hydrogels normalized to plateau G´ of the HANor + HATet group (black diamond). Addition of free Nor (blue diamond) or Tet (red diamond) molecules (1000x molar excess) to the mixture abrogates HANor crosslinking with HATet. 1,000x molar excess of free Nor is equivalent to 2.5 mM Nor-$NH_2$. 1,000x molar excess of free Tet is equivalent to 1.6 mM Tet-$NH_2$.

We next sought to determine how the inclusion of Nor and Tet moieties could impact fluid viscosity of HANor and HATet macromers in solution since this is an important parameter for developing injectable materials and bioinks for 3D printing. Alge et al. showed that solutions containing gelatin functionalized with 20% Nor and Tet pendant groups were less viscous than solutions of unmodified gelatin,[59] and this may be due to the presence of Nor and Tet interrupting with physical interactions required for the thermogelation of gelatin.[169] HANor and HATet macromers used in this study have approximately 50% and 40% of their repeat units functionalized with Nor and Tet, respectively, as confirmed by $^1$H NMR (400 MHz, $D_2O$) (Figure 8), which is significantly higher than Nor and Tet substitutions used by other Diels-Alder Nor-Tet hydrogels.[50,59] At 37 °C, the viscosity of unmodified HA ranges from 3.3 to 76.2 mPa s for 2% to 6% w/v solutions (Table 1). Nor and Tet substitutions result in a modest decrease in viscosity for 2% and 4% w/v HANor and HATet solutions, and a much larger decrease in viscosity for 6% w/v HANor (37.8 mPa s) and HATet (36.3 mPa s) solutions (Table 1). The presence of Nor and Tet results in a decrease in viscosity, and the viscosities for 2%, 4%, and 6% w/v HANor and HATet solutions are well below the upper limit of viscous bioinks and fluids (> 300 mPa s)[170,171] that can result in needle clogging and heterogeneous mixing post-hydrogel extrusion.[172]

HANor and HATet macromers can be dissolved at room temperature in aqueous media, loaded into a syringe, and mixed with a syringe coupler (Figure 6E). Upon mixing, the hydrogel solution will begin to polymerize while allowing for sufficient time to extrude through a needle prior to self-forming into a hydrogel that conforms into any shape ranging from cylindrical molds (Figure 6G) to amorphous cavities (Figure 6G). Gelation time is an important parameter of self-forming hydrogels and ideally, injectable hydrogels should polymerize within a few minutes post-injection under physiological conditions.[173] For *in vivo* applications, hydrogels that polymerize too slowly could diffuse into surrounding tissues, leading to the unwanted presence of hydrogel material away from the target site, whereas hydrogels that form too quickly can polymerize prematurely in the needle prior to reaching the targeted site. Nor-Tet hydrogels with 2% to 6% w/v macromer concentration can be readily dissolved and mixed with sufficient time to locally deliver hydrogel that is contained within a region of interest (e.g., molds, cavities).

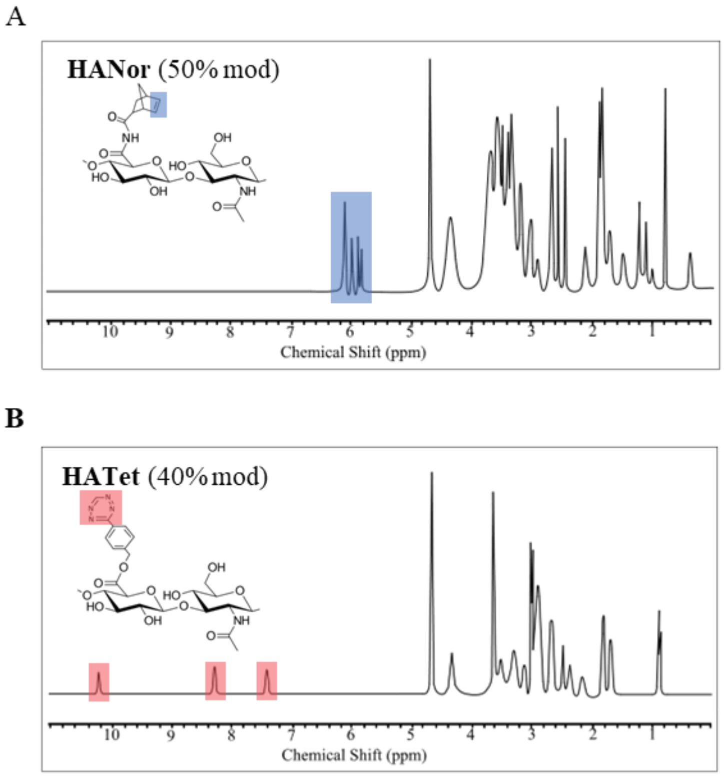

*Figure 8.* $^1$H-NMR spectra of HANor and HATet.

**Table 1**

*Viscosity of Polymers Used in Hydrogel Formation at 37 ºC. Viscosities of HA, HANor, and HATet at 2, 4, and 6% w/v*

| Polymer | 2% w/v [mPa·s] | 4% w/v [mPa·s] | 6% w/v [mPa·s] |
|---|---|---|---|
| **HA** | 3.3 ± 0.7 | 17.3 ± 2.7 | 76.2 ± 10.2 |
| **HANor** | 3.1 ± 0.5 | 16.4 ± 2.4 | 37.8 ± 5.6 |
| **HATet** | 2.4 ± 0.4 | 15.1 ± 1.7 | 36.3 ± 4.7 |

### *3.3.2 Physical Properties of Self-Forming Nor-Tet Hydrogels are Highly Tunable*

To evaluate mechanics and gelation properties of self-forming hydrogels, HANor and HATet macromers were mixed at 2%, 4%, or 6% total w/v macromer concentration. Frequency sweep rheology (0.1 to 10 Hz) at 37 °C shows that the storage modulus (G´) is above the loss modulus (G″) and that G´ is constant across a range of oscillatory frequencies (Figure 9A), demonstrating the formation of stable hydrogels post-mixing. Nor-Tet hydrogel mechanics also increase with increasing macromer concentration (Figure 9B). The range in hydrogel mechanics achieved is large, with G´ values of 1,800 ± 100 Pa (2% w/v), 6,300 ± 1,000 Pa (4% w/v), and 12,500 ± 1,100 Pa (6% w/v) (Figure 9C). To determine the elastic modulus (E), cylindrical Nor-Tet hydrogels (8 mm diameter, 2 mm height) were subject to compression testing, with E values ranging from ~5 kPa (2% w/v) to ~30 kPa (6% w/v) (Figure 10). Gelation rates also decreased with increasing macromer content. For 2% w/v Nor-Tet hydrogels, it took 5.80 ± 0.24 minutes to reach 50% of their final G´, and gelation time decreased for 4% w/v (2.04 ± 0.34 min) and 6% w/v (0.83 ± 0.44 min) hydrogels (Figure 9D).

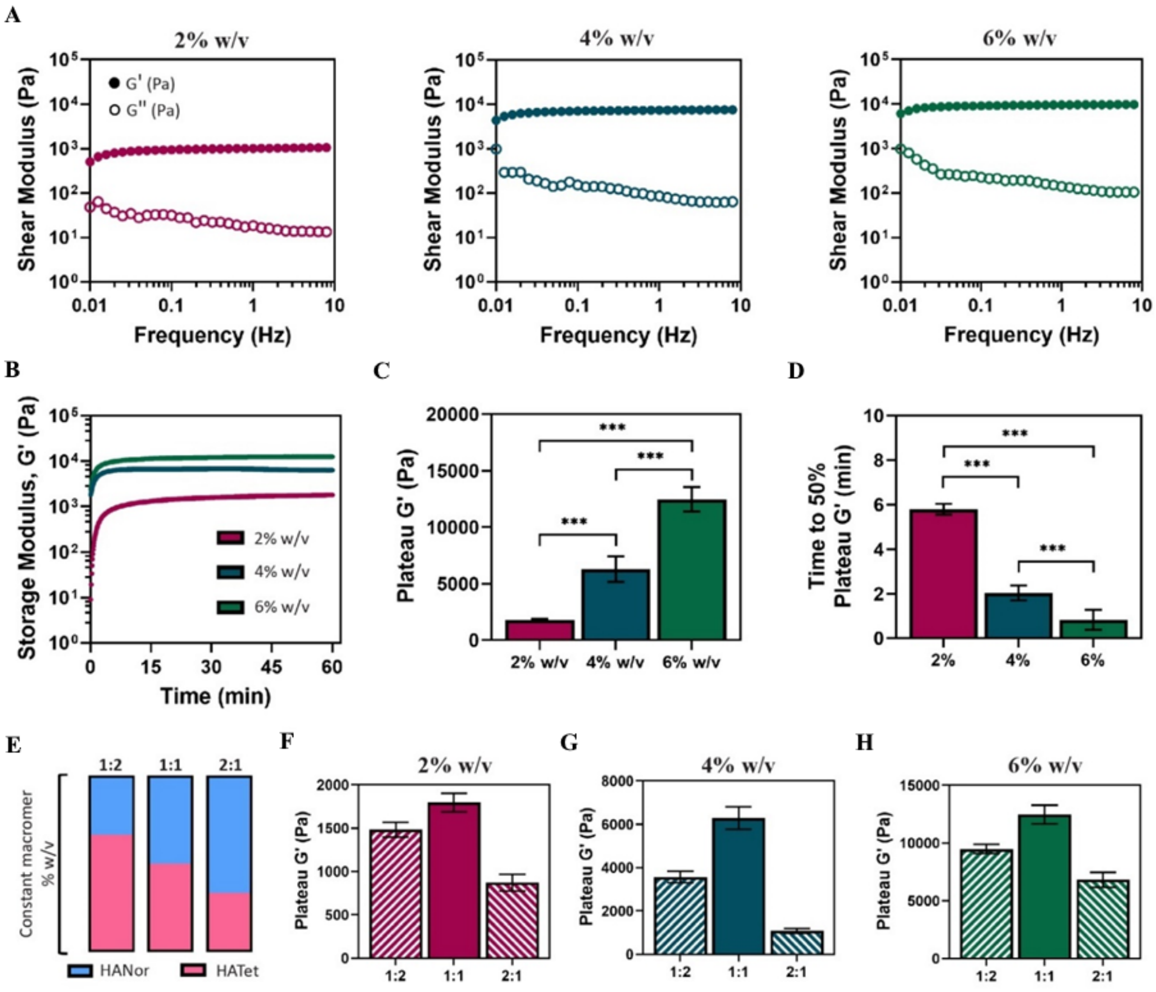

*Figure 9*. Physical characterization of self-forming hydrogels at 37 °C. **(A)** Representative frequency sweep rheology plot shows storage (G′) and loss moduli (G″) of 2%, 4%, and 6% w/v Nor-Tet hydrogels at a 1:1 stoichiometric ratio. **(B)** Representative time sweep rheology plot was used to determine **(C)** plateau G′ and **(D)** time to 50% plateau G′ of 2%, 4%, and 6% w/v Nor-Tet hydrogels at a 1:1 stoichiometric ratio. **(E)** HANor and HATet were mixed at a 1:2, 1:1, or 2:1 stoichiometric ratio and the plateau G′ was determined for **(F)** 2%, **(G)** 4%, and **(H)** 6% w/v Nor-Tet hydrogels. Bar graphs shown as mean ± SD (n ≥ 3 samples per condition) with significant differences determined with ANOVA followed by Tukey's post hoc test where ***$p < 0.005$.

The range in Nor-Tet hydrogel mechanics achieved by simply increasing the total macromer concentration is significantly larger than previous systems that use a Diels-Alder chemistry (Table 2). This could be due to irreversible bonds formed between Nor and Tet and the high degree of Nor and Tet substitution in the HANor and HATet macromers. For instance, Diels-Alder reactions between Fur or methyl-Fur and Mal are reversible, resulting in hydrogels that are unstable over time with low mechanical properties. While replacing Fur with fulvenes increases the stability of self-forming hydrogels, the mechanical properties are still low (< 1,000 Pa), possibly due to a low amount of maleimides and fulvenes present.[136] Additionally, hydrogel formation is inherently slow,[136] which could result in low retention at a target site post-injection and in increased hydrogel heterogeneity. By using Tet as the diene and Nor as the dienophile, irreversible bonds form during gelation, resulting in mechanically stable, biocompatible self-forming hydrogels. Further, by using HANor and HATet macromers with a high degree of Nor (50%) and Tet (40%) substitution, rapidly forming hydrogels with a large range of mechanics were formed, and it is expected that an even broader range of mechanical properties is possible by increasing the number of Nor and Tet moieties, either by further increasing the degree of substitution, or by using higher molecular weight HA macromers.

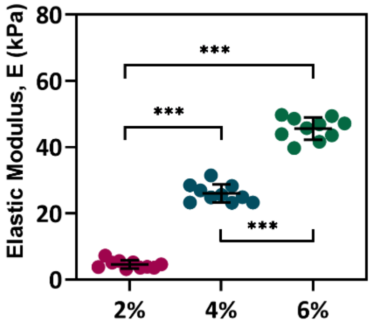

*Figure 10.* Elastic moduli of 2%, 4%, and 6% w/v Nor-Tet hydrogels. Values were determined using compression mechanical testing**.** Scatter dot plot shown as mean ± SD ($n \geq 6$ samples per condition) with significant differences determined with ANOVA followed by Tukey’s post hoc test where $***p < 0.001$.

To further explore the physical properties of self-forming Nor-Tet hydrogels, HANor and HATet were mixed at different stoichiometric ratios (HANor:HATet) at a constant total macromer concentration (Figure 9E). For 2% w/v Nor-Tet hydrogels, the plateau G´ varied for different HANor:HATet ratios, with the highest mechanics observed at a 1:1 ratio (1,800 ± 110 Pa), followed by 1:2 (1,500 ± 90 Pa) and 2:1 (900 ± 100 Pa) ratios (Figure 9F). Similarly, for 4% and 6% w/v Nor-Tet hydrogels, highest mechanics were seen at a 1:1 ratio, with second and third highest G´ observed in 1:2 and 2:1 HANor:HATet ratios, respectively (Figure 9G and 9H). The range in mechanics by simply varying the HANor:HATet ratio was significant at a constant macromer concentration. In 4% w/t Nor-Tet hydrogels there was an over 5-fold change (1,100 ± 110 to 6,300 ± 500 Pa) and in 6% w/v Nor-Tet hydrogels an almost 2-fold change (6,800 ± 700 to 12,500 ± 800 Pa) in G´ between 2:1 and 1:1 HANor:HATet ratios. These findings demonstrate that mechanical properties can be independently controlled while maintaining biopolymer concentration constant. This is useful in tuning hydrogel mechanics without changing fluid properties (e.g., viscosity) that could impact extrusion parameters.

**Table 2**

*Diene and Dienophiles Used in Diels-Alder Reactions with Corresponding Storage Moduli (G') and Gelation Times*

| Diene | Dienophile | Storage modulus, G´ | Gelation time | Reference |
|---|---|---|---|---|
| Furan | Di-Maleimide | < 1,000 Pa | 120 – 180 min | [49] |
| Methylfuran | Di-Maleimide | < 1,500 Pa | 15 min | [57] |
| Furan | Maleimide | 5,000 – 35,000 Pa | 15 – 170 min | [58] |
| Fulvene | Maleimide | < 1,000 Pa | 6 – 35 min | [136] |
| Tetrazine | Di-Norbornene | < 2,500 Pa | < 10 min | [60] |
| Tetrazine | Norbornene | < 500 Pa | 100 min | [50] |
| Tetrazine | Norbornene | < 4,500 Pa | < 15 min | [59] |

Interestingly, the rate of hydrogel formation also changed with varying HANor:HATet ratios at a constant biopolymer concentration. For 2% w/v Nor-Tet hydrogels, gelation time increased from 5.80 minutes at a 1:1 Nor:Tet ratio to 12.30 minutes for a 2:1 Nor:Tet ratio (Figure 11A). The same trends were observed for 4% and 6% w/v Nor-Tet hydrogels, with the shortest gelation time seen at a 1:1 Nor:Tet ratio, and second and third longest gelation times at 1:2 and 2:1 Nor:Tet ratios, respectively (Figure 11B, 11C). An increase in total macromer concentration corresponds to higher mechanics and a decrease in gelation kinetics,[50,59] and this observation shows that changing the amount of Nor and Tet moieties at a fixed macromer concentration also regulates gelation time.

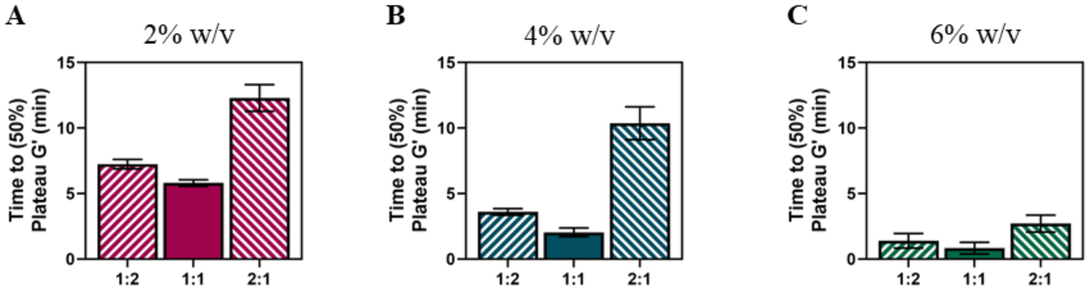

*Figure 11.* Time to 50% plateau G′ of **(A)** 2%, **(B)** 4%, and **(C)** 6% w/v Nor-Tet hydrogels at 1:2, 1:1, and 2:1 HANor:HATet stoichiometric ratios. Bar graphs shown as mean ± SD (n ≥ 3 samples per condition).

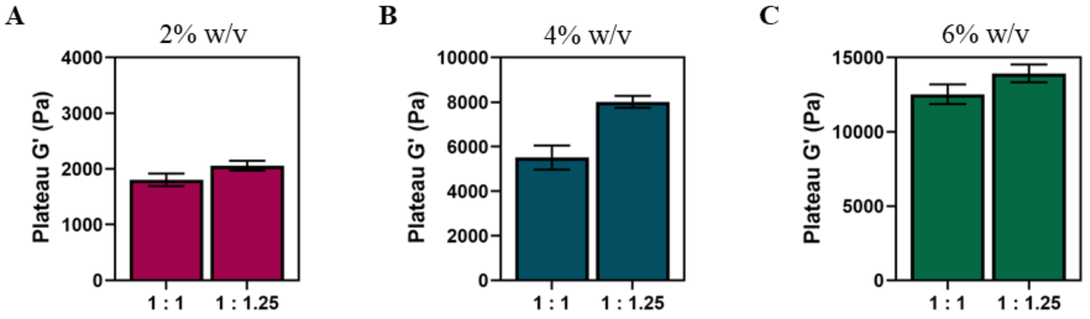

*Figure 12.* Physical characterization of Nor-Tet hydrogels at 37 ºC - Plateau G′ of **(A)** 2%, **(B)** 4%, and **(C)** 6% w/v Nor-Tet hydrogels at 1:2, 1:1, and 2:1 HANor:HATet stoichiometric ratios. Bar graphs shown as mean ± SD (n ≥ 3 samples per condition).

At a 1:1 Nor:Tet ratio, there is approximately 25% more Nor than Tet moieties, since the degree of substitution for the HANor and HATet macromers used is 50% and 40%, respectively. Thus, it is expected that the theoretical maximum stiffness (and minimum gelation time) would occur at a ratio where Nor and Tet moieties are equal. Based on 50% HANor and 40% HATet modifications, this corresponds to a 1:1.25 HANor:HATet ratio. At this optimal ratio, mechanics for 2%, 4%, and 6% w/v Nor-Tet hydrogels were higher than Nor-Tet hydrogels formed at a 1:1 HANor:HATet stoichiometric ratio (Figure 12). The storage modulus G′ increased from 1,800 to 2,100 Pa for 2% w/v, 6,300 to 8,000 Pa for 4% v/w, and 12,500 to 14,000 Pa for 6% w/v Nor-Tet hydrogels. These findings show that Diels-Alder Nor-Tet reactions are highly specific, and that maximal mechanics are achieved when the amount of Nor and Tet moieties present is equal.

### *3.3.3 Self-Forming Hydrogels can be Peptide Functionalized without Changing Mechanics*

Hydrogels formed with a Diels-Alder Nor-Tet chemistry cannot be peptide-functionalized without affecting crosslinking density or requiring a secondary photoreaction post-hydrogel polymerization.[50,60] To functionalize Nor-Tet hydrogels with adhesive RGD peptides, Alge and coworkers bound Nor-RGD to multi-arm PEG-Tet, resulting in competition between Nor-RGD and di-Nor crosslinker peptides for available Tet sites.[60] In another study, Desai et al. used a thiol-ene photopolymerization reaction to couple thiolated RGD peptides to pendant Nor moieties in pre-formed alginate Nor-Tet hydrogels.[50]. As an alternate strategy, in this study Nor-Tet hydrogels with independent control over peptide functionalization were created by tethering thiolated RGD peptides to HANor via a two-step process (Figure 13).

First, hydroxyl groups in HANor were modified with methacrylates (Me) via esterification with methacrylic anhydride,[174] resulting in an HANorMe macromer (Figure 13A). Next, Me groups in HANorMe and thiols in thiolated RGD (cRGD) peptides were covalently bound via a Michael-addition reaction,[175] resulting in HANor(cRGD+) (Figure 13B), an HANor macromer that is peptide-functionalized without altering Nor groups dedicated for Nor-Tet hydrogel formation. By varying the amount of cRGD reacted with a constant amount of HANorMe, the effective concentration of RGD was kept at 2 mM for 2%, 4%, and 6% w/v Nor-Tet hydrogels (Table 1 ). $^1$H NMR was used to confirm Nor (50%), Me (78%), and cRGD modification (Figure 13C). To maintain a constant effective concentration, the amount of cRGD peptide added to HANorMe during synthesis was adjusted accordingly. Less peptide coupling to HANorMe should occur for increasing total macromer concentration, which was confirmed by $^1$H NMR to be 17%, 9%, and 6% cRGD modification for 2%, 4%, and 6% w/v Nor-Tet hydrogels, respectively (Figure 14). At least 60% of Me sites are available for coupling after functionalization with cRGD, and these unreacted Me moieties can be used to either increase the effective concentration of cRGD or modify biochemical properties by adding other thiolated peptides.

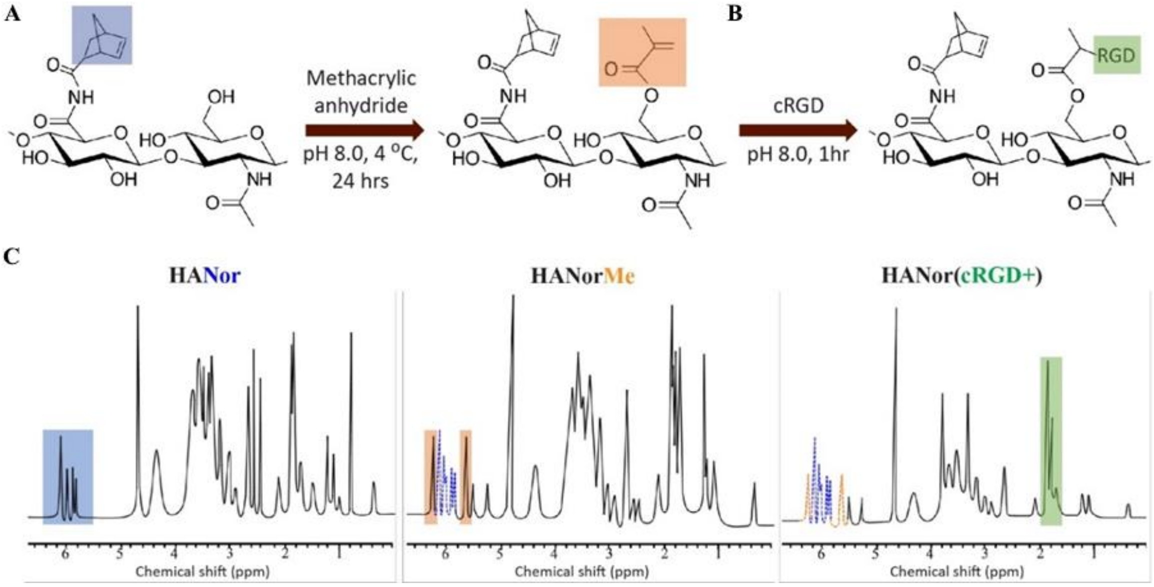

*Figure 13.* HANor macromers functionalized with thiolated peptides. **(A)** Hydroxyl groups in HANor macromers are coupled with methacrylic anhydride to form HANorMe macromers. **(B)** HANorMe macromers are then mixed with thiolated RGD adhesive peptide (cRGD) to form peptide functionalized HANor(cRGD+) macromers. **(C)** 1H NMR spectra shows peaks corresponding to norbornene (blue, left), methacrylate (orange, middle), and cRGD (green, right) modifications to the HA backbone.

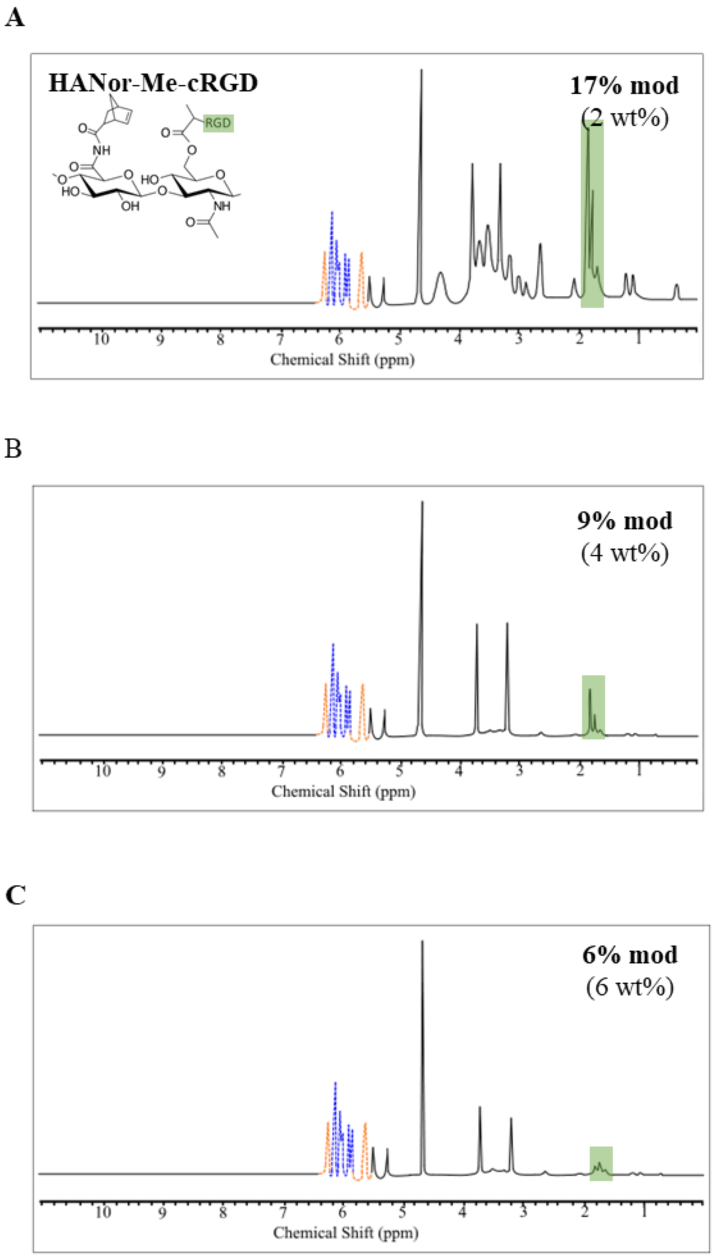

*Figure 14.* $^1$H-NMR spectra of HANor(cRGD+). Distinct peaks for cRGD peptides are seen, and these peaks decrease with increasing Nor-Tet w/v. 1H NMR spectra for HANor(cRGD+) used to form **(A)** 2%, **(B)** 4%, and **(C)** 6% w/v Nor-Tet hydrogels.

To confirm that peptide modifications to the hydroxyl group do not impact Nor moieties used for Nor-Tet binding, HATet was mixed with either HANor, HANorMe, or HANor(cRGD+) at 2%, 4%, or 6% total macromer w/v at a 1:1 macromer ratio. Time sweep rheology shows that G′ increases with increasing w/v, and that no discernable changes in gelation from Me substitution or RGD peptide functionalization are observed (Figure 15A). Final mechanical properties (plateau G´) did not change across the macromer groups for 2% (1,800 ± 110 Pa), 4% (6,300 ± 1,000 Pa), and 6% (12,500 ± 1,100 Pa) w/v Nor-Tet hydrogels (Figure 15B). Additionally, peptide functionalization did not have a significant effect on gelation times, with times to 50% plateau G´ of 5.80 ± 0.24, 2.04 ± 0.34, and 0.83 ± 0.44 minutes for 2%, 4%, and 6% w/v Nor-Tet hydrogels, respectively (Figure 15C). Elastic moduli (E) of fully formed cylindrical hydrogels yielded consistent results across the different macromer groups for 2% (4.6 ± 1.2 kPa), 4% (26.1 ± 2.7 kPa), and 6% (45.2 ± 4.1 kPa) w/v Nor-Tet hydrogels (Figure 15D). These results show that Nor-Tet hydrogels can be biofunctionalized with thiolated peptides without affecting mechanical properties and gelation kinetics. Although cRGD was used, this procedure can be applied to any thiol-containing molecule. For example, the thiol-containing cDWIVA peptide mimetic of the growth factor Bone Morphogenetic Protein 2 can be tethered for osteogenic application.[72,176,177] The effective peptide concentration can be easily tuned by varying the amount of peptide mixed with HANorMe during thiol-methacrylate peptide coupling.

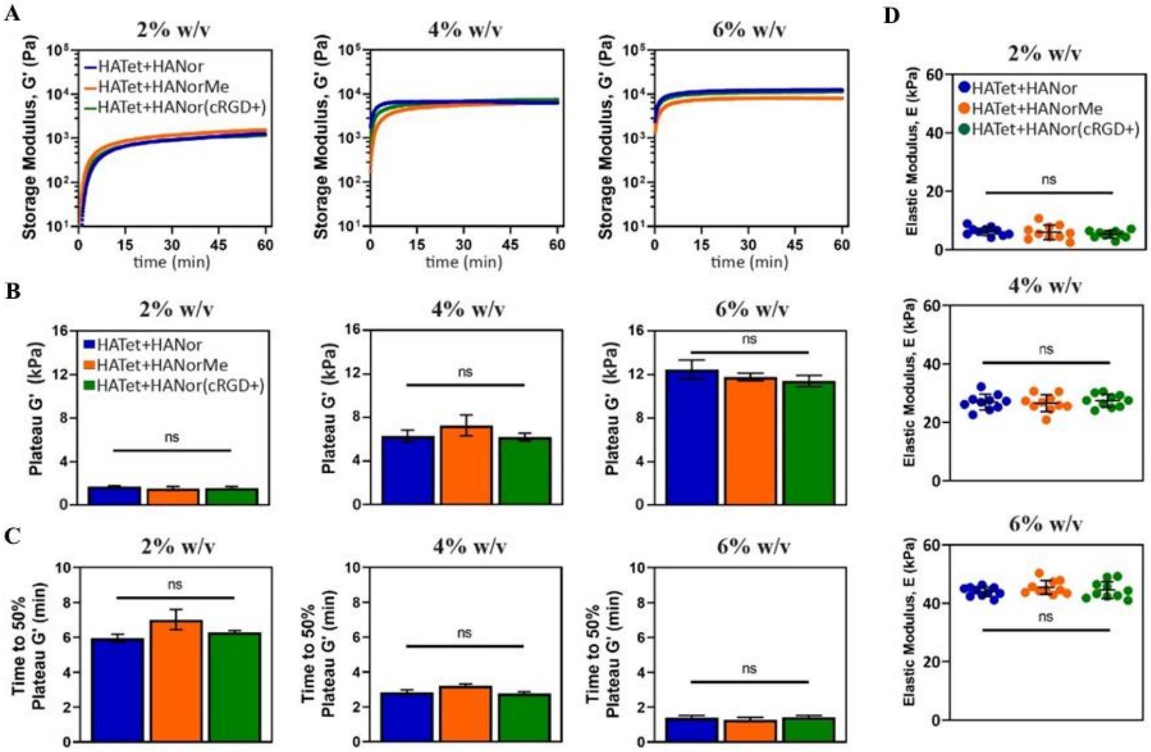

*Figure 15.* Peptide coupling does not affect mechanical properties of Nor-Tet hydrogels. **(A)** Representative time sweep rheology of G′ kinetics for 2%, 4%, and 6% w/v Nor-Tet hydrogels was used to determine **(B)** plateau G′ and **(C)** time to 50% plateau G′. **(D)** Compression testing of 2%, 4%, and 6% w/v Nor-Tet hydrogels formed in cylindrical molds was used to determine elastic modulus (E). Bar graphs shown as mean ± SD (n ≥ 3 samples per condition) with significant differences determined with ANOVA followed by Tukey's post hoc test where ns is not significant.

### *3.3.4 Cells Adhere and Proliferate on RGD-Functionalized Nor-Tet Hydrogels*

After demonstrating that Nor-Tet hydrogels can be independently functionalized with peptides without altering mechanics, their use as a biocompatible cell culture platform was investigated. Since cellular adhesion to unmodified HA hydrogels is poor,[178,179] adhesive molecules need to either be passively adsorbed or chemically bound to HA hydrogels to support cell adhesion. To confirm the bioactivity of adhesive RGD peptides, HANor with or without coupled cRGD was mixed with HATet and extruded into silicone molds (8 mm diameter, 0.5 mm height), to form adhesive (cRGD+) or nonadhesive (cRGD-) Nor-Tet hydrogels (Figure 16A). Human MSCs (MSCs, 3,000 cells $cm^{-2}$) were then cultured on top of Soft (2% w/v, 4.6 kPa E) or Stiff (6% w/t, 45.2 kPa E) self-forming Nor-Tet hydrogels (Figure 16B) and cellular adhesion and proliferation were evaluated.

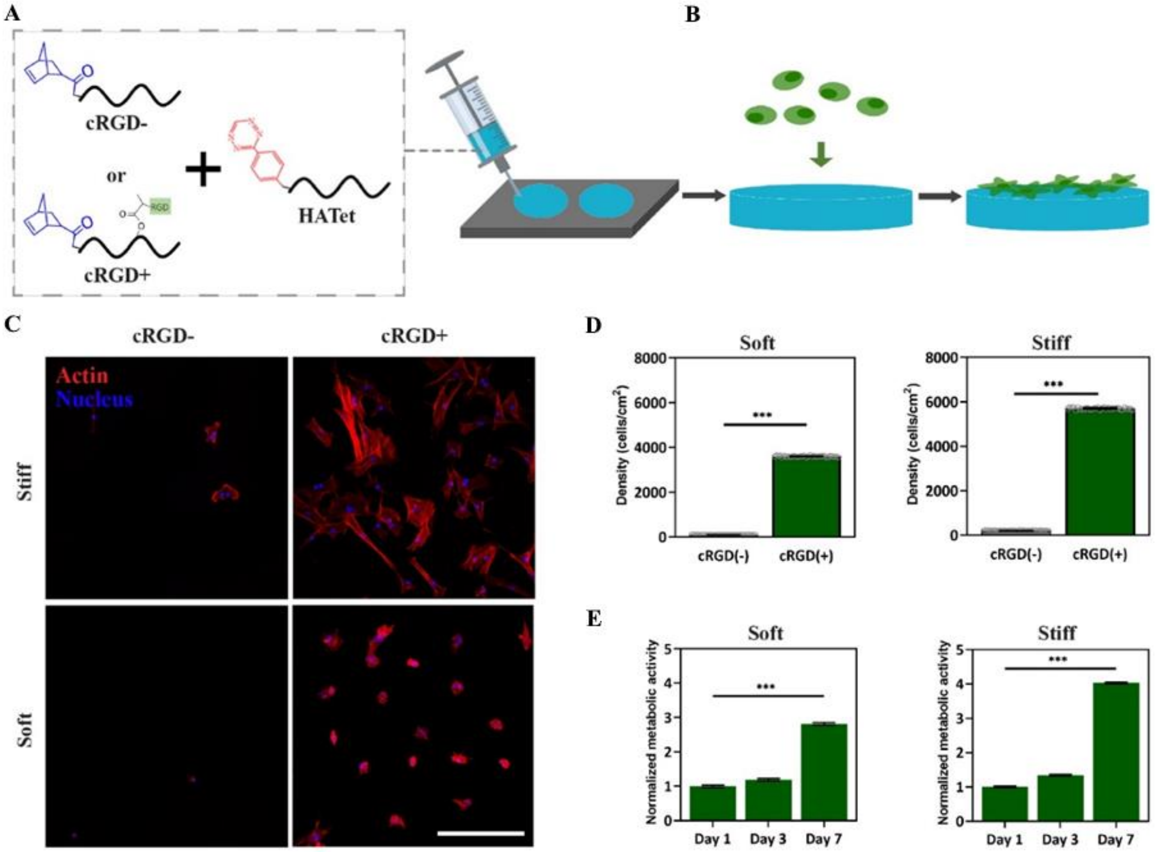

*Figure 16.* 2D cell attachment and proliferation on cRGD-functionalized Nor-Tet hydrogels. **(A)** HANor macromers with or without cRGD functionalization were mixed with HATet, injected into cylindrical molds, and **(B)** MSCs were cultured on cRGD+ and cRGD- Nor-Tet hydrogels. **(C)** Representative maximum projection images (actin, red; nuclei, blue) of MSCs on Soft or Stiff Nor-Tet hydrogels with or without covalently bound cRGD. Confocal images were used to determine MSC Density (number of nuclei cm-2) on **(D)** Soft and Stiff Nor-Tet hydrogels with or without cRGD. AlamarBlue assay was performed on day 1, 3, and 7 to quantify normalized metabolic activity of MSCs on RGD-functionalized **(E)** Soft and Stiff Nor-Tet hydrogels. Bar graphs shown as mean ± SD ($n \geq 3$ samples per condition) with significant differences determined with ANOVA followed by Tukey's post hoc test where $***p < 0.005$. Scale bar: 500 µm.

After three days in culture, representative fluorescent images of MSCs show minimal cell attachment on Soft and Stiff cRGD- hydrogels, while significant cell atttachment is observed on Soft and Stiff Nor-Tet hydrogels functionalized with RGD (Figure 16C). Quantification of cell density (number of cells $cm^{-2}$) of MSCs on Soft Nor-Tet hydrogels confirms poor cell attachment on cRGD- hydrogels (100 ± 5 cells $cm^{-2}$), whereas significant attachment was observed on cRGD+ Nor-Tet hydrogels (3,600 ± 20 cells $cm^{-2}$) (Figure 16D). Cell counts on Stiff Nor-Tet hydrogels is also higher for MSCs on cRGD+ (5,700 ± 40 cells $cm^{-2}$) hydrogels in comparison to cRGD- (201 ± 11 cells $cm^{-2}$) Nor-Tet hydrogels. The cell density on Soft and Stiff cRGD+ hydrogels was higher than the initial seeding density (3,000 cells $cm^{-2}$), suggesting that MSCs adhere and proliferate on RGD-functionalized 2D Nor-Tet hydrogels. To evaluate cell proliferation over time, MSCs were cultured on Soft and Stiff cRGD+ Nor-Tet hydrogels and metabolic activity was measured after 1, 3, and 7 days in culture using an alamarBlue assay. On both Soft and Stiff Nor-Tet hydrogels, there was a subtle increase in metabolic activity between one and three days, followed by a much larger increase between 3 and 7 days (Figure 16E). While Soft and Stiff hydrogels support MSC adhesion and proliferation, Stiff Nor-Tet hydrogels displayed higher MSC densities and metabolic activity, which is due to stiffness-dependent differences in matrix mechanosensing.[180]

### *3.3.5 Matrix Stiffness Regulates MSC Morphology and Matrix Mechanosensing on RGD-Functionalized Nor-Tet Hydrogels*

An important characteristic of stem cells is their ability to sense and respond to mechanical cues.[181] For example, MSCs on soft hydrogels that mimic the stiffness of brain tissue express neural biomarkers, whereas MSCs cultured on more rigid hydrogels preferentially differentiate into cell types present in stiffer tissues, like muscle or bone.[70]

At the cellular level, changes in cell shape and spreading occur in response to mechanical cues shortly after making initial contact with their new environment.[70,182] On a molecular level, matrix mechanosensing is led by several mechano-transducer proteins that collectively induce changes in focal adhesion maturation,[183] cytoskeletal contractility,[184] and nuclear Yes-associated protein (YAP) localization.[185] To highlight the use of the self-forming Nor-Tet hydrogels presented as a facile platform for matrix mechanosensing studies, MSCs were cultured on Soft and Stiff RGD-functionalized hydrogels for three days and stiffness-dependent changes in morphology (area, roundness, aspect ratio) and mechanosensing (nuclear YAP localization, focal adhesion maturation, actin anisotropy) were evaluated.

Representative silhouettes of MSCs on Soft and Stiff hydrogels show large differences in morphology induced by Nor-Tet hydrogel stiffness (Figure 17A). MSCs on Soft Nor-Tet hydrogels were significantly smaller (1,500 ± 600 $\mu m^2$) than MSCs on Stiff Nor-Tet hydrogels (3,500 ± 300 $\mu m^2$) (Figure 17B). MSCs were also signficantly rounder on Soft Nor-Tet hydrogels (Figure 17C) and had a larger aspect ratio on Stiff Nor-Tet hydrogels (Figure 17D). These results are consistent with morphology of MSCs on photopolymerized HA hydrogels of comparable stiffness.[186,187] For example, MSCs on softer (1 kPa) HANor hydrogels had an approximate average area of 650 $\mu m^2$, while on stiff (20 kPa) hydrogels MSC area increased to ~3,750 $\mu m^2$.[187] Similarly, on soft (~3 kPa) o-Nitrobenzyl-Methacrylate-HA hydrogels MSCs had an average area of about 1,500 $\mu m^2$ while on stiff (~15 kPa) hydrogels the area doubled to ~3,300 $\mu m^2$.[186] Although the Nor-Tet hydrogels were formed with a Diels-Alder click chemistry and not using free-radical polymerization between acrylamide and bis-acrylamide or photopolymerization reactions, stiffness-dependent changes in morphology were conserved.

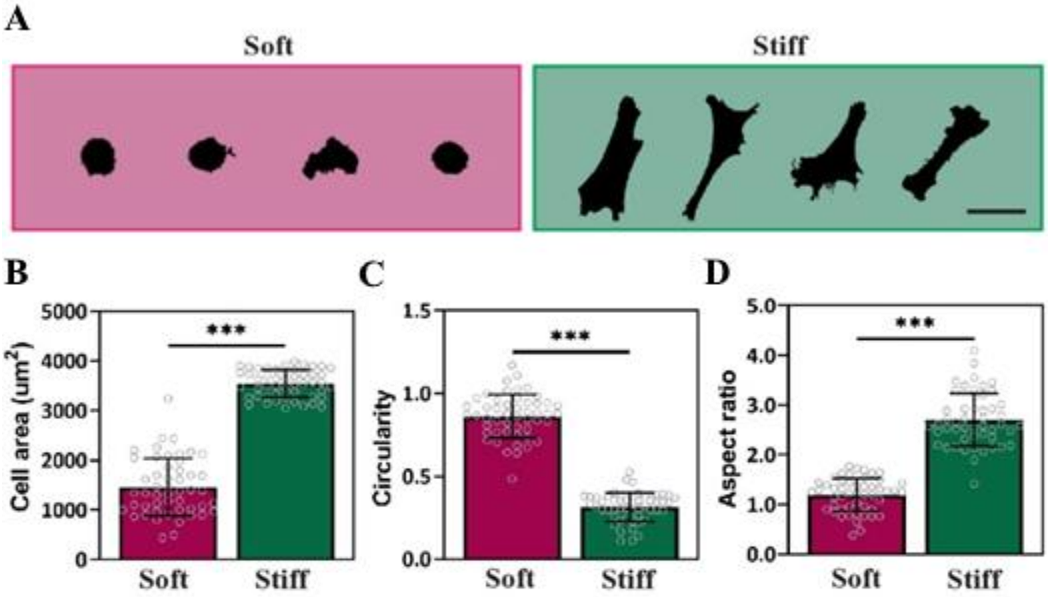

*Figure 17.* Cells on 2D Nor-Tet hydrogels display stiffness-dependent changes in cell morphology. **(A)** Representative silhouettes of MSCs on Soft and Stiff Nor-Tet hydrogels. Bar graphs show **(B)** Area, **(C)** Circularity, and **(D)** Aspect ratio of MSCs on Soft and Stiff Nor-Tet hydrogels. Bar graphs shown as mean ± SD ($n \geq 3$ samples per condition) with significant differences determined with ANOVA followed by Tukey's post hoc test where $^{***}p < 0.005$. Scale bar: 100 µm.

After establishing that MSC morphology changes in a stiffness-dependent manner on 2D Nor-Tet hydrogels, matrix mechanosensing on self-forming hydrogels was evaluated. Yes-associated protein (YAP) is a key transducer of outside-in mechanical signals,[185] and cytosolic YAP translocates to MSC nuclei with increasing stiffness on polyacrylamide and photopolymerized 2D hydrogels.[185,187] The nuclear YAP of MSCs on Stiff Nor-Tet hydrogels was significantly higher than MSCs on Soft Nor-Tet hydrogels (Figure 18A). At the cell-hydrogel interface, focal adhesions act as intermediaries that connect the local extracellular environment to the actin cytoskeleton, consequently activating mechanotransductive pathways.[188] Specifically, focal adhesion kinase (FAK) activation through the phosphorylation of tyrosine residues (pFAK) plays a role in matrix mechanosensing by responding to substrate stiffness and cytoskeletal contractility.[189] As such, pFAK maturation (length, count) and cytoskeletal alignment (actin anisotropy) were used as additional proxies for stiffness-dependent mechanosensing.

The length of pFAK increased with increasing Nor-Tet hydrogel stiffness, and so did the average number of focal adhesions per cell (Figure 18B). Actin anisotropy (actin fiber alignment) is a way to evaluate the organization of actin stress fibers, and there was a significant increase in actin anisotropy (0.24 ± 0.07 vs. 0.63 ± 0.20) between MSCs on Soft and Stiff Nor-Tet hydrogels (Figure 18C). These results show that MSCs respond to mechanical cues on 2D Nor-Tet hydrogels which highlights the versatility of these catalyst-free hydrogels as a platform to study and control matrix mechanosensing.

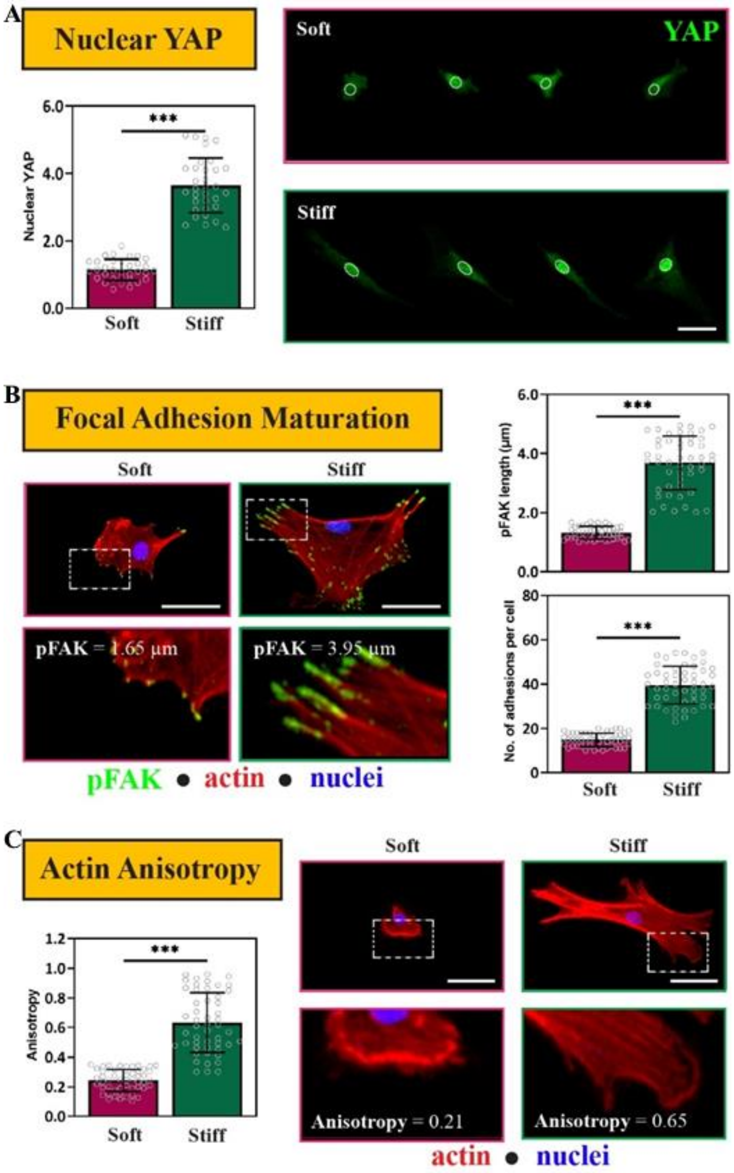

*Figure 18.* MSCs are mechanosensitive on 2D Soft and Stiff Nor-Tet hydrogels. **(A)** Representative images and Nuclear YAP (green) quantification of MSCs on Soft and Stiff Nor-Tet hydrogels. **(B)** Representative images of MSCs stained for pFAK (green), phalloidin (red), and nuclei (blue) and quantification of pFAK maturation (length, average number of adhesions per cell) and **(C)** actin anisotropy of MSCs on Soft and Stiff Nor-Tet hydrogels. Bar graphs shown as mean ± SD (n ≥ 3 samples per condition) with significant differences determined with ANOVA followed by Tukey's post hoc test where $***p < 0.005$. Scale bars: a, b, c 50 μm.

### *3.3.6 Nor-Tet Hydrogels as a Delivery Vehicle of Highly Viable Cells*

While cell injections are a widely used method to transplant cells, low cell viability and poor cell retention at the site of injection limit the efficacy of this minimally invasive technique.[190,191] Hydrogels address the limitations of liquid cell injections by shielding cells from shear stresses during extrusion and by keeping cells at the target site as the hydrogel polymerizes. To evaluate the use of Nor-Tet hydrogels as a biocompatible and injectable cell carrier, MSCs were suspended in culture medium or an RGD-functionalized Nor-Tet hydrogel solution that was loaded into a syringe and extruded through a needle tip onto cylindrical molds (Figure 19A). Syringe needles with varying inner diameters were used ranging from 160 μm (30 G) to 1,190 μm (16 G) (Figure S8a). One (D1), three (D3), and seven (D7) days post-injection, the percentage of live cells extruded through different size needles (Figure 20A) was determined for Soft (2% w/v) and Stiff (6% w/v) Nor-Tet hydrogels by analyzing confocal images stained with a Live/Dead assay (live, green; dead, red) (Figure 19B, 19C; Figure 20B, 20C). One day post-injection, cells extruded through different size needles are highly viable (> 85% viability: 16G, 20G, 26G and > 70% viability: 30G) for Soft and Stiff groups (Figure 19D, 19E). Meanwhile, MSCs suspended in culture medium (C) only had 70% viable cells one day post-injection. Seven days post-injection, MSCs in most groups remain viable (> 80% viability: 16G, 20G and 55% - 75% viability: 26G, 30G) for Soft and Stiff Nor-Tet hydrogels. The Soft and Stiff Nor-Tet hydrogels also retained their shape seven days post-injection, which demonstrates that viable MSCs can be extruded from a range of syringe needle sizes through a solution that self-forms into mechanically stable hydrogels.

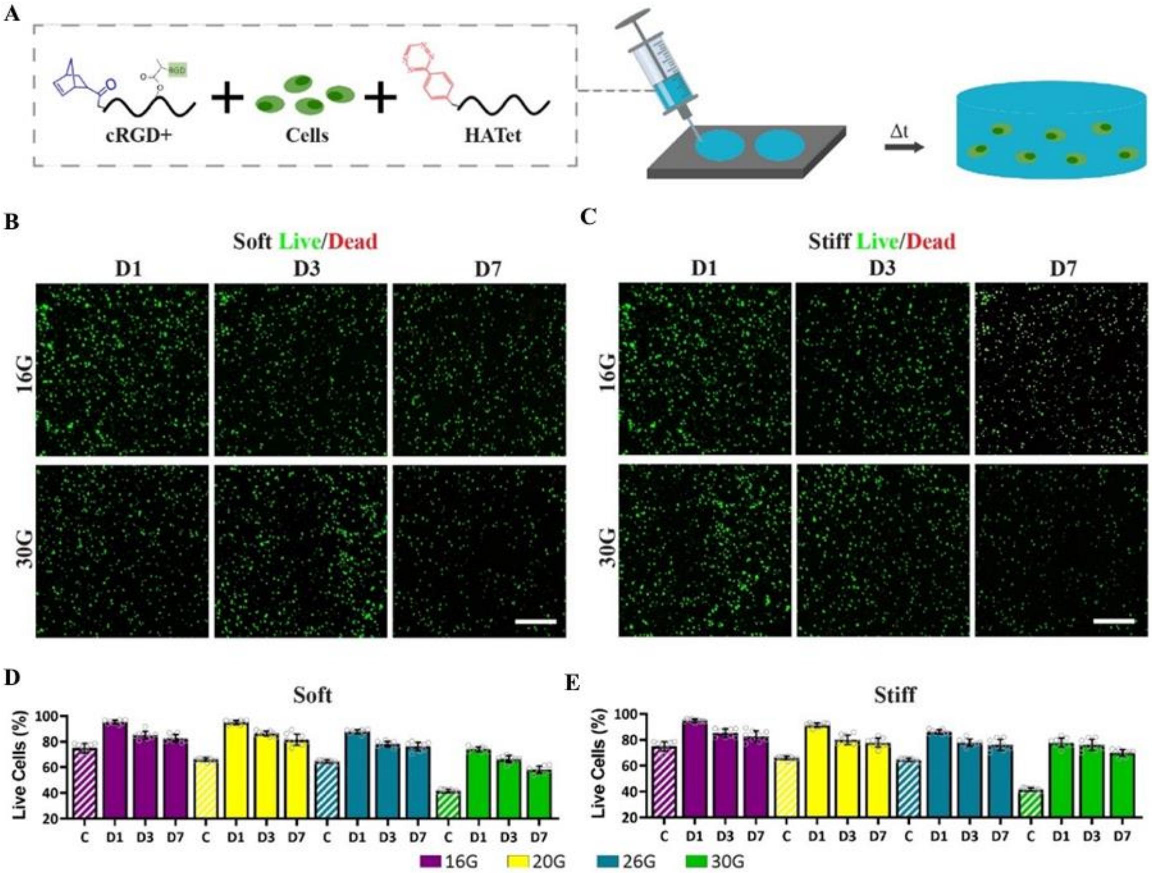

*Figure 19.* MSCs in injectable 3D Nor-Tet hydrogels are highly viable. **(A)** Nor-Tet hydrogel solutions consisting of MSCs mixed with RGD-functionalized HANor and HATet were injected into cylindrical molds via extrusion of various clinically relevant syringe needle sizes. Representative live (green) and dead (red) staining of MSCs cultured in **(B)** Soft and **(C)** Stiff Nor-Tet hydrogels. Bar graphs show percentage of live cells in **(D)** Soft and **(E)** Stiff Nor-Tet hydrogels from confocal image analysis. Bar graphs shown as mean ± SD ($n \geq 3$ samples per condition). Scale bar: 500 µm.

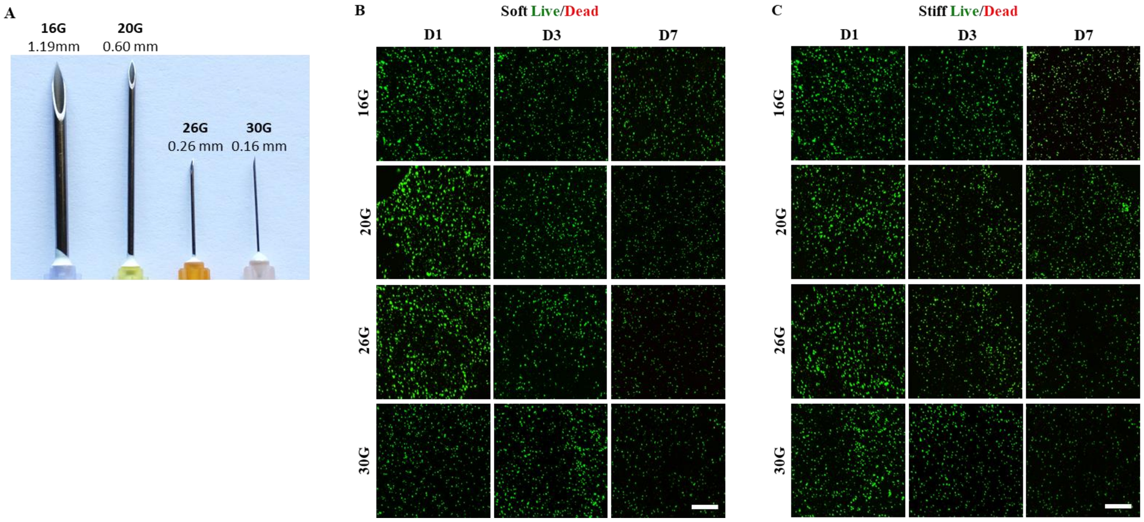

*Figure 20.* 3D viability of MSCs injected through different size syringe needles. **(A)** Needles used for extrusion have internal diameters ranging from 0.16 to 1.19 mm. Representative live (green) and dead (red) staining of MSCs extruded through different needle sizes for **(B)** Soft (2% w/v) and **(C)** Stiff (6% w/v) Nor-Tet hydrogels. Scale bars: 500 µm.

MSCs encapsulated in Soft and Stiff 3D Nor-Tet hydrogels remain spherical after 7 days in culture (Figure 21A). Further, no difference in cellular volume (Figure 21B) or sphericity (Figure 21C) were observed between MSCs in 3D Soft and Stiff Nor-Tet hydrogels. These findings are consistent with previous studies showing that cells encapsulated in covalently crosslinked hydrogels remain spherical, independent of stiffness.[71] As expected for spherical cells, nuclear YAP ratios were close to unity and did not change between Soft and Stiff Nor-Tet hydrogels (Figure 21D, 21E).

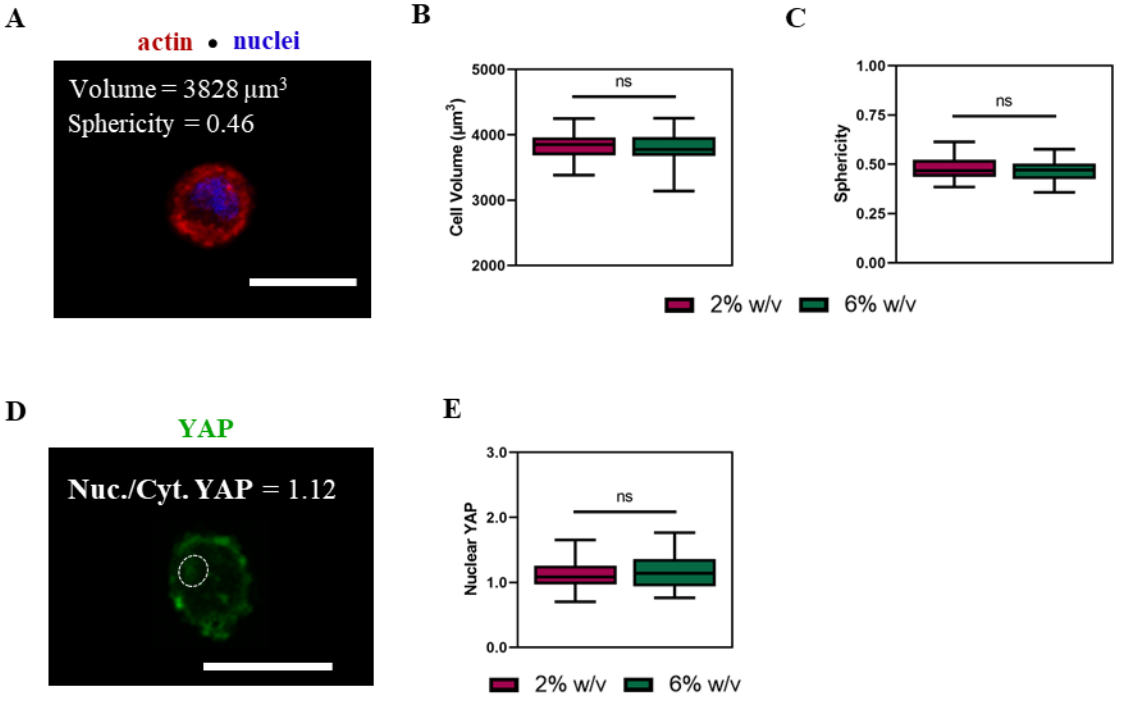

*Figure 21.* 3D morphology of MSCs encapsulated in Soft (2% w/v) and Stiff (6% w/v) Nor-Tet hydrogels. **(A)** Representative F-actin (red) and nuclear (blue) staining of an MSC encapsulated in Nor-Tet hydrogels (2% w/v shown). Quantification of **(B)** Volume and **(C)** Sphericity of MSCs in Soft and Stiff Nor-Tet hydrogels. 3D matrix mechanosensing of MSCs encapsulated in Soft (2% w/v) and Stiff (6% w/v) Nor-Tet hydrogels. **(D)** Representative image of an MSC encapsulated in a Soft Nor-Tet hydrogel stained for YAP (green). **(E)** Nuclear YAP quantification of MSCs on Soft and Stiff Nor-Tet hydrogels stained for YAP. Bar graphs shown as mean ± SD (n ≥ 3 samples per condition) with no significant differences (ns) determined with ANOVA. Scale bar: 50 µm.

### *3.3.7 3D Cell-Mediated Nor-Tet Hydrogel Degradation Directs Stem Cell Differentiation*

Stem cells can sense biophysical signals, leading to numerous cell functions including differentiation. On 2D substrates, MSC lineage commitment is dictated in part by stiffness, and this is due to stiffness-dependent changes in matrix mechanosensing.[70,192] MSCs on 2D soft materials are round and exhibit low traction forces whereas MSCs on 2D stiff substrates are spread and more contractile. While MSCs spread with increasing stiffness on 2D, this is not the case in 3D. For 3D morphology-mediated MSC differentiation to occur, encapsulated MSCs need to locally remodel their surrounding hydrogel matrix, which can be enabled by either by tuning hydrogel viscoelasticity,[193,194] or hydrogel degradation.[71,187] To demonstrate the effects of cell-mediated hydrogel degradation on MSC differentiation, Khetan et al. encapsulated MSCs in hydrogels that restrict or permit 3D cellular spreading.[71] In bipotential AD/OS (adipogenic/osteogenic) Medium, MSCs spread and preferentially differentiate into osteoblasts in 3D enzymatically degradable hydrogels, whereas MSCs in 3D non-degradable hydrogels are round and commit to an adipogenic phenotype.[71]

MSCs encapsulated in covalently crosslinked hydrogels can spread if the hydrogel contains protease-degradable components. Gelatin is enzymatically degradable and cells encapsulated in gelatin hydrogels spread,[195] while MSCs encapsulated in HA hydrogels do not. Thus, the balance between stable HA and enzymatically degradable gelatin can be leveraged to modulate the extent of 3D spreading-mediated differentiation within injectable Nor Tet hydrogels. Stable Nor-Tet hydrogels were formed by mixing HANor, HATet, and MSCs. Stiffness-matched (4.6 kPa E) Degradable Nor-Tet hydrogels were formed by mixing enzymatically degradable GelNor with HATet and MSCs. One- and seven-days post-encapsulation, the morphology of MSCs (Volume, Sphericity) were determined for Stable and Degradable Nor-Tet groups. As expected, MSCs in Stable Nor-Tet hydrogels remained small (Volume 5,198 ± 700 $\mu m^3$ on Day 1 and 5,862 ± 686 $\mu m^3$ on Day 7) and round (Sphericity 0.65 ± 0.09 on Day 1 and 0.65 ± 0.08 on Day 7) (Figure 22A). MSCs in Degradable Nor-Tet hydrogels had comparable volume (5,947 ± 849 $\mu m^3$) and sphericity (0.65 ± 0.09) after 1 day in culture, however, after 7 days there was an almost two-fold increase in volume (10,275 ± 758 $\mu m^3$) and a significant drop in sphericity (0.27 ± 0.05) (Figure 22A). Representative images of MSCs in Stable hydrogels show that they remain round for at least 7 days (Figure 22B), whereas MSCs in Degradable hydrogels are larger and display branching protrusions on Day 7 (Figure 22C). These findings show that 3D cellular spreading in Nor-Tet hydrogels can be induced simply by substituting HANor with enzymatically degradable GelNor macromer.

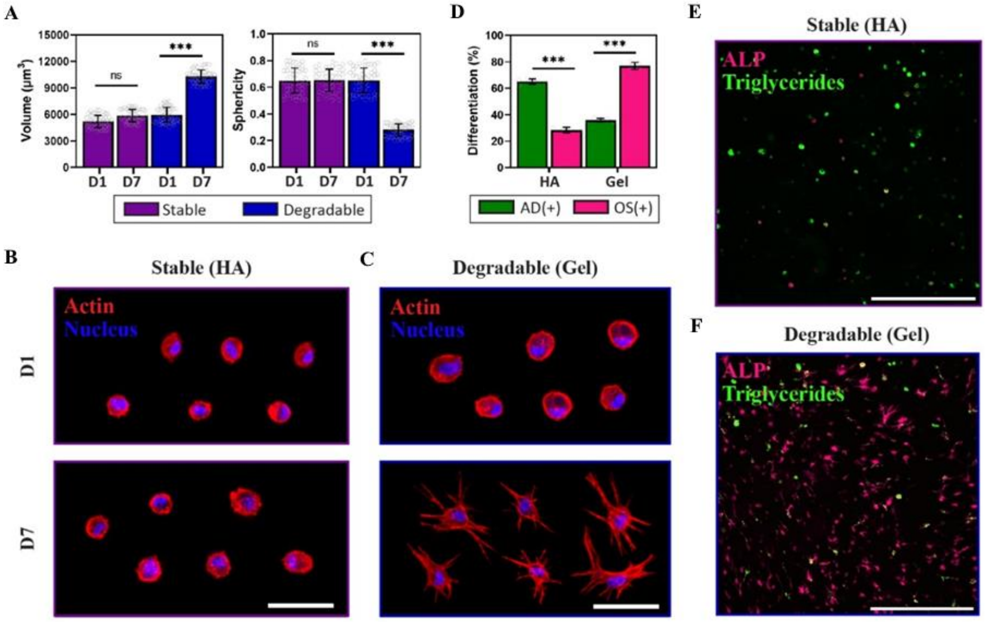

*Figure 22.* MSC spreading and differentiation can be controlled in 3D Nor-Tet hydrogels. **(A)** Quantification of MSC Volume (left) and Sphericity (right) of MSCs in Stable or Degradable Nor-Tet hydrogels after 1 and 7 days in culture. Representative images of MSCs stained for actin (red) and nuclei (blue) after 1 and 7 days in culture inside **(B)** Stable or **(C)** Degradable Nor-Tet hydrogels. **(D)** Quantification of percentage of AD(+) and OS(+) cells in Stable HA and Degradable Gel Nor-Tet hydrogels after 7 days in culture. Representative images of cells stained for ALP (magenta) and lipid droplets (green) in **(E)** Stable or **(F)** Degradable Nor-Tet hydrogels after 7 days in culture. Bar graphs shown as mean ± SD (n ≥ 3 samples per condition) with significant differences determined with ANOVA followed by Tukey's post hoc test where ***p < 0.005 and ns is not significant. Scale bars: d 50 μm; e 500 μm.

After demonstrating that encapsulated MSCs in Nor-Tet hydrogels can take on spread or round morphologies depending on the polymer backbone used, the effects of 3D cellular spreading on MSC lineage commitment was investigated. MSCs were encapsulated in Stable or Degradable Nor-Tet hydrogels, cultured in AD/OS Medium for seven days, and co-stained with alkaline phosphatase (ALP, OS biomarker) and lipid droplets (AD biomarker) to identify OS(+) and AD(+) cells, respectively. After seven days in culture, 65 ± 2% of cells in Stable HA hydrogels are AD(+) while only 28 ± 2% are OS(+) (Figure 22D). In contrast, MSCs encapsulated in Degradable hydrogels that favor 3D cellular spreading show over a 2.5-fold increase in OS(+) (77 ± 3%) cells and a significant decrease in AD(+) (36 ± 1%) cells (Figure 22D). Representative image of cells in Stable HA Nor-Tet hydrogels co-stained with ALP and lipid droplets show that cells retain a spherical morphology and most cells are AD(+) (Figure 22E). In contrast, representative image of cells in Degradable Gel Nor-Tet hydrogels are highly spread and the majority of cells display intracellular ALP (Figure 22F). These findings show that the Nor-Tet hydrogels presented are biocompatible and can regulate 3D cellular spreading and downstream differentiation by incorporating enzymatically degradable GelNor in lieu of HANor.

### 3.4 Conclusion

In this study, biocompatible Nor-Tet hydrogels are developed with tunable physical and biochemical properties. Mechanical parameters of these self-forming hydrogels are controlled by varying macromer concentration and stoichiometric ratios between Nor and Tet moieties. By modifying Nor containing macromers with thiolated peptides, bioactivity is incorporated independent of stiffness or gelation time. MSCs on 2D RGD-functionalized Nor-Tet hydrogels adhere, proliferate, and are mechanically sensitive to changes in hydrogel stiffness. MSCs in 3D Nor-Tet hydrogel solutions are more viable than MSCs injected in liquid, and 3D cellular spreading-mediated differentiation is controlled by simply substituting stable HANor with enzymatically degradable GelNor. These self-forming Nor-Tet hydrogels feature a wide range of physicochemical properties and have broad applicability in fundamental and translational research.

## 3.5 Experimental Section

### *3.5.1 HANor, HATet, and GelNor Macromer Synthesis*

To synthesize HANor, carboxyl groups in HA were modified with Nor as previously described.[196] Briefly, sodium hyaluronate (NaHA, Lifecore, 60 kDa) was converted to its tetrabutylammonium salt (HATBA) by dissolving in distilled water (2% w/v) and mixing with Dowex resin for two hours at room temperature. The resin was then vacuum filtered, and the pH was adjusted to 7.02 using tetrabutylammonium hydroxide (TBA-OH) diluted in water (1:1 v/v). The resulting HATBA solution was then frozen and lyophilized. Carboxyl groups in HATBA were then modified with Nor via amidation with 5-norbornene-2-methylamine (Nor-$NH_2$, 0.4 mmol per gram of dry HATBA) in anhydrous dimethyl sulfoxide (DMSO, 2% w/v) and benzotriazole-1-yl-oxy-tris-(dimethylamino)-phosphonium hexafluorophosphate (BOP) under nitrogen for two hours at room temperature. The reaction was quenched with cold distilled water, dialyzed (SpectraPor, 6-8 kDa molecular weight cutoff), frozen, and lyophilized. The synthesized HANor macromer had ~50% of its repeat units functionalized with Nor, as analyzed with $^1H$ NMR spectroscopy (Figure 8A). The percentage of modification was calculated by comparing the integral of the methyl HA peaks between $\delta$ 1.8-2.0 ppm to the vinyl proton peaks of norbornene between $\delta$ 6.2-6.3 ppm.[197]

To synthesize HATet macromers, carboxyl groups in HA were modified with Tet using a modified procedure described by Desai and coworkers.[198] Briefly, HATBA was dissolved (1% w/v) in 100 mM β-(N-morpholino)ethanesulfonic acid (MES) buffer (pH 6) and 1-(3-dimethylaminopropyl)-3-ethylcarbodiimide (EDC), N-hydroxysuccinimide (NHS), and tetrazine-amine (Tet-$NH_2$) were added at a 1:4:1 molar ratio at 0.5 mmol Tet per gram of HATBA and reacted overnight at room temperature. The HATet solution was then dialyzed (SpectraPor, 6-8 kDa molecular weight cutoff), frozen, and lyophilized. $^1H$ NMR spectroscopy analysis confirmed that ~40% of HATet repeat units were functionalized with Tet (Figure 8B). The percentage of modification was calculated by comparing the integral of the methyl HA peaks between δ 1.8-2.0 ppm to the carboxylic acid proton peak of tetrazine between δ10.0-10.5 ppm and aromatic proton peak of tetrazine between δ7.0-8.5 ppm.[59]

To synthesize GelNor macromers, carboxyl groups in gelatin were modified with Nor using a procedure previously described by Koshy and coworkers.[59] Briefly, gelatin (Type A, 300 bloom) was dissolved (1% w/v) in 100 mM β-(N-morpholino)ethanesulfonic acid (MES) buffer (pH 6) and 1-(3-dimethylaminopropyl)-3-ethylcarbodiimide (EDC), N-hydroxysuccinimide (NHS), and Nor-$NH_2$ were added at a 2:1:1 molar ratio at 2 mmol Nb per gram of gelatin and reacted for 4 hours at 37 °C. The GelNor solution was then dialyzed (SpectraPor, 6-8 kDa molecular weight cutoff), frozen, and lyophilized. $^1H$ NMR spectroscopy analysis confirmed that ~15% of GelNor repeat units were functionalized with Nor (Figure 23). The percentage of modification was calculated by comparing the integral of the aromatic amino acid peaks between δ 7.0-7.5 ppm to the vinyl proton peaks of norbornene between δ 6.0-6.5 ppm.[59]

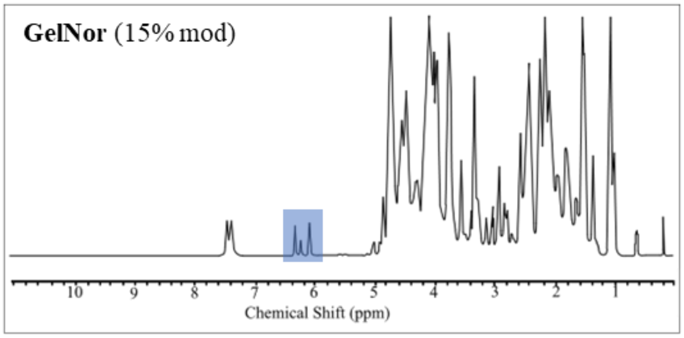

*Figure 23.* $^1$H-NMR spectra of GelNor. The percentage of modification was calculated by comparing the integral of the aromatic gelatin backbone peaks at δ 7.5 ppm to the alkene proton peaks of norbornene between δ 6.2-5.9 ppm.[127]

### *3.5.2 HANor(cRGD+) Synthesis*

To synthesize HANor(cRGD+) macromers, hydroxyl groups in HANor were first modified with methacrylates (Me) to form HANorMe via esterification with methacrylic anhydride (MA) by adapting a previously described protocol.[174] HANor was dissolved (1% w/v) in distilled water at 4 °C. A 15-fold molar excess of MA was added dropwise while maintaining pH between 8.5-9.0. After all MA was added, the solution was left stirring overnight at room temperature. The HANorMe solution was then dialyzed (SpectraPor, 6-8 kDa molecular weight cutoff), frozen, and lyophilized. $^1$H NMR spectroscopy analysis confirmed that ~60% of HANor repeat units were functionalized with Me (Figure 13C). The percentage of modification was calculated by comparing the integral of the HA peaks between δ 1.8-2.0 ppm to the alkene proton peaks of methacrylates between δ 5.5-6.5 ppm.[199]

To peptide-functionalize HANorMe, thiols in cysteine-containing peptides were coupled to Me groups in HANorMe via an aqueous Michael addition reaction.[200] Briefly, HANorMe was dissolved (1% w/v) in 200 mM triethanolamine (TEOA) buffer (pH 8) at room temperature. Thiolated RGD peptide (sequence: GCGYGRGDSPG, cRGD) in solution (50 mM in PBS) was added dropwise to reach a final cRGD concentration that corresponds to 2 mM in self-forming hydrogels of varying weight percent (2%, 4%, or 6% final w/v). Table 3 summarizes the reaction parameters to create HANor(cRGD+) macromers with appropriate cRGD concentrations. The HANor(cRGD+) solution was then dialyzed (SpectraPor, 6-8 kDa molecular weight cutoff), frozen, and lyophilized. $^1$H NMR spectroscopy analysis confirmed that 17%, 9%, and 6% of Me groups were coupled with cRGD for 2%, 4%, and 6% w/v HANor(cRGD+) macromers (Figure 14). The percentage of Me-cRGD coupling was calculated by comparing integral of the alkene proton peaks of methacrylate between δ 5.5-6.5 ppm[199] to the β and γ ethyl protons of the arginine moiety between δ 1.50-2.00 ppm.[201]

**Table 3**

*Reaction Parameters to Create HANor(Pep+) Macromers with Appropriate cRGD (Sequence: G**C**GYG**RGD**SPG; MW: 1,025 g mol$^{-1}$) Concentrations to Achieve an Effective Concentration of 2 mM*

| Macromer w/v | HANorMe (mg) | cRGD (mg) |
|---|---|---|
| 2% | 100 | 20.5 |
| 4% | 100 | 10.3 |
| 6% | 100 | 6.9 |

### *3.5.3 Preparation and Characterization of Self-Forming Hydrogels*

Rheological properties of self-forming hydrogels were measured using a Discovery Hybrid Rheometer (DHR-3, TA Instruments) with a 20 mm diameter 1° cone upper plate geometry and the lower plate was heated to a physiological temperature of 37 °C. Samples were prepared by dissolving HANor and HATet separately in PBS, followed by mixing, resulting in 2%, 4%, or 6% final w/v. Immediately after mixing, 40 µl of the solution was pipetted to the center of the rheometer stage and the shear storage (G′) and loss (G″) moduli were monitored. To confirm that click crosslinking between Nor and Tet moieties creates stable hydrogels, frequency sweeps were performed at 1% oscillatory strain while varying the frequency from 0.01 to 10 Hz. To measure plateau G′ and gelation kinetics, time sweeps were performed for 1 hour at 1 Hz and 1% oscillatory strain. Bulk mechanical properties of self-forming hydrogels were measured using a Shimadzu EZ-SX Mechanical Tester equipped with a 50 N compression load. Briefly, hydrated HANor and HATet were mixed and pipetted into cylindrical silicone molds (2 mm height, 8 mm diameter). The hydrogels were allowed to form for 30 minutes before soaking in PBS overnight at 37 °C. Formed cylindrical Nor-Tet hydrogels were compressed until 30% strain, and the elastic modulus was determined using the slope of the stress-strain curve between 10% and 20% strain.

### *3.5.4 2D Cell Attachment and Proliferation on Self-Forming Hydrogels*

Thin hydrogels were formed by dissolving HANor (with or without cRGD functionalization) and HATet separately in Growth Medium (α-Minimum Essential Medium (αMEM) supplemented with 10% fetal bovine serum (FBS, Lonza)), followed by mixing, resulting in Soft (2% w/v) and Stiff (6% w/v) hydrogel solutions. Immediately after mixing, 70 µl of the solution was pipetted into cylindrical polydimethylsiloxane (PDMS) molds (11 mm diameter, 1 mm height). The thin hydrogels were allowed to crosslink for 2 minutes followed by gently adding Growth Medium to prevent hydrogels from drying out as they continue to polymerize. To evaluate cell adhesion and proliferation, human primary MSCs (from bone marrow, Lonza) were expanded in 100 mm petri dishes in Growth Medium. MSCs were seeded on top of 2D Nor-Tet hydrogels at a density of 3,000 cells per cm$^2$. To evaluate cell attachment, cells were fixed after 3 days in culture using 10% neutral buffered formalin for 10 minutes at room temperature. Samples were washed twice with PBS after fixation and kept at 4 $^oC$ until immunostaining was performed. To evaluate cell proliferation, culture media was removed and replaced with alamarBlue working solution (Growth Medium supplemented with 10% alamarBlue Reagent, Invitrogen) after 1, 3, and 7 days in culture, and kept in the cell incubator for 4 h. Samples of the media were collected (50 µl in triplicate) and fluorescence was measured with a plate reader (560 nm excitation, 590 nm emission).

### *3.5.5 3D Cell Encapsulation in Self-Forming Hydrogels*

For cell encapsulation, cells were resuspended in RGD-functionalized HANor dissolved in Growth Medium at a density of $10^6$ cells per mL. HATet dissolved in Growth Medium was mixed, resulting in a 2% w/v hydrogel solution, which was injected into a PDMS mold (8 mm diameter, 2 mm height). The hydrogels were allowed to crosslink for 2 minutes followed by gently adding Growth Medium to prevent hydrogels from drying out as they continue to polymerize. To evaluate cell viability, culture media was removed and replaced with Live/Dead Viability working solution (Growth Medium supplemented with 1:1,000 calcein AM and 1:1,000 ethidium homodimer, Invitrogen) and kept in a cell incubator for 30 minutes prior to confocal imaging and imaging-based analysis.

### *3.5.6 Immunostaining and Imaging-Based Analysis*

After 3 days in culture, MSC-laden hydrogels were fixed in 10% formalin for 10 minutes at room temperature. Samples were then permeabilized with 0.1% Triton X-100 for 2 minutes and blocked with 3% bovine serum albumin in PBS for 30 minutes. Primary YAP or pFAK antibody (Santa Cruz Biotechnologies, 1:200) was added for 1 hour, followed by Alexa Fluor 488 secondary antibody (Life Technologies, 1:200) for 2 hours at room temperature. To visualize individual cells and nuclei, samples were stained for actin (Alexa Flour 568 phalloidin, 20 minutes, 1:100) and double stranded DNA (Hoechst, 5 minutes, 1:1,000), respectively. Confocal imaging was performed with a Nikon A1 confocal microscope.

Imaging-based cell analysis was performed using ImageJ software (National Institutes of Health). For 2D morphology analysis, the wand tracing tool was used to select cell outlines from the actin channel and the measure function was used to calculate cell area, circularity, and aspect ratio. For 2D YAP analysis, nuclear YAP localization was determined by first measuring the integrated density of YAP of five regions of interest (ROI) on the cytoplasm and nucleus of each cell, respectively. The ratio between the nuclear and cytosolic integrated densities was defined as the nuclear YAP value. To evaluate focal adhesion maturation, the  number of pFAK adhesions per cell were counted using the Find Maxima feature, and at least 10 focal adhesion lengths were measured per cell. Actin anisotropy was quantified by determining the common directionality of actin fibers within a manually-defined ROIs (at least three ROIs surrounding the cell nucleus using the FibrilTool plugin.[202]

For 3D morphology analysis, z-stacks of the actin channel were binarized using the Otsu thresholding method. Cell volume and surface area were determined using the 3D Objects Counter feature, and these values were used to calculate sphericity as previously reported.[187] For 3D YAP analysis, actin cytoskeleton and nucleus z-stacks were binarized using the Otsu thresholding method. These cellular and nuclear ROIs were then superimposed with the YAP channel to obtain 3D YAP stacks of the cytoplasmic and nuclear space. The integrated density of YAP was then quantified using the 3D Objects Counter feature and the ratio between the nuclear and cytoplasmic YAP intensity was reported as the nuclear YAP ratio.

### *3.5.7 MSC Syringe Needle Flow and Encapsulation Viability Study*

MSCs were resuspended at a cell density of $10^6$ cells per mL in either Growth Medium or an RGD-functionalized Nor-Tet hydrogel solution. The suspensions were loaded into a 1 mL syringe with an appropriate gauge needle and ejected onto a sterile glass coverslip (for cells suspended in Growth Medium) or into PDMS molds (for cells suspended in hydrogel solution) at a volumetric flow rate of 3,000 µL per min. The hydrogels were allowed to crosslink for 2 minutes followed minutes followed by gently adding Growth Medium to prevent hydrogels from drying out as they continue to polymerize. To evaluate cell viability, culture media was removed and replaced with Live/Dead Viability working solution (Growth Medium supplemented with 1:1,000 Calcein AM and 1:1,000 ethidium homodimer, Invitrogen) and kept in a cell incubator for 30 minutes prior to confocal imaging and imaging-based analysis.

### *3.5.8 Osteogenic and Adipogenic Differentiation Study*

Cells were resuspended in RGD-functionalized HANor or GelNor dissolved in Growth Medium at a density of $10^6$ cells per mL. HATet dissolved in Growth Medium was mixed with the HANor or GelNor solution, which was injected into a PDMS mold (8 mm diameter, 2 mm height). The hydrogels were allowed to crosslink for 2 minutes followed by washes in Growth Medium. Cell-laden hydrogels were cultured in Growth

Medium, hMSC Osteogenic Differentiation BulletKit$^{TM}$ Medium (Lonza) (OS Medium), hMSC Adipogenic Differentiation BulletKit$^{TM}$ Medium (Lonza) (AD Medium), or Bipotential Medium (OS Medium + AD Medium) for 7 days with media changes according to manufacturer specifications. To evaluate cell differentiation, cell-laden hydrogels were fixed with 10% neutral buffered formalin for 30 minutes. Fixed samples were stained with BODIPY (1:2500) to visualize triglycerides or Vector® Blue Alkaline Phosphatase Substrate prepared according to manufacturer specifications to visualize ALP for 30 minutes prior to confocal imaging and imaging-based analysis.

Imaging-based analysis was performed to determine the percentage of cells positive for osteogenic or adipogenic differentiation. Mean fluorescence intensity (MFI) of cellular ALP or triglycerides were determined using ImageJ software. Briefly, nuclei stacks were binarized using the Otsu thresholding method. Binarized nuclei stacks were dilated, and the nuclei stacks were subtracted from the dilated stacks resulting in rings. The rings were converted into masks and overlayed on the ALP or triglycerides channel stacks. The 3D Objects Counter feature was then applied to calculate the surface area of the rings and the Measure function was used to determine the integrated density of the rings. The MFI value of every cell was calculated by dividing its mean grey value by area. The MFI values of Growth Medium, OS Medium, and AD Medium groups were processed using a k-means clustering algorithm to determine the boundary between MSCs with low (ALP-negative or Triglyceride-negative) and high (ALP-positive or Triglyceride-negative) MFI. The selected threshold MFI covers 95% of ALP-negative cells.[203]

### *3.5.9 Statistical Analysis*

The statistical analysis was performed using GraphPad Prism 9.3.1 software. All experiments were carried out in triplicates and single cell analysis was done with at least 50 cells per group. All graphs represent mean ± standard deviation (SD). For comparisons of three or more groups: normally distributed populations were analyzed via analysis of variance (ANOVA) with a Tukey's post hoc test to correct for multiple comparisons. Differences among groups are stated as $p < 0.05$ (*), $p < 0.01$ (**), $p < 0.001$ (***), and stated as (ns) when differences between groups are not statistically significant.

# Chapter 4

# Injectable Hydrogel with Immobilized BMP-2 Mimetic Peptide for Local Bone Regeneration

**Note:** sections of this chapter have been reproduced from the following publication with permissions:

**Gultian, K. A., Gandhi, R., DeCesari, K., Romiyo, V., Kleinbart, E. P., Martin, K., Gentile, P. M., Kim, T. W. B., & Vega, S. L.** (2022). Injectable hydrogel with immobilized BMP-2 mimetic peptide for local bone regeneration. *Frontiers in Biomaterials Science, 0,* 6.

## 4.1 Abstract

Osteoporosis is a disease characterized by a decrease in bone mineral density, thereby increasing the risk of sustaining a fragility fracture. Most medical therapies are systemic and do not restore bone in areas of need, leading to undesirable side effects. Injectable hydrogels can locally deliver therapeutics with spatial precision, and this study reports the development of an injectable hydrogel containing a peptide mimic of bone morphogenetic protein-2 (BMP-2). To create injectable hydrogels, HA was modified with Nor (HANor) or Tet (HATet) which upon mixing click into covalently crosslinked Nor-Tet hydrogels. By modifying HANor macromers with methacrylates (Me), thiolated BMP-2 mimetic peptides were immobilized to HANor via a Michael addition reaction, and coupling was confirmed with $^1$H NMR spectroscopy. BMP-2 peptides presented in soluble and immobilized form increased alkaline phosphatase (ALP) expression in MSCs cultured on 2D and encapsulated in 3D Nor-Tet hydrogels. Injection of bioactive Nor-Tet hydrogels into hollow intramedullary canals of Lewis rat femurs showed a local increase in trabecular bone density as determined by micro-CT imaging. The presented work shows that injectable hydrogels with immobilized BMP-2 peptides are a promising biomaterial for the local regeneration of bone tissue and for the potential local treatment of osteoporosis.

## 4.2 Introduction

Osteoporosis is characterized by a reduction in bone mineral density and disruption of bone microarchitecture [204]. Osteoporosis is the most common chronic metabolic bone disease with an estimated 200 million people affected worldwide [205]. According to the International Osteoporosis Foundation, 1 in 3 women above the age of 50 and 1 in every 5 men will experience fragility fractures resulting from osteoporosis in their lifetime [206]. Osteoporosis increases the chances of fragility fractures after a low-level fall, with a mortality rate of up to 69% within ten years [207]. Risk factors for osteoporosis include genetics, being of postmenopausal age, substance abuse, poor dietary intake, and inactivity [208]. These risk factors disrupt bone remodeling, a dynamic physiological process in which bone tissue is resorbed by osteoclasts and formed by osteoblasts [205,209]. In osteoporosis, the rate of bone resorption is greater than the rate of bone formation, especially in major weight-bearing bones including vertebrae in the lumbar spine and femurs [205,210]. In the early stages of osteoporosis, bone loss is mainly observed in trabecular or cancellous bone, made up of a trabeculae network with high bone turnover [211–213]. Current treatments for osteoporosis are antiresorptive and anabolic drugs which can cause systemic side effects including oncogenesis [205,214]. Hormonal therapies (e.g., estrogen supplementation) are used as a last resort and only prescribed to high-risk post-menopausal women because it can cause adverse side effects including blood clots [205].

Efforts to develop alternative strategies to regenerate bone have utilized recombinant human bone morphogenetic protein 2 (BMP-2), a potent inducer of osteogenesis *in vivo* [215–219]. The osteogenic signaling cascade begins when BMP-2 binds to BMP-receptor type II, which leads to the phosphorylation (activation) of BMP-receptor type I, and ultimately to the phosphorylation of Smad1, a cytoplasmic signaling molecule for BMP-2. Phosphorylated Smad1 then localizes to the nucleus and controls gene expression to initiate osteogenic differentiation [220–222]. *In vitro*, embryonic stem cells, human MSCs, and C2C12 myoblasts exposed to BMP-2 express increased levels of cytoplasmic ALP, a well-established biomarker of osteogenesis [223,224]. Despite its osteoinductive properties, the clinical use of BMP-2 is limited by unwanted side effects. For instance, collagen scaffolds with high doses of untethered BMP-2 used for spinal fusions have resulted in serious complications including ectopic bone formation and impaired neurological function [140–142].

BMP-2 is a large and expensive growth factor, and BMP-2 based therapies are associated with inconsistent outcomes and safety concerns. Peptides that mimic the bioactivity of native BMP-2 are an inexpensive and potentially more efficacious substitute that can be incorporated into biomaterials. Specifically, the DWIVA peptide sequence from BMP-2 has high receptor-binding activity and specificity to BMP-receptor types I and II [176], and several groups have explored the use of this sequence to enhance osteogenic differentiation and bone formation [72,176,177]. Seol et al. found that osteoblast-like MC3T3-E1 cells cultured on titanium (Ti) chemically modified with DWIVA peptides had higher levels of ALP, and DWIVA-treated Ti dental implants induced increased bone formation *in vivo* [177]. MSCs encapsulated in DWIVA-functionalized self-assembling nanofibrous hydrogel networks and alginate hydrogels also commit to osteogenic lineages, as evidenced by increased ALP activity and mineralization [72,176].

Hyaluronic acid is an abundant ECM component that mediates cellular signaling, matrix organization, and morphogenesis [225,226]. HA polymers are amenable to chemical modifications through carboxyl and hydroxyl functional groups that can be used as macromers to create highly tunable hydrogels via various polymerization schemes [75,178]. For instance, Diels-Alder reactions between macromers modified with dienes (e.g., Nor) and dienophiles (e.g., Tet) yield self-forming hydrogels that can be injected [60,198]. In this study, we hypothesize that HA modified with Nor or Tet moieties can be used to create injectable DWIVA-functionalized Nor-Tet hydrogels that enhance osteogenic differentiation of MSCs *in vitro* and induce trabecular bone growth *in vivo*. To test this hypothesis, we developed an injectable HA hydrogel system by modifying HA with Nor (HANor) or Tet (HATet) moieties. BMP-2 signals were immobilized in the hydrogels by methacrylating HANor macromers (HANorMe) and pre-coupling Me- groups with thiolated DWIVA peptides via an aqueous Michael addition reaction. Osteogenic differentiation of MSCs cultured atop or within DWIVA-functionalized hydrogels were investigated by quantifying ALP via fluorescent imaging-based analysis. New trabecular bone formation in rat femurs injected with HA Nor-Tet hydrogels with or without DWIVA peptide was also evaluated using micro-computed tomography (micro-CT).

## 4.3 Results

### *4.3.1 Mechanics and Gelation Kinetics of Injectable HA Hydrogels are Preserved after DWIVA Coupling*

The percentage modification of HANor and HATet with Nor and Tet was determined to be ~50% and ~40% through $^1$H-NMR, respectively. Modification of HANor with Me provide sites for coupling thiolated DWIVA peptides to the HANor macromer backbone (Figure 24A). $^1$H-NMR shows that HANor has a Me modification of ~80%. Coupling HANorMe with 0.5 and 2.0 mM DWIVA results in 5% and 16% of Me groups bound to peptide, respectively (Figure 25). Mixing of hydrated HANorDWIVA with hydrated HATet results in hydrogel formation through crosslinking between Nor and Tet moieties (Figure 24B). Material characterization of Nor-Tet hydrogels functionalized with 0, 0.5, or 2.0 mM DWIVA shows that mechanics and gelation time are not affected by the DWIVA peptide. Additionally, DWIVA functionalization does not affect the equilibrium swelling ratio of HA Nor-Tet hydrogels (Table 4). Frequency sweep rheology (0.1 to 10 Hz) at 37 ºC shows constant storage modulus (G´) at every time point for Nor-Tet hydrogels with 0, 0.5, and 2.0 mM DWIVA, respectively (Figure 24C). Time sweep rheology (1 Hz) at 37 ºC shows that plateau G´ values are 1,767 ± 468 Pa, 1,630 ± 323 Pa, and 1,517 ± 268 Pa for Nor-Tet hydrogels with 0, 0.5, and 2.0 mM DWIVA, respectively (Figure 24D). The time to 50% plateau G´ values are 5.25 ± 0.16 min, 5.30 ± 0.24 min, and 4.93 ± 0.20 min for Nor-Tet hydrogels with 0, 0.5, and 2.0 mM DWIVA, respectively (Figure 24E). Compression testing shows elastic moduli (E) values of 4.12 ± 1.22 kPa, 4.38 ± 0.92 kPa, and 4.64 ± 1.07 kPa for Nor-Tet hydrogels with 0, 0.5, and 2.0 mM DWIVA, respectively (Figure 24F).

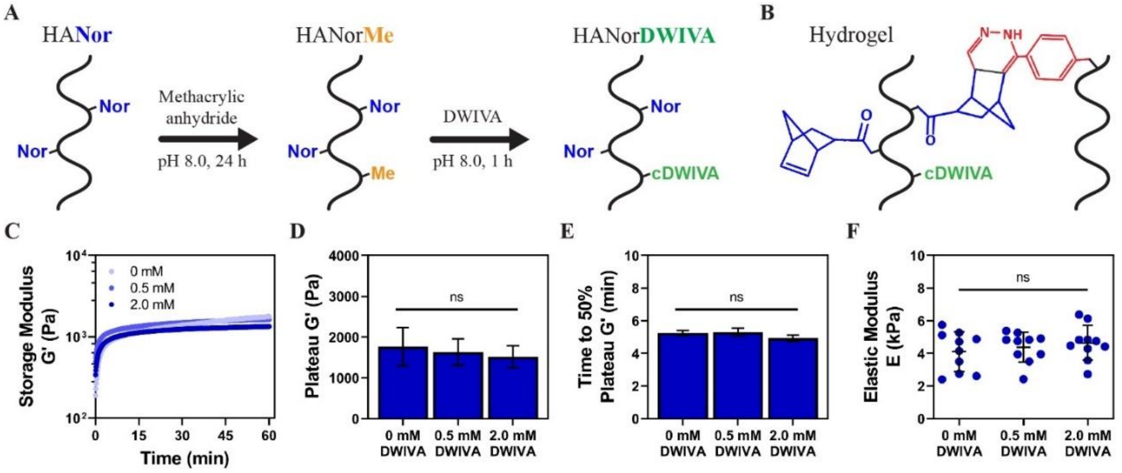

*Figure 24.* Synthesis of HANorDWIVA and characterization of DWIVA-functionalized Nor-Tet hydrogels. **(A)** Methacrylic anhydride is coupled to the HANor macromer to provide sites for DWIVA to bind through Michael addition reaction. **(B)** Crosslinking between Nor and Tet moieties in HANorDWIVA and HATet results in DWIVA-functionalized hydrogel. **(C)** Time sweep rheology of G′ kinetics is used to determine **(D)** plateau G′ and **(E)** time to 50% plateau G′ of 0, 0.5, and 2.0 mM DWIVA-functionalized Nor-Tet hydrogels. **(F)** Elastic moduli of hydrogels with 0, 0.5, and 2.0 mM DWIVA. Bar graphs and scatter dot plot are shown as mean ± SD (n ≥ 3 samples per condition) with no significant difference (ns) determined with one-way ANOVA.

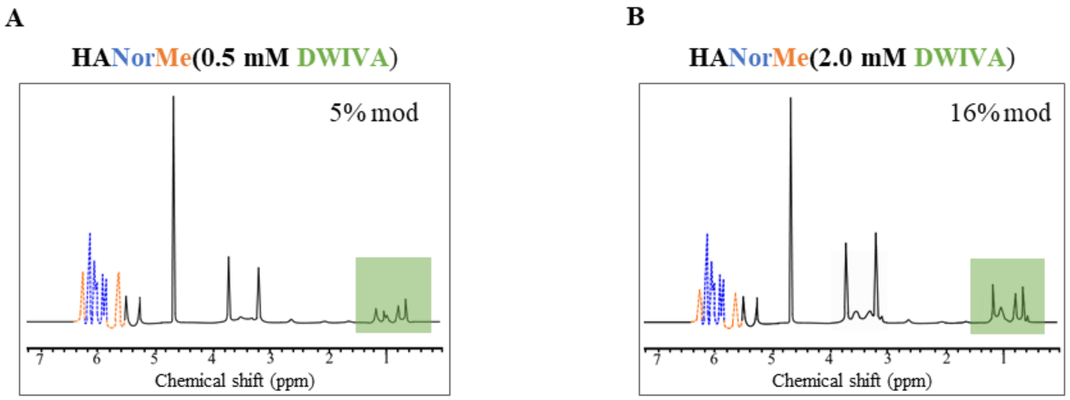

*Figure 25.* $^1$H-NMR characterization of HANor-cDWIVA. Proton peaks for Nor are between δ 6.2 to 6.3 ppm and proton peaks for Me are between δ 5.5 to 6.5 ppm. **(A)** 0.50 mM DWIVA and **(B)** 2.0 mM DWIVA peaks are between δ 0.50 to 1.50 ppm.

**Table 4**

*Equilibrium Swelling Ratio of 2% w/v Nor-Tet Hydrogels with 0, 0.5 or 2.0 mM Effective DWIVA Concentration (n ≥ 3 samples per condition)*

| Effective DWIVA Concentration (mM) | Equilibrium Swelling Ratio at 37 °C |
|---|---|
| 0 | 4,249 ± 148 |
| 0.5 | 4,260 ± 120 |
| 2.0 | 4,196 ± 133 |

### *4.3.2 Soluble Presentation of DWIVA Enhances ALP Levels of 2D MSC Cultures*

MSCs seeded on glass cultured in Growth Medium supplemented with 2.0 mM DWIVA show significantly more positive staining for ALP (dark blue) compared to cells cultured in Growth Medium or in Growth Medium supplemented with a lower (0.50 mM) DWIVA concentration (Figure 26A). Confocal images of MSC cultures stained for ALP (magenta) and nuclei (blue) show a progressive increase in ALP signal with increasing DWIVA concentration (Figure 26B). To distinguish between ALP(+) and ALP(-) MSCs, the mean fluorescence intensity (MFI) of intracellular ALP was first determined for individual MSCs using imaging-based analysis with ImageJ (Figure 27). The MFI values of the Growth Medium and OS Medium groups were processed using a k-means clustering algorithm to determine the boundary between ALP(-) and ALP(+) clusters, resulting in an MFI cutoff value of 52, which covers 95% of ALP(-) MSCs (Figure 26C). The MFI threshold value is used as a filter that assigns MSCs as ALP(-) (MFI < 52) or ALP(+) (MFI ≥ 52) (Figure 26D). Using this technique, the percentage of ALP(+) MSCs on glass is 7.5 ± 2.1% (Growth Medium), 14.1 ± 4.3% (0.5 mM DWIVA), 67.5 ± 3.7% (2.0 mM DWIVA), and 92.1 ± 3.9% (OS Medium) (Figure 26E).

### *4.3.3 Immobilized DWIVA Enhances ALP Levels of MSCs on 2D Nor-Tet Hydrogels*

HANorMe was pre-functionalized with thiolated RGD (2 mM) and with 0, 0.5, or 2 mM thiolated DWIVA. Pre-functionalized HANorMe macromers were then mixed with HATet to form Nor-Tet hydrogels that were seeded with MSCs (Figure 28A). Representative MSCs (ALP, magenta; nuclei, blue) in different treatment groups show more magenta signal in cells atop 2D hydrogels coupled with 2.0 mM DWIVA compared to cells atop hydrogels with lower DWIVA (0, 0.5 mM) concentrations (Figure 28B). A k-means clustering algorithm was applied for MFI values of MSCs on Growth Medium (negative group) and OS Medium (positive group) to determine an MFI cutoff of 50, which covers 95% of ALP(-) MSCs (Figure 28C). The percentage of ALP(+) MSCs on Nor-Tet hydrogels is 12.1 ± 4.5% (0 mM DWIVA), 19.3 ± 4.5% (0.5 mM DWIVA), 42.9 ± 3.8% (2.0 mM DWIVA), and 74.1 ± 4.1% (OS Medium) (Figure 28D).

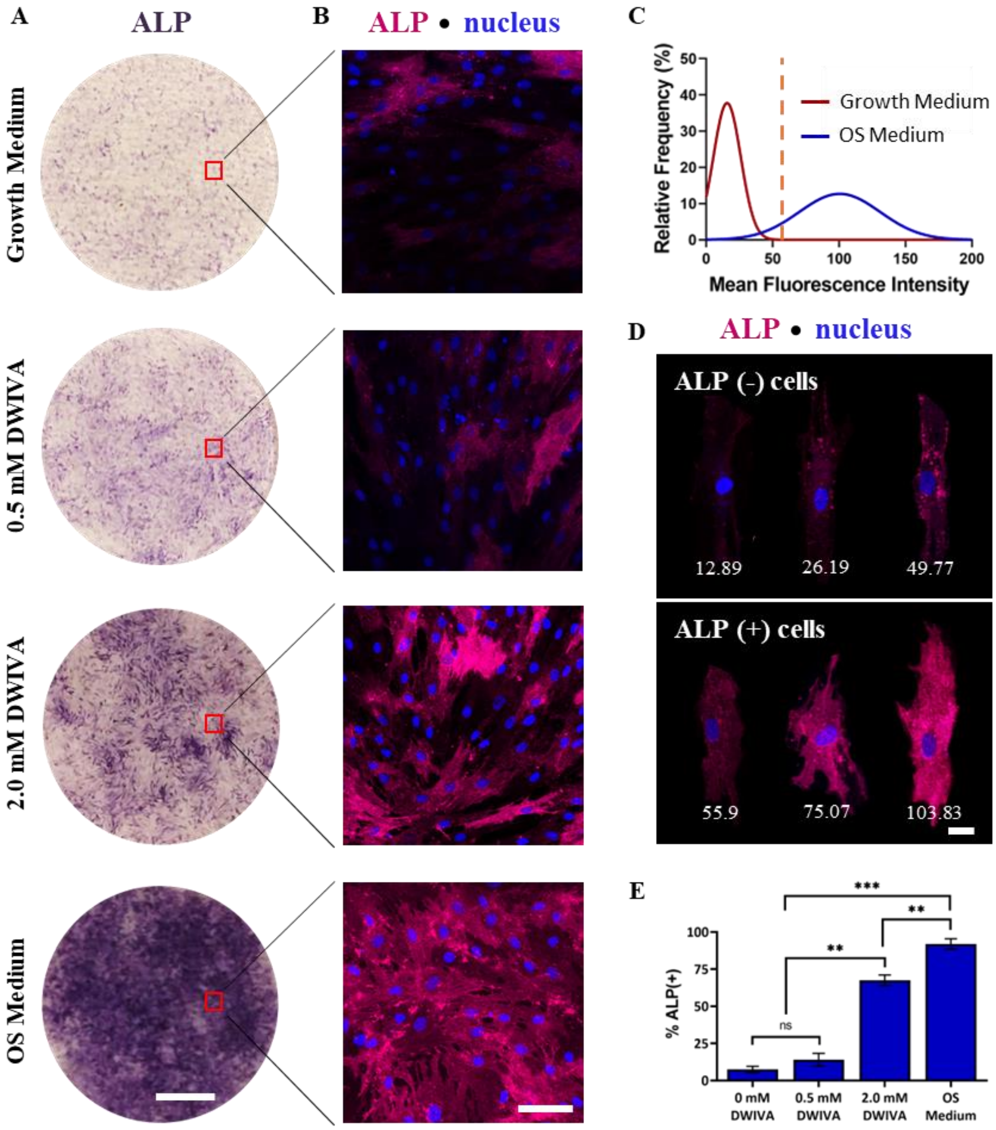

*Figure 26.* Soluble presentation of DWIVA enhances ALP levels of MSCs on glass. **(A)** Representative ALP staining of MSCs (dark blue) on glass in Growth Medium (negative control), Growth Medium supplemented with 0.5 or 2.0 mM DWIVA, and OS Medium (positive control). **(B)** Representative fluorescence staining of ALP (magenta) and nucleus (blue) of MSCs on glass in Growth Medium, Growth Medium supplemented with 0.5 or 2.0 mM DWIVA, and OS Medium. **(C)** Frequency distribution of ALP MFI of MSCs seeded on glass coverslips in Growth Medium (negative group) and OS Medium (positive group); dashed line shows MFI cutoff for ALP(-) and ALP(+) cells. **(D)** Representative cells that are ALP(-) (top, MFI < 52) and ALP(+) (bottom, MFI ≥ 52). **(E)** % ALP(+) quantification of MSCs cultured in Growth Medium with 0, 0.5, or 2.0 mM soluble DWIVA peptide and OS Medium. Bar graphs are shown as mean ± SD (n ≥ 50 cells per condition) with nonsignificant differences denoted as ns, and significant differences determined with ANOVA followed by Tukey's post hoc test where $^{**}p < 0.01$, $^{***}p < 0.001$. Scale bars: (A) 2 mm, (B) 100 µm, (D) 20 µm.

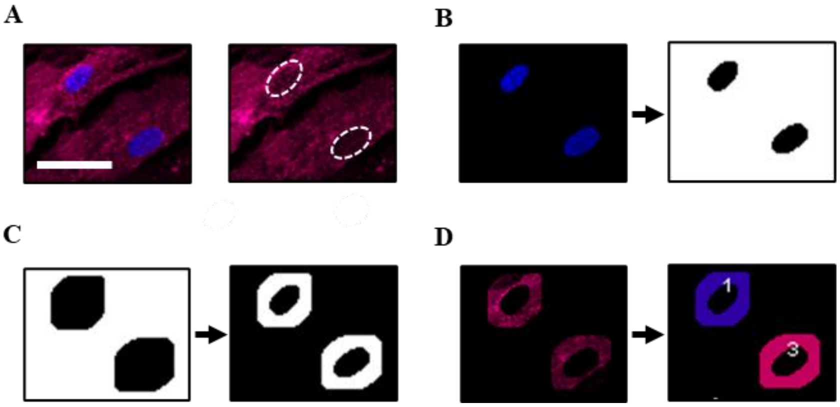

*Figure 27.* MFI determination of cytoplasmic ALP signal for single MSCs. **(A)** Representative image of two MSCs stained for ALP (magenta) and nucleus (blue and white dashed outline). **(B)** The nucleus channel is subject to an Otsu-based threshold to create a binary mask. **(C)** The nuclei masks are dilated, inverted, and overlaid with the original nuclear mask to create ring-shaped regions of interest (ROIs). **(D)** The ring-shaped ROIs are applied to the ALP channel and the 3D Objects Counter is applied to calculate MFI, which is the integrated density of ALP signal divided by the ring-shaped ROI area. Scale bar: 50 µm.

### *4.3.4 Immobilized DWIVA Enhances ALP Levels of MSCs in 3D Nor-Tet Hydrogels*

MSCs were mixed in HATet and HANor pre-functionalized with thiolated RGD (2 mM) and with 0, 0.5, or 2 mM thiolated DWIVA and added to cylindrical molds to form 3D cell-laden Nor-Tet hydrogels (Figure 29A). MSCs encapsulated in 0 mM DWIVA hydrogels and cultured in Osteogenic Medium show significantly more positive staining for ALP (dark blue) than those cultured in Growth Medium (Figure 29B). MSCs cultured in Growth Medium and encapsulated in DWIVA-functionalized HA Nor-Tet hydrogels show an increase in ALP signal with increasing DWIVA concentration (Figure 29C). A k-means clustering algorithm was applied for MSCs in 3D hydrogels in Growth Medium (negative group) and OS Medium (positive group) to determine a threshold MFI of 48, which covers 95% of ALP(-) MSCs (Figure 29D). The percentage of ALP(+) MSCs in 3D Nor-Tet hydrogels is 19.7 ± 3.5% (Growth Medium), 20.4 ± 5.5% (0.50 mM DWIVA), 56.1 ± 4.6% (2.0 mM DWIVA), and 64.7 ± 4.3% (OS Medium) (Figure 29E). Confocal images of MSCs cultured in Growth Medium and encapsulated in Nor-Tet hydrogels without (0 mM) or with (2 mM) DWIVA tethering show observable differences in ALP fluorescence (Figure 29F).

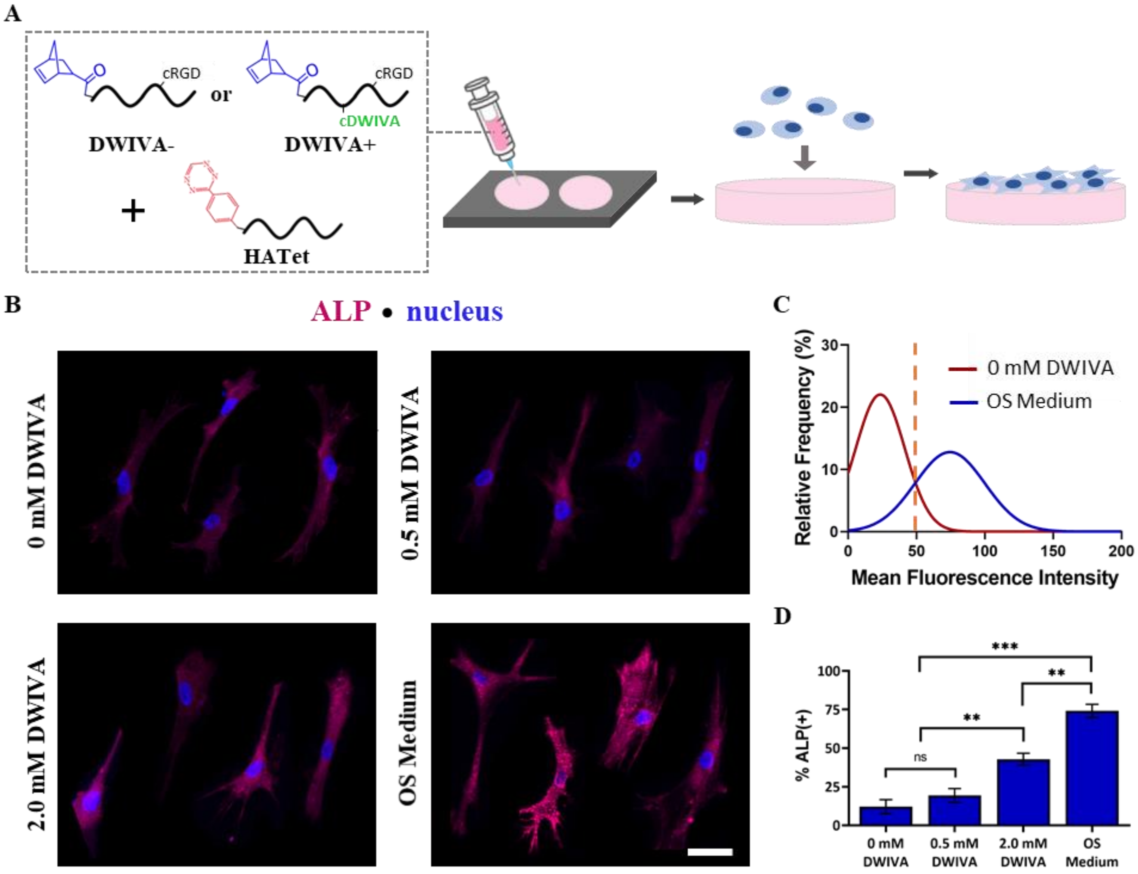

*Figure 28.* Immobilized DWIVA enhances ALP levels of MSCs on 2D Nor-Tet hydrogels. **(A)** HANor functionalized with RGD (2 mM) and DWIVA (0, 0.5, or 2 mM) were mixed with HATet, injected into cylindrical molds, and MSCs seeded atop. **(B)** Representative ALP (magenta) and nucleus (blue) staining of MSCs seeded on Nor-Tet hydrogels with 0, 0.5, or 2 mM DWIVA functionalization and OS Medium positive control. (**C**) Frequency distribution of ALP MFI of MSCs seeded on Nor-Tet hydrogels cultured in Growth Medium (negative group) or OS Medium (positive group); dashed line shows MFI cutoff for ALP(-) and ALP(+) cells. **(D)** % ALP(+) quantification of MSCs cultured on Nor-Tet hydrogels in Growth Medium with 0, 0.5, or 2.0 mM immobilized DWIVA. Bar graphs are shown as mean ± SD, (n ≥ 50 cells per condition) with nonsignificant differences denoted as ns, and significant differences determined with ANOVA followed by Tukey's post hoc test where $^{**}p < 0.01$, $^{***}p < 0.001$. Scale bar: (B) 20 µm.

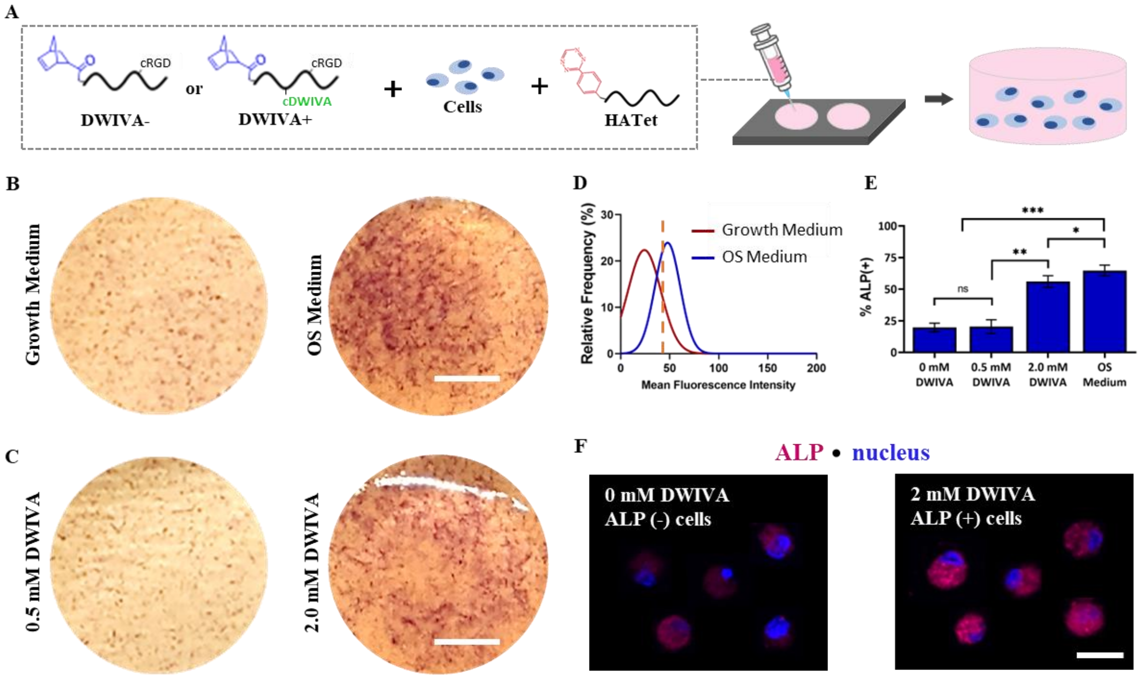

*Figure 29.* Immobilized DWIVA enhances ALP levels of MSCs in 3D Nor-Tet hydrogels. **(A)** MSCs were resuspended in RGD-functionalized HANor with or without DWIVA coupling, mixed with HATet, and injected into cylindrical molds. Representative ALP staining of MSCs (dark blue) in 3D Nor-Tet hydrogels with **(B)** 0 mM DWIVA and Growth Medium or OS Medium and **(C)** Growth Medium with 0.5 mM or 2.0 mM DWIVA coupling. **(D)** Frequency distribution of ALP MFI of MSCs encapsulated in 3D Nor-Tet hydrogels (0 mM DWIVA) cultured in Growth Medium (negative group) or OS Medium (positive group); dashed line shows MFI cutoff for ALP(-) and ALP(+) cells. **(E)** % ALP(+) quantification of MSCs cultured in 3D Nor-Tet hydrogels functionalized with 0, 0.5, or 2.0 mM immobilized DWIVA. **(F)** Representative images of single MSCs (ALP, magenta; nuclei, blue) in Growth Medium with 0 mM or 2.0 mM DWIVA coupling. Bar graphs are shown as mean ± SD, (n ≥ 50 cells per condition) with nonsignificant differences denoted as ns, and significant differences determined with ANOVA followed by Tukey's post hoc test where $^{*}p < 0.05$, $^{**}p < 0.01$, $^{***}p < 0.001$. Scale bars: (B, C) 2 mm, (F) 20 μm.

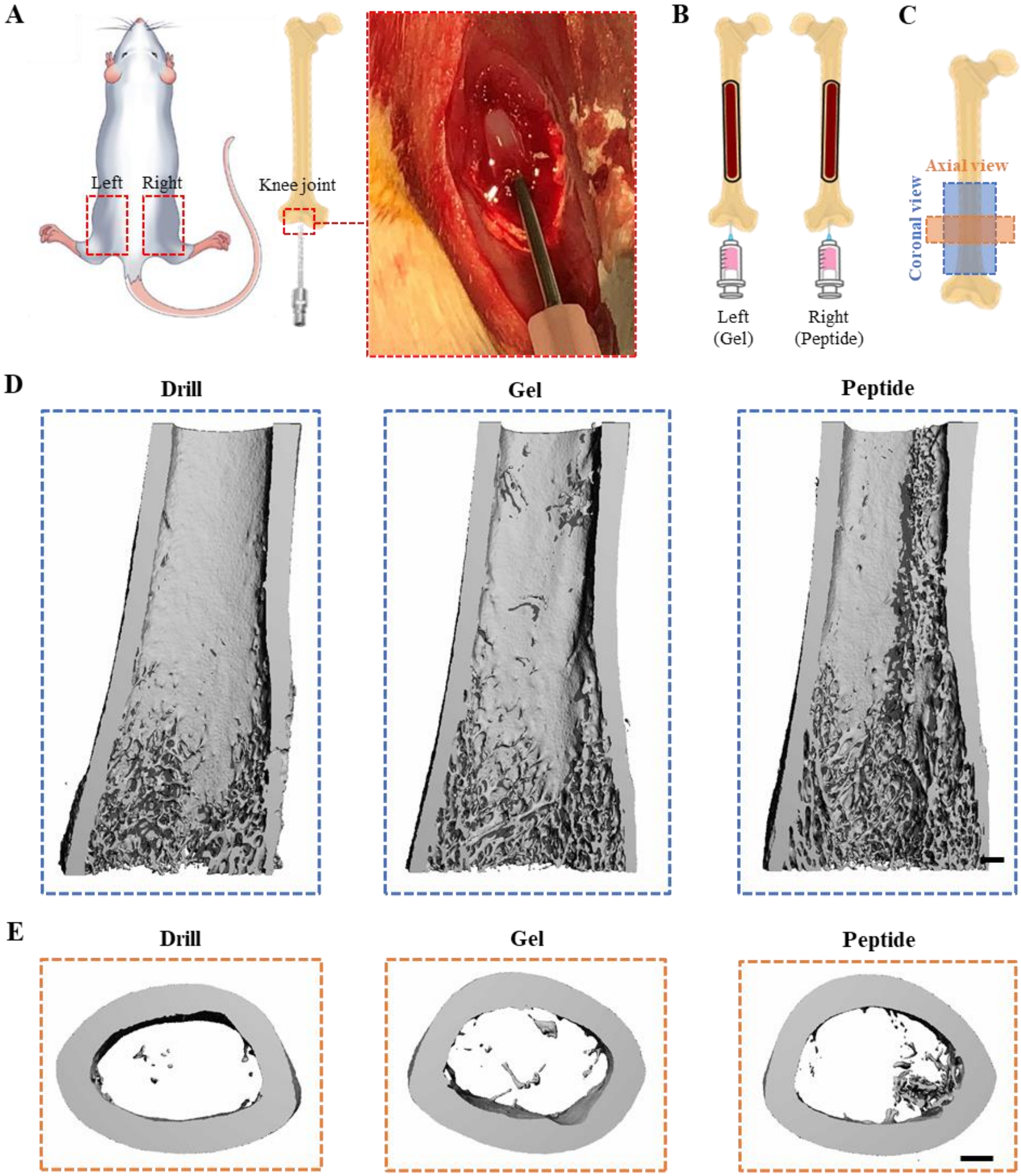

*Figure 30.* DWIVA-functionalized hydrogels induce trabecular bone growth *in vivo*. **(A)** The knee joint is exposed, and a drill is used to clear the femoral canal. **(B)** The left femur is injected with Nor-Tet hydrogels (Gel group) and the right femur is injected with DWIVA-containing Nor-Tet hydrogels (Peptide group). **(C)** Schematic shows 3D regions of interest that were imaged using micro-CT (blue rectangle, coronal view of distal shaft; orange rectangle, axial view of distal shaft center). Representative micro-CT scans of **(D)** the distal shaft and **(E)** the distal shaft center of drilled femurs, and drilled femurs injected with Gel and Peptide. Scale bars: (D), (E) 500 μm.

### *4.3.5 Injectable HA Hydrogels with Immobilized DWIVA Induce Trabecular Bone Growth*

To evaluate bone growth *in vivo*, the left and right knee joints of 8-week-old male Lewis rats were opened surgically under sterile conditions. The intercondylar notch of each distal femur was identified, and the intramedullary space of the femur was cleared of native trabecular bone and bone marrow using a 1 mm drill. (Figure 30A). Nor-Tet hydrogel solutions without peptide (Gel group) and with 2.0 mM DWIVA peptide (Peptide group) were injected into the left and right femurs, respectively (Figure 30B). Four weeks post-injection, rats were euthanized, and femurs were harvested. Microcomputed tomography (micro-CT) was used to image the distal shaft and to create 3D coronal views of the distal shaft and 3D axial views of the distal shaft center (Figure 30C). Increased trabecular bone growth is observed in femurs injected with Peptide-containing Nor-Tet hydrogels when compared to femurs injected with Gel alone, as seen by 3D coronal (Figure 30D) and 3D axial (Figure 30E) views.

## 4.4 Discussion

In this study, we developed DWIVA-functionalized self-forming hydrogels that enhance osteogenesis *in vitro* and induce bone growth *in vivo*. While there are other chemistries for forming hydrogels such as photopolymerization and thermogelation, they require some type of catalyst while self-forming hydrogels do not. This method of forming hydrogels makes it suitable for injectability or other applications where catalysts may not be readily available. The hydrogel macromers consist of HA modified with Nor or Tet moieties which upon mixing form covalent networks by undergoing an inverse electron demand Diels-Alder reaction (Figure 31). The 2% w/v macromer formulation used across this entire study allows for sufficient time to extrude the mixed solution without forming inside a syringe or clogging the needle. While this chemistry has been used to develop biocompatible PEG [60], alginate (Desai et al., 2015), and gelatin [59] self-forming hydrogels, it is challenging to incorporate bioactive motifs into Diels-Alder hydrogels. Here, the carboxyl groups of HA were modified with Nor and Tet, leaving the hydroxyl groups in HA free for additional modifications. This allowed us to pre-functionalize HANor with DWIVA by first modifying hydroxyl groups on HANor with Me moieties, followed by coupling with thiolated DWIVA via a Michael-addition reaction (Figure 24A). Since DWIVA was coupled to hydroxyl groups, we hypothesized that this should have no impact on Nor-Tet interactions from moieties coupled to carboxyl groups of HA (Figure 24B). To test our hypothesis, we performed rheological tests of 2% w/v HA Nor-Tet hydrogels formed by mixing HATet with HANorMe pre-coupled with different concentrations of DWIVA (0, 0.5, 2.0 mM) (Figure 24C-E). While there was a slight decrease in the storage modulus (G´) and gelation time, this was not a significant decrease and may be due to slight variability from time taken to mix and add solutions to the rheometer stage between samples. HA Nor-Tet hydrogels were also pre-formed in cylindrical molds, stored in PBS at 37 °C overnight, and compression testing was performed to measure the effects of DWIVA coupling on elastic moduli (E) (Figure 24F). The hydrogels retained their cylindrical geometry at physiological temperature and DWIVA had no effect on stiffness.

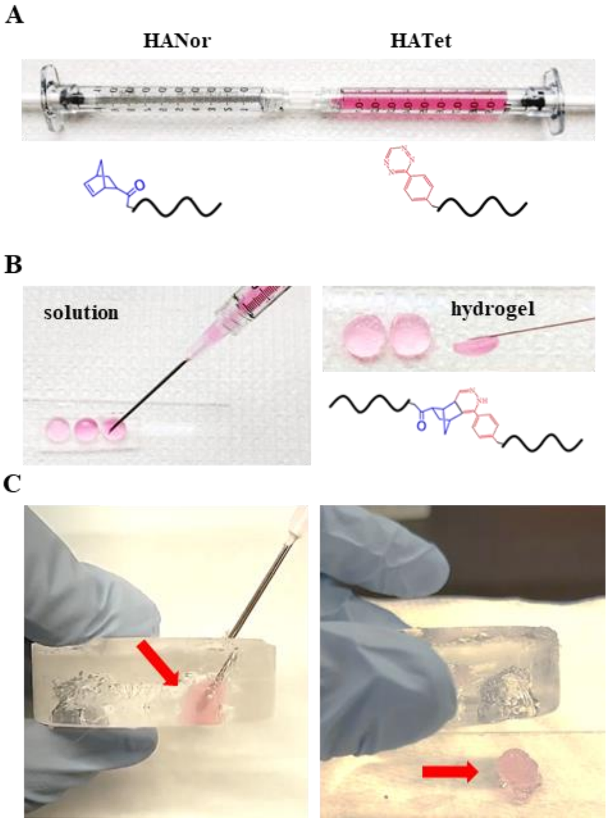

*Figure 31.* Nor-Tet hydrogel polymerization. **(A)** HANor and HATet macromers rapidly dissolve at room temperature and are loaded into syringes for mixing through a Luer-Lock syringe coupler. Mixed macromers remain in solution with ample time for extrusion into **(B)** molds or **(C)** cavities.

DWIVA is the active motif in the wrist epitope of bone morphogenetic protein 2 (BMP-2) [176], and growth medium supplemented with BMP-2 causes an osteogenic response on cultured cells [227,228]. Soluble BMP-2 has been incorporated with implantable biomaterial scaffolds for bone regeneration [140–142]. Due to diffusion of untethered BMP-2 and its short half-life, high doses of the growth factor was required and serious complications such as ectopic bone formation have been observed [140–142]. Efforts to tether growth factors were limited by low conjugation efficiency and are costly [72]. Alternatively, short chain mimics of BMP-2 such as DWIVA are cheap to synthesize and can be tethered easily. To evaluate the osteogenic properties of DWIVA, MSCs were seeded on glass and cultured in Growth Medium supplemented with low (0.5 mM) or high (2.0 mM) concentrations of soluble DWIVA. After 7 days in culture, MSCs were stained for ALP, a well-established biomarker of osteogenesis [72,176]. MSCs cultured in Growth Medium and in OS Medium served as control groups and had the lowest and highest observable amount of ALP, respectively (Figure 26A-B). To quantify percentage of ALP(+) MSCs, a mean fluorescence intensity (MFI) histogram of cytoplasmic ALP from MSCs cultured in Growth Medium (negative control) and OS Medium (positive control) was used to identify a cutoff MFI value for ALP(+) cells (Figure 26C). The threshold MFI was set such that 95% of MFI values for MSCs in the ALP(-) group (Growth Medium) were classified as ALP(-). This technique is an adaptation of a k-means clustering-based approach to assign cells to a subpopulation based on specific metrics [203], and it minimizes bias for identifying ALP(+) MSCs. Using this approach for MSCs on glass, the threshold MFI was determined to be 52. The Growth Medium and OS Medium ALP MFI histograms had very little overlap and had peak values of 18 and 102, respectively (Figure 26C). Although glass is extremely stiff and rigid substrates favor osteogenic differentiation [70], synergy between high mechanics and soluble DWIVA was only observed at high (2.0 mM) DWIVA concentrations. There was no significant difference in ALP(+) MSCs between Growth Medium and low (0.5 mM) DWIVA concentration, while 67% of MSCs were ALP(+) in the high DWIVA concentration group (Figure 26E).

After demonstrating that soluble DWIVA induces increased ALP, we evaluated the osteogenic effects of immobilized DWIVA. Here, HANorMe was first pre-coupled with 2 mM thiolated RGD and different concentrations of thiolated DWIVA (0, 0.5, 2.0 mM). To form peptide-functionalized HA Nor-Tet hydrogels, bioactive HANor was mixed with

HATet and the solution polymerized on cylindrical molds, and MSCs were seeded on top (Figure 28A). Since MSCs do not readily adhere to HA, all groups included 2.0 mM RGD, a peptide motif of adhesive fibronectin [229]. MSCs attached on all groups, and after 7 days increased intracellular ALP levels were observed with increasing DWIVA concentration (Figure 28B). To minimize bias while identifying ALP(+) MSCs, MFI histograms of MSCs on HA Nor-Tet hydrogels cultured in Growth Medium (negative group) and OS Medium (positive group) were used to identify a threshold MFI (Figure 28C). Through k-means clustering, the cutoff MFI for ALP(+) MSCs was determined to be 50, which is slightly lower than the threshold for the glass group ($\text{MFI} \geq 52$). There was also significantly more overlap between MFI values for the negative and positive groups, and the MFI peak for the OS Medium group decreased from 102 to 76 (Figure 28C). The decrease in MFI for the positive group could be attributed to the mechanical properties of the HA Nor-Tet hydrogels. At a total macromer concentration of 2% w/v, HA Nor-Tet hydrogels were about 5 kPa, and this low stiffness does not favor osteogenesis [70]. Despite being on soft hydrogels, almost 50% of MSCs on Nor-Tet hydrogels with a high concentration (2.0 mM) of immobilized DWIVA were ALP(+) (Figure 28D). Future studies that evaluate the synergistic effects of higher mechanics and immobilized DWIVA on osteogenic differentiation may show increased ALP(+) cells at lower DWIVA concentrations.

To investigate the osteogenic effects of immobilized DWIVA in 3D environments, MSCs were suspended in pre-hydrogel solution consisting of HATet and HANor pre-functionalized with thiolated RGD and different concentrations of thiolated DWIVA (0, 0.5, 2.0 mM) and extruded into molds (Figure 29A). Gross images of 0 mM DWIVA hydrogels stained for ALP show low and high levels of ALP expression of samples cultured in Growth Medium and Osteogenic Medium, respectively (Figure 29B). These control groups confirm that encapsulated MSCs can express ALP in the presence of osteogenic growth factors. A qualitative observation between gross images of hydrogels cultured in Growth Medium with low (0.5 mM) and high (2.0 mM) DWIVA coupling display increased ALP staining with increasing DWIVA concentration (Figure 29C). MSCs are not only highly viable in HA Nor-Tet hydrogels post-extrusion (Figure 32) but respond to immobilized DWIVA in 3D self-forming hydrogels. Using the same k-means clustering approach for the 2D studies, the threshold MFI was determined to be 48, which is slightly lower than the glass (MFI ≥ 52) and 2D hydrogel (MFI ≥ 50) groups. Significant overlap between the negative (Growth Medium) and positive (OS Medium) relative frequency curves was also observed (Figure 29D). Although percentage of ALP(+) MSCs increased with increasing DWIVA concentration, only about 50% of MSCs were classified as ALP(+), even for the OS Medium group (Figure 29E). MSCs encapsulated in the HA Nor-Tet hydrogels remain spherical (Figure 29F), while degradation-mediated cellular traction is necessary for cellular spreading and osteogenesis in 3D hydrogels [71]. MSCs encapsulated in DWIVA hydrogels amenable to cell remodeling may be more osteoinductive than those in restrictive hydrogels like the HA Nor-Tet hydrogels used in this study. For example, MSCs in 3D gelatin-based Nor-Tet hydrogels are able to remodel the surrounding hydrogel [59], and replacing the HA backbone of HANorDWIVA with gelatin would allow for 3D cell spreading and DWIVA signaling.

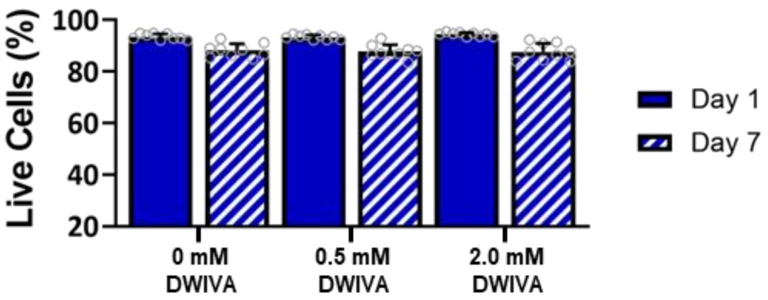

*Figure 32.* MSCs in Nor-Tet hydrogels are highly viable. Nor-Tet hydrogel solutions consisting of MSCs mixed with RGD-functionalized HANor with different concentrations of DWIVA (0, 0.5, or 2.0 mM) and HATet were injected into cylindrical molds via extrusion through a 16 G needle. Bar graph shows percentage of live cells after 1 day and 7 days from confocal images. Bar graphs shown as mean ± SD (n ≥ 3 samples per condition).

After validating the osteogenic properties of DWIVA-functionalized HA Nor-Tet hydrogels *in vitro*, we were interested in evaluating the ability to grow bone tissue in regions prone to osteoporotic fragility fractures. Specifically, femur fractures can lead to a total hip replacement, and forming nascent trabecular bone in the femur would help prevent fractures from occurring in the first place. To examine the effectiveness of HA Nor-Tet hydrogels in locally regenerating bone *in vivo,* DWIVA-coupled self-forming hydrogels (2 mM) were injected into hollow rat femurs (Figure 30A, 5B). A high DWIVA concentration was chosen since the percentage of ALP(+) MSCs was highest at 2.0 mM DWIVA. MSCs in HA Nor-Tet hydrogels without DWIVA functionalization expressed minimal ALP levels and this formulation was injected in contralateral femurs and served as a negative control group. 4 weeks post-injection, the femurs were harvested and micro-CT imaging was utilized to examine the differences in new trabecular bone growth in femurs that were kept hollow (Drill) or injected with uncoupled (Gel) or DWIVA-coupled (Peptide) self-forming hydrogels. 3D coronal views of the distal shaft for the Drill and Gel groups shows minimal trabecular bone along the shaft with trabeculae in the metaphysis (bottom), whereas in the Peptide group significant trabecular bone growth is observed along the shaft (Figure 30D). 3D axial views of the distal shaft center reveal almost no trabecular bone in the Drill group, with increasing trabeculae seen in the Gel and Peptide groups (Figure 30E). Since the Gel and Peptide groups were acellular, bone regeneration in the trabecular space would have had to be produced by native cells that migrated into the hydrogel. The migration of native cells into the trabecular space may have been aided by the presence of hyaluronidase, an enzyme that breaks down HA by cleaving its glycosidic bonds, in the femoral shaft [230]. Although DWIVA-functionalized hydrogels were exposed to hyaluronidase *in vivo*, the bioactivity of the hydrogel was preserved as shown by improved trabecular bone growth in the Peptide group. Additionally, since hyaluronidase cleaves the glycosidic bonds in the hyaluronic chain, exposure to the enzyme should not interfere with DWIVA conjugation. Enzymatic degradation of HA hydrogels *in vivo* could be replicated *in vitro* by adding exogeneous hyaluronidase. By doing so, we will be able to compare the degradation rate of the hydrogel with the rate of trabecular bone formation.

Together, these findings show that injectable, DWIVA-functionalized hydrogels can locally regenerate bone *in vivo* and present opportunities for follow-up studies. Bone regeneration after a fracture can take 6 – 12 weeks [231], and the osteogenic effects of DWIVA at later time-points has not been determined. Furthermore, the bioavailability of DWIVA in soluble and tethered form has not been evaluated and it is an area that warrants further study. While we showed that the high (2.0 mM) DWIVA peptide concentration group displayed osteogenic properties *in vitro* and *in vivo*, the peptide coupling chemistry presented here can be used to evaluate the osteoinductive properties of DWIVA at higher peptide concentrations. The HA Nor-Tet hydrogels are amenable to 2D and 3D MSC culture, and the inclusion of DWIVA has an osteogenic effect on resident MSCs. Thus, it would be interesting to evaluate the synergistic effects of MSCs and DWIVA in regenerating bone *in vivo*. Besides the DWIVA wrist epitope of BMP-2, BMP-2 also has a knuckle epitope with the active sequence KIPKASSVPTELSAISTLYLG (KIPKA) [72,176]. The KIPKA sequence is believed to bind to BMP receptor II. Since both receptors I and II are involved in the signaling cascade for BMP-2, it would be beneficial to explore the independent effect of KIPKA and the synergistic effects of KIPKA and DWIVA sequences in locally regenerating bone.

## 4.5 Conclusion

We developed an injectable hydrogel with DWIVA, an immobilized mimetic peptide of BMP-2, and demonstrated that it that can regenerate trabecular bone in femurs. We first showed that the effective concentration of DWIVA peptide in self-forming hydrogels can be controlled by changing the amount of peptide added during coupling with HANorMe macromers. We also confirmed that the bioactivity of the DWIVA peptide is preserved post-coupling by showing that ALP expression is enhanced in human MSCs seeded atop (2D) or within (3D) DWIVA-functionalized HA Nor-Tet hydrogels. This hydrogel system has the potential to be used as a targeted therapeutic to improve bone density locally, which is imperative in reducing the incidence of osteoporotic fragility fractures.

## 4.6 Experimental Section

### *4.6.1 Materials*

Sodium hyaluronate (NaHA, 60 kDa, HA60K-5) was purchased from Lifecore Biomedical (Chaska, MN). Dowex® resin 50WX2 hydrogen form 100-200 mesh, methacrylic anhydride (MA), triethanolamine (TEOA), and Fast Blue RR Assay (fast blue) were purchased from Sigma Aldrich (Burlington, MA). Dimethyl sulfoxide (DMSO), benzotriazole-1-yl-oxy-tris-(dimethylamino)-phosphonium hexafluorophosphate (BOP), β-(N-morpholino)ethanesulfonic acid (MES), and SpectraPor 6-8 kDa molecular weight cutoff dialysis tubing were purchased from Millipore Sigma (St. Louis, MO). Tetrabutylammonium hydroxide (TBA-OH) was purchased from Acros Organics (Geel, Belgium). 5-norbornene-2-methylamine (Nor-$NH_2$) and N-hydroxysuccinimide (NHS) were purchased from TCI America (Portland, OR). 1-(3-dimethylaminopropyl)-3-ethylcarbodiimide (EDC) and Hoechst were purchased from Thermo Scientific (Waltham, MA). Tetrazine-amine (Tet-$NH_2$) was purchased from Kerafast (Boston, MA). Thiol-containing peptide mimic of BMP-2 with sequence GCGGGDWIVAG (DWIVA) was purchased from GenScript (Piscataway, NJ). Human MSCs from bone marrow and Osteogenic Differentiation BulletKit$^{TM}$ Medium (OS Medium) were purchased from Lonza (Walkersville, MD). Minimum essential medium alpha (MEM-α) with no nucleosides, penicillin/streptomycin (10,000 U/ml), and fetal bovine serum (FBS) were purchased from Gibco (Waltham, MA). Silicone elastomer, Sylgard$^{TM}$ 184 was purchased from Electron Microscopy Sciences (Hatfield, PA). Isoflurane solution and 70% isopropyl alcohol were purchased from Covetrus (Portland, ME). Buprenorphine SR 1mg/mL and meloxicam SR 2mg/mL were purchased from ZooPharm (Laramie, WY). 2%

chlorohexidine was purchased through Covetrus (Portland, ME) and supplied by Vedco (Saint Joseph, MO).

### *4.6.2 HANor Synthesis*

Carboxyl groups in HA were modified with Nor as previously described [196]. Briefly, NaHA was converted to its tetrabutylammonium salt (HATBA) by dissolving in distilled water (2% w/v) and mixing with Dowex resin (3 g resin per 1 g NaHA) for two hours at room temperature. The resin was then vacuum filtered, and the pH was adjusted to 7.02 using TBA-OH diluted in water (1:1 v/v). The resulting HATBA solution was frozen and lyophilized. Carboxyl groups in HATBA were then modified with Nor via amidation with Nor-$NH_2$ (0.4 mmol per 1 g of HATBA) in anhydrous DMSO (0.5 ml per 0.1 g HATBA) and BOP (0.38 g per 1 g HATBA) under nitrogen for two hours at room temperature. The reaction was quenched with cold distilled water, dialyzed with SpectraPor dialysis tubing, frozen, and lyophilized. The synthesized HANor macromer had ~50% of its repeat units functionalized with Nor, as analyzed with $^1H$ NMR spectroscopy. The percentage of modification was calculated by comparing the integral of the methyl HA peaks between $\delta$ 1.8 to 2.0 ppm to the vinyl proton peaks of Nor between $\delta$ 6.2 to 6.3 ppm [197].

### *4.6.3 HATet Synthesis*

Carboxyl groups in HA were modified with Tet using a modified procedure previously described [50]. Briefly, HATBA was dissolved (1% w/v) in 100 mM MES buffer (pH 6). EDC, NHS, and Tet-$NH_2$ were added at a 1:4:1 molar ratio at 0.5 mmol Tet per g of HATBA and reacted overnight at room temperature. The HATet solution was then dialyzed with SpectraPor dialysis tubing, frozen, and lyophilized. $^1H$ NMR spectroscopy analysis confirmed that ~40% of HATet repeat units were functionalized with Tet. The percentage of modification was calculated by comparing the integral of the methyl HA peaks between δ 1.8 to 2.0 ppm to the aromatic proton peak of Tet between δ 10.4 ppm [59].

#### *4.6.4 HANorDWIVA Synthesis*

Hydroxyl groups in HANor were first modified with Me to form HANorMe via esterification with MA by adapting a previously described protocol [174]. HANor was dissolved (1% w/v) in distilled water at 4 °C. A 15-fold molar excess of MA was added dropwise while maintaining pH between 8.5 and 9.0. After all MA was added, the solution was left stirring overnight at room temperature. The HANorMe solution was then dialyzed with SpectraPor dialysis tubing, frozen, and lyophilized. $^1$H NMR spectroscopy analysis confirmed that ~60% of HANorMe repeat units were functionalized with Me. The percentage of modification was calculated by comparing the integral of the HA peaks between δ 1.8 to 2.0 ppm to the alkene proton peaks of Me between δ 5.5 to 6.5 ppm [199].

To peptide-functionalize HANorMe, thiols in cysteine-containing peptides were coupled to Me groups in HANorMe via an aqueous Michael addition reaction [200]. Briefly, HANorMe was dissolved (1% w/v) in 200 mM TEOA buffer (pH 8) at room temperature. Thiolated DWIVA (sequence: G**C**GGGDWIVAG) in solution (50 mM in PBS) was added dropwise to reach a final DWIVA concentration that corresponds to an effective concentration of either 0.50 mM or 2 mM for 2% w/v HA Nor-Tet hydrogels (Table 5) [72,176]. The HANorDWIVA solution was then dialyzed with SpectraPor dialysis tubing, frozen, and lyophilized. $^1$H NMR spectroscopy analysis confirmed that 10% (for 0.5 mM) and 40% (for 2 mM) of Me groups were coupled with DWIVA. The percentage of Me-DWIVA coupling was calculated by comparing the integral of alkene proton peaks of Me between δ 5.5 to 6.5 ppm [199] to the protons in the amino group of cysteine moiety between δ 0.50 to 1.50 ppm [72].

**Table 5**

*Reaction Parameters to Create DWIVA-Functionalized HANorMe Macromers*

| Effective DWIVA Concentration (mM) | HANorMe (mg) | cDWIVA (mg) |
|---|---|---|
| 0.5 | 100 | 3.97 |
| 2.0 | 100 | 15.86 |

### *4.6.5 Characterization of Nor-Tet Hydrogels*

To characterize the hydrogels, rheology and compression mechanical testing were performed. Rheological properties of Nor-Tet hydrogels were measured using a Discovery Hybrid Rheometer (DHR-3, TA Instruments, New Castle, DE) with a 20 mm diameter 1° cone upper plate geometry and a lower plate temperature of 37 °C. Samples were prepared by dissolving HANor (with or without DWIVA functionalization) and HATet separately in PBS, followed by mixing at a 1:1 stoichiometric ratio, resulting in a final macromer concentration of 2% w/v. Immediately after mixing, 40 µl of the solution was pipetted to the center of the rheometer stage and the shear storage (G′) and loss (G″) moduli were monitored. To measure plateau G′ and gelation kinetics, time sweeps were performed for 1 hour at 1 Hz and 1% oscillatory strain. Bulk mechanical properties of 2% w/v self-forming hydrogels were measured using an EZ-SX Mechanical Tester (Shimadzu, Long Beach, CA) equipped with a 50 N compression load. Briefly, hydrated HANor or HANorDWIVA and HATet were mixed and pipetted into cylindrical polydimethylsiloxane (PDMS) molds (2 mm height, 8 mm diameter). The hydrogels were allowed to form for 30 minutes before incubating in PBS overnight at 37 ˚C. Formed cylindrical Nor-Tet hydrogels were compressed until 30% strain, and the elastic modulus (E) was determined using the slope of the stress-strain curve between 10% and 20% strain.

### *4.6.6 Cell Culture*

Human primary MSCs were cultured in 100 mm petri dishes in Growth Medium (MEM-α supplemented with 10% FBS and 1% P/S). To study the effects of soluble DWIVA on stem cell cultures, MSCs were seeded on top of glass coverslips (12 mm diameter) at a density of 3,000 cells per $cm^2$. After 6 hours in culture, media was replaced with either Growth Medium (0 mM DWIVA), Growth Medium supplemented with low (0.50 mM) or high (2.0 mM) DWIVA, or OS Medium.

To study the effects of tethered DWIVA on 2D hydrogel cultures, 2% w/v HA Nor-Tet hydrogels with varying degrees of DWIVA functionalization (0, 0.5, 2 mM) were formed on PDMS molds (11 mm diameter, 1 mm height) for 30 minutes followed by incubation in Growth Medium for 30 minutes at 37 ˚C. MSCs were seeded on top of these hydrogels at a density of 3,000 cells per $cm^2$. To study the effects of DWIVA in 3D hydrogel cultures, MSC-laden ($2 \times 10^6$ cells/ml) 2% w/v Nor-Tet hydrogels with varying degrees of DWIVA functionalization (0, 0.5, 2 mM) were formed on PDMS molds (8 mm diameter, 2 mm height) for 2 minutes followed by incubation in Growth Medium for 30 minutes at 37 ˚C. Appropriate media were replenished every 48 hours and all experiments were cultured for 7 days.

### *4.6.7 Staining and Imaging Based Analysis*

After 7 days in culture, samples were fixed with 10% neutral buffered formalin for 10 mins (glass, 2D hydrogels) or 30 mins (3D hydrogels) at room temperature. To visualize cellular ALP, fast blue was added for 1 hour (glass, 2D hydrogels) or 3 hours (3D hydrogels). To visualize individual nuclei, samples were stained for double stranded DNA with Hoechst (1:1000) for 5 mins (glass, 2D hydrogels) or 15 mins (3D hydrogels). Acquisition of immunofluorescence images was performed with a Nikon A1 confocal microscope. Images were taken at 20x magnification and at laser wavelengths of 405 nm (nuclei) and 640 nm (ALP) (glass, 2D and 3D hydrogels). Image stacks were taken at height of 200 µm with a step size of 3.2 µm (3D hydrogels).

Mean fluorescence intensity (MFI) of cellular ALP was determined using ImageJ software (National Institute of Health, Bethesda, MD, USA). Briefly, nuclei stacks were binarized using the Otsu thresholding method. Binarized nuclei stacks were dilated, and the nuclei stacks were subtracted from the dilated stacks resulting in rings. The rings were converted into masks and overlayed on the ALP channel stacks. The 3D Objects Counter feature was then applied to calculate the surface area of the rings and the Measure function was used to determine the integrated density of the rings. The MFI value of every cell was calculated by dividing its mean grey value by area. The MFI values of Growth Medium and OS Medium groups were processed using a k-means clustering algorithm to determine the boundary between MSCs with low (ALP-negative) and high (ALP-positive) MFI. The selected threshold MFI covers 95% of ALP-negative cells [203].

### *4.6.8 Animal Protocol*

The animal experiment was approved by the Cooper University Health Care's Institutional Animal Care and Use Committee (IACUC). Experiments were performed on 8-week-old male Lewis rats (Charles River Laboratories, Raleigh, NC) weighing approximately 275-300 g. The rats were housed in a 12-hour dark-light cycle where they had access to food and water ad libitum. The rats were randomly divided into three groups: drilled canal alone, injectable hydrogel, and injectable hydrogel with 2 mM DWIVA peptide. The procedures were performed under anesthesia using inhaled isofluorane solution and buprenorphine SR. Once anesthetized, surgical sites were prepared by shaving the ventral aspect of the abdomen and hind legs and scrubbed with 2% chlorohexidine and 70% isopropyl alcohol. A standard median parapatellar approach to bilateral knees was performed. The distal femurs were exposed, and the femoral notch was identified. Utilizing a 1 mm sterile drill, the intramedullary canal was drilled and checked on fluoroscopy for placement. Three passes with the drill were performed to adequately remove native bone marrow and trabecular bone. The femurs were then filled with 0.2 ml of 2% w/v self-forming hydrogel solution via injection using a 25-gauge syringe. Bone wax was placed over the hole after injection. Closure of the arthrotomy and skin was performed with Vicryl sutures. Following closure of the surgical sites, animals were given meloxicam SR (2mg/ml) for pain alleviation and subsequently returned to their housing where they were monitored until they recovered from the surgical anesthesia. All rats were euthanized 4 weeks post-injection and the left and right femurs were harvested. The femurs were fixed with 10% neutral-buffered formalin for 24 hours, washed with distilled water, and stored in 70% ethanol at 4 ºC until micro-CT imaging.

#### *4.6.9 Micro-CT*

The distal shaft (midshaft down to the metaphysis) of extracted femurs were scanned using micro-CT (micro-CT 45, ScancoMedical AG, Brüttisellen, Switzerland) at 10.4 µm isotropic resolution, with 55 kVp energy, and 400 ms integration time. This region was chosen to evaluate the effects of injectable DWIVA hydrogels on trabecular bone formation. At the center of the distal shaft, a 200-slice-thick volume of interest (VOI) was identified, Gaussian filtered (sigma = 1.2, support = 2), and bone was identified by applying a global threshold (220 mg hydroxyapatite per $cm^3$). Manufacturer-provided software for 3D standard microstructural analysis was used to generate 3D axial views of the 200-slice-thick VOIs and coronal views of the 1031-slice-thick distal shaft.

### *4.6.10 Statistical Analysis*

Statistical analysis was performed using GraphPad Prism (version 9.3.1, GraphPad Software, Inc., La Jolla, CA). All experiments were carried out in triplicate and single cell analysis was done with at least 50 cells per group. All graphs represent mean ± standard deviation (SD). Analysis of variance (ANOVA) was performed followed by Tukey’s test for post-hoc analysis. Differences among groups are stated as $p < 0.05$ (*), $p < 0.01$ (**), $p < 0.001$ (***), and (ns) when differences between groups are not statistically significant.

# Chapter 5

## BMP-2 Functionalized Injectable Hydrogels with Human Mesenchymal Stem Cells Enhance Femoral Trabecular Bone Growth

### 5.1 Abstract

Prevalence of osteoporotic fractures due to a decrease in bone mineral density is rapidly increasing with the aging population. Most therapies for osteoporosis are systemic and do not restore bone in areas of need. Injectable hydrogels can locally delivery therapeutics at precise locations. This study reports the addition of human MSCs to the injectable hydrogel that we previously developed which contains a peptide mimic of bone morphogenetic protein-2 (BMP-2). Injection of MSC-laden bioactive Nor-Tet hydrogels into hollow intramedullary canals of Lewis rat femurs showed a local temporal increase in trabecular bone density and increase in the formation of osteoid tissues as determined by micro-CT imaging and histological staining. The presented work shows that injectable hydrogels with MSCs and immobilized BMP-2 peptides are a promising biomaterial for the local regeneration of bone tissues specifically for the potential local treatmnet of osteoporosis.

### 5.2 Introduction

The prevalence of osteoporotic fractures is projected to increase substantially due to the growth in aged population.[205] Currently, individuals affected with osteoporosis experience fragility fractures with a mortality rate of up to 69% within 10 years.[207] Osteoporosis is characterized by a reduction in bone mineral density due to the disruption of the natural bone remodelling process.[204] Bone remodeling is a physiological balance between osteoblasts forming new bone and osteoclasts absorbing the bone matrix.[232]

Factors such as hormonal changes after reaching post-menopausal age, genetics, and inactive lifestyle can disrupt the natural bone remodelling process and lead to loss of bone mass density or osteoporosis.[208,210,233] In osteoporosis, bone loss in mainly observed in trabecular or cancellous bone, made up of a trabeculae network with high bone turnover.[211–213] Current treatments for osteoporosis are antiresorptive drugs which can cause systemic side effects, and estrogen supplementation which can cause blood clots.[205,214]

Growth factors play an important role in bone formation. For example, after a fracture an inflammatory reaction occurs at the site wherein a large number of growth factors including transforming growth factor-β (TGF-β), vascular endothelial growth factor (VEGF), and bone morphogenetic protein-2 (BMP-2) are recruited to the fracture site.[234] Upon arrival, these factors promote blood flow, recruit stem cells, and induce their differentiation into osteoblasts to accelerate fracture repair.[235] BMP-2 has been identified as a potent inducer of osteogenesis *in vivo*.[215–219] BMP-2 binds to cell BMP-receptor type II, which leads to the activation of BMP-receptor type I, and to the activation of Smad1, a cytoplasmic signaling molecular for BMP-2. Activated Smad1 then localizes to the nucleus and controls gene expression to initiate osteogenic differentiation.[220–222]

Efforts to develop strategies to regenerate bone have utilized the DWIVA peptide sequence from BMP-2, which has high receptor binding affinity and specificity to BMP-receptor types I and II[176], to enhance osteogenic differentiation of human MSCs and bone formation.[72,176,177]. Seol et al. found that MC3T3-E1 cells cultured on titanium chemically modified with DWIVA peptides had higher levels of alkaline phosphatase, a biomarker for osteogenic differentiation. Additionally, the DWIVA-treated titanium dental implants induced increased bone formation *in vivo*. In a previous study, we demonstrated the use of an injectable HA hydrogel with immobilized DWIVA peptide which increased ALP expression in encapsulated MSCs.[236] Additionally, we showed that injection of this HA hydrogel into hollow intramedullary canals of Lewis rat femurs resulted in local increase in trabecular bone density. HA is an abundant ECM component that mediates cellular signaling, matrix organization, and morphogenesis.[225,226] Injectability of this HA hydrogel is owed to the Inverse Electron Demand Diels-Alder reaction between Nor and Tet moieites on the HA backbone. In this study, we hypothesize that local trabecular bone density can be improved by co-delivering MSCs through the injectable HA hydrogel. To test this hypothesis, we incorporated MSCs in the injectable hydrogel system developed in our previous study and injected into hollow femurs of Lewis rats. New trabecular bone formation in rat femurs injected with MSC-laden HA Nor-Tet hydrogels with or without DWIVA peptide was evaluated using micro-CT and histological analysis through Hematoxyline & Eosin (H&E), Masson's Trichrome, and Tartrate-Resistant Acid Phosphatase (TRAP) staining.

## 5.3 Results and Discussion

### *5.3.1 MSC-Laden Injectable DWIVA-functionalized Nor-Tet Hydrogels Regenerate More Trabecular Bone Compared to Acellular Hydrogels*

We were interested in evaluating the ability to grow bone tissue in regions prone to osteoporotic fragility fractures. Specifically, femur fractures can lead to a total hip replacement, and forming trabecular bone in the femur would help prevent fractures in the first place. To examine the effectiveness of MSC-laden HA Nor-Tet hydrogels in locally regenerating bone *in vivo*, MSC-laden and DWIVA-coupled self-forming hydrogels (2 mM) were injected into hollow rat femurs (Figure 33A). A high concentration of DWIVA was chosen since it was shown in our previous study that a high concentration of DWIVA peptide resulted in highest osteogenic MSC differentiation *in vitro* and most trabecular bone regeneration *in vivo* using Nor-Tet hydrogels [236]. Specifically, the left and right knee joints of 8-week-old male Lewis rats were opened surgically under sterile conditions. The intercondylar notch of each distal femur was identified, and the intramedullary space of the femur was cleared of native trabecular bone and bone marrow using a 1 mm drill (Figure 33A). Hydrogel solutions were prepared by dissolving HATet and HANor pre-functionalized with thiolated RGD (2.0 mM) and thiolated DWIVA (2.0 mM) separately and mixing prior to injection. Nor-Tet hydrogel solutions without peptide (control gel, CG group) were injected into the left femurs (Figure 33B). Meanwhile, Nor-Tet hydrogel solutions with 2.0 mM DWIVA peptide without MSCs (experimental biologic, EB group) or with MSCs (experimental biological with cells, EBC group) were injected into the right femurs (Figure 33B). One group was not injected with any material (control drill, CD).

Injected hydrogels fill the femoral canal shown by an X-ray image (Figure 33C). Rats were euthanized at 2 and 4 weeks post-injection and femurs were harvested. Micro-CT imaging was utilized to examine the differences in new trabecular bone growth in femurs that were kept hollow (CD), or injected with uncoupled (CG), DWIVA-coupled (EB), or MSC-laden DWIVA-coupled (EBC) self-forming hydrogels. Specifically, Micro-CT was used to image the distal shaft and to create 3D coronal views of the distal shaft and 3D axial views of the distal shaft center (Figure 33D). At 2 weeks post-injection, increased trabecular bone growth is observed in EB and EBC groups when compared to the CD and CG groups as seen by 3D coronal (Figure 34A) and 3D axial (Figure 34B) views. Similarly at 4 weeks post-injection, 3D coronal (Figure 34C) and 3D axial (Figure 34D) views show increased trabecular bone growth in EB and EBC groups at 4 weeks post injection (Figure 34C, 34D). Between the EB and EBC groups at 2 and 4 weeks post-injection, higher trabecular bone growth is seen in the EBC group.

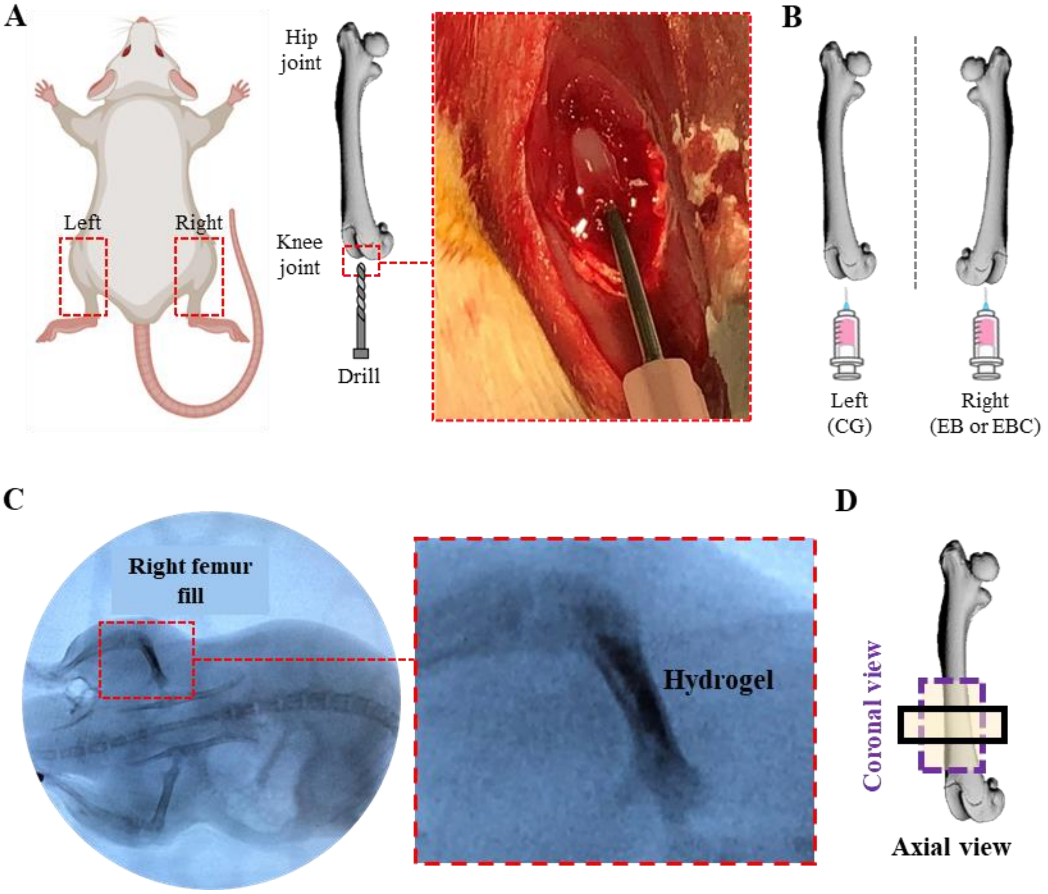

*Figure 33.* Experimental design for *in vivo* study. **(A)** A drill is used to clear the femoral canal. **(B)** The left femur is injected with Nor-Tet hydrogels (CG) and the right femur is injected with DWIVA-containing Nor-Tet hydrogels without MSCs (EB) or with MSCs (EBC). **(C)** Nor-Tet hydrogels with Omnipaque™ contrast agent completely fills the femoral canal. **(D)** Schematic shows 3D regions of interest that were imaged using micro-CT (dashed violet rectangle, coronal view of distal shaft; black rectangle, axial view of distal shaft center).

Cortical bone morphometry reveals that cortical bone thickness (Ct.Th) at 2 and 4 weeks post-injection shows no significant difference across all groups, with values ranging from 0.422 ± 0.029 mm to 0.531 ± 0.028 mm (Figure 35A). Similarly, the average cortical surface area (Ct.Ar), average cortical area of the periosteal envelope (Tt.Ar), and average cortical area fraction (Ct.Ar/Tt.Ar) are not significantly different across all groups, with values ranging from 4.434 ± 0.404 $mm^2$ to 5.244 ± 0.244 $mm^2$ (Ct.Ar) (Figure 35B), 4.443 ± 0.406 $mm^2$ to 5.3145 ± 0.234 $mm^2$ (Tt.Ar) (Figure 35C), and 0.976 ± 0.001 to 0.998 ± 0.002 (Ct.Ar/Tt.Ar) (Figure 35D). These values indicate that injection of CG, EB, or EBC hydrogels does not have any effect on the calcified or cortical bone already present in the femoral shaft.

Quantification of the trabecular bone volume (BV/TV) for the EB group shows values of 0.018 ± 0.004 and 0.049 ± 0.008 at 2 and 4 weeks post-injection (Figure 35A). Bone volume for the EBC group was highest, with values of 0.035 ± 0.005 and 0.066 ± 0.006 at 2 and 4 weeks post-injection (Figure 35A). For the CG, EB, and EBC groups, the 4-week bone volume is up to 4x that of the 2-week point. Similarly, the number of trabeculae (Tb.N) and thickness of trabeculae (Tb.Th) was highest for the EBC group at the 4-week point, with values of 1.12 ± 0.11 $mm^{-1}$ (1.5x EB at 4 weeks) (Figure 35B) and 0.063 ± 0.004 mm (1.20x EB at 4 weeks) (Figure 35C), respectively. The spacing between trabeculae (Tb.Sp) was lowest for the EBC group, with a value of 1.22 ± 0.38 mm (0.30x EB at 4 weeks) (Figure 35D). Since the CG and EB groups were acellular, bone regeneration in the trabecular space would have had to be produced by native cells that migrated into the hydrogels which may have been aided by hyaluronidase, an enzyme that breaks down HA by cleaving its glycosidic bonds, in the femoral shaft [230]. The addition of MSCs to the DWIVA-functionalized self-forming hydrogels eliminated the need to wait for native cells to migrate into the hydrogels, which could explain the temporal improvement in trabecular bone growth observed between EB and EBC groups.

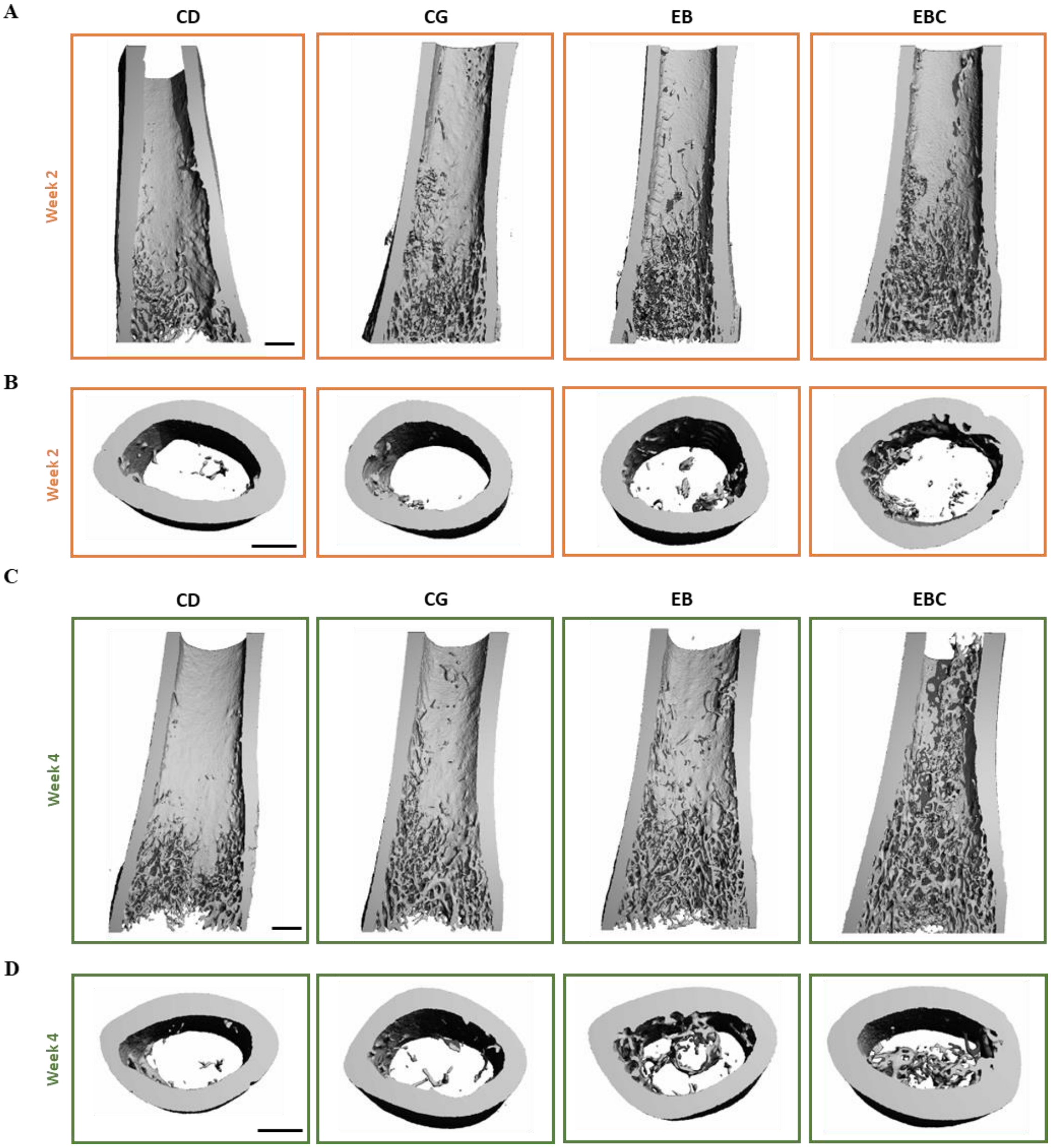

*Figure 34.* Representative micro-CT images of Volumes of Interest (VOIs). **(A)** Coronal views of Week 2 groups. **(B)** Axial views of Week 2 groups. **(C)** Coronal views of Week 4 groups. **(D)** Axial views of Week 4 groups. Scale bar: 1 mm.

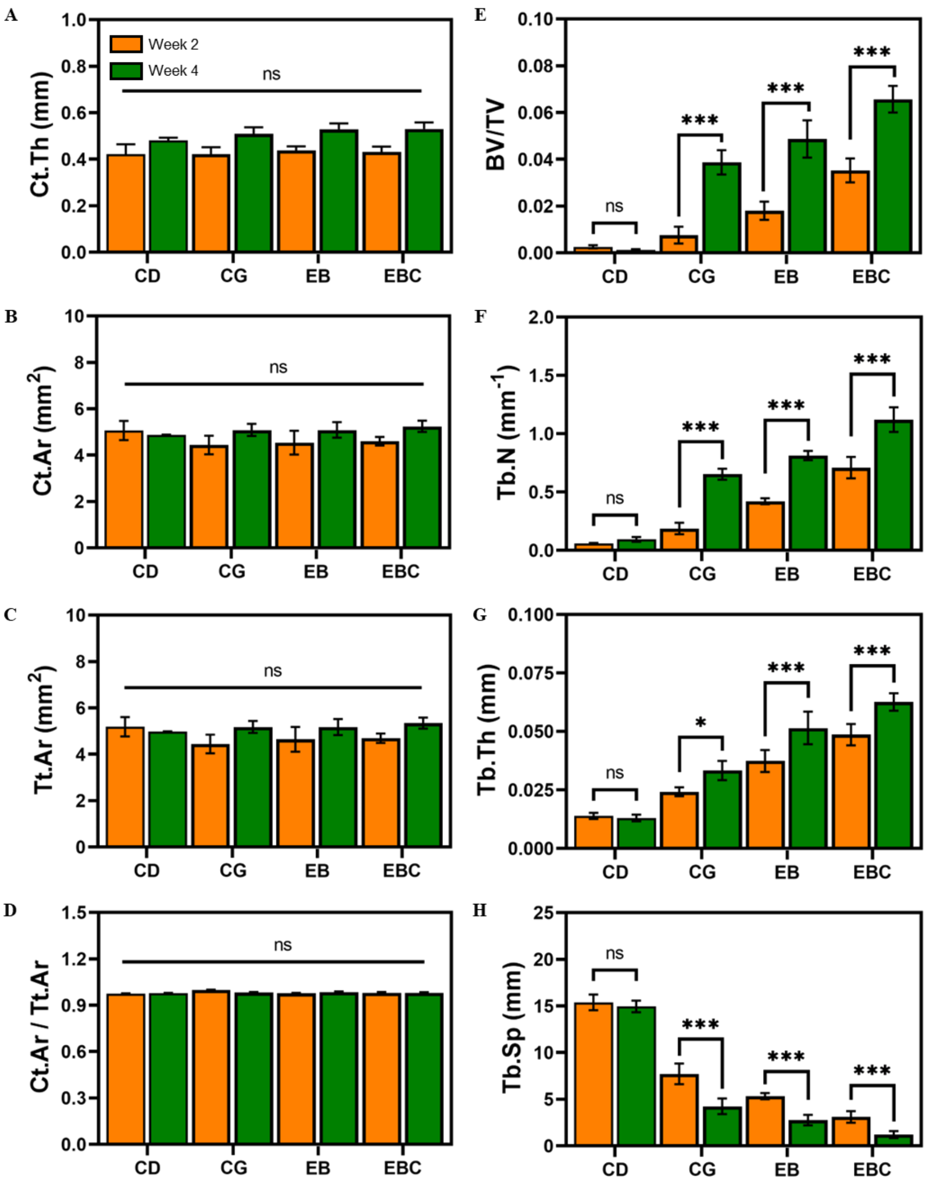

*Figure 35.* Cortical and trabecular morphometry of VOIs. **(A)** Average cortical thickness. **(B)** Average cortical surface area. **(C)** Average cortical area of the periosteal envelope. **(D)** Cortical area fraction. **(E)** Trabecular bone volume fraction. **(F)** Average number of trabeculae per unit length. **(G)** Average trabecular thickness. **(H)** Average trabecular separation.

### *5.3.2 Histology Shows Increased Calcified Trabecular Bone Produced After Injection with MSC-laden Self-Forming Hydrogels*

To further evaluate the newly formed trabecular bone after injection with EB and EBC hydrogels into the femoral shaft, H&E, Masson's Trichrome, and Tartrate resistant acid phosphatase (TRAP) stains were performed. The harvested femurs were decalcified for ease of sectioning prior to embedding in paraffin to form blocks for sectioning. Thin coronal sections (5 µm thick) were processed and stained (Figure 36A) and images at the center of the VOI were taken and analyzed (Figure 36B). For the EB group, some osteoid tissues were detected at 2 weeks (Figure 37A, 37B, Figure 38A, 38B, Figure 39A, 39B) while some new calcified trabeculae (NB) were detected at 4 weeks (Figure 37E, 37F, Figure 38E, 38F, Figure 39E, 39F). For the EBC group, many osteoid tissues were detected at 2 weeks (Figure 37C, 37D, Figure 38C, 38D, Figure 39C, 39D) while many osteoid tissues and many NB were detected at 4 weeks (Figure 37G, 37H, Figure 38G, 38H, Figure 39G, 39H). Osteoid tissue is an unmineralized tissue that eventually undergoes calcification and is deposited as layers in the bone matrix [237,238]. At 2 weeks post-injection, the EBC group contained a higher number of osteoid tissues compared to the EB group. Additionally, at 4 weeks post-injection, the EBC group had denser newly formed trabecular bone and possessed a higher number of osteoid tissues compared to the EB group. These results indicate that delivering MSCs with DWIVA-functionalized self-forming hydrogels accelerates growth of calcified trabecular bone. TRAP stain can also identify osteoclasts which are cells that degrade bone to initiate normal bone remodeling (Figure 39).[239] By performing a staining protocol which can identify osteoblasts, we will be able to determine the ratio between osteoblasts and osteoclasts. By doing so, we will be able to compare bone remodeling across groups.

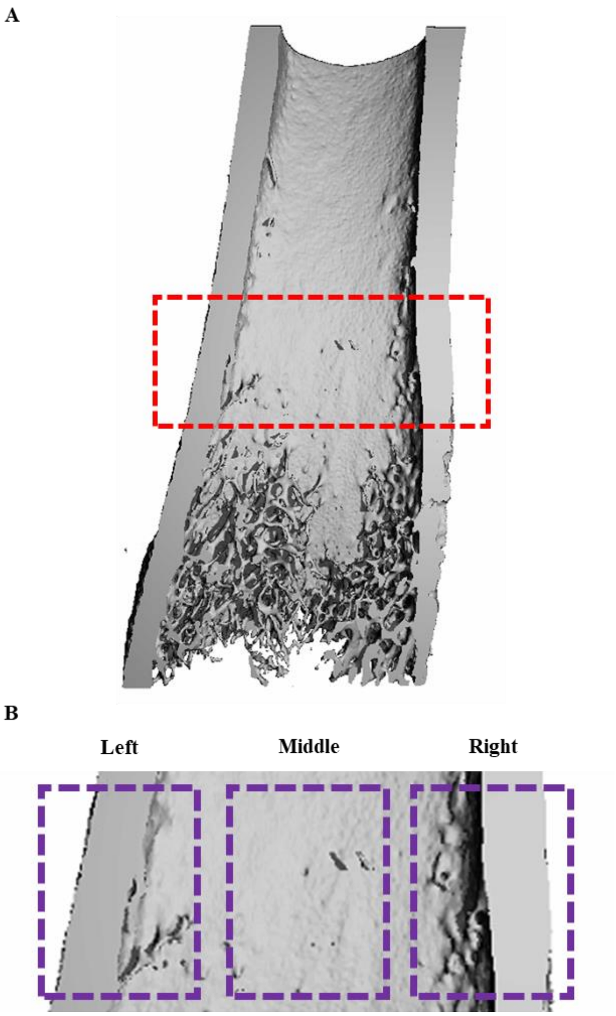

*Figure 36.* Targeted areas for histological staining and analysis. **(A)** The Volume of Interest is composed of 1091 slices. The middle 50 slices was selected for trabecular morphometry. **(B)** The Left, Middle, and Right sections of histologically stained slices were selected for imaging.

Together, these findings show that injectable, MSC-laden, DWIVA-functionalized hydrogels can locally regenerate bone *in vivo* and present opportunities for follow-up studies. The osteogenic effects of MSCs and DWIVA together at later time-points (for up to 12 weeks) has not been determined. Furthermore, bioavailability of DWIVA and the effects of presenting higher DWIVA peptide concentrations *in vivo* has not been evaluated and warrants further study. Besides the DWIVA wrist epitope of BMP-2, BMP-2 also has a knuckle epitope KIPKA which is believed to bind to BMP receptor II. [72,176] Since both receptors I and II play an active role in the signaling cascade for BMP-2, it would be beneficial to explore the independent effect of KIPKA and the synergistic effects of KIPKA and DWIVA sequences in locally regenerating trabecular bone.

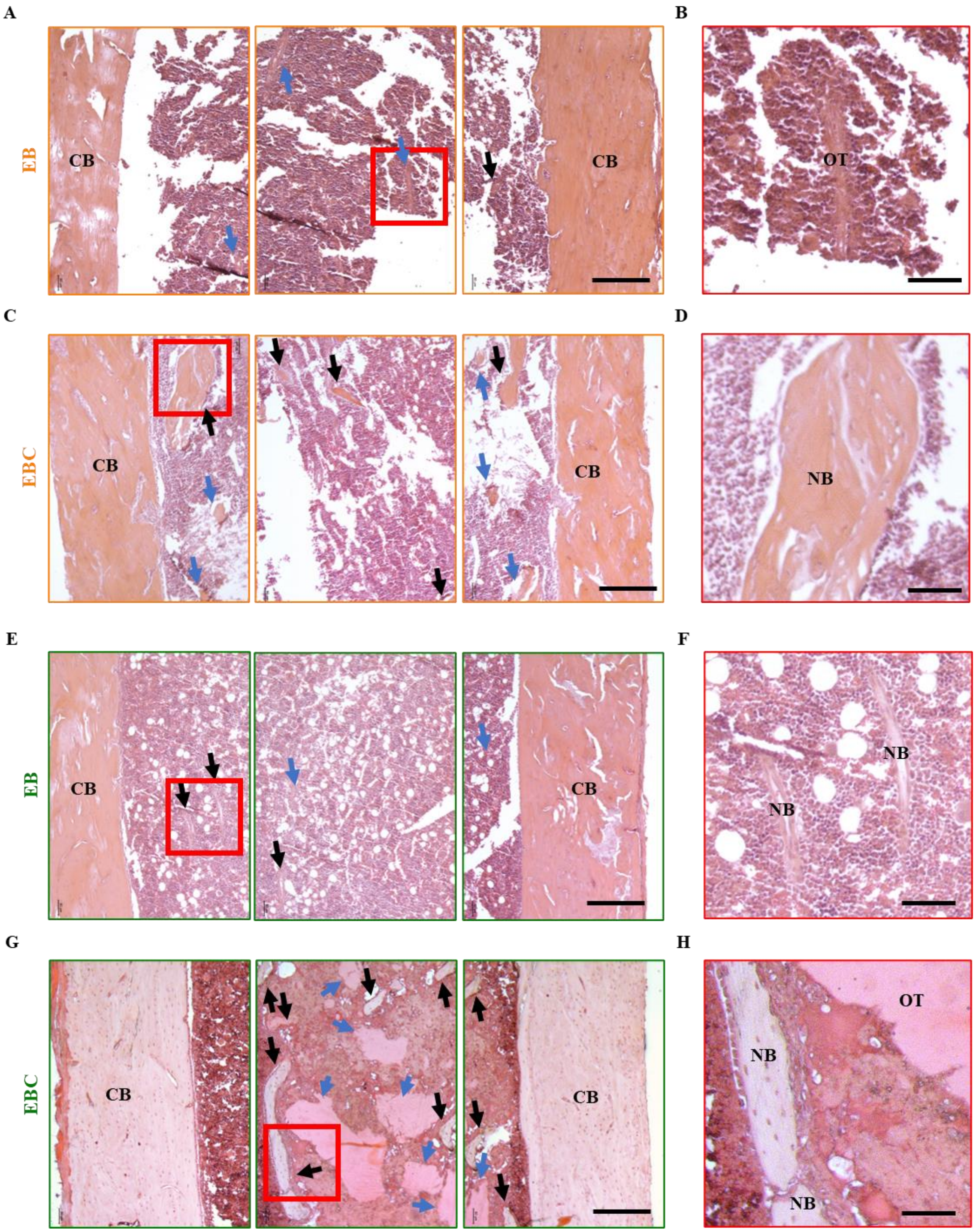

*Figure 37.* Sections stained with H&E (CB: calcified bone; NB: new calcified trabecular bone; OT: osteoid tissue; blue arrows: osteoid tissues; black arrows: new calcified trabecular bone). **(A)** Week 2 EB group (10x). **(B)** Boxed section in A, Middle (35x). **(C)** EBC group (10x). **(D)** Boxed section C, Left (35x). **(E)** Week 4 EB group (10x). **(F)** Boxed section in E, Left (35x). **(G)** Week 4 EBC group (10x). **(H)** Boxed section in G, Middle (35x). Scale bar: A,C,E,G 200 μm; B,D,F,H 50 μm.

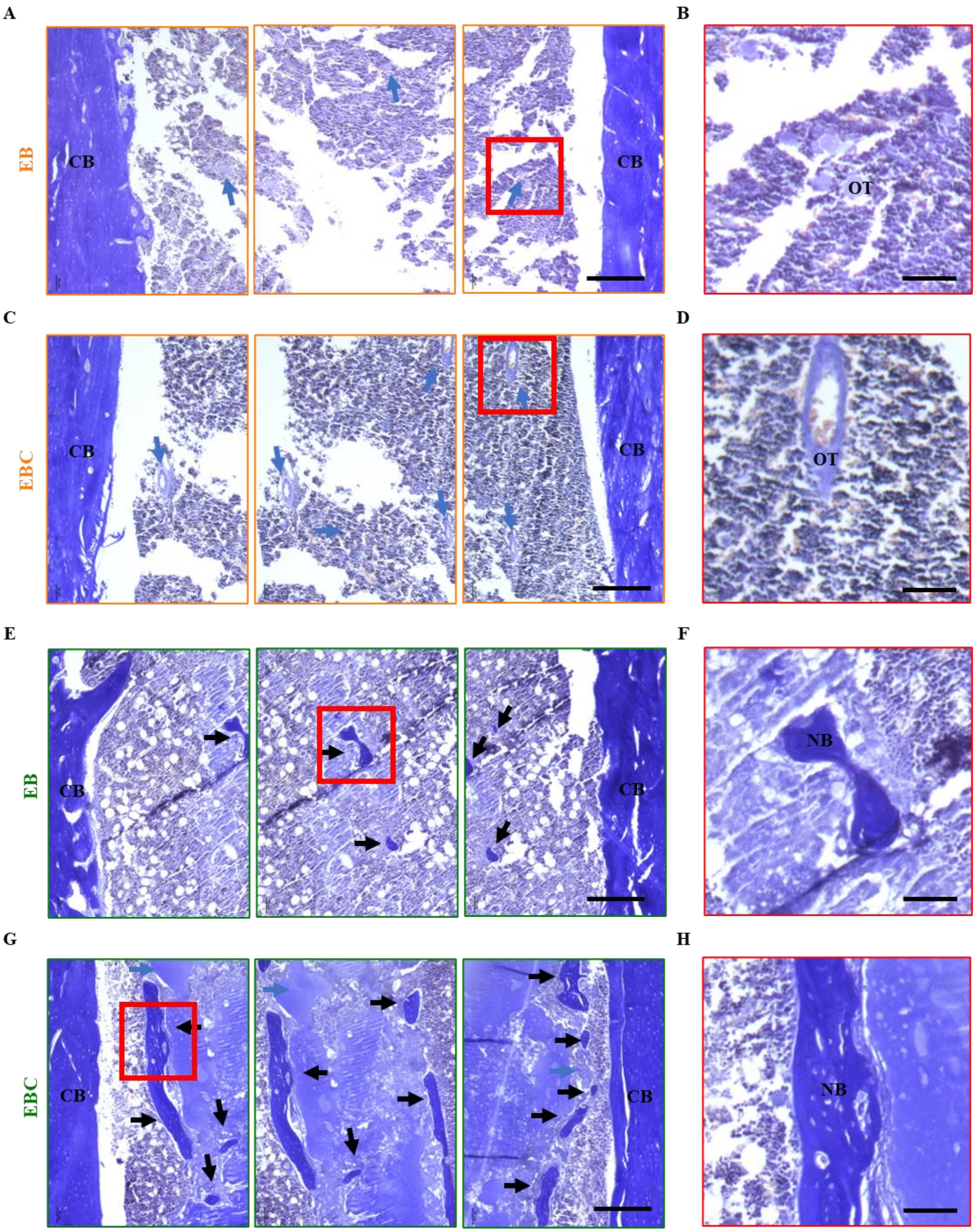

*Figure 38.* Sections stained with Masson's Trichrome (CB: calcified bone; NB: new calcified trabecular bone; OT: osteoid tissue; blue arrows: osteoid tissues; black arrows: new calcified trabecular bone). **(A)** Week 2 EB group (10x). **(B)** Boxed section in A, Right (35x). **(C)** EBC group (10x). **(D)** Boxed section C, Right (35x). **(E)** Week 4 EB group (10x). **(F)** Boxed section in E, Middle (35x). **(G)** Week 4 EBC group (10x). **(H)** Boxed section in G, Left (35x). Scale bar: A,C,E,G 200 μm; B,D,F,H 50 μm.

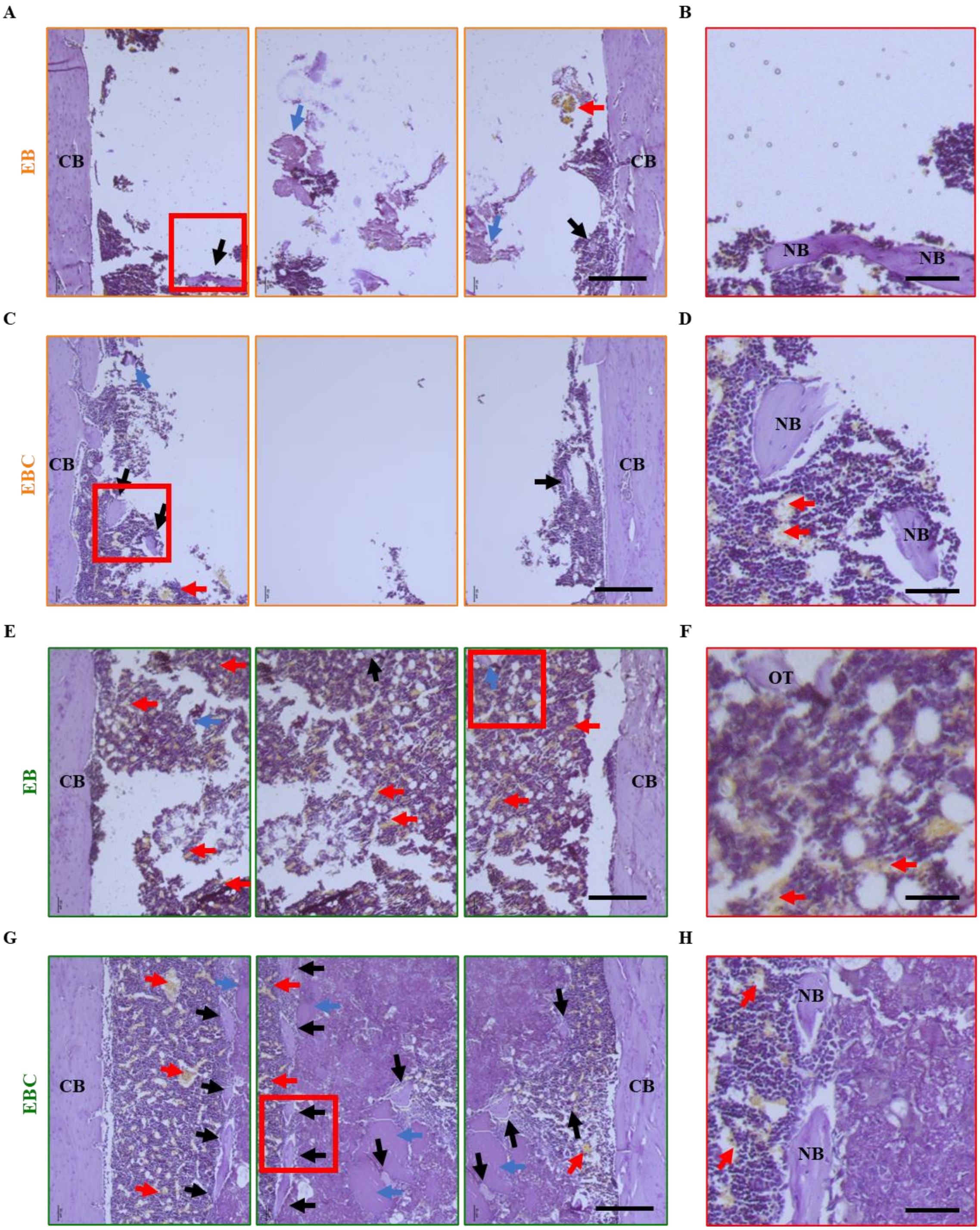

*Figure 39.* Sections stained with TRAP (CB: calcified bone; NB: new calcified trabecular bone; OT: osteoid tissue; red arrows: osteoclasts; blue arrows: osteoid tissues; black arrows: new calcified trabecular bone). **(A)** Week 2 EB group (10x). **(B)** Boxed section in A, Left (35x). **(C)** EBC group (10x). **(D)** Boxed section C, Left (35x). **(E)** Week 4 EB group (10x). **(F)** Boxed section in E, Right (35x). **(G)** Week 4 EBC group (10x). **(H)** Boxed section in G, Middle (35x). Scale bar: A,C,E,G 200 µm; B,D,F,H 50 µm.

## 5.4 Conclusion

We demonstrated that injectable hydrogels with DWIVA, an immobilized mimetic peptide of BMP-2, and human MSCs can regenerate trabecular bone in femurs. Additionally, we showed that bone maturity and osteoid tissue formation is more pronounced in injectable hydrogel groups with MSCs when compared to its acellular counterpart. This hydrogel system has the potential to be used as a targeted therapeutic to improve bone density locally, which is important in reducing the incidence of osteoporotic fragility fractures.

## 5.4 Experimental Section

### *5.5.1 Materials*

Sodium hyaluronate (NaHA, 60 kDa, HA60K-5) was purchased from Lifecore Biomedical (Chaska, MN). Dowex® resin 50WX2 hydrogen form 100-200 mesh, methacrylic anhydride (MA), triethanolamine (TEOA), and Fast Blue RR Assay (fast blue) were purchased from Sigma Aldrich (Burlington, MA). Dimethyl sulfoxide (DMSO), benzotriazole-1-yl-oxy-tris-(dimethylamino)-phosphonium hexafluorophosphate (BOP), β-(N-morpholino)ethanesulfonic acid (MES), and SpectraPor 6-8 kDa molecular weight cutoff dialysis tubing, Tartrate-Resistant Acid Phosphatase Stain Kit, and Leukocyte Alkaline Phosphatase Kit were purchased from Millipore Sigma (St. Louis, MO). Tetrabutylammonium hydroxide (TBA-OH) was purchased from Acros Organics (Geel, Belgium). 5-norbornene-2-methylamine (Nor-$NH_2$) and N-hydroxysuccinimide (NHS) were purchased from TCI America (Portland, OR). 1-(3-dimethylaminopropyl)-3-ethylcarbodiimide (EDC) was purchased from Thermo Scientific (Waltham, MA). Tetrazine-amine (Tet-$NH_2$) was purchased from Kerafast (Boston, MA). Thiol-containing peptide mimic of BMP-2 with sequence GCGGGDWIVAG (DWIVA) was purchased from

GenScript (Piscataway, NJ). Human MSCs from bone marrow was purchased from Lonza (Walkersville, MD). Minimum essential medium alpha (MEM-α) with no nucleosides, penicillin/streptomycin (10,000 U/ml), and fetal bovine serum (FBS) were purchased from Gibco (Waltham, MA). Omnipaque™ (350 mg I/ml) was purchased from CMX Medical Imaging (Tukwila, WA). Isoflurane solution and 70% isopropyl alcohol were purchased from Covetrus (Portland, ME). Buprenorphine SR 1mg/mL and meloxicam SR 2mg/mL were purchased from ZooPharm (Laramie, WY). 2% chlorohexidine was purchased through Covetrus (Portland, ME) and supplied by Vedco (Saint Joseph, MO). Hematoxylin and Eosin Stain Kit was purchased from Sakura Finetek USA Inc. (Torrance, CA). Masson's Trichrome for Connective Tissue was purchased from Electron Microscopy Sciences (Hatfield, PA). Xylene, Ethanol, and Ethylenediamine Tetraacetic Acid (EDTA) was purchased from VWR International (Radnor, PA).

### *5.5.2 HANor, HATet, HANorDWIVA Synthesis*

Refer to Chapter 4, Sections 4.6.2 to 4.6.4 for the complete description of macromer synthesis.

### *5.5.3 Cell Culture*

Human primary MSCs were cultured in 100 mm petri dishes in Growth Medium (MEM-α supplemented with 10% FBS and 1% P/S). To study the effects of MSC-laden DWIVA Nor-Tet hydrogels, MSCs were resuspended in the Nor-Tet precursor solution (2 x $10^6$ cells/ml).

### *5.5.4 Animal Protocol*

The animal experiment was approved by the Cooper University Health Care's Institutional Animal Care and Use Committee (IACUC). Experiments were performed on

8-week-old male Lewis rats (Charles River Laboratories, Raleigh, NC) weighing approximately 275-300 g. The rats were housed in a 12-hour dark-light cycle where they had access to food and water ad libitum. The rats were randomly divided into three groups: drilled canal alone, injectable hydrogel, and injectable hydrogel with 2 mM DWIVA peptide. The procedures were performed under anesthesia using inhaled isofluorane solution and buprenorphine SR. Once anesthetized, surgical sites were prepared by shaving the ventral aspect of the abdomen and hind legs and scrubbed with 2% chlorohexidine and 70% isopropyl alcohol. A standard median parapatellar approach to bilateral knees was performed. The distal femurs were exposed, and the femoral notch was identified. Utilizing a 1 mm sterile drill, the intramedullary canal was drilled and checked on fluoroscopy for placement. Three passes with the drill were performed to adequately remove native bone marrow and trabecular bone. The femurs were then filled with 0.2 ml of 2% w/v self-forming hydrogel solution via injection using a 25-gauge syringe. Bone wax was placed over the hole after injection. Closure of the arthrotomy and skin was performed with Vicryl sutures. Following closure of the surgical sites, animals were given meloxicam SR (2mg/ml) for pain alleviation and subsequently returned to their housing where they were monitored until they recovered from the surgical anesthesia. All rats were euthanized 4 weeks post-injection and the left and right femurs were harvested. The femurs were fixed with 10% neutral-buffered formalin for 24 hours, washed with distilled water, and stored in 70% ethanol at 4 ºC until micro-CT imaging.

### *5.5.5 Micro-CT*

The distal shaft (midshaft down to the metaphysis) of extracted femurs were scanned using micro-CT (micro-CT 45, ScancoMedical AG, Brüttisellen, Switzerland) at

10.4 µm isotropic resolution, with 55 kVp energy, and 400 ms integration time. This region was chosen to evaluate the effects of injectable DWIVA hydrogels on trabecular bone formation. At the center of the distal shaft, a 200-slice-thick volume of interest (VOI) was identified, Gaussian filtered (sigma = 1.2, support = 2), and bone was identified by applying a global threshold (220 mg hydroxyapatite per $cm^3$). Manufacturer-provided software for 3D standard microstructural analysis was used to generate 3D axial views of the 200-slice-thick VOIs and coronal views of the 1031-slice-thick distal shaft.

### *5.5.6 Histological Staining and Imaging*

Extracted femurs were decalcified by soaking in 150 mM EDTA solution for 2 – 3 weeks with replenishment every 48 hours. Decalcified femurs by paraffin embedded and sectioned at the Histology Core of Penn Center for Musculoskeletal Disorders (PCMD). Prior to histological staining, tissue sections were deparaffinized and rehydrated using xylene and graded ethanol. H&E, Masson's Trichrome, TRAP, and ALP stains were performed according to manufacturer specifications. Stained samples were imaged with a Leica DMIRE2 inverted microscope.

### *5.5.7 Statistical Analysis*

Statistical analysis was performed using GraphPad Prism (version 9.3.1, GraphPad Software, Inc., La Jolla, CA). All experiments were carried out in triplicate and single cell analysis was done with at least 50 cells per group. All graphs represent mean ± standard deviation (SD). Analysis of variance (ANOVA) was performed followed by Tukey's test for post-hoc analysis. Differences among groups are stated as $p < 0.05$ (*), $p < 0.01$ (**), $p < 0.001$ (***), and (ns) when differences between groups are not statistically significant.

# Chapter 6

# Summary and Future Directions

## 6.1 Research Summary

The overarching goal of this dissertation is to develop an injectable hydrogel biomaterial system that allows high control over the biophysical properties of the hydrogel while independently incorporating biochemical modifications for biomedical applications. These objectives help address three significant needs that limit the use of hydrogels for a broader range of biomedical applications: (1) highly tunable injectable hydrogels with a wide range of biophysical properties and amenability to chemical modifications, (2) simple method of biofunctionalization without compromising the biophysical properties of the hydrogel, (3) injectability while maintaining high viability of encapsulated cells.

In this dissertation, we report that HA macromers modified with Nor or Tet click into covalently crosslinked hydrogels upon mixing. We demonstrated that a broad elastic moduli can be obtained by varying macromer concentrations and ratios. In addition, we developed a method of peptide prefunctionalization of the hydrogels without affecting hydrogel mechanics and gelation time. Human MSCs cultured atop the injectable hydrogels adhered and exhibited stiffness-dependent differences in matrix mechanosensing. MSCs injected in the hydrogel solutions through narrow syringe needles remained highly viable which demonstrates the use of these hydrogels to locally deliver cells and peptides.  Substitution of HA with enzymatically-degradable gelatin created cell-responsive injectable hydrogels and encapsulated MSCs preferentially differentiated into adipocytes or osteoblasts.

Next, we apply our injectable hydrogel system to develop a potential local treatment for osteoporosis or the loss of bone mass density. The injectable hydrogels were functionalized with a peptide mimic of bone morphogenetic protein 2 (BMP-2) and we demonstrated the increase in the osteogenic biomarker expression of cells cultured atop (2D) or encapsulated (3D) within the injectable hydrogels. Injection of this bioactive hydrogel into hollow rat femurs showed a local increase in trabecular bone density. We also showed that by adding MSCs into the injected hydrogel, the formation of osteoid tissues and new trabecular bone was greatly increased.

In summary, the work presented here shows that injectable hydrogels crosslinked through the Inverse Electron Demand Diels Alder Reaction of Nor and Tet and prefunctionalized through our method can be utilized as a robust biomaterial for biomedical applications.

In order to advance this work, several limitations must be addressed. Although the IEDDA reaction between Nor and Tet is rapid, specific, and amenable to cell encapsulation, it is challenging to dissociate gelation time and mechanics since Nor-Tet-bonds control both parameters simultaneously. We hypothesize that macromers pre-coupled with peptides and modified with multiple reactive groups can be designed to create injectable and bioactive hydrogels with modular control over gelation kinetics and mechanics. As such, studying the effects of interplay between macromer size and Nor and Tet modification and macromer pre-coupling on hydrogel kinetics and mechanics, will improve our control of hydrogel properties (**Section 6.2.1**). The bone regeneration aspect of this hydrogel system utilized the wrist epitope of BMP-2 while the native osteogenic signaling cascade of BMP-2 involves both its knuckle and wrist epitopes. We hypothesize that simultaneous functionalization of Nor-Tet hydrogels with the wrist (DWIVA) and knuckle (KIPKA) epitopes of BMP-2 will have synergistic effects in bone regeneration (**Section 6.2.2**). The method of functionalization developed in this dissertation allows coupling of any thiolated molecules. We are interested in utilizing the injectable Nor-Tet in the restoration of soft tissues. Specifically, by coupling adhesive molecules to the macromers, an injectable biomaterial for the restoration of the lamina propria can be created (**Section 6.2.3**). Beyond tissue engineering, this hydrogel system can be used to develop real-time dosimeter and spacer which could improve the treatment plans generated for patients undergoing radiation treatment to eliminate cancerous tumors (**Section 6.2.4**).

## 6.2 Future Directions

### *6.2.1 Investigating the Role of Bioactive and Multifunctional Macromers on Decoupling Hydrogel Gelation Kinetics and Mechanics*

Although covalently crosslinked hydrogels are used as 3D scaffolds for cells and biologically active molecules, many crosslinking strategies produce harmful radical species and cross-react with cells and proteins. To obviate these concerns, the IEDDA click reaction between Nor and Tet is a highly specific crosslinking chemistry that has been recently exploited to form hydrogels without external stimuli. Although this click chemistry scheme is rapid, specific, and amenable to cell encapsulation, it is challenging to dissociate gelation time and mechanics since Nor-Tet- bonds control both parameters simultaneously. While this dissertation presented a method for controlling hydrogel mechanics, pre-coupling Nor-Tet hydrogels with bioactive peptides and controlling cell-mediated degradation, there is great interest in creating injectable hydrogels with decoupled physical properties (gelation time and mechanics) and bioactivity. This level of control would allow for a systematic investigation on the effects of physicochemical parameters on cell-hydrogel interactions over time, which would accelerate the rational design of injectable materials for minimally invasive interventions.

The central hypothesis of this study is macromers with an additional methacrylate (Me-) reactive groups can be pre-loaded with a higher concentration of thiolated peptides or with multiple peptides via a Michael-addition reaction. These biofunctionalized macromers can then be used to form hydrogels with tunable bioactivity without affecting mechanics (Nor-Tet- interactions). Testing these hypotheses will culminate in the first injectable hydrogel with modular control over bioactivity, gelation kinetics, and physical properties.

To test this hypothesis, two studies are proposed: study the effects of (1) the interplay between macromer size and Nor- and Tet- modification and (2) macromer pre-coupling with thiolated biomimetic peptides on gelation kinetics and hydrogel mechanics. Preliminary data from these studies shows that macromer size and percent of Nor modification have direct effects on the mechanics and gelation kinetics of Nor-Tet hydrogels. Additionally, loading of thiolated peptide can be controlled by changing the amount of methacrylate sites available for pre-coupling. To improve control and design of injectable hydrogel properties, future work needs to explore a wider array of macromer sizes, including that of the HATet macromer. Further, the feasibility of loading multiple bioactive peptides should be interrogated. Results from these future studies will significantly improve our understanding of cell-hydrogel interactions with applications in regenerative medicine. Hydrogels with tunable gelation kinetics and mechanics can be used to create mechanically stable hydrogels that slowly polymerize, which will significantly improve interdigitation between injectable material and surrounding tissues. By pre-coupling macromers with biomimetic peptides, biochemical signals can be incorporated into self-forming hydrogels without changing crosslink density, allowing for the study of 3D cell-hydrogel interactions with unprecedented control.

### (1) Effects of macromer size and Nor- and Tet- modification

Small and large HANor macromers were synthesized using HA with 60 kDa (small) or 200 kDa (large) molecular weights which were modified with 20% or 50% Nor moieties. HATet macromer was synthesized using 60 kDa HA modified with 40% Tet moieties. A per mole analysis of the macromers was performed to determine the number of Nor and Tet moieties available for crosslinking (Table 6). The HANor and HATet macromers were hydrated and mixed to a final concentration of 2% w/v prior to loading onto a rheometer stage. The gelation of the hydrogel was monitored for 60 mins at 37 ºC. Although the available units of Tet moieties for crosslinking was constant across the groups, the magnitude of the storage moduli (G´) between the 60 kDa and 200 kDa groups and between 20% and 50% modification are distinct (Figure 40A) with values of 1,768 ± 435 (60 kDa, 50% mod), 1,370 ± 420 Pa (60 kDa, 20% mod), 3,369 ± 560 (200 kDa, 50% mod), and 2,764 ± 480 Pa (200 kDa, 20% mod) (Figure 40B). The time to reach 50% of the plateau G´ also varied with the HANor macromer size and percent Nor modification, with values of 8.58 ± 0.25 min (60 kDa, 50% mod), 11.93 ± 0.46 min (60 kDa, 20% mod), 2.77 ± 0.10 min (200 kDa, 50% mod), and 4.38 ± 0.24 min (200 kDa, 20% mod) (Figure 40C). The bulk mechanics of the hydrogel also showed dependence on the HANor macromer size and percent Nor modification, with values of 6.89 ± 1.19 kPa (60 kDa, 50% mod), 4.32 ± 1.01 kPa (60 kDa, 20% mod), 12.27 ± 2.13 kPa (200 kDa, 50% mod), and 9.24 ± 0.77 kPa (200 kDa, 20% mod) (Figure 40D).

**Table 6**

*Available Units of Norbornene and Tetrazine Moieties Per Mole of HANor or HATet Macromer*

| Macromer | % Mod | Available Units |
|---|---|---|
| 60 kDa HATet | 40% | 60 Tet |
| 60 kDa HANor | 20% | 30 Nor |
| 60 kDa HANor | 50% | 75 Nor |
| 200 kDa HANor | 20% | 100 Nor |
| 200 kDa HANor | 50% | 249 Nor |

In three of the four groups (60 kDa 50% mod, 200 kDa 50% mod, and 200 kDa 20% mod), the number of Nor moieties is in excess compared to the number of available Tet moieties for crosslinking (Table 6). Although the same amount of Tet was consumed in these groups, there were significant differences observed in the gelation kinetics and mechanics of the hydrogels. These differences could be due to the nature of the networks created by using a macromer with a larger size. The solvent replacement method revealed that the percentage porosity of the hydrogels decreased with the increase in macromer size and percent Nor modification, with values of 50.77 ± 3.23% (60 kDa, 50% mod), 65.85 ± 4.52% (60 kDa, 20% mod), 25.17 ± 2.75% (200 kDa, 50% mod), and 33.88 ± 3.15% (200 kDa, 20% mod) (Figure 40E) Meanwhile, hydrogel swelling increased with the increase in macromer size and percent Nor modification, with values of 34.57 ± 1.94% (60 kDa, 50% mod), 46.82 ± 1.37% (60 kDa, 20% mod), 8.68 ± 0.89% (200 kDa, 50% mod), and 23.29 ± 1.88% (200 kDa, 20% mod) (Figure 40F). These results show that by using a larger macromer, the crosslinks created during hydrogel formation change the porosity and swelling properties of the hydrogel and thus affect mechanical properties of the hydrogels. As for the effect on gelation kinetics, the higher number of Nor moieties available for crosslinking could have accelerated the reactions between the Nor and Tet moieties. During active crosslinking formation, the pink color of the precursor solution disappears as the hydrogel forms (Figure 40G). This change in color can used to monitor the speed of Nor-Tet reactions in the presence of different concentrations of Nor molecules.

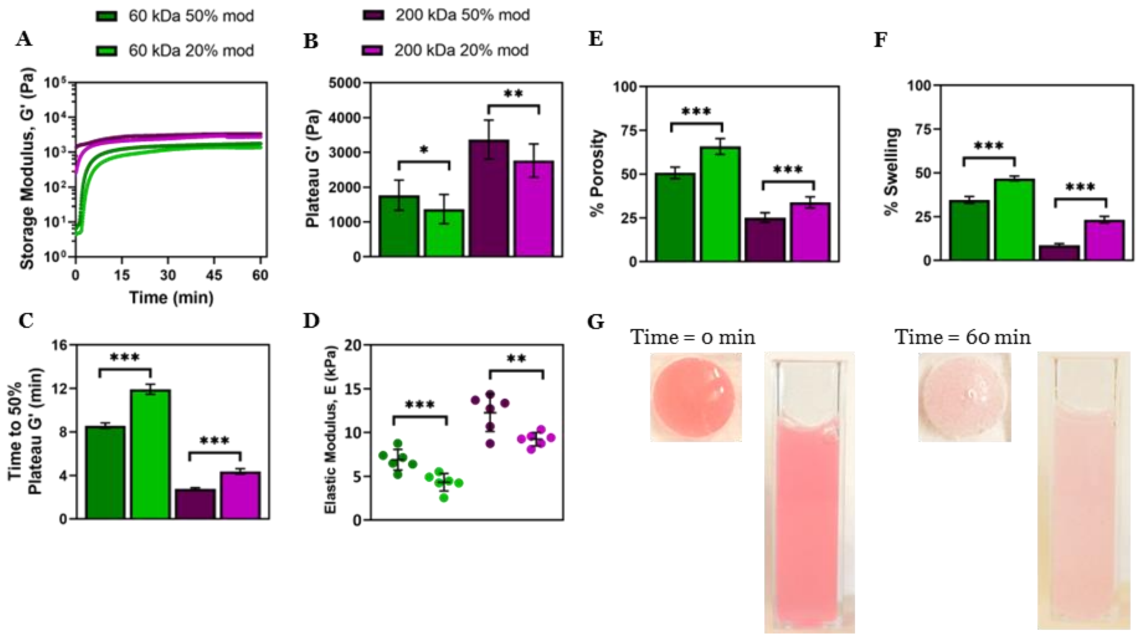

*Figure 40.* Effects of macromer size and modification on physical characterization of self-forming hydrogels at 37 °C. **(A)** Representative time sweep rheology plot shows storage (G´) moduli and was used to determine **(B)** plateau G´ and **(C)** time to 50% plateau G´ of self-forming hydrogels. **(D)** Compressive elastic modulus E. **(E)** Percentage porosity and **(F)** Percentage swelling of self-formign hydrogels. **(G)** Color change of the hydrogel as gelation reaches completion. Bar graphs shown as mean ± SD (n ≥ 3 samples per condition) with significant differences determined with ANOVA followed by Tukey’s post hoc test where $*p < 0.05$, $**p < 0.01$, and $***p < 0.005$.

### (2) Effects of macromer pre-coupling with thiolated biomimetic peptides

HANor (60 kDa, 50% mod) macromers were modifed with Methacrylate (Me) sites (HANorMe) at 20% or 80% Me modification. A Michael-addition reaction was performed to pre-couple RGD peptides at increasing concentrations (2 mM, 4 mM, and 6 mM) (HANorRGD). HANorRGD and HATet (60 kDa, 40% mod) macromers were hydrated and mixed to a final concentration of 2% w/v prior to loading onto a rheometer stage. The gelation of the hydrogel was monitored for 60 mins at 37 ºC. We determined that macromer mechanics and gelation kinetics are unchanged after pre-coupling with RGD peptide, as shown by G´ evolution (Figure 41A), plateau G´ (Figure 41B), and time to reach 50% of plateau G´ (Figure 41C).

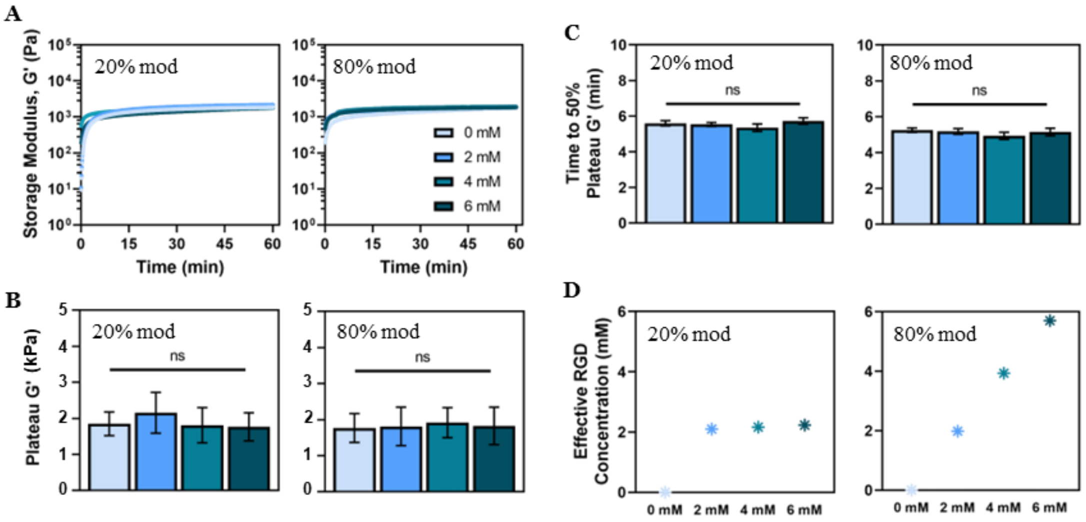

*Figure 41*. Mechanics of hydrogels loaded with RGD peptide at various concentrations. **(A)** Representative time sweep rheology plot shows storage (G´) moduli of peptide-loaded hydrogels at 20% and 80% Me modification and was used to determine **(B)** plateau G´ and **(C)** time to 50% plateau G´ of self-forming hydrogels. **(D)** Effective RGD peptide concentration determined using $^1$H-NMR. Bar graphs shown as mean ± SD (n ≥ 3 samples per condition). Differences between groups are stated as (ns) when differences between groups are not statistically significant.

$^1$H-NMR was used to quantify the effective concentration of RGD peptide pre-coupled onto the HANorMe macromers. At 20% Me modification, a maximum effective concentration of 2 mM RGD was achieved while up to 6 mM of RGD was pre-coupled at 80% Me modification. These results show that peptide loading can be controlled by changing the amount of available Me sites for coupling of thiolated peptides. By increasing the percent Me modification, a higher concentration of thiolated peptide or potentially lower concentration of multiple peptides can be loaded.

### *6.2.2 Exploring the Independent effect of KIPKA and the Synergistic Effects of KIPKA and DWIVA Sequences in Locally Regenerating Bone*

Efforts to develop alternative strategies to regenerate bone have utilized bone morphogentic protein 2 (BMP-2), a potent inducer of osteogenesis *in vivo*.[215–219] The osteogenic signaling cascade begins when BMP-2 binds to BMP-receptor type II, which leads to the phosphorylation (activation) of BMP-receptor type I, and ultimately to the phosphorylation of Smad1, a cytoplasmic signaling molecule for BMP-2. Phosphorylated Smad1 then localizes to the nucleus and controls gene expression to initiate osteogenic differentiation.[220–222] The DWIVA peptide sequence from BMP-2 is equivalent to the wrist epitope of BMP-2 which binds to BMP-receptor type I while having high receptor-binding activity and specificity to BMP-receptor types I and II.[176]

In this dissertation, we demonstrated that DWIVA peptides presented in soluble and immobilized form increased alkaline phosphatase (ALP) expression in MSCs cultured on 2D and encapsulated in 3D Nor-Tet hydrogels. Injection of DWIVA-functionalized Nor-Tet hydrogels into hollow intramedullary canals of Lewis rat femurs showed a local increase in trabecular bone density as determined by micro-CT imaging. By injecting MSC-laden DWIVA-functionalized Nor-Tet hydrogels into hollow rat femurs, new trabecular bone growth and osteoid tissue formation increased and maturity of calcified trabecular bone was achieved at an earlier time point. Besides the DWIVA wrist epitope of BMP-2, BMP-2 has a knuckle epitope with the active sequence KIPKASSVPTELSAISTLYLG (KIPKA) that is believed to bind to BMP receptor

II.[72,176,240] Since both receptors I and II are involved in the signaling cascade for BMP-2, it would be beneficial to explore the independent effect of KIPKA and the synergistic effects of KIPKA and DWIVA sequences in locally regenerating bone.

The central hypothesis of this study is specific combinations of KIPKA and DWIVA peptides have synergistic effect in locally regenerating bone. To test this hypothesis, two studies are proposed: (1) determining the ratio between KIPKA and DWIVA which will result in maximal osteogenic differentiation of MSCs cultured on 2D and encapsulated in 3D Nor-Tet hydrogels; and (2) evaluating new trabecular bone growth and osteoid tissue formation after injecting Nor-Tet hydrogels functionalized with KIPKA and DWIVA into hollow rat femurs. Preliminary data from these studies show that KIPKA peptide presented in soluble form at concentrations of 0.5 and 2.0 mM shows increased ALP expression in MSCs cultured on glass (Figure 42). Future work needs to focus on the osteogenic effects of KIPKA on MSCs cultured on 2D and encapsulated in 3D hydrogels and to determine the concentrations of KIPKA and DWIVA that will result in maximal osteogenic differentiation. By completing these two studies, KIPKA and DWIVA can be incorporated within injectable hydrogels which can be used as a promising biomaterial for the local regeneration of bone tissue and for the potential local treatment of osteoporosis.

### (1) Determining the effective ratio between KIPKA and DWIVA

To study the effects of soluble KIPKA on stem cell cultures, MSCs were seeded on top of glass coverslips (12 mm diameter) at a density of 3,000 cells per cm$^2$. After 6 h in culture, media was replaced with either Growth Medium (0 mM KIPKA), Growth Medium supplemented with low (0.50 mM) or high (2.0 mM) KIPKA, or OS Medium (Osteogenic Differentiation BulletKit$^{TM}$ Medium, Lonza). MSCs seeded on glass cultured in Growth

Medium supplemented with 2.0 mM KIPKA show significantly more positive staining for ALP (dark blue) compared to cells cultured in Growth Medium or in Growth Medium supplemented with a lower (0.50 mM) KIPKA concentration (Figure 42A). Confocal images of MSC cultures stained for ALP (magenta) and nuclei (blue) show a progressive increase in ALP signal with increasing KIPKA concentration (Figure 41B).

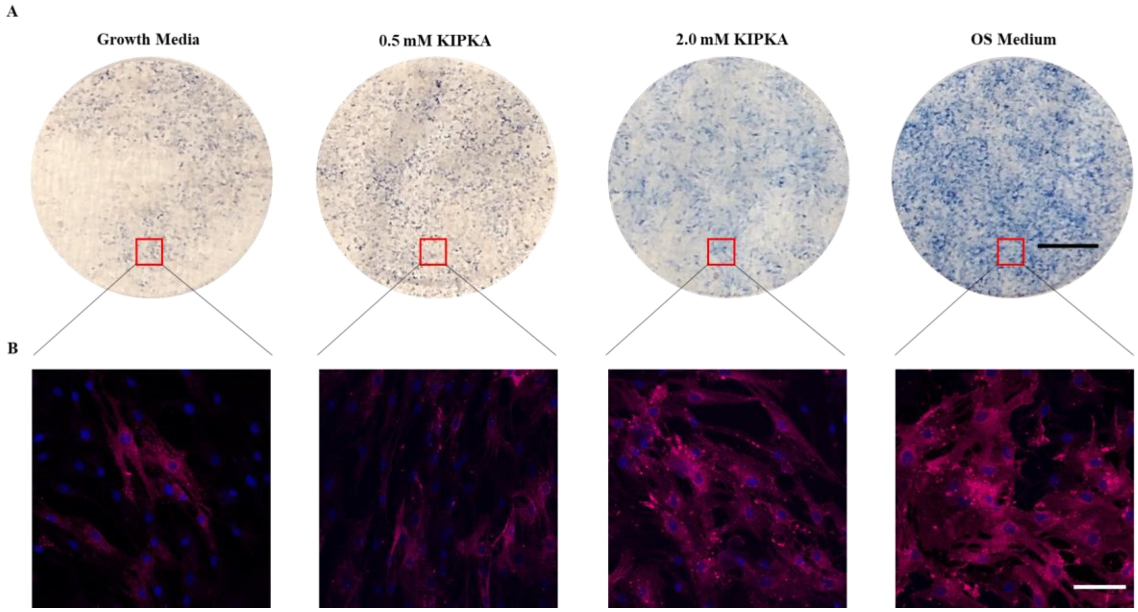

*Figure 42.* Soluble presentation of KIPKA enhances ALP levels of MSCs on glass. **(A)** Representative ALP staining of MSCs (blue) on glass in Growth Medium (negative control), Growth Medium supplemented with 0.5 or 2.0 mM KIPKA, and OS Medium (positive control). **(B)** Representative fluorescence staining of ALP (magenta) and nucleus (blue) of MSCs on glass in Growth Medium, Growth Medium supplemented with 0.5 or 2.0 mM DWIVA, and OS Medium. Scale bars: A: 2 mm, B: 100 µm.

### *6.2.3 Injectable Self-Healing Bioinks to Restore Vocal Folds*

Up to 9% of the general population suffer from disorders of the larynx which affect their quality of life and sometimes causing them to lose their jobs.[241,242] Treatments for disorders of the larynx include laryngeal surgery and vocal fold (VF) augmention.[243] In VF augmentation, biomaterials that are biologically inert, biocompatible with host tissue, and mimic the rheological properties of native VF tissue, are used to supplement the VF tissue in cases of unilateral paralysis, vocal atrophy, and sulcus vocalis.[244] However, no biomaterial-based intervention exists that can adequately restore native VF tissue.[244] Current biomaterials for VF augmentation include collagen-based or HA-based products which require a catalyst to polymerize and lack proper mechanical stability and biomaterial-tissue adhesion thereby limiting their use for restoring VF tissue in a minimally invasive manner.

Establishment of the tissue engineering principles and advancements in biotechnologies within the last decade have significantly enhanced our understanding of physiological and pathological aspects of both healthy and injured VF tissues.[245] Numerous efforts have been made to repair and restore VF tissue. However, current biomaterial strategies to restore the mucosal wave in native lamina propria have only shown limited success.[244,245] The main limitations of biomaterial-based approaches are cytotoxic polymerization strategies, inadequate mechanical properties, and poor adhesion to local VF tissue upon implantation. Due to a lack of adhesive motifs, most current clinical strategies focus on injectable biomaterials that mainly bulk VF tissue and are physically held in place within the VF tissue. Adhesion to surrounding VF without limiting the oscillatory function of the local tissue is a requisite for an adequate biomaterial-based strategy.[245] Injectable hydrogels, particularly those derived from HA, have seen an increased role in restoring the lamina propria.[246–250] Although injectable HA hydrogels are extremely promising due to the viscoelastic properties and biocompatibility of HA, most HA-based injectable hydrogel strategies rely on complex polymerization strategies, generally feature viscoelastic properties inferior to native VF tissue, and lack adhesive motifs to adequately integrate with surrounding VF tissue. An ideal injectable VF implant should be self-healing – it should form in the absence of an external catalyst, with tunable gelation time. The self-healing behavior is typically associated with a shear-thinning response when hydrogels are extruded from narrow channels/nozzles, thus making them good candidates for VF bioinks. Self-healing bioinks can be delivered to locally restore VF tissue with high precision and control. By tuning functional moieties, this new class of injectable, self-healing bioinks can feature viscoelastic properties that match surrounding lamina propria, with the inclusion of adhesive motifs to adhere to local tissue *in situ* to prevent dislodgement during self-sustained VF oscillations (Figure 43).

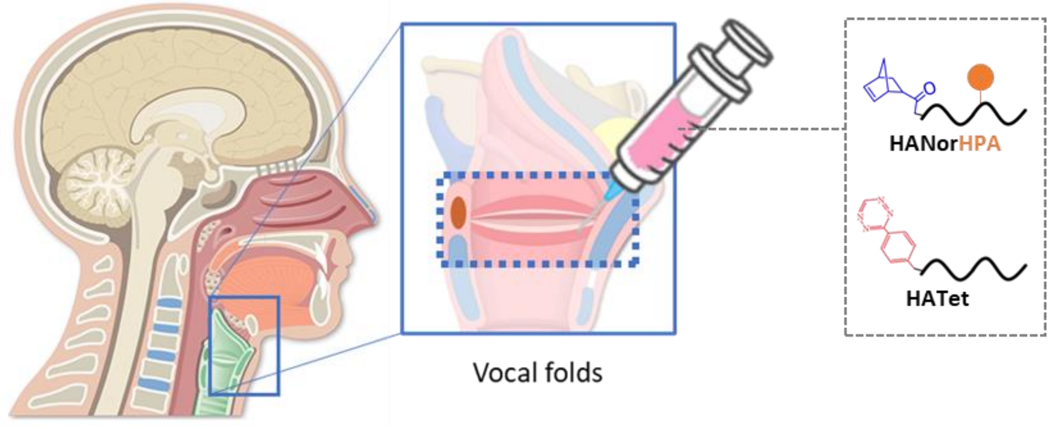

*Figure 43.* Proposed injection mechanism for restoration of vocal folds.

The central hypothesis of this study is *in situ* deposition of self-healing hydrogels will create stable and functional VF implants with tissue-like mechanics and adhesion. To test this hypothesis, two studies are proposed: (1) developing and characterizing self-healing HA-based hydrogel bioinks and (2) evaluating biological responses of self-healing HA-based hydrogels. To form adhesive self-healing hydrogels, we will modify HANor and

HATet macromers with non-toxic, phenol-containing molecule (hydroxyphenyl propionic acid, HPA) due to the ability of phenol to serve as a biocompatible tissue adhesive.[251]

### (1) Developing and characterizing self-healing HA-based hydrogel bioinks

We propose to explore the use of HA-based hydrogels to replace tissue voids post-VF wound closures. This novel hydrogel system will satisfy two criteria after bioprinting onto a VF site: (i) self-healing with tunable mechanics and (ii) adhesion with surrounding tissue. Two major limitations of hydrogel-based interventions for VF repair are the necessity of a catalyst (light, enzyme) and their inability to robustly adhere to surrounding tissue. To form self-healing hydrogels, we will employ the IEDDA reaction between pendant Nor and Tet on modified HA macromers. Tissue adhesives for VF regeneration need to satisfy several criteria, including the ability to adhere in moist environments, tunable curing, and biocompatibility.[244,245] Fibrin glue is a common adhesive used for VF repair, but it has several limitations, including an increased risk for fibrinogenesis and inflammation at treatment site.[252,253] Although commercially available alternatives to fibrin exist, these products involve multiple components and due to their underlying chemistry are toxic with increasing adhesive strength.[254] Phenol-based hydrogels continue to emerge as tissue adhesives due to their high biocompatibility and tunable adhesion strength.[251] Thus, we will modify HANor macromers with HPA (HANorHPA) due to its phenolic contents.

### (2) Evaluating biological responses of self-healing HA-based hydrogels

The first study will address several criteria essential for the success of this system such as rapid gelation, adhesivity, and VF-like mechanical properties. Since the hydrogels will interact with surrounding VF-tissue, foreign-body responses need to be evaluated. As a first step towards this, it is extremely important that cells native to VF tissue are biocompatible to the HANorHPA and HATet hydrogel macromers and the hydrogel formation process. Thus, the biocompatibility of human VF fibroblasts atop (2D) and within (3D) self-healing hydrogels will be evaluated. Human VF fibroblast primary cells will be used to test biological responses to self-healing hydrogels. Since these bioinks will be used in injectable applications, all hydrogels used for biological response studies will be loaded to dual-barrel syringes with mixing tips and extruded through needles of different gauge sizes into molds for hydrogels to form. To assess biological responses, human VF fibroblasts will be seeded on top (2D) or encapsulated within (3D) self-healing hydrogels. Appropriate hydrogel formulations determined in study (1) with the inclusion of a thiolated RGD peptide (2 mM, sequence: GCRGDSPGGG) will be used to form hydrogels using the different needle gauge sizes identifed in study (1). To evaluate viability, a Live/Dead assay will be used for fibroblast cultures after 1, 7, 14, and 21 days of culture. To ensure that the hydrogel environment does not affect metabolic activity, an Alamar Blue assay will be employed. Alamar Blue will also be used as an indirect measure of proliferation, and that is another marker that will be checked to ensure that self-healing hydrogels do not affect resident cells in surrounding tissues.

### *6.2.4 Injectable Dosimeter for Real-Time, in vivo Verification of Magnetic Resonance-Guided Radiation Therapy*

Cancer is the leading cause of death in every country of the world.[255,256] Along with surgery and chemotherapy, radiation therapy or radiotherapy is an important modality used in cancer treatments.[257,258] Radiation therapy contributes 40% towards curative treatment and it is highly cost effective and accounts to only about 5% of the total cost of cancer care.[259]

Advances in imaging techniques, computerized treatment planning systems, and radiation treatment machines have rapidly increased the progress in the field of radiation therapy. One advancement is the use of radiation-sensitive gels or gel dosimeters composed of radiation-sensitive chemicals to record and display the radiation dose and distribution throughout a three-dimensional volume.[260] Fricke gel dosimeters contain ferrous sulphate and exhibit nuclear magnetic resonance (NMR) relaxation properties upon irradiation. In Fricke gel dosimeters, radiation induces the conversion of ferrous ions ($Fe^{2+}$) into ferric ions ($Fe^{3+}$) which could be quantified using NMR relaxation measurements or with magnetic resonance imaging (MRI) (Figure 44A).[260–262] Another advancement is the development of a self-forming injectable hydrogel spacer which shields healthy tissues surrounding tumors during radiation therapy. Specifically, the SpaceOAR$^{TM}$ hydrogel by Boston Scientific, the only commercially-available hydrogel spacer, is a self-forming PEG-based hydrogel that is injected between the prostate and rectum pior to radiation therapy for the treatment prostate cancer (Figure 44B).[263–265]

Studies have shown that the SpaceOAR$^{TM}$ hydrogel spacer is effective in reducing rectal radiation exposure and may lower the risk of clinically important gastrointestinal tract complications.[263–265] However, there is no material that has the combined attributes of a gel dosimeter and spacer for radiation therapy. The development of a hydrogel dosimeter-spacer will improve treatment plans for radiation therapy by giving the ability to directly assess the 3D radiation dose at the target tissue in real-time while protecting healthy tissues.

The central hypothesis of this study is injectable self-forming Nor-Tet hydrogels can be used as dosimeter-spacer materials by incorporating radiation-sensitive components. To test this hypothesis, two studies are proposed: (1) incorporate radiation-sensitive chemicals to Nor-Tet hydrogels and test radiation response, and (2) evaluate efficacy after injection into a tissue model. Preliminary data from these studies shows that HA Nor-Tet dosimeter-spacers are more sensitive to changes in radiation intensity compared to gelatin Fricke gel dosimeters. Additionally, increasing the concentration of acid ($H^+$ ions) in the Nor-Tet hydrogels also increase the hydrogel's sensitivity. Injection of HA Nor-Tet dosimeter-spacer into swine cadaver shows its capability as a spacer and real-time dosimeter. To improve the sensitivity and biocompatibility of the Nor-Tet hydrogel dosimeter-spacer, future work needs to identify the ideal $H^+$ concentration to balance sensitivity and *in vivo* safety. Additionally, the tunability of hydrogel mechanics and its effect of sensitivity to radiation should be interrogated to create more stable hydrogels for various tissue applications.

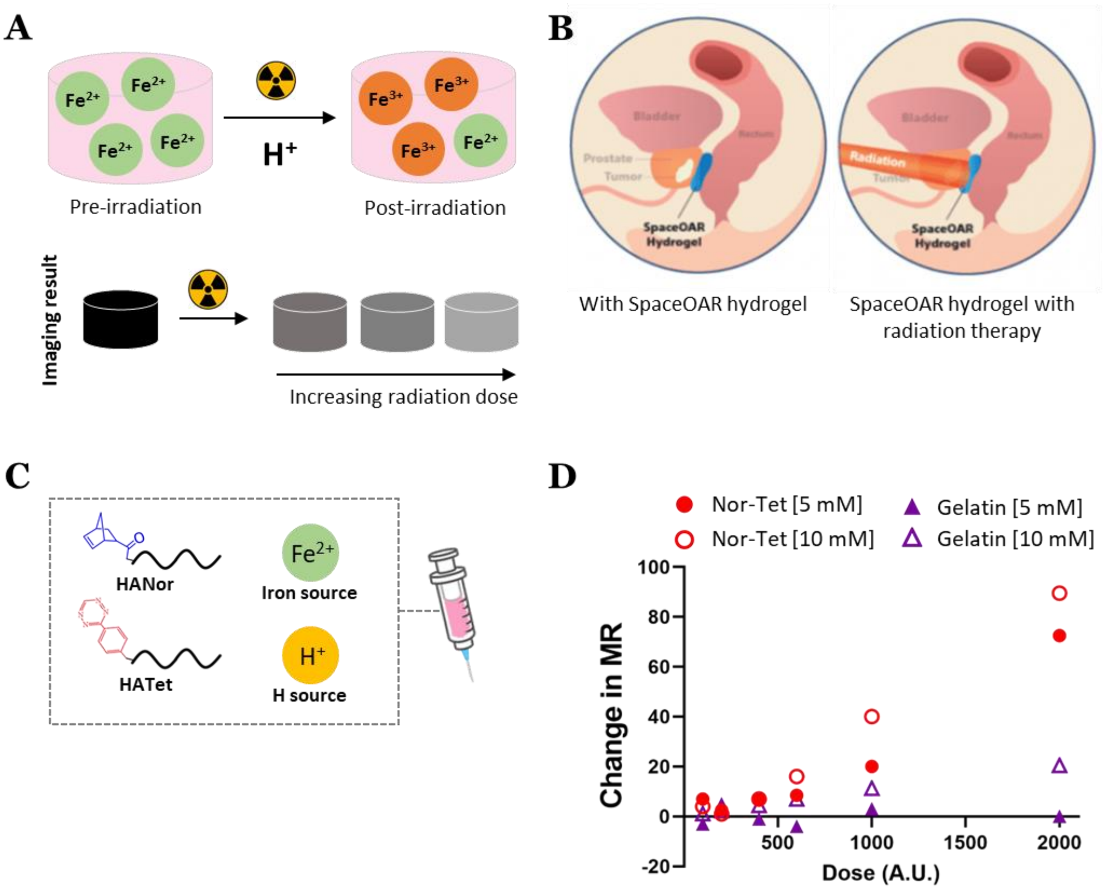

*Figure 44.* Dosimeter and spacer function for radiation therapy. **(A)** Radiation dose is measured in Fricke gel dosimeters by monitoring the conversion of $Fe^{2+}$ to $Fe^{3+}$ upon irradiation. This conversion is visualized with magnetic resonance imaging where regions with high radiation dose appear brighter than regions with low radiation dose. **(B)** The SpaceOAR$^{TM}$ hydrogel spacer shields the rectal tissue from radiation during treatment for prostate cancer. **(C)** Formulation of our HA Nor-Tet dosimeter-spacer hydrogel. **(D)** Measurement of the sensitivity to radiation dose of our HA Nor-Tet dosimeter-spacer compared to conventional gelation dosimeters.

(1) Incorporate radiation-sensitive chemicals to Nor-Tet hydrogels and test radiation response

HANor and HATet macromers were hydrated to a final concentration of 1% w/v and sulfuric acid ($H^+$ source) (final concentration of 5 mM or 10 mM) and ferrous ammonium sulfate hexahydrate ($Fe^{2+}$ source) (final concentration of 10 mM) were added. The hydrogels were formed in cuvettes and irradiated at various radiation doses (Figure

44C). Relative changes in magnetic resonance (MR) were calculated and determined. The HA Nor-Tet dosimeter-spacer hydrogels exhibited greater sensitivy to the increase in radiation dose compared to conventional gelatin-based dosimeters (Figure 6.D). At a sulfuric acid concentration of 10 mM, the Nor-Tet hydrogels showed a 5-fold increase in change in MR compared to gelatin dosimeters with comparative acid concentration.

To improve the design of this hydrogel dosimeter-spacer, further studies must explore radiation radiation response (a) at body temperature, (b) as a function of time post-manufacture, and (c) after repeated weekly irradiations to model a treatment plan.

(2) Evaluate efficacy after injection into a tissue model

HANor and HATet macromers were hydrated to a final concentration of 1% w/v and sulfuric acid ($H^+$ source) (final concentration of 5 mM) and ferrous ammonium sulfate hexahydrate ($Fe^{2+}$ source) (final concentration of 10 mM) were added. The macromers were loaded into a syringe, mixed, and injected into swine cadaver (Figure 45A) and irradiated at a dose of of 200 A.U. MRI imaging and quantification of MR at the target site pre- and post- irradiation shows an increase in MR (Figure 45B).

To improve the design of this hydrogel dosimeter-spacer, further studies must explore hydrogel radiation response at increasing radiation doses and perform *in vivo* tests to evaluate the performance of this dosimeter-spacer in live models.

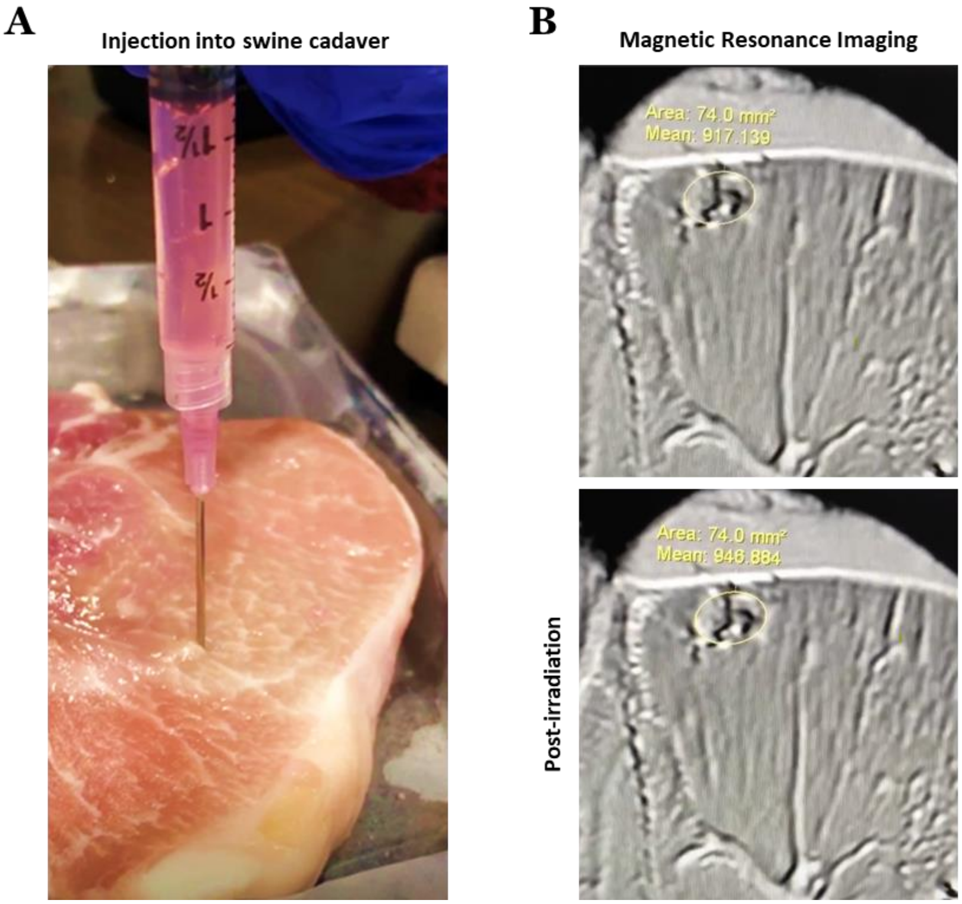

*Figure 45.* Injection of HA Nor-Tet dosimeter-spacer into swine cadaver tissue. **(A)** HA-Nor-Tet precursor solution is injected into target site and irradiated with 200 A.U. dose of radiation. **(B)** MR imaging shows increase in MR post-irradiation of the target site (yellow oval).

### 6.3 Concluding Remarks

The hydrogel system developed in this dissertation is versatile since it can form hydrogels with a broader range of mechanical properties, gelation time, and biochemical modifications compared to its self-forming IEDDA predecessors. The injectable aspect of this hydrogel system can transform surgical procedures into outpatient treatments, in which therapeutics can be locally delivered into a patient without the need for surgery. This injectable hydrogel system can also be used as (i) an efficient delivery vehicle for cell therapies by promoting high cell viability post-injection; and (ii) as material to promote new tissue growth. This injectable hydrogel system does not need expensive equipment which may not be available in other laboratories or cytotoxic catalysts to form. Moreover, its clinical utility is improved through its self-forming aspect. Through this simple hydrogel formation mechanism, more laboratories can explore tissue engineering or cellular mechanosensing which can further the advancements in the field.

## 6.4 Overview of the Appendix

In addition to this body of knowledge, we explored cell-material interactions with different materials and studied novel cell sources for stem cell-based applications. **Appendix A** is a review of developmental microenvironments and signals present in bone and cartilage ECM, with a focus on applying hydrogel-based screening approches to identify biomaterial microenvironments that promote stem cell-mediated bone and cartilage tissue regeneration. **Appendix B** is a study which aimed to improve our understanding the cellular mechanosensing of iMSCs on engineered materials with defined mechanics. This study reports that iMSCs are a promising stem cell source for basic and applied research due to their homogeneity and high sensitivity to engineered mechanical signals. Lastly, **Appendix C** explored the use of decellularized plant tissues with microtopographies that resemble cancellous bone and skeletal muscle as a biomaterial for tissue regeneration. This study reports that plant tissues with defined microarchitecture can reproducibly regulate MSC morphology, mechanosensing, and differentiation.

# References

[1] L. Brannon-Peppas, Elsevier, **1990**, pp. 45–66.

[2] K. Y. Lee, D. J. Mooney, *Chem. Rev.* **2001**, *101*, 1869.

[3] J. L. Drury, R. G. Dennis, D. J. Mooney, *Biomaterials* **2004**, *25*, 3187.

[4] J. M. van Bemmelen, *Zeitschrift für Anorg. Chemie* **1894**, *5*, 466.

[5] E. I. du P. de Nemours, *Ind. Eng. Chem.* **1936**, *28*, 1160.

[6] O. Wichterle, D. Lím, *Nat. 1960 1854706* **1960**, *185*, 117.

[7] T. R. Hoare, D. S. Kohane, *Polymer (Guildf).* **2008**, *49*, 1993.

[8] A. S. Hoffman, *Adv. Drug Deliv. Rev.* **2012**, *64*, 18.

[9] N. Annabi, A. Tamayol, J. A. Uquillas, M. Akbari, L. E. Bertassoni, C. Cha, G. Camci-Unal, M. R. Dokmeci, N. A. Peppas, A. Khademhosseini, *Adv. Mater.* **2014**, *26*, 85.

[10] A. S. Hoffman, **2002**, *54*, 3.

[11] C. Fan, D. A. Wang, *Tissue Eng. Part B. Rev.* **2017**, *23*, 451.

[12] G. Tao, Y. Wang, R. Cai, H. Chang, K. Song, H. Zuo, P. Zhao, Q. Xia, H. He, *Mater. Sci. Eng. C* **2019**, *101*, 341.

[13] L. García-Fernández, M. Olmeda-Lozano, L. Benito-Garzón, A. Pérez-Caballer, J. San Román, B. Vázquez-Lasa, *Mater. Sci. Eng. C* **2020**, *110*, 110702.

[14] X. Ma, T. Xu, W. Chen, H. Qin, B. Chi, Z. Ye, *Carbohydr. Polym.* **2018**, *179*, 100.

[15] L. M. Caballero Aguilar, S. M. Silva, S. E. Moulton, *J. Control. Release* **2019**, *306*, 40.

[16] P. Wang, S. Huang, Z. Hu, W. Yang, Y. Lan, J. Zhu, A. Hancharou, R. Guo, B. Tang, *Acta Biomater.* **2019**, *100*, 191.

[17] S. Naahidi, M. Jafari, M. Logan, Y. Wang, Y. Yuan, H. Bae, B. Dixon, P. Chen, *Biotechnol. Adv.* **2017**, *35*, 530.

[18] J. Li, D. J. Mooney, *Nat. Rev. Mater.* **2016**, *1*, DOI 10.1038/natrevmats.2016.71.

[19] D. Loessner, C. Meinert, E. Kaemmerer, L. C. Martine, K. Yue, P. A. Levett, T. J. Klein, F. P. W. Melchels, A. Khademhosseini, D. W. Hutmacher, *Nat. Protoc. 2016 114* **2016**, *11*, 727.

[20] N. A. Peppas, J. Z. Hilt, A. Khademhosseini, R. Langer, *Adv. Mater.* **2006**, *18*, 1345.

[21] M. F. Akhtar, M. Hanif, N. M. Ranjha, *Saudi Pharm. J.* **2016**, *24*, 554.

[22] M. R. Singh, S. Patel, D. Singh, *Nanobiomaterials Soft Tissue Eng. Appl. Nanobiomaterials* **2016**, 231.

[23] Y. Deng, J. Ren, G. Chen, G. Li, X. Wu, G. Wang, G. Gu, J. Li, *Sci. Reports 2017 71* **2017**, *7*, 1.

[24] C. Shao, M. Wang, H. Chang, F. Xu, J. Yang, *ACS Sustain. Chem. Eng.* **2017**, *5*, 6167.

[25] J. L. Drury, D. J. Mooney, *Biomaterials* **2003**, *24*, 4337.

[26] J. Zhu, *Biomaterials* **2010**, *31*, 4639.

[27] M. C. Cushing, K. S. Anseth, *Science (80-. ).* **2007**, *316*, 1133.

[28] F. Brandl, F. Sommer, A. Goepferich, *Biomaterials* **2007**, *28*, 134.

[29] M. Bonnet, T. Trimaille, J. M. Brezun, F. Feron, D. Gigmes, T. Marqueste, P. Decherchi, *Mater. Sci. Eng. C* **2020**, *107*, 110354.

[30] M. M. Mannarino, M. Bassett, D. T. Donahue, J. F. Biggins, *J. Biomater. Sci. Polym. Ed.* **2020**, *31*, 601.

[31] H. Vihola, A. Laukkanen, L. Valtola, H. Tenhu, J. Hirvonen, *Biomaterials* **2005**, *26*, 3055.

[32] A. Hejčl, J. Šedý, M. Kapcalová, D. A. Toro, T. Amemori, P. Lesný, K. Likavčanová-Mašínová, E. Krumbholcová, M. Přádný, J. Michálek, et al., *Stem Cells Dev.* **2010**, *19*, 1535.

[33] M. Guvendiren, J. A. Burdick, *Nat. Commun.* **2012**, *3*, 792.

[34] M. Liu, X. Zeng, C. Ma, H. Yi, Z. Ali, X. Mou, S. Li, Y. Deng, N. He, *Bone Res. 2017 51* **2017**, *5*, 1.

[35] J. George, C. C. Hsu, L. T. B. Nguyen, H. Ye, Z. Cui, *Biotechnol. Adv.* **2020**, *42*, DOI 10.1016/j.biotechadv.2019.03.009.

[36] J.-A. Yang, J. Yeom, B. Woo Hwang, A. S. Hoffman, S. K. Hahn, *Prog. Polym. Sci.* **2014**, *39*, 1973.

[37] N. A. Peppas, P. Bures, W. Leobandung, H. Ichikawa, *Eur. J. Pharm. Biopharm.* **2000**, *50*, 27.

[38] L. Klouda, A. G. Mikos, *Eur. J. Pharm. Biopharm.* **2008**, *68*, 34.

[39] H. B. Bohidar, S. S. Jena, *J. Chem. Phys.* **1998**, *98*, 8970.

[40] M. Boustta, P. E. Colombo, S. Lenglet, S. Poujol, M. Vert, *J. Control. Release* **2014**, *174*, 1.

[41] C. Hiemstra, L. J. Van Der Aa, Z. Zhong, P. J. Dijkstra, J. Feijen, *Macromolecules* **2007**, *40*, 1165.

[42] Z. Q. Liu, Z. Wei, X. L. Zhu, G. Y. Huang, F. Xu, J. H. Yang, Y. Osada, M. Zrínyi, J. H. Li, Y. M. Chen, *Colloids Surfaces B Biointerfaces* **2015**, *128*, 140.

[43] K. T. Nguyen, J. L. West, *Biomaterials* **2002**, *23*, 4307.

[44] S. Lin-Gibson, R. L. Jones, N. R. Washburn, F. Horkay, *Macromolecules* **2005**, *38*, 2897.

[45] B. M. April Kloxin, C. J. Kloxin, C. N. Bowman, K. S. Anseth, A. M. Kloxin, C. J. Kloxin, C. N. Bowman, K. S. Anseth, *Adv. Mater* **2010**, *22*, 3484.

[46] B. D. Fairbanks, M. P. Schwartz, A. E. Halevi, C. R. Nuttelman, C. N. Bowman, K. S. Anseth, *Adv. Mater.* **2009**, *21*, 5005.

[47] L. F. Tietze, G. Kettschau, Springer, Berlin, Heidelberg, **1997**, pp. 1–120.

[48] D. C. Rideout, R. Breslow, *J. Am. Chem. Soc.* **2002**, *102*, 7816.

[49] C. M. Nimmo, S. C. Owen, M. S. Shoichet, *Biomacromolecules* **2011**, *12*, 824.

[50] R. M. Desai, S. T. Koshy, S. A. Hilderbrand, D. J. Mooney, N. S. Joshi, *Biomaterials* **2015**, *50*, 30.

[51] J. Wang, F. Zhang, W. P. Tsang, C. Wan, C. Wu, *Biomaterials* **2017**, *120*, 11.

[52] A. M. Jordan, S. E. Kim, K. Van De Voorde, J. K. Pokorski, L. T. J. Korley, *ACS Biomater. Sci. Eng.* **2017**, *3*, 1869.

[53] J. Seuring, S. Agarwal, *ACS Macro Lett.* **2013**, *2*, 597.

[54] S. J. Bidarra, C. C. Barrias, P. L. Granja, *Acta Biomater.* **2014**, *10*, 1646.

[55] F. J. O'Brien, *Mater. Today* **2011**, *14*, 88.

[56] E. R. Ruskowitz, C. A. Deforest, *ACS Biomater. Sci. Eng.* **2019**, *5*, 2111.

[57] L. J. Smith, S. M. Taimoory, R. Y. Tam, A. E. G. Baker, N. Binth Mohammad, J. F. Trant, M. S. Shoichet, *Biomacromolecules* **2018**, *19*, 926.

[58] S. Kirchhof, F. P. Brandl, N. Hammer, A. M. Goepferich, *J. Mater. Chem. B* **2013**, *1*, 4855.

[59] S. T. Koshy, R. M. Desai, P. Joly, J. Li, R. K. Bagrodia, S. A. Lewin, N. S. Joshi, D. J. Mooney, *Adv. Healthc. Mater.* **2016**, *5*, 541.

[60] D. L. Alge, M. A. Azagarsamy, D. F. Donohue, K. S. Anseth, *Biomacromolecules* **2013**, *14*, 949.

[61] R. Jin, P. J. Dijkstra, R. Jin, P. J. Dijkstra, *Biomed. Appl. Hydrogels Handb.* **2010**, 203.

[62] J. Maitra, V. K. Shukla, V. Kumar Shukla, *Am. J. Polym. Sci.* **2014**, *969*, 25.

[63] A. Chenite, C. Chaput, D. Wang, C. Combes, M. D. Buschmann, C. D. Hoemann, J. C. Leroux, B. L. Atkinson, F. Binette, A. Selmani, *Biomaterials* **2000**, *21*, 2155.

[64] L. S. Nair, C. T. Laurencin, *Prog. Polym. Sci.* **2007**, *32*, 762.

[65] W. Shi, Y. Ji, X. Zhang, S. Shu, Z. Wu, *J. Pharm. Sci.* **2011**, *100*, 886.

[66] S. Piluso, B. Hiebl, S. N. Gorb, A. Kovalev, A. Lendlein, A. T. Neffe, *Int. J. Artif. Organs* **2011**, *34*, 192.

[67] S. E. Holt, A. Rakoski, F. Jivan, L. M. Pérez, D. L. Alge, *Macromol. Rapid Commun.* **2020**, *41*, 2000287.

[68] Z. Zhang, C. He, X. Chen, *Polym. 2020, Vol. 12, Page 884* **2020**, *12*, 884.

[69] H. Shin, S. Jo, A. G. Mikos, *Biomaterials* **2003**, *24*, 4353.

[70] A. J. Engler, S. Sen, H. L. Sweeney, D. E. Discher, *Cell* **2006**, *126*, 677.

[71] S. Khetan, M. Guvendiren, W. R. Legant, D. M. Cohen, C. S. Chen, J. A. Burdick, *Nat. Mater.* **2013**, *12*, 458.

[72] C. M. Madl, M. Mehta, G. N. Duda, S. C. Heilshorn, D. J. Mooney, *Biomacromolecules* **2014**, *15*, 445.

[73] F. Rizzo, N. S. Kehr, *Adv. Healthc. Mater.* **2021**, *10*, DOI 10.1002/adhm.202001341.

[74] J. H. Lee, *Biomater. Res.* **2018**, *22*, DOI 10.1186/s40824-018-0138-6.

[75] C. B. Highley, G. D. Prestwich, J. A. Burdick, *Curr. Opin. Biotechnol.* **2016**, *40*, 35.

[76] N. A. Peppas, K. B. Keys, M. Torres-Lugo, A. M. Lowman, *J. Control. Release* **1999**, *62*, 81.

[77] M. D. Baumann, C. E. Kang, J. C. Stanwick, Y. Wang, H. Kim, Y. Lapitsky, M. S. Shoichet, *J. Control. Release* **2009**, *138*, 205.

[78] J. Nicolas, S. Magli, L. Rabbachin, S. Sampaolesi, F. Nicotra, L. Russo, *Biomacromolecules* **2020**, *21*, 1968.

[79] H. F. Oldenkamp, J. E. Vela Ramirez, N. A. Peppas, *Regen. Biomater.* **2019**, *6*, 1.

[80] K. Hosoyama, C. Lazurko, M. Muñoz, C. D. McTiernan, E. I. Alarcon, *Front. Bioeng. Biotechnol.* **2019**, *7*, 205.

[81] I. W. Hamley, *Chem. Rev.* **2017**, *117*, 14015.

[82] M. Gregoritza, F. P. Brandl, *Eur. J. Pharm. Biopharm.* **2015**, *97*, 438.

[83] V. Crescenzi, L. Cornelio, C. Di Meo, S. Nardecchia, R. Lamanna, *Biomacromolecules* **2007**, *8*, 1844.

[84] P. L. Golas, K. Matyjaszewski, *Chem. Soc. Rev.* **2010**, *39*, 1338.

[85] H. C. Kolb, M. G. Finn, K. B. Sharpless, *Angew. Chemie Int. Ed.* **2001**, *40*, 2004.

[86] H. C. Kolb, K. B. Sharpless, *Drug Discov. Today* **2003**, *8*, 1128.

[87] C. M. Nimmo, M. S. Shoichet, *Bioconjug. Chem.* **2011**, *22*, 2199.

[88] E. Lallana, F. Fernandez-Trillo, A. Sousa-Herves, R. Riguera, E. Fernandez-Megia, *Pharm. Res.* **2012**, *29*, 1134.

[89] K. W. Li, L. Cen, C. Zhou, A. K. Zhang, F. Yao, L. H. Tan, L. Q. Xu, G. D. Fu, *Macromol. Mater. Eng.* **2016**, *301*, 1374.

[90] M. A. Tasdelen, Y. Yagci, *Angew. Chemie Int. Ed.* **2013**, *52*, 5930.

[91] Y. Yu, C. Deng, F. Meng, Q. Shi, J. Feijen, Z. Zhong, *J. Biomed. Mater. Res. Part A* **2011**, *99A*, 316.

[92] J. L. Young, A. J. Engler, *Biomaterials* **2011**, *32*, 1002.

[93] F. Yu, X. Cao, J. Du, G. Wang, X. Chen, *ACS Appl. Mater. Interfaces* **2015**, *7*, 24023.

[94] S. C. Owen, S. A. Fisher, R. Y. Tam, C. M. Nimmo, M. S. Shoichet, *Langmuir* **2013**, *29*, 7393.

[95] O. Diels, K. Alder, *Justus Liebigs Ann. Chem.* **1928**, *460*, 98.

[96] R. B. Woodward, R. Hoffmann, *Angew. Chemie Int. Ed. English* **1969**, *8*, 781.

[97] R. B. Woodward, T. J. Katz, *Tetrahedron Lett.* **1959**, *1*, 19.

[98] J. Sauer, R. Sustmann, *Angew. Chemie Int. Ed. English* **1980**, *19*, 779.

[99] K. N. Houk, Y. T. Lin, F. K. Brown, *J. Am. Chem. Soc.* **1986**, *108*, 554.

[100] M. J. S. Dewar, J. J. P. Stewart, S. Olivella, *J. Am. Chem. Soc.* **1986**, *108*, 5771.

[101] J. Sauer, *Angew. Chemie Int. Ed. English* **1966**, *5*, 211.

[102] S. Kirchhof, A. Strasser, H. J. Wittmann, V. Messmann, N. Hammer, A. M. Goepferich, F. P. Brandl, *J. Mater. Chem. B* **2014**, *3*, 449.

[103] A. C. Knall, M. Hollauf, C. Slugovc, *Tetrahedron Lett.* **2014**, *55*, 4763.

[104] N. A. Peppas, *Curr. Opin. Colloid Interface Sci.* **1997**, *2*, 531.

[105] Z. Zhao, Z. Wang, G. Li, Z. Cai, J. Wu, L. Wang, L. Deng, M. Cai, W. Cui, *Adv. Funct. Mater.* **2021**, *31*, 2103339.

[106] M. Montiel-Herrera, A. Gandini, F. M. Goycoolea, N. E. Jacobsen, J. Lizardi-Mendoza, M. Recillas-Mota, W. M. Argüelles-Monal, *Carbohydr. Polym.* **2015**, *128*, 6.

[107] H. Wei, X. Yang, H. Chu, J. Li, *Polym. Eng. Sci.* **2019**, *59*, 1999.

[108] H. Wei, W. Li, H. Chen, X. Wen, J. He, J. Li, *Carbohydr. Polym.* **2020**, *241*, DOI 10.1016/j.carbpol.2020.116351.

[109] S. Wang, Y. Niu, P. Jia, Z. Liao, W. Guo, R. C. Chaves, K. H. Tran-Ba, L. He, H. Bai, S. Sia, et al., *Bioact. Mater.* **2022**, *15*, 316.

[110] O. Guaresti, C. García-Astrain, R. H. Aguirresarobe, A. Eceiza, N. Gabilondo, *Carbohydr. Polym.* **2018**, *183*, 278.

[111] M. Zhang, J. Wang, Z. Jin, *Int. J. Biol. Macromol.* **2018**, *114*, 381.

[112] D. qiang Li, S. ya Wang, Y. jie Meng, Z. wei Guo, M. mei Cheng, J. Li, *Carbohydr. Polym.* **2021**, *268*, DOI 10.1016/j.carbpol.2021.118244.

[113] O. Guaresti, C. García–Astrain, T. Palomares, A. Alonso–Varona, A. Eceiza, N. Gabilondo, *Int. J. Biol. Macromol.* **2017**, *102*, 1.

[114] M. Fan, Y. Ma, Z. Zhang, J. Mao, H. Tan, X. Hu, *Mater. Sci. Eng. C* **2015**, *56*, 311.

[115] S. Kirchhof, M. Gregoritza, V. Messmann, N. Hammer, A. M. Goepferich, F. P. Brandl, *Eur. J. Pharm. Biopharm.* **2015**, *96*, 217.

[116] C. García-Astrain, L. Avérous, *Carbohydr. Polym.* **2018**, *190*, 271.

[117] R. Debone Piazza, J. V. Brandt, C. Carvalho dos Santos, R. Fernando Costa Marques, M. Jafelicci Junior, *Med. DEVICES SENSORS* **2021**, *4*, DOI 10.1002/mds3.10151.

[118] D. S. B. Anugrah, K. Ramesh, M. Kim, K. Hyun, K. T. Lim, *Carbohydr. Polym.* **2019**, *223*, DOI 10.1016/j.carbpol.2019.115070.

[119] S. A. P. Siboro, D. S. B. Anugrah, K. Ramesh, S. H. Park, H. R. Kim, K. T. Lim, *Carbohydr. Polym.* **2021**, *260*, DOI 10.1016/j.carbpol.2021.117779.

[120] H. T. Hoang, S. H. Jo, Q. T. Phan, H. Park, S. H. Park, C. W. Oh, K. T. Lim, *Carbohydr. Polym.* **2021**, *260*, DOI 10.1016/J.CARBPOL.2021.117812.

[121] T. T. Vu, M. Gulfam, S. H. Jo, S. H. Park, K. T. Lim, *Carbohydr. Polym.* **2022**, *278*, 118964.

[122] Y. J. Jo, M. Gulfam, S. H. Jo, Y. S. Gal, C. W. Oh, S. H. Park, K. T. Lim, *Carbohydr. Polym.* **2022**, *286*, 119303.

[123] M. Gulfam, S. H. Jo, S. W. Jo, T. T. Vu, S. H. Park, K. T. Lim, *NPG Asia Mater. 2022 141* **2022**, *14*, 1.

[124] H. T. Hoang, T. T. Vu, V. Karthika, S. H. Jo, Y. J. Jo, J. W. Seo, C. W. Oh, S. H. Park, K. T. Lim, *Carbohydr. Polym.* **2022**, *288*, 119389.

[125] L. R. Brown, **2005**, *2*, 29.

[126] M. Gregoritza, V. Messmann, A. M. Goepferich, F. P. Brandl, *J. Mater. Chem. B* **2016**, *4*, 3398.

[127] S. T. Koshy, D. K. Y. Zhang, J. M. Grolman, A. G. Stafford, D. J. Mooney, *Acta Biomater.* **2018**, *65*, 36.

[128] C. E. Ziegler, M. Graf, M. Nagaoka, H. Lehr, A. M. Goepferich, *Biomacromolecules* **2021**, *22*, 3223.

[129] A. Famili, K. Rajagopal, *Mol. Pharm.* **2017**, *14*, 1961.

[130] M. Wei, Y. I. Hsu, T. A. Asoh, M. H. Sung, H. Uyama, *J. Mater. Chem. B* **2021**, *9*, 3584.

[131] Y. Yang, Z. Zhu, R. Gao, J. Yuan, J. Zhang, H. Li, Z. Xie, Y. Wang, *Acta Biomater.* **2021**, *128*, 163.

[132] J. Yan, B. Gundsambuu, M. Krasowska, K. Platts, P. Facal Marina, C. Gerber, S. C. Barry, A. Blencowe, *J. Mater. Chem. B* **2022**, *10*, 3329.

[133] V. Delplace, P. E. B. Nickerson, A. Ortin-Martinez, A. E. G. Baker, V. A. Wallace, M. S. Shoichet, *Adv. Funct. Mater.* **2020**, *30*, DOI 10.1002/adfm.201903978.

[134] R. Z. Lin, H. Y. Chang, *Biotechnol. J.* **2008**, *3*, 1172.

[135] D. Xing, L. Ma, C. Gao, *J. Bioact. Compat. Polym.* **2017**, *32*, 382.

[136] C. M. Madl, S. C. Heilshorn, *Chem. Mater.* **2019**, *31*, 8035.

[137] G. F. Sousa, S. Afewerki, D. Dittz, F. E. P. Santos, D. O. Gontijo, S. R. A. Scalzo, A. L. C. Santos, L. C. Guimaraes, E. M. Pereira, L. S. Barcelos, et al., *J. Funct. Biomater. 2022, Vol. 13, Page 45* **2022**, *13*, 45.

[138] N. Contessi Negrini, A. Angelova Volponi, P. T. Sharpe, A. D. Celiz, *ACS Biomater. Sci. Eng.* **2021**, *7*, 4330.

[139] Y. Zhang, H. Chen, T. Zhang, Y. Zan, T. Ni, M. Liu, R. Pei, *Biomater. Sci.* **2018**, *6*, 2578.

[140] L. B. E. Shields, G. H. Raque, S. D. Glassman, M. Campbell, T. Vitaz, J. Harpring, C. B. Shields, *Spine (Phila. Pa. 1976).* **2006**, *31*, 542.

[141] K. R. Garrison, S. Donell, J. Ryder, I. Shemilt, M. Mugford, I. Harvey, F. Song, *Health Technol. Assess.* **2007**, *11*, DOI 10.3310/HTA11300.

[142] D. A. Wong, A. Kumar, S. Jatana, G. Ghiselli, K. Wong, *Spine J.* **2008**, *8*, 1011.

[143] S. H. Park, J. Y. Seo, J. Y. Park, Y. B. Ji, K. Kim, H. S. Choi, S. Choi, J. H. Kim, B. H. Min, M. S. Kim, *NPG Asia Mater.* **2019**, *11*, DOI 10.1038/s41427-019-0130-1.

[144] E. de Sousa Araújo, T. Domingues Stocco, G. Fernandes de Sousa, S. Afewerki, F. R. Marciano, M. Alexandre Finzi Corat, M. Michelle Machado de Paula, T. Ferreira Cândido Lima Verde, M. Cristina Moreira Silva, A. Oliveira Lobo, *Colloids Surfaces B Biointerfaces* **2021**, *205*, DOI 10.1016/j.colsurfb.2021.111850.

[145] J. S. Temenoff, A. G. Mikos, *Biomaterials* **2000**, *21*, 2405.

[146] R. Liu, S. Zhang, X. Chen, *J. Tissue Eng. Regen. Med.* **2020**, *14*, 1333.

[147] J. P. Gong, Y. Katsuyama, T. Kurokawa, Y. Osada, *Adv. Mater.* **2003**, *15*, 1155.

[148] P. Lin, S. Ma, X. Wang, F. Zhou, *Adv. Mater.* **2015**, *27*, 2054.

[149] Y. Zhang, Y. Li, W. Liu, *Adv. Funct. Mater.* **2015**, *25*, 471.

[150] D. Zhao, J. Huang, Y. Zhong, K. Li, L. Zhang, J. Cai, *Adv. Funct. Mater.* **2016**, *26*, 6279.

[151] S. Azevedo, A. M. S. Costa, A. Andersen, I. S. Choi, H. Birkedal, J. F. Mano, *Adv. Mater.* **2017**, *29*, 1700759.

[152] X. Bai, S. Lü, Z. Cao, C. Gao, H. Duan, X. Xu, L. Sun, N. Gao, C. Feng, M. Liu, *Chem. Eng. J.* **2016**, *288*, 546.

[153] M. H. Ghanian, H. Mirzadeh, H. Baharvand, *Biomacromolecules* **2018**, *19*, 1646.

[154] X. Bai, S. Lü, Z. Cao, B. Ni, X. Wang, P. Ning, D. Ma, H. Wei, M. Liu, *Carbohydr. Polym.* **2017**, *166*, 123.

[155] X. Bai, S. Lü, H. Liu, Z. Cao, P. Ning, Z. Wang, C. Gao, B. Ni, D. Ma, M. Liu, *Carbohydr. Polym.* **2017**, *175*, 557.

[156] C. Levinson, M. Lee, L. A. Applegate, M. Zenobi-Wong, *Acta Biomater.* **2019**, *99*, 168.

[157] A. M. Bhosale, J. B. Richardson, *Br. Med. Bull.* **2008**, *87*, 77.

[158] C. Yu, H. Gao, Q. Li, X. Cao, *Polym. Chem.* **2020**, *11*, 3169.

[159] V. X. Truong, M. P. Ablett, S. M. Richardson, J. A. Hoyland, A. P. Dove, *J. Am. Chem. Soc.* **2015**, *137*, 1618.

[160] K. H. Vining, A. Stafford, D. J. Mooney, *Biomaterials* **2019**, *188*, 187.

[161] H. S. Abandansari, M. H. Ghanian, F. Varzideh, E. Mahmoudi, S. Rajabi, P. Taheri, M. R. Nabid, H. Baharvand, *Biomaterials* **2018**, *170*, 12.

[162] H. Wei, S. Li, Z. Liu, H. Chen, Y. Liu, W. Li, G. Wang, *Int. J. Biol. Macromol.* **2022**, *194*, 962.

[163] M. K. Nguyen, D. S. Lee, *Macromol. Biosci.* **2010**, *10*, 563.

[164] T. Garg, S. Singh, A. K. Goyal, *Crit. Rev. Ther. Drug Carrier Syst.* **2013**, *30*, 369.

[165] T. Ma, X. Gao, H. Dong, H. He, X. Cao, *Appl. Mater. Today* **2017**, *9*, 49.

[166] B. V. Slaughter, S. S. Khurshid, O. Z. Fisher, A. Khademhosseini, N. A. Peppas, *Adv. Mater.* **2009**, *21*, 3307.

[167] W. M. Gramlich, I. L. Kim, J. A. Burdick, *Biomaterials* **2013**, *34*, 9803.

[168] R. L. Sala, M. Y. Kwon, M. Kim, S. E. Gullbrand, E. A. Henning, R. L. Mauck, E. R. Camargo, J. A. Burdick, *Tissue Eng. Part A* **2017**, *23*, 935.

[169] L. Guo, R. H. Colby, C. P. Lusignan, A. M. Howe, *Macromolecules* **2003**, *36*, 10009.

[170] A. K. Miri, A. Khalilpour, B. Cecen, S. Maharjan, S. R. Shin, A. Khademhosseini, *Biomaterials* **2019**, *198*, 204.

[171] K. Hölzl, S. Lin, L. Tytgat, S. Van Vlierberghe, L. Gu, A. Ovsianikov, *Biofabrication* **2016**, *8*, DOI 10.1088/1758-5090/8/3/032002.

[172] S. Wüst, M. E. Godla, R. Müller, S. Hofmann, *Acta Biomater.* **2014**, *10*, 630.

[173] M. Patenaude, N. M. B. Smeets, T. Hoare, *Macromol. Rapid Commun.* **2014**, *35*, 598.

[174] K. A. Smeds, M. W. Grinstaff, *J. Biomed. Mater. Res.* **2001**, *54*, 115.

[175] D. P. Nair, M. Podgórski, S. Chatani, T. Gong, W. Xi, C. R. Fenoli, C. N. Bowman, *Chem. Mater.* **2014**, *26*, 724.

[176] J.-Y. Lee, J.-E. Choo, Y.-S. Choi, J.-S. Suh, S.-J. Lee, C.-P. Chung, Y.-J. Park, *Biomaterials* **2009**, *30*, 3532.

[177] Y.-J. Seol, Y.-J. Park, S.-C. Lee, K.-H. Kim, J.-Y. Lee, T.-I. Kim, Y.-M. Lee, Y. Ku, I.-C. Rhyu, S.-B. Han, et al., *J. Biomed. Mater. Res. Part A* **2006**, *77A*, 599.

[178] J. A. Burdick, G. D. Prestwich, A. Burdick, G. D. Prestwich, *Adv. Mater.* **2011**, *23*, 41.

[179] J. R. Glass, K. T. Dickerson, K. Stecker, J. W. Polarek, *Biomaterials* **1996**, *17*, 1101.

[180] R. G. Wells, *Hepatology* **2008**, *47*, 1394.

[181] F. Guilak, D. M. Cohen, B. T. Estes, J. M. Gimble, W. Liedtke, C. S. Chen, *Cell Stem Cell* **2009**, *5*, 17.

[182] P. P. Provenzano, P. J. Keely, *J. Cell Sci.* **2011**, *124*, 1195.

[183] A. M. Pasapera, S. V. Plotnikov, R. S. Fischer, L. B. Case, T. T. Egelhoff, C. M. Waterman, *Curr. Biol.* **2015**, *25*, 175.

[184] R. McBeath, D. M. Pirone, C. M. Nelson, K. Bhadriraju, C. S. Chen, *Dev. Cell* **2004**, *6*, 483.

[185] S. Dupont, L. Morsut, M. Aragona, E. Enzo, S. Giulitti, M. Cordenonsi, F. Zanconato, J. Le Digabel, M. Forcato, S. Bicciato, et al., *Nature* **2011**, *474*, 179.

[186] A. M. Rosales, S. L. S. L. S. L. Vega, F. W. DelRio, J. A. Burdick, K. S. Anseth, *Angew. Chemie - Int. Ed.* **2017**, DOI 10.1002/anie.201705684.

[187] S. R. Caliari, S. L. Vega, M. Kwon, E. M. Soulas, J. A. Burdick, *Biomaterials* **2016**, *103*, 314.

[188] B. Geiger, J. P. Spatz, A. D. Bershadsky, *Nat. Rev. Mol. Cell Biol.* **2009**, *10*, 21.

[189] C. S. Chen, J. Tan, J. Tien, *Annu. Rev. Biomed. Eng.* **2004**, *6*, 275.

[190] B. A. Aguado, W. Mulyasasmita, J. Su, K. J. Lampe, S. C. Heilshorn, *Tissue Eng. - Part A* **2012**, *18*, 806.

[191] L. Cai, R. E. Dewi, S. C. Heilshorn, *Adv. Funct. Mater.* **2015**, *25*, 1344.

[192] D. E. Discher, P. Janmey, Y.-L. Wang, *Science* **2005**, *310*, 1139.

[193] O. Chaudhuri, L. Gu, D. Klumpers, M. Darnell, S. A. Bencherif, J. C. Weaver, N. Huebsch, H. Lee, E. Lippens, G. N. Duda, et al., *Nat. Mater.* **2016**, *15*, 326.

[194] R. K. Das, V. Gocheva, R. Hammink, O. F. Zouani, A. E. Rowan, *Nat. Mater.* **2016**, *15*, 318.

[195] K. Yue, G. Trujillo-de Santiago, M. M. Alvarez, A. Tamayol, N. Annabi, A. Khademhosseini, *Biomaterials* **2015**, *73*, 254.

[196] S. L. Vega, M. Y. Kwon, K. H. Song, C. Wang, R. L. Mauck, L. Han, J. A. Burdick, *Nat. Commun.* **2018**, *9*, 614.

[197] W.-K. Miao, A. Yi, Y.-K. Yan, L.-J. Ren, D. Chen, C.-H. Wang, W. Wang, *Polym. Chem.* **2015**.

[198] R. M. Desai, S. T. Koshy, S. A. Hilderbrand, D. J. Mooney, N. S. Joshi, *Biomaterials* **2015**, *50*, 30.

[199] F. Yousefi, S. Kandel, N. Pleshko, *Appl. Spectrosc.* **2018**, *72*, 1455.

[200] G. Z. Li, R. K. Randev, A. H. Soeriyadi, G. Rees, C. Boyer, Z. Tong, T. P. Davis, C. R. Becer, D. M. Haddleton, *Polym. Chem.* **2010**, *1*, 1196.

[201] Y. Vida, D. Collado, F. Najera, S. Claros, J. Becerra, J. A. Andrades, E. Perez-Inestrosa, **2016**, DOI 10.1039/c6ra06177j.

[202] A. Boudaoud, A. Burian, D. Borowska-Wykręt, M. Uyttewaal, R. Wrzalik, D. Kwiatkowska, O. Hamant, *Nat. Protoc.* **2014**, *9*, 457.

[203] S. L. Vega, E. Liu, P. J. Patel, A. B. Kulesa, A. L. Carlson, Y. Ma, M. L. Becker, P. V. Moghe, *J. Biomol. Screen.* **2012**, *17*, 1151.

[204] N. C. Wright, A. C. Looker, K. G. Saag, J. R. Curtis, E. S. Delzell, S. Randall, B. Dawson-Hughes, *J. Bone Miner. Res.* **2014**, *29*, 2520.

[205] T. Sozen, L. Ozisik, N. Calik Basaran, *Eur. J. Rheumatol.* **2017**, *4*, 46.

[206] C. Cooper, *Osteoporos. Int.* **1999**, *9*, S2.

[207] L. C. Hofbauer, *Endocr. Abstr.* **2013**, *32*, DOI 10.1530/endoabs.32.s8.2.

[208] D. J. M. Van der Voort, P. P. Geusens, G. J. Dinant, *Osteoporos. Int. 2001 128* **2001**, *12*, 630.

[209] D. A. Corral, M. Amling, M. Priemel, E. Loyer, S. Fuchs, P. Ducy, R. Baron, G. Karsenty, *Proc. Natl. Acad. Sci.* **1998**, *95*, 13835.

[210] D. D. Deligianni, Y. F. Missirlis, K. E. Tanner, W. Bonfield, *J. Mater. Sci. Mater. Med.* **1991**, *2*, 168.

[211] G. Osterhoff, E. F. Morgan, S. J. Shefelbine, L. Karim, L. M. McNamara, P. Augat, *Injury* **2016**, *47*, S11.

[212] B. Li, R. M. Aspden, *J. Bone Miner. Res.* **1997**, *12*, 641.

[213] R. M. Zebaze, A. Ghasem-Zadeh, A. Bohte, S. Iuliano-Burns, M. Mirams, R. I. Price, E. J. Mackie, E. Seeman, *Lancet (London, England)* **2010**, *375*, 1729.

[214] K. N. Tu, J. D. Lie, C. K. V. Wan, M. Cameron, A. G. Austel, J. K. Nguyen, K. Van, D. Hyun, *Pharm. Ther.* **2018**, *43*, 92.

[215] M. Mehta, K. Schmidt-Bleek, G. N. Duda, D. J. Mooney, *Adv. Drug Deliv. Rev.* **2012**, *64*, 1257.

[216] N. Murakami, N. Saito, J. Takahashi, H. Ota, H. Horiuchi, M. Nawata, T. Okada, K. Nozaki, K. Takaoka, *Biomaterials* **2003**, *24*, 2153.

[217] Y. Takahashi, M. Yamamoto, Y. Tabata, *Biomaterials* **2005**, *26*, 4856.

[218] K. Tsuji, A. Bandyopadhyay, B. D. Harfe, K. Cox, S. Kakar, L. Gerstenfeld, T. Einhorn, C. J. Tabin, V. Rosen, *Nat. Genet.* **2006**, *38*, 1424.

[219] F. N. K. Kwong, J. A. Hoyland, A. J. Freemont, C. H. Evans, *J. Orthop. Res.* **2009**, *27*, 752.

[220] J. L. Wrana, *Cell* **2000**, *100*, 189.

[221] K. A. Waite, C. Eng, *Nat. Rev. Genet.* **2003**, *4*, 763.

[222] Y. Ito, K. Miyazono, *Curr. Opin. Genet. Dev.* **2003**, *13*, 43.

[223] J. S. Park, H. N. Yang, S. Y. Jeon, D. G. Woo, K. Na, K.-H. Park, *Biomaterials* **2010**, *31*, 6239.

[224] B. Zhao, T. Katagiri, H. Toyoda, T. Takada, T. Yanai, T. Fukuda, U. Chung, T. Koike, K. Takaoka, R. Kamijo, *J. Biol. Chem.* **2006**, *281*, 23246.

[225] B. P. Toole, *Semin. Cell Dev. Biol.* **2001**, *12*, 79.

[226] B. P. Toole, *Nat. Rev. Cancer* **2004**, *4*, 528.

[227] J. E. Samorezov, E. B. Headley, C. R. Everett, E. Alsberg, *J. Biomed. Mater. Res. Part A* **2016**, *104*, 1387.

[228] W. C. Prall, F. Haasters, J. Heggebö, H. Polzer, C. Schwarz, C. Gassner, S. Grote, D. Anz, M. Jäger, W. Mutschler, et al., *Biochem. Biophys. Res. Commun.* **2013**, *440*, 617.

[229] S. P. Massia, J. A. Hubbell, *Anal. Biochem.* **1990**, *187*, 292.

[230] S. P. Zhong, D. Campoccia, P. J. Doherty, R. L. Williams, L. Benedetti, D. F. Williams, *Biomaterials* **1994**, *15*, 359.

[231] H. Yingjie, Z. Ge, W. Yisheng, Q. Ling, W. Y. Hung, L. Kwoksui, P. Fuxing, *Bone* **2007**, *41*, 631.

[232] N. A. Sims, N. C. Walsh, *Curr. Osteoporos. Rep.* **2012**, *10*, 109.

[233] K. Matsuo, N. Irie, *Arch. Biochem. Biophys.* **2008**, *473*, 201.

[234] A. H. R. W. Simpson, L. Mills, B. Noble, *J. Bone Jt. Surg. - Ser. B* **2006**, *88*, 701.

[235] J. R. Lieberman, A. Daluiski, T. A. Einhorn, *J. Bone Joint Surg. Am.* **2002**, *84*, 1032.

[236] K. A. Gultian, R. Gandhi, K. DeCesari, V. Romiyo, E. P. Kleinbart, K. Martin, P. M. Gentile, T. W. B. Kim, S. L. Vega, *Front. Biomater. Sci.* **2022**, *0*, 6.

[237] L. H. Trammell, A. M. Kroman, *Res. Methods Hum. Skelet. Biol.* **2013**, 361.

[238] D. W. Lee, K. T. Koo, Y. J. Seol, Y. M. Lee, Y. Ku, I. C. Rhyu, C. P. Chung, T. Il Kim, *J. Periodontal Implant Sci.* **2010**, *40*, 132.

[239] B. Boyce, Z. Yao, L. Xing, *Crit. Rev. Eukaryot. Gene Expr.* **2009**, *19*, 171.

[240] X. He, J. Ma, E. Jabbari, *Langmuir* **2008**, *24*, 12508.

[241] E. Van Houtte, K. Van Lierde, E. D'Haeseleer, S. Claeys, *Laryngoscope* **2010**, *120*, 306.

[242] L. de Araújo Pernambuco, A. Espelt, P. M. M. Balata, K. C. de Lima, *Eur. Arch. Oto-Rhino-Laryngology* **2015**, *272*, 2601.

[243] P. S. Mallur, C. A. Rosen, *Clin. Exp. Otorhinolaryngol.* **2010**, *3*, 177.

[244] G. Molteni, G. Bergamini, A. Ricci-Maccarini, C. Marchese, A. Ghidini, M. Alicandri-Ciufelli, M. P. Luppi, L. Presutti, *Otolaryngol. - Head Neck Surg.* **2010**, *142*, 547.

[245] T. Walimbe, A. Panitch, P. M. Sivasankar, *J. Voice* **2017**, *31*, 416.

[246] X. Chen, S. L. Thibeault, *Tissue Eng. - Part A* **2012**, *18*, 2528.

[247] N. Sahiner, A. K. Jha, D. Nguyen, X. Jia, *J. Biomater. Sci. Polym. Ed.* **2008**, *19*, 223.

[248] X. Jia, J. A. Burdick, J. Kobler, R. J. Clifton, J. J. Rosowski, S. M. Zeitels, R. Langer, *Macromolecules* **2004**, *37*, 3239.

[249] A. J. E. Farran, S. S. Teller, A. K. Jha, T. Jiao, R. A. Hule, R. J. Clifton, D. P. Pochan, R. L. Duncan, X. Jia, *Tissue Eng. - Part A* **2010**, *16*, 1247.

[250] J. K. Kutty, K. Webb, *J. Tissue Eng. Regen. Med.* **2010**, *4*, 62.

[251] Y. Lee, J. W. Bae, D. H. Oh, K. M. Park, Y. W. Chun, H. J. Sung, K. D. Park, *J. Mater. Chem. B* **2013**, *1*, 2407.

[252] S. Kitahara, Y. Masuda, Y. Kitagawa, *J. Laryngol. Otol.* **2005**, *119*, 825.

[253] R. González-Herranz, E. Amarillo, E. Hernández-García, J. Montojo Woodeson, G. Plaza-Mayor, *J. Voice* **2017**, *31*, 342.

[254] L. X. Chen, M. Coulombe, F. Barthelat, A. Rammal, L. Mongeau, K. Kost, *Laryngoscope* **2019**, *129*, 2139.

[255] F. Bray, M. Laversanne, E. Weiderpass, I. Soerjomataram, *Cancer* **2021**, *127*, 3029.

[256] H. Sung, J. Ferlay, R. L. Siegel, M. Laversanne, I. Soerjomataram, A. Jemal, F. Bray, *CA. Cancer J. Clin.* **2021**, *71*, 209.

[257] G. Delaney, S. Jacob, C. Featherstone, M. Barton, *Cancer* **2005**, *104*, 1129.

[258] A. C. Begg, F. A. Stewart, C. Vens, *Nat. Rev. Cancer* **2011**, *11*, 239.

[259] G. C. Barnett, C. M. L. West, A. M. Dunning, R. M. Elliott, C. E. Coles, P. D. P. Pharoah, N. G. Burnet, *Nat. Rev. Cancer* **2009**, *9*, 134.

[260] G. S. Ibbott, *J. Phys. Conf. Ser.* **2004**, *3*, 58.

[261] A. Appleby, E. A. Christman, A. Leghrouz, *Med. Phys.* **1987**, *14*, 382.

[262] R. J. Schulz, A. F. DeGuzman, D. B. Nguyen, J. C. Gore, *Phys. Med. Biol.* **1990**, *35*, 1611.

[263] N. Armstrong, A. Bahl, M. Pinkawa, S. Ryder, C. Ahmadu, J. Ross, S. Bhattacharyya, E. Woodward, S. Battaglia, J. Binns, et al., *Urology* **2021**, *156*, e74.

[264] H. A. Payne, M. Pinkawa, C. Peedell, S. K. Bhattacharyya, E. Woodward, L. E. Miller, *Med. (United States)* **2021**, *100*, DOI 10.1097/MD.0000000000028111.

[265] K. Van Gysen, A. Kneebone, F. Alfieri, L. Guo, T. Eade, *J. Med. Imaging Radiat. Oncol.* **2014**, *58*, 511.

[266] R. Langer, J. P. Vacanti, *Science (80-. ).* **1993**, *260*, 920.

[267] R. Langer, *Pharm. Res.* **1997**, *14*, 840.

[268] V. Bisceglie, *Z. Krebsforsch.* **1934**, *40*, 122.

[269] C. Loebel, J. A. Burdick, *Cell Stem Cell* **2018**, *22*, 325.

[270] D. W. Hutmacher, in *Biomater. Silver Jubil. Compend.*, Elsevier Science, **2006**, pp. 175–189.

[271] A. I. Caplan, *J. Cell. Physiol.* **2007**, *213*, 341.

[272] C. Frantz, K. M. Stewart, V. M. Weaver, *J. Cell Sci.* **2010**, *123*, 4195.

[273] E. A. Makris, A. H. Gomoll, K. N. Malizos, J. C. Hu, K. A. Athanasiou, *Nat. Rev. Rheumatol.* **2015**, *11*, 21.

[274] D. R. Bogdanowicz, H. H. Lu, *Ann. N. Y. Acad. Sci.* **2017**, *1410*, 3.

[275] B. K. Hall, T. Miyake, *BioEssays* **2000**, *22*, 138.

[276] N. S. Stott, T.-X. Jiang, C.-M. Chuong, *J. Cell. Physiol.* **1999**, *180*, 314.

[277] E. J. Mackie, Y. A. Ahmed, L. Tatarczuch, K.-S. Chen, M. Mirams, *Int. J. Biochem. Cell Biol.* **2008**, *40*, 46.

[278] C. Maes, T. Kobayashi, M. K. Selig, S. Torrekens, S. I. Roth, S. Mackem, G. Carmeliet, H. M. Kronenberg, *Dev. Cell* **2010**, *19*, 329.

[279] A. I. Alford, K. M. Kozloff, K. D. Hankenson, *Int. J. Biochem. Cell Biol.* **2015**, *65*, 20.

[280] A. H. Gomoll, T. Minas, *Wound Repair Regen.* **2014**, *22*, 30.

[281] J. M. Patel, K. S. Saleh, J. A. Burdick, R. L. Mauck, *Acta Biomater.* **2019**, *93*, 222.

[282] A. J. Sophia Fox, A. Bedi, S. A. Rodeo, *Sport. Heal. A Multidiscip. Approach* **2009**, *1*, 461.

[283] S. A. Oberlender, R. S. Tuan, *Cell Adhes. Commun.* **1994**, *2*, 521.

[284] M. F. Pittenger, A. M. Mackay, S. C. Beck, R. K. Jaiswal, R. Douglas, J. D. Mosca, M. A. Moorman, D. W. Simonetti, S. Craig, D. R. Marshak, *Science (80-. ).* **1999**, *284*, 143.

[285] N. J. Steinmetz, S. J. Bryant, *Acta Biomater.* **2011**, *7*, 3829.

[286] R. O. Hynes, *Cell* **1992**, *69*, 11.

[287] M. Takeichi, *Science* **1991**, *251*, 1451.

[288] L. Xu, P. A. Overbeek, L. W. Reneker, *Exp. Eye Res.* **2002**, *74*, 753.

[289] K. Gravdal, O. J. Halvorsen, S. A. Haukaas, L. A. Akslen, *Clin. Cancer Res.* **2007**, *13*, 7003.

[290] W. Kim, M. Kim, E. Jho, *Biochem. J.* **2013**, *450*, 9.

[291] S. A. Oberlender, R. S. Tuan, *Development* **1994**, *120*.

[292] A. M. Delise, R. S. Tuan, *Dev. Dyn.* **2002**, *225*, 195.

[293] R. S. Tuan, in *J. Bone Jt. Surg. - Ser. A*, **2003**, pp. 137–141.

[294] E. Sadot, I. Simcha, M. Shtutman, A. Ben-Ze'ev, B. Geiger, *Proc. Natl. Acad. Sci. U. S. A.* **1998**, *95*, 15339.

[295] D.-A. Yu, J. Han, B.-S. Kim, *Int. J. stem cells* **2012**, *5*, 16.

[296] L. Bian, M. Guvendiren, R. L. Mauck, J. A. Burdick, *Proc. Natl. Acad. Sci. U. S. A.* **2013**, *110*.

[297] S. L. Vega, M. Kwon, R. L. Mauck, J. A. Burdick, *Ann. Biomed. Eng.* **2016**, *44*, 1921.

[298] M. Y. Kwon, S. L. Vega, W. M. Gramlich, M. Kim, R. L. Mauck, J. A. Burdick, *Adv. Healthc. Mater.* **2018**, 1701199.

[299] J. Fang, B. K. Hall, *Int. J. Dev. Biol.* **1999**, *43*, 335.

[300] F. P. Barry, J. M. Murphy, *Int. J. Biochem. Cell Biol.* **2004**, *36*, 568.

[301] F. Barry, R. E. Boynton, B. Liu, J. M. Murphy, *Exp. Cell Res.* **2001**, *268*, 189.

[302] N. Jaiswal, S. E. Haynesworth, A. I. Caplan, S. P. Bruder, *J. Cell. Biochem.* **1997**, *64*, 295.

[303] S. Fatherazi, D. Matsa-Dunn, B. L. Foster, R. B. Rutherford, M. J. Somerman, R. B. Presland, *J. Dent. Res.* **2009**, *88*, 39.

[304] H. Tada, E. Nemoto, B. L. Foster, M. J. Somerman, H. Shimauchi, *Bone* **2011**, *48*, 1409.

[305] F. Langenbach, J. Handschel, *Effects of Dexamethasone, Ascorbic Acid and β-Glycerophosphate on the Osteogenic Differentiation of Stem Cells in Vitro*, **2013**.

[306] G. Xiao, R. Gopalakrishnan, D. Jiang, E. Reith, M. D. Benson, R. T. Franceschi, *J. Bone Miner. Res.* **2002**, *17*, 101.

[307] D. Hong, H.-X. Chen, Y. Xue, D.-M. Li, X.-C. Wan, R. Ge, J.-C. Li, *J. Steroid Biochem. Mol. Biol.* **2009**, *116*, 86.

[308] J. E. Phillips, C. A. Gersbach, A. M. Wojtowicz, A. J. García, *J. Cell Sci.* **2006**, *119*, 581.

[309] N. Indrawattana, G. Chen, M. Tadokoro, L. H. Shann, H. Ohgushi, T. Tateishi, J. Tanaka, A. Bunyaratvej, *Biochem. Biophys. Res. Commun.* **2004**, *320*, 914.

[310] H. Messai, Y. Duchossoy, A.-M. Khatib, A. Panasyuk, D. R. Mitrovic, *Mech. Ageing Dev.* **2000**, *115*, 21.

[311] N. Turner, R. Grose, *Nat. Rev. Cancer* **2010**, *10*, 116.

[312] T. Ito, R. Sawada, Y. Fujiwara, T. Tsuchiya, *Cytotechnology* **2008**, *56*, 1.

[313] H. H. Luu, W.-X. Song, X. Luo, D. Manning, J. Luo, Z.-L. Deng, K. A. Sharff, A. G. Montag, R. C. Haydon, T.-C. He, *J. Orthop. Res.* **2007**, *25*, 665.

[314] V. Devescovi, E. Leonardi, G. Ciapetti, E. Cenni, *Chir. Organi Mov.* **2008**, *92*, 161.

[315] L. A. Fortier, J. U. Barker, E. J. Strauss, T. M. McCarrel, B. J. Cole, *Clin. Orthop. Relat. Res.* **2011**, *469*, 2706.

[316] J. M. Ross, in *Front. Tissue Eng.*, Pergamon, **1998**, pp. 15–27.

[317] S.-H. Kim, J. Turnbull, S. Guimond, *J. Endocrinol.* **2011**, *209*, 139.

[318] S. A. Baeurle, M. G. Kiselev, E. S. Makarova, E. A. Nogovitsin, *Polymer (Guildf).* **2009**, *50*, 1805.

[319] H. Zhu, N. Mitsuhashi, A. Klein, L. W. Barsky, K. Weinberg, M. L. Barr, A. Demetriou, G. D. Wu, *Stem Cells* **2006**, *24*, 928.

[320] V. N. Patel, D. L. Pineda, M. P. Hoffman, *Matrix Biol.* **2017**, *57–58*, 311.

[321] S. Ricard-Blum, F. Ruggiero, *Pathol. Biol.* **2005**, *53*, 430.

[322] S. M. Mithieux, A. S. Weiss, *Adv. Protein Chem.* **2005**, *70*, 437.

[323] J. H. Miner, P. D. Yurchenco, *Annu. Rev. Cell Dev. Biol.* **2004**, *20*, 255.

[324] P. Singh, C. Carraher, J. E. Schwarzbauer, *Annu. Rev. Cell Dev. Biol.* **2010**, *26*, 397.

[325] A. S. Rowlands, P. A. George, J. J. Cooper-White, *Am. J. Physiol. Physiol.* **2008**, *295*, C1037.

[326] G. M. Harris, M. E. Piroli, E. Jabbarzadeh, *Adv. Funct. Mater.* **2014**, *24*, 2396.

[327] J. H. Wen, L. G. Vincent, A. Fuhrmann, Y. S. Choi, K. C. Hribar, H. Taylor-Weiner, S. Chen, A. J. Engler, *Nat. Mater.* **2014**, *13*, 979.

[328] M. Breitbach, T. Bostani, W. Roell, Y. Xia, O. Dewald, J. M. Nygren, J. W. U. Fries, K. Tiemann, H. Bohlen, J. Hescheler, et al., *Blood* **2007**, *110*, 1362.

[329] J. Du, X. Chen, X. Liang, G. Zhang, J. Xu, L. He, Q. Zhan, X.-Q. Feng, S. Chien, C. Yang, *Proc. Natl. Acad. Sci. U. S. A.* **2011**, *108*, 9466.

[330] Y.-R. V Shih, K.-F. Tseng, H.-Y. Lai, C.-H. Lin, O. K. Lee, *J. Bone Miner. Res.* **2011**, *26*, 730.

[331] M. Akhmanova, E. Osidak, S. Domogatsky, S. Rodin, A. Domogatskaya, *Stem Cells Int.* **2015**, *2015*, 1.

[332] A. R. Cameron, J. E. Frith, G. A. Gomez, A. S. Yap, J. J. Cooper-White, *Biomaterials* **2014**, *35*, 1857.

[333] A. R. Cameron, J. E. Frith, J. J. Cooper-White, *Biomaterials* **2011**, *32*, 5979.

[334] O. Chaudhuri, L. Gu, M. Darnell, D. Klumpers, S. A. Bencherif, J. C. Weaver, N. Huebsch, D. J. Mooney, *Nat. Commun.* **2015**, *6*, 6365.

[335] H. Lee, L. Gu, D. J. Mooney, M. E. Levenston, O. Chaudhuri, *Nat. Mater.* **2017**, *16*, 1243.

[336] O. Chaudhuri, *Biomater. Sci.* **2017**, *5*, 1480.

[337] N. Huebsch, P. R. Arany, A. S. Mao, D. Shvartsman, O. A. Ali, S. A. Bencherif, J. Rivera-Feliciano, D. J. Mooney, *Nat. Mater.* **2010**, *9*, 518.

[338] R. J. Wade, J. A. Burdick, *Mater. Today* **2012**, *15*, 454.

[339] M. Ventre, P. Netti, M. Ventre, P. A. Netti, *Gels* **2016**, *2*, 12.

[340] Stevens MM, George JH, *Science (80-. ).* **2005**, *310*, 1135.

[341] M. J. P. Biggs, R. G. Richards, S. McFarlane, C. D. W. Wilkinson, R. O. C. Oreffo, M. J. Dalby, *J. R. Soc. Interface* **2008**, *5*, 1231.

[342] O. Zinger, G. Zhao, Z. Schwartz, J. Simpson, M. Wieland, D. Landolt, B. Boyan, *Biomaterials* **2005**, *26*, 1837.

[343] S. L. Vega, V. Arvind, P. Mishra, J. Kohn, N. Sanjeeva Murthy, P. V. Moghe, *Acta Biomater.* **2018**, *76*, 21.

[344] S. R. Caliari, J. A. Burdick, *Nat. Methods* **2016**, *13*, 405.

[345] S. Varghese, J. H. Elisseeff, *Adv. Polym. Sci.* **2006**, *203*, 95.

[346] A. D. Rape, M. Zibinsky, N. Murthy, S. Kumar, S. Chien, *Nat. Commun.* **2015**, *6*, 8129.

[347] R. A. Marklein, J. A. Burdick, *Soft Matter* **2010**, *6*, 136.

[348] X. Tong, J. Jiang, D. Zhu, F. Yang, *ACS Biomater. Sci. Eng.* **2016**, *2*, 845.

[349] S.-H. Lee, J. J. Moon, J. L. West, *Biomaterials* **2008**, *29*, 2962.

[350] S. J. Bryant, J. L. Cuy, K. D. Hauch, B. D. Ratner, *Biomaterials* **2007**, *28*, 2978.

[351] S. Suri, C. E. Schmidt, *Acta Biomater.* **2009**, *5*, 2385.

[352] R. Sunyer, A. J. Jin, R. Nossal, D. L. Sackett, *PLoS One* **2012**, *7*, e46107.

[353] L. G. Vincent, Y. S. Choi, B. Alonso-Latorre, J. C. del Álamo, A. J. Engler, *Biotechnol. J.* **2013**, *8*, 472.

[354] J. R. Tse, A. J. Engler, *PLoS One* **2011**, *6*, e15978.

[355] C. C. Lin, C. S. Ki, H. Shih, *J. Appl. Polym. Sci.* **2015**, *132*, 1.

[356] M. M. J. Caron, P. J. Emans, M. M. E. Coolsen, L. Voss, D. A. M. Surtel, A. Cremers, L. W. van Rhijn, T. J. M. Welting, *Osteoarthr. Cartil.* **2012**, *20*, 1170.

[357] H. Baharvand, S. M. Hashemi, S. Kazemi Ashtiani, A. Farrokhi, *Int. J. Dev. Biol.* **2006**, *50*, 645.

[358] X. -F. Tian, B. -C. Heng, Z. Ge, K. Lu, A. J. Rufaihah, V. T. -W. Fan, J. -F. Yeo, T. Cao, *Scand. J. Clin. Lab. Invest.* **2008**, *68*, 58.

[359] M. Nii, J. H. Lai, M. Keeney, L.-H. Han, A. Behn, G. Imanbayev, F. Yang, *Acta Biomater.* **2013**, *9*, 5475.

[360] Y. Jiang, J. Chen, C. Deng, E. J. Suuronen, Z. Zhong, *Biomaterials* **2014**, *35*, 4969.

[361] A. S. Caldwell, G. T. Campbell, K. M. T. Shekiro, K. S. Anseth, *Adv. Heal. Care Mater.* **2017**, *6*, 1.

[362] X. Zhao, S. Liu, L. Yildirimer, H. Zhao, R. Ding, H. Wang, W. Cui, D. Weitz, *Adv. Funct. Mater.* **2016**, *26*, 2809.

[363] F. Li, V. X. Truong, H. Thissen, J. E. Frith, J. S. Forsythe, *ACS Appl. Mater. Interfaces* **2017**, *9*, 8589.

[364] F. Li, V. X. Truong, P. Fisch, C. Levinson, V. Glattauer, M. Zenobi-wong, H. Thissen, J. S. Forsythe, J. E. Frith, *Acta Biomater.* **2018**, *77*, 48.

[365] D. G. Anderson, S. Levenberg, R. Langer, *Nat. Biotechnol.* **2004**, *22*, 863.

[366] S. Sharma, M. Floren, Y. Ding, K. R. Stenmark, W. Tan, S. J. Bryant, *Biomaterials* **2017**, *143*, 17.

[367] A. Dolatshahi-Pirouz, M. Nikkhah, A. K. Gaharwar, B. Hashmi, E. Guermani, H. Aliabadi, G. Camci-Unal, T. Ferrante, M. Foss, D. E. Ingber, et al., *Sci. Rep.* **2015**, *4*, 3896.

[368] C. J. Flaim, S. Chien, S. N. Bhatia, *Nat. Methods* **2005**, *2*, 119.

[369] H. V Unadkat, M. Hulsman, K. Cornelissen, B. J. Papenburg, R. K. Truckenmüller, A. E. Carpenter, M. Wessling, G. F. Post, M. Uetz, M. J. T. Reinders, et al., *Proc. Natl. Acad. Sci. U. S. A.* **2011**, *108*, 16565.

[370] A. Ranga, S. Gobaa, Y. Okawa, K. Mosiewicz, A. Negro, M. P. Lutolf, *Nat. Commun.* **2014**, *5*, 1909.

[371] V. Z. Beachley, M. T. Wolf, K. Sadtler, S. S. Manda, H. Jacobs, M. R. Blatchley, J. S. Bader, A. Pandey, D. Pardoll, J. H. Elisseeff, *Nat. Methods* **2015**, *12*, 1197.

[372] T. J. Klein, J. Malda, R. L. Sah, D. W. Hutmacher, *Tissue Eng. Part B Rev.* **2009**, *15*, 143.

[373] I. Louzao, B. Koch, V. Taresco, L. Ruiz-Cantu, D. J. Irvine, C. J. Roberts, C. Tuck, C. Alexander, R. Hague, R. Wildman, et al., *ACS Appl. Mater. Interfaces* **2018**, *10*, 6841.

[374] P. Occhetta, M. Centola, B. Tonnarelli, A. Redaelli, I. Martin, M. Rasponi, *Sci. Rep.* **2015**, *5*, 10288.

[375] A. M. Hilderbrand, E. M. Ovadia, M. S. Rehmann, P. M. Kharkar, C. Guo, A. M. Kloxin, *Curr. Opin. Solid State Mater. Sci.* **2016**, *20*, 212.

[376] C. Yang, M. W. Tibbitt, L. Basta, K. S. Anseth, *Nat. Mater.* **2014**, *13*, 645.

[377] J. A. Shadish, G. M. Benuska, C. A. DeForest, *Nat. Mater.* **2019**, 1.

[378] P. M. Gawade, J. A. Shadish, B. A. Badeau, C. A. DeForest, *Adv. Mater.* **2019**, *31*, 1902462.

[379] F. AJ, G. JF, K. NN, *Exp. Hematol.* **1976**, *4*, 267.

[380] A. Halim, A. D. Ariyanti, Q. Luo, G. Song, *Stem Cell Rev. Reports* **2020**, *16*, 661.

[381] C. M. Kolf, E. Cho, R. S. Tuan, *Arthritis Res. Ther. 2007 91* **2007**, *9*, 1.

[382] S. W. Wong, S. Lenzini, M. H. Cooper, D. J. Mooney, J. W. Shin, *Sci. Adv.* **2020**, *6*, DOI 10.1126/sciadv.aaw0158.

[383] Y.-K. Wang, C. S. Chen, *J. Cell. Mol. Med.* **2013**, *17*, 823.

[384] E. K. F. Yim, E. M. Darling, K. Kulangara, F. Guilak, K. W. Leong, *Biomaterials* **2010**, *31*, 1299.

[385] R. Siddappa, R. Licht, C. van Blitterswijk, J. de Boer, *J. Orthop. Res.* **2007**, *25*, 1029.

[386] N. Ozeki, T. Muneta, H. Koga, Y. Nakagawa, M. Mizuno, K. Tsuji, Y. Mabuchi, C. Akazawa, E. Kobayashi, K. Matsumoto, et al., *Osteoarthr. Cartil.* **2016**, *24*, 1061.

[387] G. M. de Peppo, I. Marcos-Campos, D. J. Kahler, D. Alsalman, L. Shang, G. Vunjak-Novakovic, D. Marolt, *Proc. Natl. Acad. Sci.* **2013**, *110*, 8680.

[388] M. McGrath, E. Tam, M. Sladkova, A. AlManaie, M. Zimmer, G. M. de Peppo, *Stem Cell Res. Ther. 2019 101* **2019**, *10*, 1.

[389] B. Jiang, L. Yan, X. Wang, E. Li, K. Murphy, K. Vaccaro, Y. Li, R.-H. Xu, *Stem Cells* **2019**, *37*, 572.

[390] D. Paull, A. Sevilla, H. Zhou, A. K. Hahn, H. Kim, C. Napolitano, A. Tsankov, L. Shang, K. Krumholz, P. Jagadeesan, et al., *Nat. Methods 2015 129* **2015**, *12*, 885.

[391] M. Sladkova, M. Palmer, C. Öhman, J. Cheng, S. Al-Ansari, M. Saad, H. Engqvist, G. M. de Peppo, *J. Tissue Eng. Regen. Med.* **2018**, *12*, 715.

[392] F.-J. Lv, R. S. Tuan, K. M. C. Cheung, V. Y. L. Leung, *Stem Cells* **2014**, *32*, 1408.

[393] R. U, C. I, P. V, H. M, J. G, M. I, M. R, A. J, *Stem cell Rev. reports* **2009**, *5*, 378.

[394] G. M. De Peppo, S. Svensson, M. Lennerås, J. Synnergren, J. Stenberg, R. Strehl, J. Hyllner, P. Thomsen, C. Karlsson, G. M. de Peppo, et al., *Tissue Eng. - Part A* **2010**, *16*, 2161.

[395] G. Halder, S. Dupont, S. Piccolo, *Nat. Rev. Mol. Cell Biol.* **2012**, *13*, 591.

[396] A. Islam, T. Mbimba, M. Younesi, O. Akkus, *Acta Biomater.* **2017**, *58*, 244.

[397] C. Y. Tay, Y. L. Wu, P. Cai, N. S. Tan, S. S. Venkatraman, X. Chen, L. P. Tan, *NPG Asia Mater.* **2015**, *7*, e199.

[398] *Use of Laboratory Animals in Biomedical and Behavioral Research*, National Academies Press, **1988**.

[399] E. Insuasti-Cruz, V. Suárez-Jaramillo, K. A. Mena Urresta, K. O. Pila-Varela, X. Fiallos-Ayala, S. A. Dahoumane, F. Alexis, *Adv. Healthc. Mater.* **2022**, *11*, DOI 10.1002/adhm.202101389.

[400] D. W. Green, G. S. Watson, J. A. Watson, D. J. Lee, J. M. Lee, H. S. Jung, *Acta Biomater.* **2016**, *42*, 33.

[401] A. C. Bilirgen, M. Toker, S. Odabas, A. K. Yetisen, B. Garipcan, S. Tasoglu, *ACS Biomater. Sci. Eng.* **2021**, *7*, 926.

[402] S. Iravani, R. S. Varma, *Green Chem.* **2019**, *21*, 4839.

[403] D. J. Modulevsky, C. M. Cuerrier, A. E. Pelling, *PLoS One* **2016**, *11*, DOI 10.1371/journal.pone.0157894.

[404] N. Contessi Negrini, N. Toffoletto, S. Farè, L. Altomare, *Front. Bioeng. Biotechnol.* **2020**, *8*, 723.

[405] D. J. Modulevsky, C. Lefebvre, K. Haase, Z. Al-Rekabi, A. E. Pelling, *PLoS One* **2014**, *9*, 97835.

[406] Y. W. Cheng, D. J. Shiwarski, R. L. Ball, K. A. Whitehead, A. W. Feinberg, *ACS Biomater. Sci. Eng.* **2020**, *6*, 3046.

[407] J. R. Gershlak, S. Hernandez, G. Fontana, L. R. Perreault, K. J. Hansen, S. A. Larson, B. Y. K. Binder, D. M. Dolivo, T. Yang, T. Dominko, et al., *Biomaterials* **2017**, *125*, 13.

[408] A. Salehi, M. A. Mobarhan, J. Mohammadi, H. Shahsavarani, M. A. Shokrgozar, A. Alipour, *Gene* **2020**, *757*, 144852.

[409] R. Mcbeath, D. M. Pirone, C. M. Nelson, K. Bhadriraju, C. S. Chen, *Cell Shape, Cytoskeletal Tension, and RhoA Regulate Stem Cell Lineage Commitment Several Studies Have Noted That Changes in Cell Shape Themselves Can Alter the Differentiation of Precommitted Mesenchymal Lineages. Spiegelman and Ginty (1983)*, **2004**.

[410] K. Kimura, M. Ito, M. Amano, K. Chihara, Y. Fukata, M. Nakafuku, B. Yamamori, J. Feng, T. Nakano, K. Okawa, et al., *Science (80-. ).* **1996**, *273*, 245.

[411] K. A. Kilian, B. Bugarija, B. T. Lahn, M. Mrksich, *Proc. Natl. Acad. Sci. U. S. A.* **2010**, *107*, 4872.

[412] B. C. Heng, X. Zhang, D. Aubel, Y. Bai, X. Li, Y. Wei, M. Fussenegger, X. Deng, *Front. Cell Dev. Biol.* **2020**, *8*, DOI 10.3389/fcell.2020.00735.

[413] C. Chen, Y. Zhu, R. Wang, Y. Han, H. Zhou, *J. Healthc. Eng.* **2022**, *2022*, 1.

[414] X. Cun, L. Hosta-Rigau, *Nanomaterials* **2020**, *10*, 2070.

[415] M. J. Dalby, N. Gadegaard, R. Tare, A. Andar, M. O. Riehle, P. Herzyk, C. D. W. Wilkinson, R. O. C. Oreffo, *Nat. Mater.* **2007**, *6*, 997.

[416] P. Kasten, I. Beyen, P. Niemeyer, R. Luginbühl, M. Bohner, W. Richter, *Acta Biomater.* **2008**, *4*, 1904.

[417] P. Y. Wang, W. T. Li, J. Yu, W. B. Tsai, *J. Mater. Sci. Mater. Med.* **2012**, *23*, 3015.

[418] Y. S. Lewis, *Spices and Herbs for the Food Industry*, Food Trade Press, **1984**.

[419] H. B. Sowbhagya, *Crit. Rev. Food Sci. Nutr.* **2014**, *54*, 389.

[420] R. Crang, S. Lyons-Sobaski, R. Wise, *Plant Anat.* **2018**, 181.

[421] J. C. Thimm, D. J. Burritt, W. A. Ducker, L. D. Melton, *Planta* **2000**, *212*, 25.

[422] A. Carlsbecker, Y. Helariutta, G. Coupland, S. P. Monguio, *Curr. Opin. Plant Biol.* **2005**, *8*, 512.

[423] B. R. MacIntosh, P. F. Gardiner, A. J. McComas, *Skeletal Muscle: Form and Function*, Human Kinetics, **2006**.

[424] P. Milovanovic, Z. Vukovic, • Djordje Antonijevic, D. Djonic, • Vladimir Zivkovic, S. Nikolic, M. Djuric, *J. Mater. Sci. Mater. Med.* **2017**, *28*, 71.

# Appendix A

## Hydrogel Screening Approaches for Bone and Cartilage Tissue Regeneration

**Note:** Sections of this chapter have been reproduced from the following publication with permissions:

**Benmassaoud, M. M.*, Gultian, K. A.*, DiCerbo, M.*, & Vega, S. L. (2020).** Hydrogel screening approaches for bone and cartilage tissue regeneration. *Annals of the New York Academy of Sciences*, *1460*(1), 25–42.

* Authors contributed equally

## A.1 Abstract

The ECM of bone and cartilage presents stem cells with a dynamic and complex array of biochemical and biomechanical signals that regulate proliferation and differentiation into bone and cartilage tissue-producing cells. Due to the multitude of signals present in these ECM, it is challenging to develop biomaterials that accurately recapitulate bone and cartilage tissues, thereby limiting the ability to present cells with multiple biochemical and biomechanical factors for enhanced biomaterial-induced osteogenic and chondrogenic differentiation. Conventional techniques to evaluate stem cell responses to engineered materials are laborious and time-consuming and high-throughput screening techniques can address these limitations. This review overviews developmental microenvironments and signals present in bone and cartilage ECM, with a focus on applying hydrogel-based screening approaches to identify biomaterial microenvironments that promote stem cell-mediated bone and cartilage tissue regeneration.

## A.2 Introduction

Musculoskeletal tissue engineering (MTE) seeks to develop biological substitutes to repair or restore bone, cartilage, and connective tissues. MTE is a specialized form of tissue engineering, which uses scaffolds, cells, and bioactive factors to create functional tissue substitutes.[266] Tissue engineering emerged from the need for adequate medical interventions to treat tissue loss and organ failure.[267] One of the earliest examples of tissue engineering dates back to 1933, when Bisceglie implanted a membrane containing mouse tumor cells into the abdominal cavity of a pig, and found that the membrane protected tumor cells from immune responses to the implant.[268] Since then, due to advances in cell biology, material science, and medicine, tremendous progress has been made in using cells and scaffolds to create functional musculoskeletal tissues.[269,270]

Engineering biomaterials with properties that promote bone and cartilage regeneration is gaining high interest within MTE, particularly those that allow for guided mesenchymal stem cell (MSC) differentiation. MSCs are an attractive stem cell source for MTE because they can be autologous (patient-derived) and have the potential to differentiate into cells present in musculoskeletal tissues.[271] To harness the power of stem cells, biomaterials can be designed with differentiation-inducing signals present *in vivo*. Although tissue engineering has seen rapid growth in developing increasingly complex biomaterials, currently it is not possible to engineer environments that present cells with the spatial and temporal complexity of signals in the ECM of musculoskeletal tissues. This limits the role of biomaterials in regenerative medicine, since the ECM provides structural support and signals necessary for development, repair, and homeostasis.[272] As a result, biomaterials are not representative of native ECMs and the cooperative role of multifactorial stimuli on stem cell differentiation has not been fully realized.

Techniques to rapidly investigate the synergistic effects of multiple biochemical and biomechanical factors on stem cell differentiation are critical for designing biomaterials that promote bone and cartilage regeneration. Although long bone fractures typically heal with established medical interventions, larger fractures fail to do so. Endogenous cartilage repair is extremely limited and the standard surgical intervention for large cartilage defects is arthroplasty, which fails to restore native cartilage properties and function.[273] Alternative stem cell-based approaches to restore cartilage and bone tissue could address current shortcomings in clinical interventions. Taken together, the goals of this review are to: 1) provide an overview of bone and cartilage ECM, 2) summarize biophysical and biochemical ECM signals that influence osteogenic and chondrogenic differentiation of MSCs, and 3) highlight high-throughput hydrogel-based screening techniques that can be applied to design biomaterials suitable for robust bone and cartilage formation. This review is not meant to be comprehensive and focus is given to signals present in bone and cartilage ECM that have been extensively explored in biomaterials as scaffolds for osteogenic and chondrogenic MSC differentiation.

### A.3 Bone and Cartilage ECM

*In vivo*, stem cell behavior is guided by interactions with neighboring cells and dynamic signals presented by their residing ECM. The ECM provides resident stem cells with structural support and a complex milieu of biochemical and biomechanical signals that collectively regulate stemness, proliferation, and differentiation.[274] These interactions are highly dynamic and changes to the ECM from prolonged use, aging, injury, or disease can have profound effects on stem cell growth and function. A major goal of MTE is to develop biomaterials that act as a scaffolding material and provide signals that instruct stem cells to differentiate into cell types present in musculoskeletal tissues. Although a common approach is to investigate how signals present in mature tissues can be applied to biomaterials, there are a growing number of studies that investigate the impact that developmental signals have on stem cell differentiation.

During embryonic limb development, mesenchymal progenitor cells aggregate and form condensations.[275,276] This environment is rich in cell-cell interactions and cells in the condensations differentiate into chondrocytes which form a cartilaginous core. As cells proliferate and secrete cartilage extracellular components, the cartilaginous core grows and begins to take the shape of endochondral bone.[276,277] A periosteal bone collar forms and the cartilage model is invaded by osteoblast progenitor cells, initiating the formation of the primary ossification center, resulting in chondrocyte hypertrophy and vascularization. The secondary centers of ossification then form, which are separated by the growth plate, which is responsible for longitudinal bone growth.[277] At the proximal ends, the articular-epiphyseal growth cartilage (AEGC) shapes the epiphysis and in mature bone, the growth plate disappears, the AEGC is replaced by bone, and the remaining articular cartilage is at the proximal ends of the bone.[278] The development of articular cartilage and endochondral bone is summarized in Figure A.1A.[277]

Mature bone and cartilage ECM have distinct characteristics. Osteoblasts, osteoclasts, and osteocytes are the three main cells types in bone. Osteoblasts are derived from MSCs and are bone-forming cells that line bone surfaces or mature and form into osteocytes, which are surrounded by bone tissue and help regulate growth, repair, and breakdown of bone.[233] Osteoclasts on the other hand are bone resorptive cells that are derived from osteoclast progenitor cells.[279] Figure A.1B shows a simplified schematic of the dynamic cellular anatomy of the bone ECM.[279] Once injured, bones have the intrinsic ability to heal due to cellular signaling between these cell types and dense vascularization.[218] In contrast to bone, cartilage lacks this regenerative ability, largely due to the avascular nature of cartilage tissues.[280] Chondrocytes are resident cells in cartilage tissue and secrete cartilage ECM, primarily consisting of type II collagen, proteoglycans, and HA (Figure A.1C).[281] Despite its inability to rapidly heal, articular cartilage is highly durable and can withstand a lifetime of complex and dynamic compression events.[282]

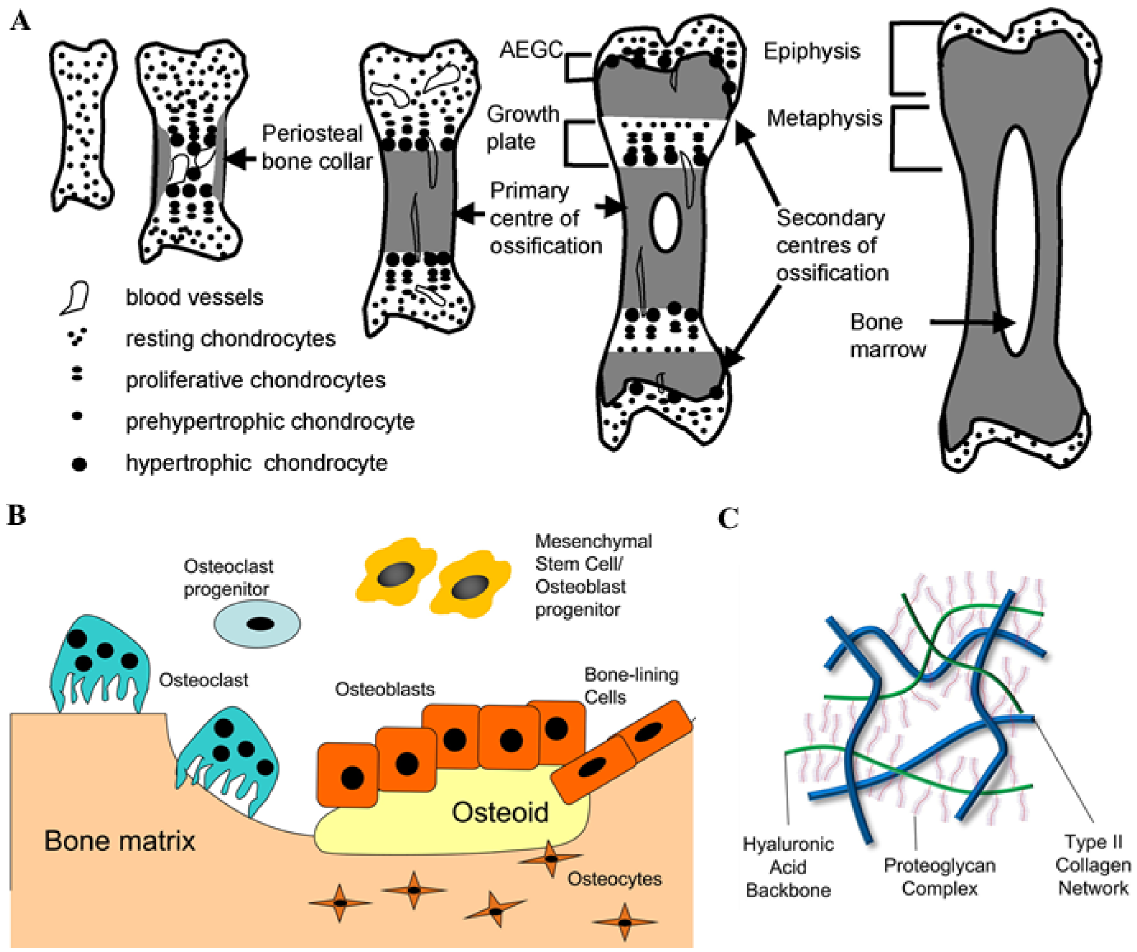

*Figure A. 1.* Overview of bone and cartilage ECM. **(A)** Endochondral ossification model shows the development of articular cartilage and endochondral bone during embryonic limb development.[277] **(B)** Cellular anatomy of the bone ECM.[279] **(C)** Main ECM components of articular cartilage tissue.[281]

## A.4 ECM-Inspired Factors that Influence Bone and Cartilage Differentiation

Developmental microenvironments and the ECM of bone and cartilage contain a plethora of signals that can stimulate MSCs to differentiate into osteoblasts and chondrocytes. These factors can be categorized as cell-cell interactions and interactions with biophysical and biochemical signals present in the ECM. *Cell-Cell Interactions* in the form of direct cell-cell communication through cadherins are present in the early stages of endochondral ossification and are crucial for chondrocyte differentiation.[283] The ECM controls the release and presentation of several *Soluble Signals* that have been identified and are routinely used for osteogenic and chondrogenic differentiation in MSC cultures.[284] *Cell-Matrix Interactions* also occur between cells and surrounding ECM proteins that can be categorized as glycosaminoglycans (complex polysaccharides with amino groups) and fibrous proteins (elongated polypeptide chains). *Physical Stimuli* including matrix stiffness and mechanical loading can also act as regulators of mechanotransduction-mediated MSC lineage commitment.[70,285] Due to the various ECM signals that regulate stem cell lineage commitment (Figure A.2),[274] tools to identify the optimal content and concentration of cell-cell and cell-ECM signals for osteogenic and chondrogenic differentiation would result in a more robust class of biomaterials for bone and cartilage tissue regeneration.

### *A.4.1 Cell-Cell Interactions*

Physical contact between cells is mediated by integrins, including cell adhesion molecules (CAMs).[286] Cadherins are a type of CAM which participate in cell adhesion, and form adherens junctions that allow for communication between cells when connected.[287–289] Cadherins contain an extracellular binding domain that mediate cell-cell interactions in a calcium dependent manner, and an intracellular domain that is implicated in intracellular signaling pathways, including β-catenin signaling.[287] Indeed, β-catenin is important for cell-cell junction formation and Wnt signaling.[290] N-cadherin is a cadherin that is implicated in directing cell-cell interactions during embryonic limb development.[291–293] Once the extracellular domain of N-cadherin is active, the cytoplasmic binding domain forms a complex with β-catenin, thus localizing β-catenin to the membrane and protecting it from degradation, allowing for its nuclear localization and subsequent activation of several pathways.[294]

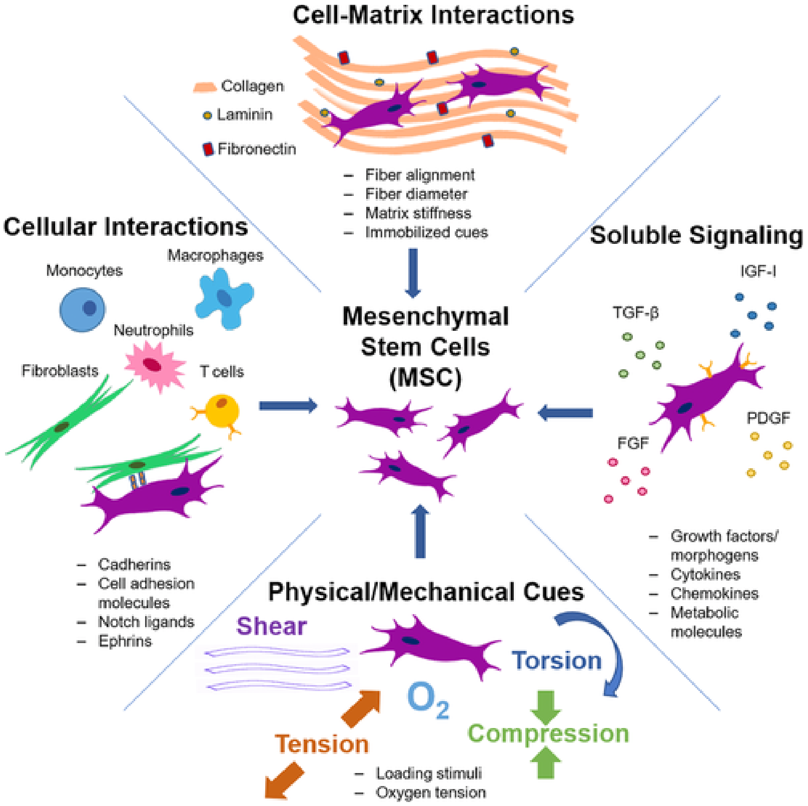

*Figure A. 2.* Schematic summarizing ECM signals that can regulate MSC behavior.[274]

N-cadherin signaling is critical for cartilage differentiation, as chondrogenesis relies heavily on cell-cell interactions.[295] With recent advances in bioactive materials and peptide synthesis, peptides that feature N-cadherin-like binding activity have been designed and used to investigate the effects of cell-cell interactions on chondrogenic signaling and differentiation. Bian et al. showed that an N-cadherin peptides enhance chondrogenic differentiation of MSCs encapsulated in HA hydrogels.[296] Vega and coworkers reported that N-cadherin peptides increase β-catenin signaling and Kwon et al. recently showed that the transient presentation of N-cadherin peptides does not enhance chondrocyte differentiation.[297,298] During developmental mesenchymal condensation, neural cell adhesion molecules (N-CAM) also regulate cell-cell interactions that precede the formation of long bones.[275] Interestingly, although cells featured increased N-CAM expression during mesenchymal condensation, its role in chondrogenic differentiation is not clearly established.[299]

### *A.4.2 Soluble Signals*

MSCs cultured *in vitro* can be differentiated into chondrocytes and osteoblasts by adding soluble factors to culture media.[300] MSCs will undergo chondrogenic differentiation *in vitro* if they are in a pellet culture (3D, high cell-cell contact), in serum-free medium supplemented with a member of the transforming growth factor beta (TGF-β) superfamily of cytokines.[300] With this culture setup, MSCs lose their fibroblastic morphology and commence the expression of cartilage-specific ECM components. Within the TGF-β superfamily, TGF-β1, TGF-β2, and TGF-β3 all act as chondroinductive soluble factors, with the most efficacious response coming from TGF-β2, and TGF-β3.[301] In the presence of TGF-β3, MSCs synthesize aggrecan, type II collagen, and other cartilage ECM components present in native articular cartilage.[301]

Osteogenic differentiation can be achieved by culturing MSCs on 2D substrates with cell culture media (e.g., Minimum Essential Medium and 10% Fetal Bovine Serum) supplemented with β-glycerophosphate, ascorbic acid, and dexamethasone.[302] MSCs under these conditions adopt an osteoblastic morphology, an upregulation of alkaline phosphatase, and after at least two weeks in culture deposit a calcium-rich mineralized

ECM. The transition from a naïve MSC to a differentiated osteoblast requires critical steps resulting from these soluble factors. For instance, β-glycerophosphate acts as a signaling molecule that stimulates the expression of several osteogenic-specific genes, including osteopontin (OPN) and bone morphogenetic protein 2 (BMP-2).[303,304] β-glycerophosphate also contains phosphates necessary for cells to produce hydroxylapatite, a mineral present in bone ECM.[305] Ascorbic acid facilitates osteogenic differentiation by increasing type I collagen (ColI) secretion, which stimulates interactions between ColI and α2β1 integrins, leading to downstream mitogen-activated protein kinase (MAPK) signaling and subsequent activation of runt-related transcription factor 2 (Runx2).[306] Dexamethasone is an osteoinductive soluble factor that also regulates Runx2 expression via several mechanisms, including interactions with transcriptional co-activator with PDZ-binding motif (TAZ) and activation of MAPK phosphatase 1 (MKP-1).[307,308]

The bone and cartilage ECM contain additional signaling molecules that stimulate osteogenic and chondrogenic differentiation. The presence and accessibility of these soluble signals are regulated by glycosaminoglycans (GAGs) and fibrous proteins present in the ECM. Some of these soluble factors include insulin-like growth factors (IGFs), fibroblast growth factors (FGFs), and bone morphogenetic proteins (BMPs). IGFs are well-known regulators of energy metabolism and growth, and IGF-1 in combination with TGF-β3 enhances the chondroinductive effects of TGF-β, by transcriptionally regulating cartilage-specific genes.[309,310] FGFs are a class of growth factors that regulate a wide range of cellular functions including proliferation and differentiation.[311] For example, MSCs cultured with FGF-2 expressed increased levels of bone (i.e., alkaline phosphatase, ALP) and cartilage (i.e., type II collagen) specific biomarkers, suggesting that FGF_2 increases the bipotential differentiation potential of MSCs *in vitro*.[312] BMPs are growth factors that have been widely studied for their osteoinductive properties. *In vitro*, BMPs can regulate MSC differentiation into osteoblasts, with BMP-2 and BMP-7 being the most osteoinductive.[313] Growth factors and their role in bone and cartilage ECM repair have also been reviewed previously.[314,315]

### *A.4.3 Cell-Matrix Interactions*

The ECM of musculoskeletal tissues is comprised of two major classes of macromolecules: proteoglycans and fibrous proteins, which include collagen, elastin, laminin, and fibronectin.[272] The ECM serves as a physical scaffold for cells and as a reservoir for growth factors that mediate cell adhesion, growth, differentiation, and migration.[272,316,317] Due to its large influence on cellular behavior, there is tremendous interest in MTE to incorporate ECM components into biomaterials for bone and cartilage tissue formation.

GAGs are complex polysaccharides that make up most of the cartilage ECM and play an important role in many physiological functions. Chondroitin sulfate (CS) is a type of sulfated GAG that provides structural support for surrounding tissues. In cartilage, CS promotes resistance to compression which eventually keeps tissues from developing rheumatoid diseases.[318] HA is a non-sulfated GAG that interacts with cell surface receptors including CD44 and CD168, which induce cell migration and chondrogenic differentiation in MSCs.[296,319] Heparin sulfate (HS) is a linear polysaccharide that attaches to ECM proteins and other protein ligands in the ECM. The main function of HS is the regulation of growth factor binding and signaling on the surface of cells.[320]

In addition to serving as a physical scaffold, the ECM also contains a multitude of cell adhesion proteins which dynamically regulate cell survival, proliferation, and differentiation. Collagen fibrils are a major component of bone and cartilage ECM, constituting up to 30% of the total protein mass of many multicellular organisms.[272] Collagen fibrils are trimeric molecules that provide structural support and serve as a scaffold to which cells and proteins (e.g., laminin, fibronectin) bind.[321] Elastin is an ECM protein that is instrumental in providing elasticity and resilience in different tissues including ligaments, tendons, and cartilage.[322] Laminin is another fibrous protein in the ECM consisting of a large chain of soluble multi-adhesive matrix proteins and constitutes most of the basal lamina.[272] This protein has high binding affinity sites for adhesive proteins found on the surface of cells and to integrins which are found in the plasma membrane.[323] Like laminin, fibronectin has high binding affinity sites for collagen and integrins found on the surface of cells. The primary function of fibronectin is to bind with a wide range of collagen types. Through this attachment, fibronectin can regulate cell shape, and facilitate cell migration and differentiation.[324]

### *A.4.4 Physical Stimuli*

ECM proteins and growth factors have been at the center of research for regulating and inducing stem cell differentiation. More recently, there has been increased interest in investigating the role of physical cues (substrate stiffness, viscoelasticity, culture dimensionality, topography) in regulating stem cell lineage commitment. A seminal study by Engler et al. showed that stem cell differentiation is guided by the stiffness of cell culture substrates. For instance, matrices with stiffness that mimic muscle promote myogenic differentiation in MSCs whereas stiffer matrices that mimic collagenous bone promoted osteogenic differentiation.[70] Since this pivotal study, other groups have also reported that MSC differentiation is stiffness-dependent.[325–327] This phenomenon has been observed *in vivo* as well. For example, in a cardiac transplant, scar tissue of high stiffness MSCs differentiated into osteoblasts rather than cardiac muscle.[328]

The role of matrix stiffness on stem cell differentiation is largely attributed to how cells attach to their substrate. MSCs are adherent cells and were observed to adhere more strongly to stiffer substrates than in softer substrates.[192] Moreover, in soft substrates, MSCs exhibit less spread area and lower proliferation rates. Fewer stress fibers are also observed in soft substrates, which suggests decreased mechanical activity. Integrins and myosins regulate the ability of MSCs to exert pulling forces on the substrate. The combination of these elements allows cells to sense the stiffness of their microenvironment. The amount of integrins on the surface of the cells scales with substrate stiffness such that more surface integrins are present with stiffer substrates.[329] For example, in stiff substrates, integrin α2 was upregulated and resulted in increased osteogenic differentiation of MSCs.[330] Myosin is responsible for focal adhesions which relate to the amount of tension between cells and their substrate, and ultimately to sensing of substrate stiffness.[70] Absence of myosin completely prevents differentiation of MSCs into any cell lineage.[331]

Native ECMs are also inherently viscoelastic, featuring both elastic and viscous properties. Matrix viscoelasticity affects the ability of stem cells to sense their mechanical environment. Studies on the effects of viscous properties of matrices (i.e., loss modulus) on stem cell behavior have shown that viscous properties play an important role in stem cell proliferation, morphology, and lineage commitment.[332,333] An important characteristic of viscoelastic matrices is stress relaxation which affects stem cell behavior. Higher stress relaxation results in increased cell spreading on soft substrate and interestingly this phenomena is less pronounced on stiffer substrates.[334] Stress relaxation also affects MSC differentiation. Faster stress relaxation is important for osteogenic and adipogenic differentiation.[193,335] Techniques for developing and characterizing viscoelastic hydrogels for cell culture are summarized in a recent review by Chaudhuri.[336]

In addition to stiffness and elasticity, culture dimensionality and topography also have a significant impact on stem cell behavior. In 2D environments, cells spread in a stiffness-dependent manner,[70] whereas in 3D environments, in physically and covalently crosslinked hydrogels stem cells tend to adopt a spherical morphology, regardless of stiffness.[337,338] If hydrogels are formed with degradable crosslinkers, cell spreading in 3D is achieved, even at low stiffness that would inhibit spreading on 2D environments.[339] Topographical features ranging from nanoscale to mesoscale can also greatly impact cell behavior, largely due to how topography affects the presentation of sites for adhesion.[340] Surface roughness and surface patterns can have an impact on stem cell morphology and differentiation. For example, Biggs et al. showed that topographical roughness at the nanoscale influences the presence and location of adhesive complexes in human osteoblasts.[341] Additionally, Zinger et al. showed that bone differentiation markers of MG63 osteoblast-like cells varied on different surface microtopographies.[342] More recently, Vega et al. showed that micropatterns created by phase-separation affect MSC fiber alignment, focal adhesions, and osteogenic differentiation.[343]

## A.5 Hydrogel Screening Approaches for Bone and Cartilage Tissue Regeneration

The ECM is composed of macromolecules and growth factors that provide structural strength, matrix resiliency, and support tissue cohesiveness. In addition to acting as a scaffolding material, the ECM also provides signals involved in cell attachment, proliferation, migration, and differentiation. To harness the influential effects of ECM signals on stem cell behavior, biomaterials are designed to recrete key aspects of ECM microenvironments. Due to the multitude of interdependent signals that the ECM presents resident stem cells with, developing high-throughput platforms to screen combinations of these signals could accelerate the discovery of new biomaterials for tissue regeneration. Hydrogels are highly tunable biomaterials that can expose stem cells to a variety of microenvironments.[344,345] Conventional techniques to evaluate the role of ECM components on stem cell differentiation are laborious and time-consuming and therefore it is impractical to systematically investigate the effects of multiple ECM factors on bone and cartilage tissue formation. In this section, *Combinatorial Hydrogels* and *Microgel Microarrays* that can be applied towards identifying optimal combinations of factors for bone and cartilage tissue regeneration will be explored.

### *A.5.1 Combinatorial Hydrogels*

The ECM provides mechanical, chemical, and physical cues to regulate many cellular functions including stem cell differentiation. Due to the complexity of *in vivo* environments, there is growing interest in developing platforms to rapidly screen multiple combinations of ECM components to identify regenerative biomaterials. Hydrogels have been considered due to their biocompatibility and ability to incorporate bioactive signals. Hydrogels can be designed with chemical handles that enable spatial patterning of biochemical and biomechanical signals.[346–348] Specifically, certain chemistries are amenable to the use of light to introduce signals spatially and temporally, via photomasks (discrete patterning) or sliding opaque masks (gradient patterning).

Combinatorial hydrogels are a class of hydrogels that allow for the study of cellular responses to multiple biophysical (e.g., crosslink density) and biochemical (e.g., ligand tethering) signals. Combinatorial hydrogels are typically created in a two-step process, starting with the formation of a base hydrogel, followed by a subsequent chemical modification between unreacted groups in the base hydrogel and crosslinker or peptides to incorporate biophysical or biochemical signals, respectively. Since light is the catalyst for these modifications, a sliding opaque mask can be used to introduce a gradient of a signal, whereas a photomask can pattern signals in discrete regions. Depending on the availability of unreacted groups in the base hydrogel, this process can be repeated several times, resulting in multiple signals presented within one hydrogel. Combinatorial hydrogels can be used to rapidly screen cell responses to combinations of developmental signals or cues present in native tissues. The effects of dimensionality can also be explored since cells can either be cultured atop (2D) or encapsulated within (3D) combinatorial hydrogels.

Using light to spatially pattern signals onto hydrogels was initially explored using laser scanning lithography[349] and photomasks.[350,351] In a seminal study, Marklein et al. used stationary photomasks and sliding opaque masks to create hydrogels with spatially-defined mechanics.[347] Here, HA was modified with methacrylate groups which allowed for stiffness-patterned hydrogels to form via a two-step process: 1) Michael-type addition reaction between a dithiol crosslinker and methacrylates to form a soft hydrogel and 2) radical crosslinking of unreacted methacrylates using a photoinitiator and ultraviolet

(UV) light. Since light is the catalyst for the radical crosslinking step, spatial variations in hydrogel mechanics could be introduced by either applying a photomask that exposes specific hydrogel regions to light, or by applying a sliding mask that controls the amount of light exposure to different regions of the hydrogel (Figure A.3A). MSCs were cultured atop these hydrogels and stiffness-dependent trends in proliferation and cell area were observed. Sunyer et al. employed a similar approach to create stiffness gradients of different steepness by varying the ratio between acrylamide and bis-acrylamide crosslinking in polyacrylamide (PA) hydrogels.[352] PA hydrogels have also been used to investigate MSC migration and differentiation.[353,354]

Hydrogel photopatterning described above uses the same light-induced reaction to both form and pattern hydrogels, which limits patterns to an increase in crosslink density. To introduce biochemical patterns, the use of click reactions has emerged as a technique to form non-patterned hydrogels followed by light-mediated patterning that does not affect mechanics.[355] There are several chemistries that can be employed for this orthogonal approach. For example, Alge et al. used a Tet-Nor inverse electron demand Diels-Alder reaction chemistry to form PEG hydrogels that can be photopatterned with Nor-modified peptides.[60] Gramlich and coworkers used a thiol-Nor chemistry to create HA hydrogels amenable to multiple modifications with mono-thiolated peptides and di-thiol crosslinkers to introduce spatiotemporal biochemical and physical changes, respectively.[167] Using this scheme and an opaque sliding mask, a gradient of mono-thiolated peptide can be formed, such that peptide concentration (fluorescence) corresponds to the amount of light exposure (Figure A.3B).[196]

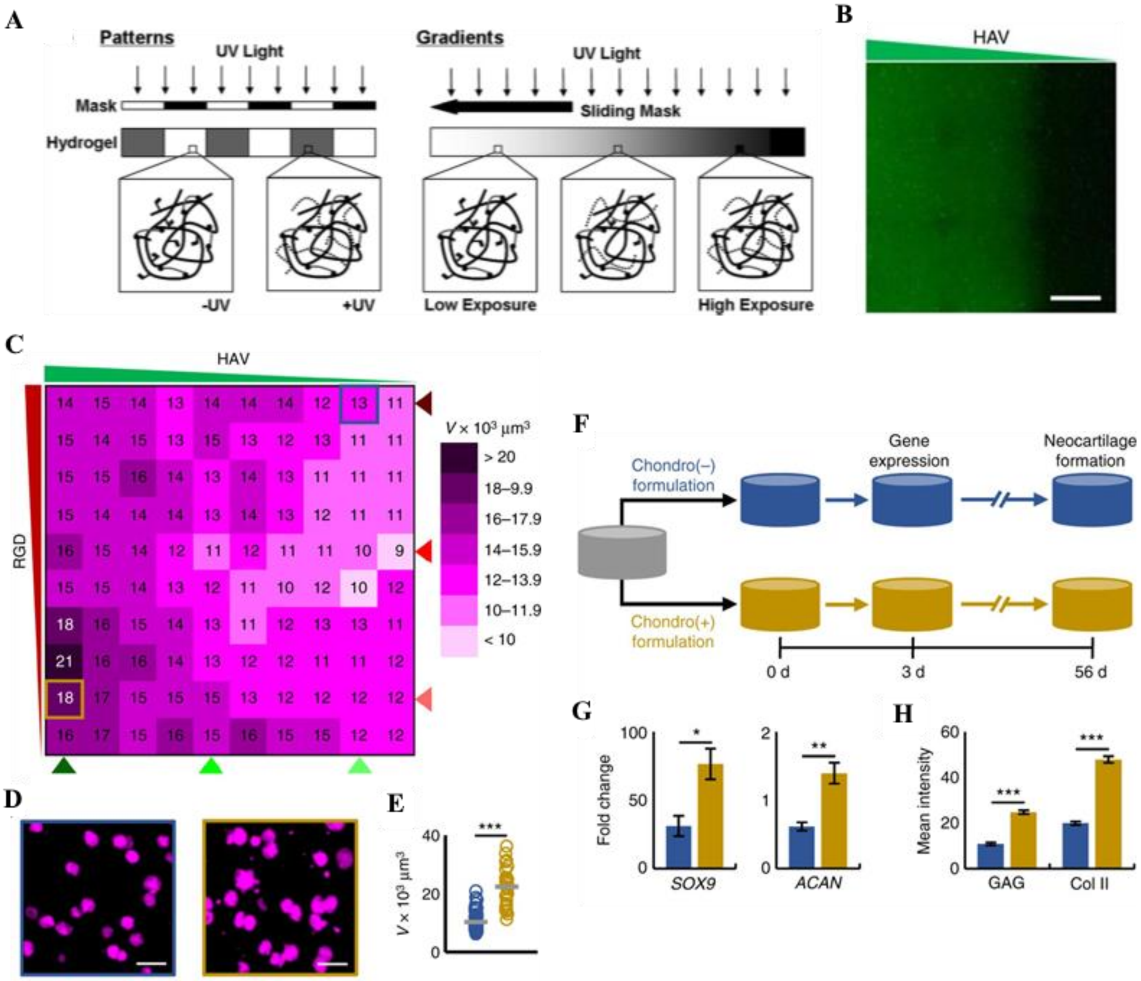

*Figure A. 3.* Examples of combinatorial hydrogels and their applications. **(A)** Hydrogel photopatterning is accomplished by using a stationary photomask or an opaque sliding mask, since patterning only occurs in the presence of light.[347] **(B)** An opaque sliding mask was used to photopattern a fluorescein-labeled thiolated peptide gradient onto a 5 mm hydrogel. **(C)** Heat map analysis of aggrecan produced by encapsulated MSCs in a combinatorial hydrogel with thiolated HAV and RGD gradients. **(D-E)** Representative maximum projection images and quantification of bins corresponding to low (blue outline) and high (gold outline) aggrecan production. **(F)** Peptide combinations identified from screen in **(C)** were used to create discrete hydrogels that resulted in **(G)** 3-day gene expression and **(H)** collagen matrix consistent with screen predictions.[196] Scale bars: B, 1 mm; D, 50 µm.

The use of click chemistry can be used to pattern multiple gradients onto base hydrogels sequentially. For instance, opaque sliding masks were used to create an HA-based hydrogel whose stiffness and matrix ligand density can be systematically manipulated using distinct wavelengths of light.[346] Like previous studies, a Michael-addition reaction was employed to create soft methacrylated HA hydrogels. To create a stiffness gradient, a visible light photoinitiator and a gradient photomask were used to irradiate the hydrogel with different intensities of visible light. Next, to create a biochemical gradient, the gradient photomask was rotated 90 degrees with respect to the stiffness gradient and the hydrogel was exposed to varying intensities of UV light. The UV light resulted in selective exposure of thiol residues that can be conjugated to fibronectin for spatial patterning of this biochemical protein. The authors then used this combinatorial hydrogel to culture MSCs and found that MSCs preferentially differentiated into adipocytes and osteoblasts on different regions of the hydrogels.[346]

A similar two gradient system was also developed by Tong and coworkers.[348] In this study, the authors created a PEG-based hydrogel to generate perpendicular gradients of mechanical and biochemical signals. Eight-arm PEG was modified with Nor and linear PEG was modified with thiols on each end. A click chemistry reaction between Nor and thiols was initiated using a photoinitiator and UV light, and a sliding mask was used to control the reaction time of this light-mediated reaction. After several washes to remove unbound PEG-thiol, the hydrogels were incubated in a thiolated peptide containing the Arg-Gly-Asp (RGD) sequence from fibronectin and using a sliding mask and light, a perpendicular gradient of RGD peptide was created. The authors found that stiffer regions corresponded to increased cell elongation, and the RGD peptide increased cell area.

Although 2D combinatorial hydrogels can be used to rapidly screen the effects of one or two ECM signals across a range of concentrations, the extent to which ECM signals control cell behavior is highly dependent on dimensionality (2D vs. 3D). For example, stem cells atop hydrogels of increasing stiffness experience increased mechanical activity; however, the opposite trend is observed if the cells are encapsulated within protease-degradable hydrogels of increasing stiffness.[187] Additionally, significant gene expression differences are observed between 2D and 3D chondrocyte cultures,[356] and the roles of dimensionality have been observed with other phenotypes as well.[357,358] To better mimic native ECMs, there is increasing interest in developing high-throughput systems to identify 3D environments that regulate stem cell differentiation.

Chemistries for developing combinatorial hydrogels that are amenable to 3D cell culture have been recently developed and applied to identify osteoinductive and chondroinductive microenvironments. To identify mechanical and biochemical signals that favor osteogenic differentiation of adult stem cells, Nii et al. created combinatorial hydrogels with independently tunable biochemical and mechanical properties. To tune mechanical properties, PEG-diacrylate (PEGDA) hydrogels were fabricated at different weight percentages. To tune biochemical properties, fibronectin and laminin were incorporated into hydrogels at different concentrations. Of 36 combinations tested, the authors found that PEGDA hydrogels with intermediate stiffness (~50 kPa) with low fibronectin (10 µg/ml) produced maximal osteocalcin gene expression, regardless of laminin concentration.[359]

The limited options available for treatment of cartilage defects have prompted the development of tissue engineering-based strategies, specifically those involving stem cell-based biomaterial constructs. Although several MSC chondroinductive factors have been identified, it remains challenging to screen the cooperative effects of multiple parameters on stem cell chondrogenesis. Vega et al. developed a hydrogel platform with biochemical gradients of peptides that mimic cell-cell and cell-matrix signals present during cartilage development.[196] Chondrogenesis varied spatially in these hydrogels based on the local biochemical environment, as indicated by 7-day aggrecan expression levels (Figure A.3C-A.3E). From 100 combinations investigated, discrete MSC-containing hydrogels were formulated, resulting in significant 56-day cartilage-specific matrix production consistent with screening predictions (Figure A.3F-A.3H).

Although combinatorial hydrogels can be used to investigate the impact of multiple signals on stem cell differentiation within one hydrogel, this technique has its limitations. The most limiting factor of combinatorial hydrogels is their inability to exclude paracrine signaling from neighboring cells that are exposed to a different set of culture conditions. A low seeding density could reduce these effects, and heterogeneity within a region of interest could also be determined by evaluating biomarker histograms and other metrics. Discrete hydrogels with one unique combination of different signals would obviate this concern, and emerging techniques for miniaturizing discrete hydrogels provides an opportunity to use them for high-throughput screening studies.

### *A.5.2 Microgel Microarrays*

Microgels are hydrogels in the micrometer scale that have been used for numerous tissue engineering applications ranging from targeted and controlled drug delivery to cell culture platforms.[360] As miniaturized cell culture platforms, microgels are particularly appealing due to their biocompatibility and ability to expose cells to a variety of microenvironments within a small space.[361] Due to their size, microgels can also be used for targeted cell delivery to regenerate bone and cartilage. For example, Zhao et al. used a microfluidic fabrication technique to create microgels made of methacrylated gelatin (GelMA) encapsulated with MSCs.[362] These microgels were highly reproducible in size and supported MSC viability, spreading, and osteogenesis. Furthermore, the authors showed that these microgels could be injected in a bone defect and form new bone. For cartilage tissue regeneration, Li et al. employed a similar microfluidic technique.[363] Nor-modified gelatin (GelNor) macromers were used to form microgels using 2-arm thiolated PEG as the crosslinker.[363] Using this scheme, the authors were able to fabricate GelNor microgels of different sizes that supported MSC cultures and type II collagen production. In a follow-up study, Li et al. showed that these microgels could be used as an injectable hydrogel system that can then be bonded using 4-arm PEG-thiol.[364]

There is a limited ability to design functional tissue structures because it is challenging to recapitulate the complexity of native tissue environments. To investigate effects of multiple components on cellular behavior in a rapid, cost-effective manner, microgels in tandem with high throughput screening techniques are being developed. With the use of microarrays, this critical issue is addressed, and the primary goal of these platforms is to identify combinations of biomaterials that can promote, direct, and manipulate stem cells to differentiate and synthesize tissue matrix.

Anderson et al. developed a monomer microarray design consisting of pairwise combinations of 25 different monomers at a 70:30 ratio, resulting in 576 combinations in triplicate.[365] The authors were one of the first to develop a high-throughput platform to investigate the effects of different polymer chemistries on cell behavior. This 2D miniaturized system consists of using a fluid handling system to spot combinations of acrylate, diacrylate, dimethacrylate, and triacrylate monomers on a layer of poly(hydroxyethyl methacrylate) (pHEMA). Human embryonic stem cells (ESCs) were cultured on this polymer array and different cellular responses were observed based on fluorescence of various markers (Figure A.4A-A.4D).[365] Using this platform, ESC proliferation was assessed, and new arrays with “hit” polymer combinations that supported ESC growth could be explored further.

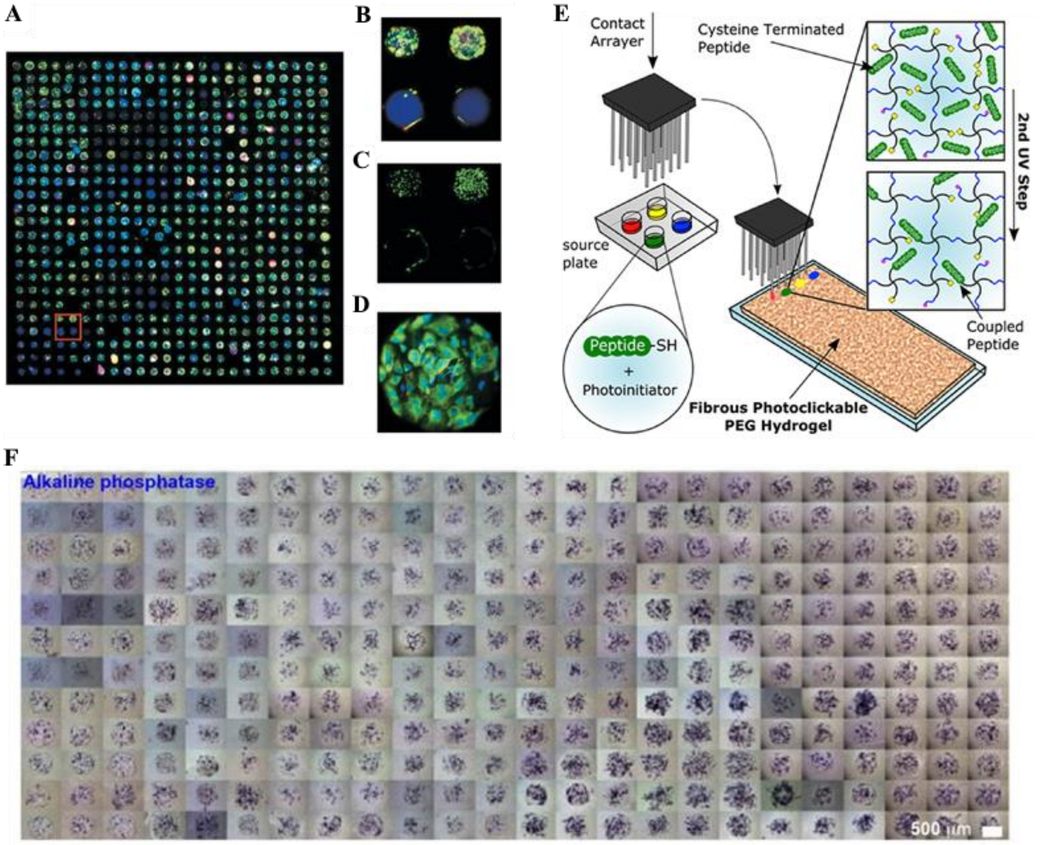

*Figure A. 4.* Examples of microgel microarrays and their applications. **(A)** 2D matrix microarray of 576 pairwise combinations of 25 different monomers. Embryonic stem cells express varying degrees of biomarkers cytokeratin 7 (green) and vimentin (red). **(B-C)** Single polymer spots show differences in biomarker expression and cell count. **(D)** Polymer spot with positive-control expression of keratin 7 (green).[365] **(E)** Schematic depicting how to spot thiolated peptides onto fibrous poly(ethylene glycol) hydrogels.[366] **(F)** 3D microgel microarray with encapsulated MSCs express varying degrees of osteogenic biomarker alkaline phosphatase (blue) in response to different protein combinations.[367]

Using a similar procedure, Flaim et al. developed an ECM microarray platform for the culture of patterned cells atop combinatorial hydrogel matrix mixtures.[368] A robotic DNA spotter was used to investigate the effects of combinations of different ECM molecules on the maintenance of primary hepatocyte phenotype and hepatocyte differentiation of ESCs. Using fluorescent expression of hepatocyte-specific markers, the authors found ECM protein combinations that supported hepatocyte function and promoted ESC differentiation to a hepatocyte lineage. Specifically, the authors found that secreted albumin from primary rat hepatocytes is highest when cultured on type IV collagen and lower when they are cultured on fibronectin and laminin. It was also determined that collagen I was a major determinate in the differentiation of mouse ES cells.[368] Since this platform relies on fluorescent readouts present in cells, this technique can be adapted to probe the effects of ECM proteins on the osteogenic and chondrogenic differentiation of MSCs.

Surface topography is also extremely influential in evoking specific cellular responses and high-throughput screening tools have been developed to investigate the effects of topography on cellular behavior. For example, Unadkat et al. used mathematical algorithms to design over 2,000 unique topographies using 3 primitive shapes, which were etched on a poly(lactic acid) topographical chip.[369] Using this platform, the authors found topographies that favored MSC proliferation and differentiation to an osteogenic phenotype.[369] To incorporate topography to microgels, Sharma et al. developed a microarray system consisting of microgels printed onto electrospun fibrous poly(ethylene glycol) hydrogels (Figure A.4E).[366] The underlying topography was characterized using SEM and confocal microscopy, and using contact array printing and UV light, five different thiolated peptides were used to investigate the effects of peptide concentration and underlying topography on cell adhesion and morphology. This platform presented a photoclickable peptide microarray platform that allows for screening the effects of peptides and hydrogel fibers on cell behavior. Although only cell morphology was investigated, this platform can easily be adapted to investigate the effects of hydrogel topography and peptides on chondrogenic and osteogenic MSC differentiation.

Although there are several examples of using robotic spotters to create microgel microarrays, most of these studies are limited to 2D hydrogels. Dimensionality is an important parameter that regulates a multitude of cell behaviors and thus microgels amenable to 3D culture may more accurately mimic native bone and cartilage environments. Dolatshahi-Pirouz et al. developed a 3D cell-laden microarray platform for combinatorial screening of human MSC differentiation in response to multiple ECM proteins and growth factors.[367] Microgel units were composed of GelMA, encapsulated MSCs, ECM proteins, and microgels were exposed to bone morphogenic proteins. The cell-laden hydrogel constructs were created using an automated printing strategy. MSC responses to ECM proteins and growth factors were evaluated by assessing the combinatorial effects of these factors on osteogenic differentiation (Figure A.4F). The authors found that combinations of fibronectin, osteocalcin, and laminin resulted in higher ALP expression compared to individual contributions from these ECM proteins. Although the microarray platform for forming microgels was used to evaluate the osteogenic potential of 96 different 3D environments, this technique can be easily adapted to look at additional ECM molecules and differentiation outcomes (e.g., MSC differentiation into chondrocytes).

Using a more advanced robotic spotter, Ranga et al. developed a microarray platform that can synthesize over 1,000 unique environments for 3D cell culture.[370] Using this setup, the authors were able to assess the combined effects of matrix elasticity, hydrogel degradation, and different ECM proteins on the proliferation of ESCs. The authors found that ESCs in 3D microgels of low matrix stiffness exhibited increased proliferation and self-renewal. In addition to population-based assays within each microgel, the authors also reported systems-level analyses at multiple scales. This type of data analysis for multifactorial conditions could prove extremely useful for identifying MSC environments that favor osteogenic and chondrogenic differentiation.

The techniques presented thus far have focused on synthetic or naturally derived materials to create high-throughput screening platforms. To expose cells to the chemical complexity of native ECMs, Beachley et al. developed novel 2D and 3D tissue ECM arrays for screening biological responses to tissue specific scaffold microenvironments.[371] Proteomic complexity of the natural ECM was retained from soluble tissue components that were mechanically fragmented, and the authors characterized their effects on cell adhesion, proliferation, and gene expression of human adipose-derived stem cells. ECM array outputs were used in conjunction with proteomic composition to construct specific networks composed of suspected proteins responsible for tissue-specific differences in cell function. Using *in vitro* arrays, the authors were able to discover drivers of the *in vivo* biological response thereby linking ECM components to cellular signaling pathways, which can help uncover potentially overlapping mechanisms across different cell processes. Notably, the authors found that overall osteogenic differentiation was similar in 2D and 3D tissue arrays. However, 2D arrays displayed a higher amount of calcified matrix than 3D cellular macrotissues.

### A.6 Summary and Future Directions

Biochemical and biomechanical factors derived from development and musculoskeletal ECMs can provide signals necessary for MSC differentiation into resident cells present in bone and cartilage tissue. Current techniques evaluate cellular responses to engineered materials by changing biomaterial parameters one at a time, which is time consuming and ineffective. To accelerate this slow iterative process, novel high-throughput platforms that can simultaneously assess cellular responses to many conditions have been developed. In this review, two hydrogel-based systems to rapidly screen cell behavior were highlighted (Summarized in Table A.1). Combinatorial hydrogels are hydrogels with one or two gradients of biophysical and/or biochemical signals. Combinatorial hydrogels with two gradients typically feature the second gradient perpendicular to the first gradient, thereby exposing cells to combinations of two factors. Although this screening technique has been developed in 2D and 3D configurations, combinatorial hydrogels have only been limited to two gradients. Using the same click chemistries used to form two gradients, it could be possible to introduce a third gradient (e.g., in the z-direction) to recapitulate zonal organization present in numerous tissues including cartilage.[372]

**Table A. 1**

*Summary of Select Techniques to Investigate Cell-Biomaterial Interactions*

| Combinatorial Hydrogel | Cell Type | Overview of Technique | Select Findings |
|---|---|---|---|
| Rape et al.[88] | Glioblastoma (U373-MG GBM) cells; MSCs. | Patterned photomask used to create a gradient of stiffness and a perpendicular gradient of fibronectin in a two-step process. | MSCs on top of combinatorial hydrogel (2D) had high osteogenic marker expression on regions of high stiffness and high fibronectin. |
| Tong et al.[90] | Fibroblasts | Sliding opaque photomask used to create a gradient of stiffness and a perpendicular gradient of RGD in a two-step process. | Fibroblasts on top of combinatorial hydrogel (2D) displayed high elongation and area in regions of high stiffness and high RGD. |
| Nii et al.[105] | MSCs | Macromer weight percent used to tune mechanics; biochemical properties were varied by incorporating fibronectin and laminin at different concentrations. | MSCs encapsulated in hydrogels (3D) of intermediate stiffness (~55 kPa) and low fibronectin (10 µg/ml) had high osteogenic gene expression. |
| Vega et al.[100] | MSCs | Sliding opaque photomask used to create a gradient of N-cadherin mimetic peptide (HAV) and a perpendicular gradient of RGD in a two-step process. | MSCs encapsulated in combinatorial hydrogel (3D) had high chondrogenic marker expression in regions of high HAV and low RGD. |

| Microgel Microarrays | Cell Type | Overview of Technique | Select Findings |
|---|---|---|---|
| Flaim et al.[112] | Primary hepatocytes; ESCs | Contact deposition-type microarrayer used to spot ECM mixtures of ColI, ColIII, ColIV, laminin, and fibronectin onto a hydrogel surface. | ESCs on top of ECM spots (2D) had high hepatocyte biomarker expression on ECM compositions on matrices containing ColI and fibronectin. |
| Sharma et al.[114] | Ten cell types including chondrocytes, osteoblasts, MSCs | Contact deposition-type microarrayer used to bind thiolated adhesive peptide mixtures onto a fibrous hydrogel. | Cells on top of peptide regions (2D) displayed differences in cell attachment and morphology based on peptide mixtures and cell types. |
| Dolatshahi-Pirouz et al.[115] | MSCs | Combinations of ECM proteins and MSC-containing hydrogel solution were mixed in 384-well plates. A contact microarrayer was used to use these solutions to form microgels on a treated glass slide. | MSCs encapsulated in microgels (3D) expressed varying levels of osteogenic biomarkers based on microgel composition. |

Microgel microarrays have been used to identify biomaterial combinations that control cell behavior including stem cell differentiation. A major advantage of this system over combinatorial hydrogels is that each test condition is discrete, thereby removing the concern for paracrine signaling from cells in adjacent conditions. Microgel microarrays have been explored in 2D polymer spots, hydrogel fibers, and as 2D and 3D microgels with a multitude of biochemical and biophysical properties. There have been significant advances in how cellular information is gathered and interpreted as well. From single-cell to population-based, different methods for analyzing how stem cells respond to microgel environments are helping home in on the role of specific biomaterial parameters on stem cell behavior.

Although this review focused on combinatorial hydrogels and microgel microarrays, there are other platforms that can be applied to identify biomaterials for bone and cartilage tissue regeneration. For example, Louzao et al. developed a technique to screen hundreds of potential biomaterial bioinks for 3D printing.[373] Although the main application of this platform was drug release and cytocompatibility, this method can be easily adapted to identify osteoinductive and chondroinductive bioinks. Microfluidic devices can also be tailored as high-throughput platforms amenable to 3D MSC culture. Occhetta et al. designed a microfluidic platform that delivers specific concentrations of factors under continuous flow.[374] Combining microfluidics with high-throughput has particular applicability in mimicking native environments with shear and other fluid forces.

Most high-throughput screening approaches present cells with different biochemical and biophysical factors spatially, but often fail to investigate the temporal effects of ECM-inspired factors. 4D culture platforms consist of 3D biomaterials that change with time.[375] To introduce dynamic changes, a catalyst is needed, and due to the spatial fidelity of photomasks, light is an attractive stimulant to induce temporal changes. There are several examples of hydrogels that can change with time. To introduce dynamic changes in mechanics, Guvendiren et al. developed soft hydrogels that stiffen with light.[33] Additionally, Yang et al. developed photodegradable hydrogels that soften with light,[376] and Rosales et al. developed photodegradable hydrogels that soften with light that can be re-stiffened via kinetic crosslinking using a photoinitiator and light.[186] To introduce biochemical changes temporally, Shadish et al. used sortase-mediated transpeptidation to reversibly immobilize proteins, enzymes, and growth factors with spatiotemporal fidelity,[377] and more recently Gawade and colleagues tethered recombinant proteins to hydrogels using stimuli-sensitive crosslinkers that can be released on-demand via single and double user-defined input combinations of enzymes, reductants, and light.[378] A better understanding of the spatial and temporal presentation of ECM factors during development and repair in tandem with emerging hydrogel platforms will result in next-generation screening tools for cartilage and bone tissue regeneration.

# Appendix B

## Human Induced Mesenchymal Stem Cells Display Increased Sensitivity to Matrix Stiffness

**Note:** Sections of this chapter have been reproduced from the following publication with permissions:

**Gultian, K. A., Gandhi, R., Sarin, K., Sladkova-Faure, M., Zimmer, M., de Peppo, G. M., & Vega, S. L. (2022).** Human induced mesenchymal stem cells display increased sensitivity to matrix stiffness. *Scientific Reports 2022 12:1*, *12*(1), 1–9.

## B.1 Abstract

The clinical translation of MSCs is limited by population heterogeneity and inconsistent responses to engineered signals. Specifically, the extent in which MSCs respond to mechanical cues varies significantly across MSC lines. Although induced pluripotent stem cells (iPSCs) have recently emerged as a novel cell source for creating highly homogeneous MSC (iMSC) lines, cellular mechanosensing of iMSCs on engineered materials with defined mechanics is not well understood. Here, we tested the mechanosensing properties of three human iMSC lines derived from iPSCs generated using a fully automated platform. Stiffness-driven changes in morphology were comparable between MSCs and iMSCs cultured atop hydrogels of different stiffness. However, contrary to tissue derived MSCs, no significant changes in iMSC morphology were observed between iMSC lines atop different stiffness hydrogels, demonstrating a consistent response to mechanical signals. Further, stiffness-driven changes in mechanosensitive biomarkers were more pronounced in iMSCs than MSCs, which shows that iMSCs are more adaptive and responsive to mechanical cues than MSCs. This study reports that iMSCs are a promising stem cell source for basic and applied research due to their homogeneity and high sensitivity to engineered mechanical signals.

## B.2 Introduction

MSCs are non-hematopoietic cells capable of differentiating into cells that produce various mesodermal tissues, including osteoblasts, adipocytes, and chondrocytes.[284] MSCs are present in numerous stem cell niches including bone marrow and adipose tissue and can be expanded *in vitro* by plating onto tissue culture polystyrene (TCPS), which causes them to adhere, adopt a spindle-like shape, and proliferate into fibroblastic colony-forming units.[379] Owing to their unique properties and ease of expansion, MSCs have been extensively studied and used in numerous clinical trials for the treatment of various medical disorders.[269,380]

*In vivo*, the multifunctional phenotype of MSCs is regulated by chemical and physical cues of the tissue microenvironment.[381] which influence numerous functions including migration, differentiation, and paracrine signaling.[382] To regulate stem cell behavior outside of the body, biomaterials are used to recapitulate specific properties of tissue microenvironments. For example, ECM elasticity and tissue-level stiffness are strong drivers of cellular mechanosensing and phenotypic commitment *in vitro*.[70] Engler et. al showed that MSCs atop soft hydrogels that mimic the stiffness of brain tissue express neuronal biomarkers, whereas MSCs on rigid substrates produce osteocalcin, a bone tissue-specific protein secreted by osteoblasts.[70] MSC mechanosensing precedes stiffness-mediated differentiation, with higher mechanics resulting in increased focal adhesion size,[383] actin alignment,[384] and YAP (Yes-associated protein) localization to the nucleus.[185]

Although engineered mechanical cues can regulate MSC mechanosensing *in vitro*, donor variability between MSC lines derived from adult tissues is significant, resulting in inconsistent responses to engineered signals.[385] These challenges limit the possibility of manufacturing high quality, homogeneous MSC lines in large numbers needed for basic research and stem cell-based therapies.[386] To overcome this challenge, induced pluripotent stem cells (iPSCs) have recently been differentiated into functional MSCs (iMSCs), displaying phenotypic similarities.[387,388] However, there are only a limited number of studies that have explored the use of iMSCs,[389] and the effects of mechanical signals on iMSC mechanosensing is not well understood.

In this study, we evaluated cell-material interactions of three human iMSC lines derived from iPSCs generated using a robotic, fully automated platform, which results in the production of highly reproducible iMSC lines.[390] We report that iMSCs are more responsive to matrix stiffness than human MSCs derived from adult tissues, and that stiffness-mediated changes in cellular mechanosensing are more consistent across different iMSC lines.

## B.3 Results and Discussion

### *B.3.1 Automated manufacturing of iPSC lines enables consistent production of iMSCs*

Manual production of human iPSC lines is time consuming and can result in significant line-to-line variability. To enable consistent production of high-quality and highly reproducible iMSC lines, fibroblasts from human skin biopsies were reprogrammed into stem cells using the NYSCF Global Stem Cell Array®, a modular, robotic platform for high-throughput production, maintenance, and differentiation of iPSCs (Figure B.1A). Three iPSC lines were manufactured and validated by their positive OCT4 and TRA-1-60 expression (Figure B.2), visual confirmation of colonies on TCPS (Figure B.1B), and additional quality control metrics including sterility, karyotyping, genotyping, pluripotency expression profile, and differentiation capacity.[390]

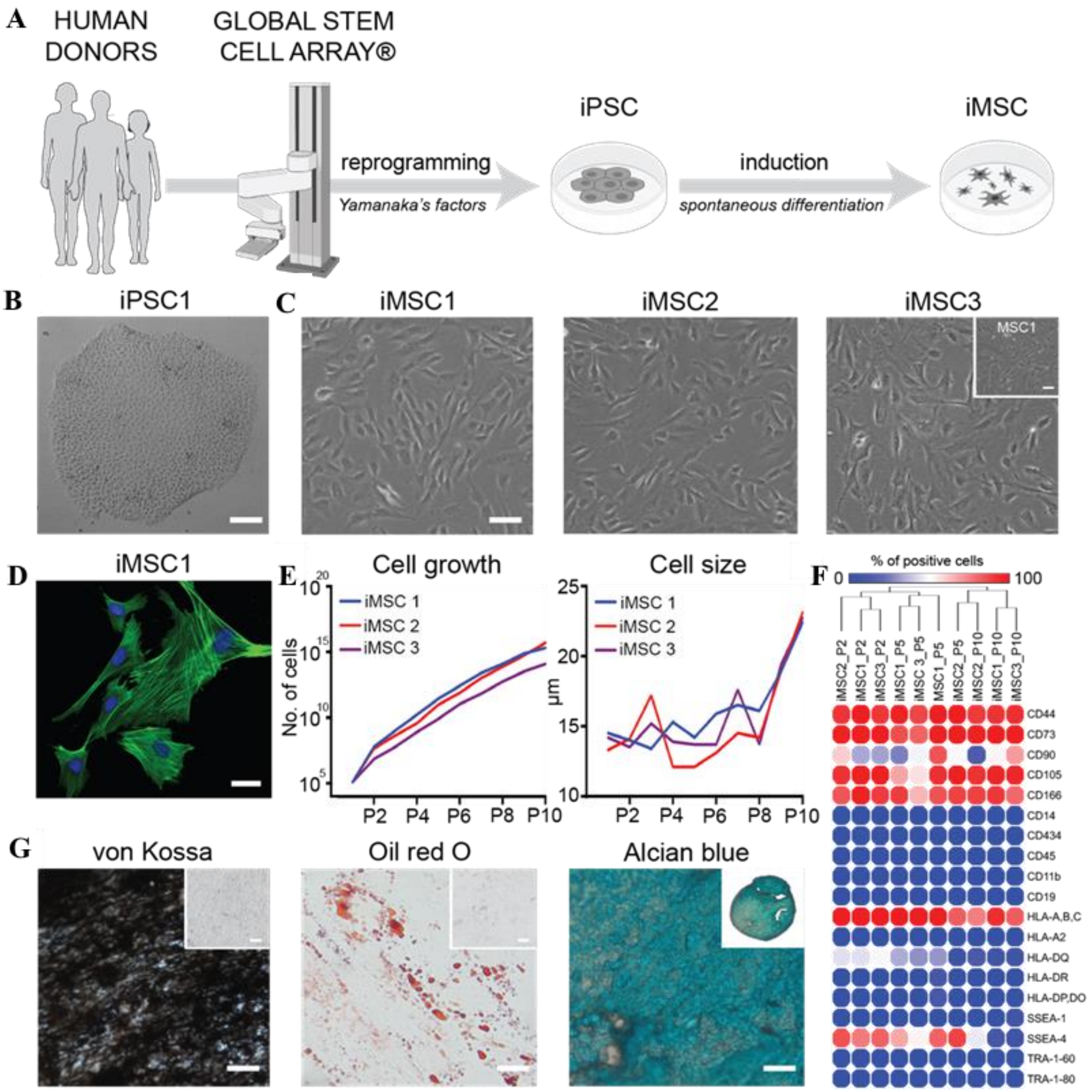

*Figure B. 1.* Derivation and characterization of human iMSC lines. **(A)** Schematic of automated reprogramming of human fibroblasts into iPSC lines using a NYSCF Global Stem Cell Array®. **(B)** Representative brightfield image of iPSC colony generated using automated platform. Scale bar, 100 µm. **(C)** Representative brightfield images of iMSC lines derived from three different donors at passage 5. Inset shows commercially available bone marrow derived MSCs at passage 5. Scale bar, 50 µm. **(D)** Representative confocal image of iMSCs stained for actin (green) and nuclei (blue). Scale bar, 20 µm. **(E)** Plots of cell growth and average cell length for 3 iMSC lines over 10 passages. **(F)** Hierarchical clustering of surface marker screening data for 3 iMSC lines at passage 2, 5, and 10 and MSCs at passage 5. **(G)** Representative brightfield images of iMSCs (line 1) differentiated towards osteogenic (von Kossa), adipogenic (Oil Red O), and chondrogenic (Alcian blue) tissues. Insets represent negative controls and full-size cartilage spheroids. Scale bar, 20 µm.

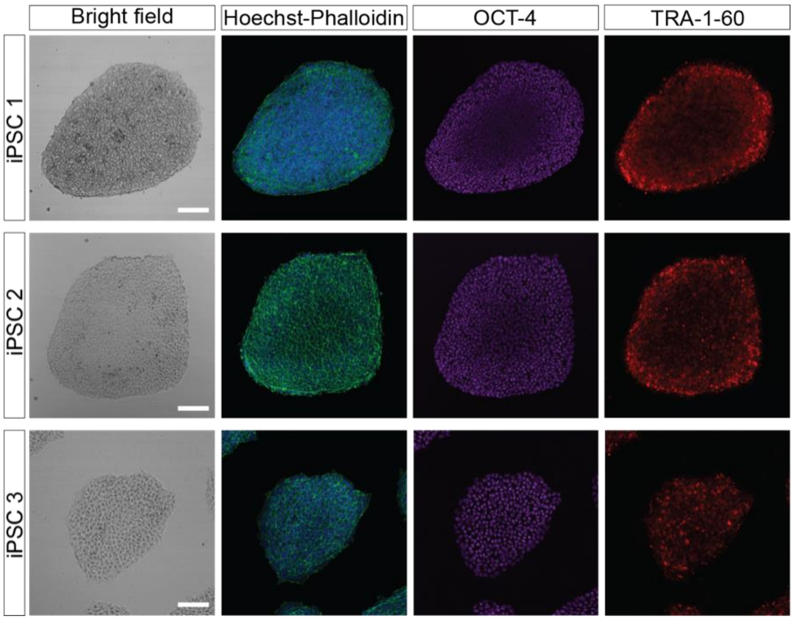

*Figure B. 2.* Morphology and expression of pluripotency markers. Representative bright field images show that human iPSC lines form colonies. Representative fluorescence images show consistent colony morphology (phalloidin, green; Hoescht, blue) and that human iPSC lines are positive for pluripotency markers OCT-4 (purple) and TRA-1-60 (red). Scale bar: 100 µm.

Manufactured iMSC lines adhere to tissue culture polystyrene (TCPS), feature a spindle-like morphology (Figure B.1C), and exhibit pronounced actin fibers (Figure B.1D). These morphological traits are comparable to human MSCs isolated from adult tissues and cultured atop TCPS substrates. The *in vitro* expansion rate (Figure B.1E, left) was consistent across all iMSC lines and iMSCs divided faster than adult MSCs in accordance with previously published data.[389,391] Interestingly, *in vitro* expansion over ten passages also results in a reproducible and progressive increase in average cellular length, which is a phenomenon also observed in tissue derived MSCs (Figure 1e, right).

All iMSC lines are negative for the pluripotency markers OCT4 and TRA-1-60, confirming that they do not dedifferentiate into iPSCs or iPSC-like cells after at least ten passages on TCPS (Figure B.3). A cell surface marker screening panel also confirmed that iMSCs are negative for other typical pluripotency and hematopoietic markers (Figure B.1F, blue circles). Importantly, iMSCs express mesenchymal markers including CD44, CD73, CD90, CD105, and CD166 similarly to MSCs isolated from adult tissues (Figure B.1F, red circles and Table B.1).[392] iMSCs also express SSEA-4 at early passages, as seen in multipotent subpopulations of human MSCs isolated from bone marrow and other tissues.[393] The cell surface marker screening panel also shows that the iMSC lines express lower levels of human leukocyte antigens (HLA) class II, which suggests iMSCs are more immunoprivileged than adult MSCs.[389,394]

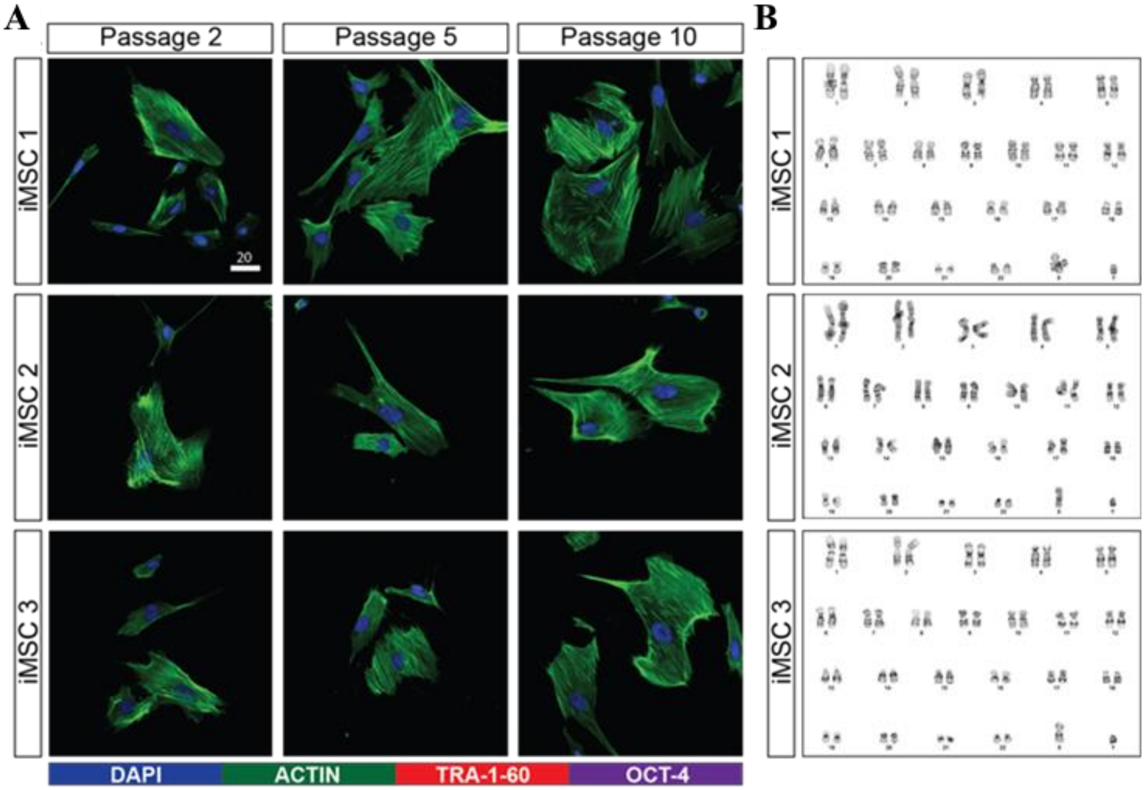

*Figure B. 3.* Lack of pluripotency and genomic integrity of human iMSCs. **(A)** Representative fluorescent images show that human iMSCs lack expression of TRA-1 (red) and OCT-4 (purple) pluripotency markers. Scale bar, 20 µm. **(B)** G-banding of derived human iMSC lines.

In addition to these phenotypic features, the ability to differentiate towards osteogenic, adipogenic, and chondrogenic lineages *in vitro* is a hallmark trait of MSCs.[284] By exposing iMSCs to soluble differentiation factors, we demonstrate that iMSCs give rise to osteogenic, adipogenic, and chondrogenic lineages as evidenced by von Kossa, Oil Red O, and Alcian blue staining, respectively (Figure B.1G and Figure B.4). Taken together, these findings confirm that iMSCs are phenotypically similar and possess the differentiation capacity of human MSCs.

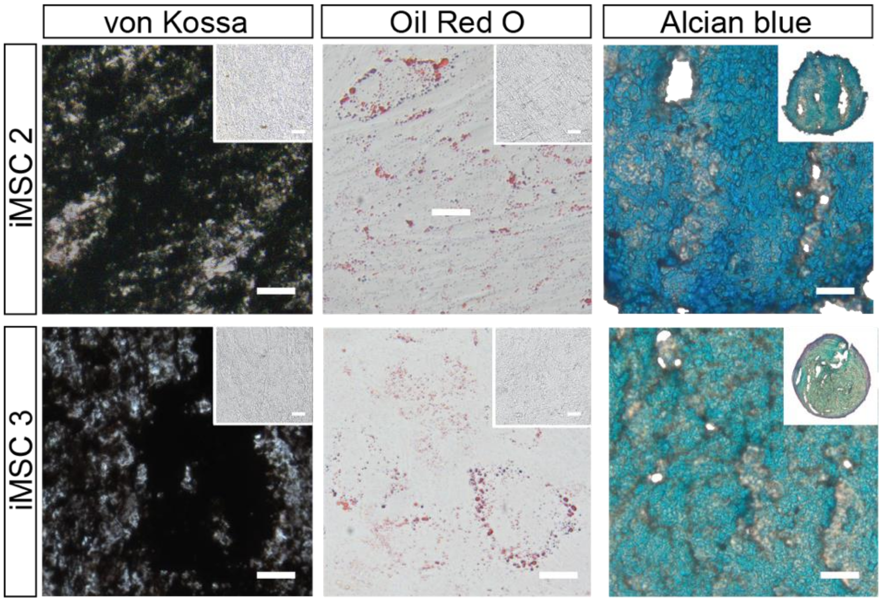

*Figure B. 4.* Multidifferentiation potential of human iMSC lines. Micrographs showing the osteogenic (von Kossa), adipogenic (Oil Red O), and chondrogenic (Alcian blue) differentiation potential of human iMSCs (lines 2 and 3). Insets represent negative controls and full-size cartilage spheroids. Scale bars, 20 µm.

## Table B. 1

*Global Surface Marker Profile. Percentage of Positive Human iPSCs at passage 2 (P2), 5 (P5), 10 (P10), and MSCs at P5 for 246 Surface Markers*

| **Surface marker** | **iMSC 1 P2** | **iMSC 2 P2** | **iMSC 3 P2** | **iMSC 1 P5** | **iMSC 2 P5** | **iMSC 3 P5** | **iMSC 1 P10** | **iMSC 2 P10** | **iMSC 3 P10** | **BMSC P5** |
|---|---|---|---|---|---|---|---|---|---|---|
| **CD1a** | 0.715 | 0.841 | 0.468 | 0.459 | 0.498 | 0.591 | 0.904 | 0.273 | 0.694 | 0.188 |
| **CD1b** | 0.555 | 0.314 | 0.702 | 0.615 | 0.363 | 0.603 | 0.566 | 0.188 | 0.84 | 0.327 |
| **CD1d** | 0.451 | 0.303 | 0.48 | 0.551 | 0.276 | 0.693 | 0.978 | 0.304 | 0.398 | 0.278 |
| **CD2** | 0.972 | 0.802 | 0.681 | 0.276 | 0.436 | 0.557 | 0.386 | 0.0552 | 0 | 0.195 |
| **CD3** | 0.84 | 0.4 | 0.874 | 0.334 | 1.12 | 0.498 | 3.48 | 1.3 | 2.79 | 0.435 |
| **CD4** | 1.08 | 0.709 | 0.838 | 0.581 | 0.18 | 0.378 | 0.41 | 0.353 | 0.4 | 2.61 |
| **CD4v4** | 0.862 | 0.766 | 0.845 | 0.571 | 0.246 | 0.621 | 0.345 | 0.264 | 0.82 | 2.01 |
| **CD5** | 0.714 | 0.549 | 0.903 | 0.477 | 0.202 | 0.412 | 0.582 | 0.17 | 0.177 | 0.617 |
| **CD6** | 0.815 | 0.386 | 0.476 | 0.635 | 0.268 | 0.421 | 0.38 | 0.0709 | 1.18 | 0.255 |
| **CD7** | 2.63 | 0 | 0 | 0.805 | 0.497 | 0.34 | 1.22 | 0.436 | 0.208 | 0.426 |
| **CD8a** | 1.19 | 0.651 | 1.12 | 0.497 | 0.361 | 0.596 | 0.763 | 0.0648 | 0.629 | 0.278 |
| **CD8b** | 0.616 | 0.244 | 0.615 | 0.573 | 0.435 | 0.636 | 0.418 | 0.0725 | 1.69 | 0.52 |
| **CD10** | 70.2 | 17.2 | 85.3 | 40.9 | 7.72 | 67.7 | 44.7 | 11.8 | 47.9 | 11.7 |
| **CD11a** | 0.929 | 0.37 | 0.753 | 0.803 | 0.264 | 0.124 | 0.409 | 0.124 | 1.68 | 0.206 |
| **CD11b** | 0.712 | 0.58 | 0.856 | 0.545 | 0.259 | 0.345 | 0.702 | 0.403 | 0.546 | 0.274 |
| **CD11c** | 0.62 | 0.695 | 0.513 | 0.575 | 0.349 | 0.508 | 0.567 | 0.177 | 1.16 | 0.442 |
| **CD13** | 96.7 | 90.7 | 97.8 | 80.8 | 64.8 | 69 | 78.3 | 68 | 62.6 | 91.6 |
| **CD14** | 0.757 | 0.938 | 0.879 | 0.423 | 0.414 | 0.474 | 1.22 | 0.397 | 0.605 | 0.326 |
| **CD15** | 0.806 | 0.62 | 0.655 | 1.13 | 0.369 | 1.42 | 0.822 | 0.466 | 6.44 | 0.355 |
| **CD15s** | 0.63 | 0.773 | 0.846 | 0.682 | 0.397 | 0.631 | 1.02 | 0.233 | 0.525 | 0.753 |
| **CD18** | 1.12 | 0.724 | 0.663 | 0.647 | 0.281 | 0.582 | 0.692 | 0.623 | 0.977 | 0.776 |
| **CD19** | 0.445 | 0.358 | 0.782 | 0.586 | 0.242 | 0.438 | 0.41 | 0.215 | 0.234 | 0.412 |
| **CD20** | 0.569 | 0.224 | 0.634 | 0.367 | 0.211 | 0.394 | 0.483 | 0 | 0 | 0.296 |
| **CD21** | 0.92 | 0.365 | 0.306 | 0.459 | 0.189 | 0.46 | 0.587 | 0 | 0.791 | 0.285 |
| **CD22** | 0.668 | 0.726 | 0.74 | 0.895 | 0.206 | 0.677 | 1.29 | 0.254 | 2.54 | 0.738 |
| **CD23** | 0.531 | 0.446 | 0.549 | 0.456 | 0.188 | 0.336 | 0.949 | 0.177 | 0.956 | 0.237 |
| **CD24** | 14 | 50 | 3.96 | 12.1 | 87.1 | 1.45 | 2.02 | 18 | 1.06 | 3.66 |
| **CD25** | 0.784 | 0.779 | 0.72 | 0.586 | 0.402 | 0.396 | 0.272 | 0.116 | 0.581 | 0.363 |
| **CD26** | 21.9 | 11.6 | 6.58 | 15.4 | 2.21 | 3.21 | 14.8 | 2.06 | 3.31 | 6.9 |
| **CD27** | 0.489 | 0.828 | 0.392 | 0.53 | 0.32 | 0.366 | 0.55 | 0.34 | 0.988 | 0.274 |
| **CD28** | 0.652 | 0.67 | 0.466 | 0.484 | 0.319 | 0.327 | 0.792 | 0.0575 | 0.573 | 0.324 |
| **CD29** | 97.9 | 94.4 | 94.2 | 83.7 | 47.2 | 74.8 | 75.2 | 57.3 | 56.3 | 86.5 |
| **CD30** | 0.505 | 0.798 | 0.421 | 0.476 | 0.434 | 0.563 | 0.435 | 0.18 | 1.6 | 0.545 |
| **CD31** | 0.558 | 0.521 | 0.331 | 0.74 | 0.244 | 0.745 | 1.14 | 0.348 | 1.08 | 0.468 |
| **CD32** | 0.68 | 1.19 | 0.566 | 0.573 | 0.217 | 0.646 | 0.859 | 0.266 | 0.726 | 0.759 |
| **CD33** | 0.562 | 0.435 | 0.595 | 0.483 | 0.215 | 0.346 | 0.442 | 0.0603 | 0.401 | 0.868 |
| **CD34** | 1.17 | 0.566 | 2.22 | 1.21 | 0.292 | 1.31 | 0.637 | 0.203 | 0.63 | 0.904 |
| **CD35** | 0.591 | 0.792 | 0.33 | 0.447 | 0.225 | 0.544 | 0.216 | 0.158 | 0.261 | 0.364 |
| **CD36** | 1.02 | 0.759 | 0.714 | 0.718 | 0.2 | 0.575 | 0.913 | 0.171 | 0.899 | 0.903 |
| **CD37** | 0.826 | 3.4 | 0.936 | 0.442 | 0.188 | 0.327 | 0.147 | 0 | 0.211 | 0.446 |
| **CD38** | 2.83 | 1.52 | 1 | 1.03 | 0.105 | 0.674 | 0.292 | 0 | 0.194 | 0.416 |

| | | | | | | | | | | |
|---|---|---|---|---|---|---|---|---|---|---|
| **CD39** | 0.917 | 0.594 | 1.37 | 0.706 | 0.401 | 0.757 | 0.601 | 0.361 | 0.671 | 0.631 |
| **CD40** | 9.11 | 4.44 | 12.5 | 7.99 | 2.2 | 8.3 | 1.31 | 1.03 | 8.09 | 0.481 |
| **CD41a** | 0.475 | 0.803 | 0.502 | 0.379 | 0.453 | 0.358 | 0.686 | 0.0586 | 1.09 | 0.492 |
| **CD41b** | 0.895 | 1.04 | 0.81 | 0.517 | 0.455 | 0.574 | 0.901 | 0.187 | 0.956 | 0.405 |
| **CD42a** | 0.874 | 0.625 | 0.55 | 0.804 | 0.325 | 0.472 | 0.371 | 0.271 | 0.924 | 0.293 |
| **CD42b** | 0.487 | 0.771 | 0.345 | 0.475 | 0.245 | 0.448 | 0.637 | 0.165 | 0.347 | 0.574 |
| **CD43** | 1.16 | 1.07 | 0.746 | 0.391 | 0.247 | 0.56 | 0.278 | 0 | 0.397 | 0.525 |
| **CD44** | 100 | 90.8 | 90.2 | 95.7 | 98.1 | 87 | 90.9 | 89.2 | 91.8 | 98.5 |
| **CD45** | 0.972 | 0.695 | 0.519 | 0.467 | 0.364 | 0.204 | 0.681 | 0.191 | 0.634 | 0.29 |
| **CD45RA** | 0.934 | 0.611 | 0.721 | 0.526 | 0.526 | 0.698 | 0.726 | 0.18 | 1.08 | 0.351 |
| **CD45RB** | 0.615 | 0.537 | 0.466 | 0.4 | 0.352 | 0.567 | 0.284 | 0.235 | 1.2 | 0.53 |
| **CD45RO** | 0.792 | 0.915 | 0.927 | 0.355 | 0.3 | 0.461 | 0.785 | 0.235 | 0 | 0.296 |
| **CD46** | 98.8 | 99.2 | 98.9 | 96.8 | 88.5 | 95.6 | 91.1 | 79.5 | 88.8 | 94.1 |
| **CD47** | 98.1 | 89.6 | 95.6 | 91.7 | 42 | 82.6 | 68.8 | 46.1 | 67.2 | 89.8 |
| **CD48** | 0.559 | 0.639 | 0.547 | 0.546 | 0.455 | 0.516 | 0.625 | 0.181 | 0.203 | 0.343 |
| **CD49a** | 42.3 | 50.3 | 49.9 | 12 | 11.1 | 32.4 | 1.54 | 9.64 | 13.1 | 44.3 |
| **CD49b** | 89.8 | 59 | 84.3 | 94 | 91.9 | 90.4 | 98.1 | 92.4 | 97.3 | 89.5 |
| **CD49c** | 99.3 | 93.8 | 98 | 83.7 | 95.2 | 76.2 | 91.9 | 81.3 | 82.6 | 76.1 |
| **CD49d** | 56.1 | 68.9 | 67.9 | 78.4 | 78.2 | 69.2 | 48.5 | 66.7 | 11.4 | 60.3 |
| **CD49e** | 91.8 | 86.1 | 90.3 | 91.2 | 97.2 | 89.5 | 91.6 | 96.6 | 93 | 90.1 |
| **CD50** | 2.58 | 1.34 | 3.76 | 1.58 | 0.357 | 1.29 | 0.423 | 0.0576 | 0.409 | 6.23 |
| **CD51/61** | 50.9 | 75.6 | 18.4 | 77.3 | 62.5 | 34.9 | 73 | 66.9 | 62.4 | 50.9 |
| **CD53** | 0.212 | 0.515 | 0.474 | 0.479 | 0.172 | 0.353 | 0.588 | 0.229 | 1.31 | 0.236 |
| **CD54** | 76.7 | 47 | 57.9 | 58.7 | 62.6 | 63.4 | 77.8 | 79.9 | 82.4 | 16.9 |
| **CD55** | 74.1 | 83.1 | 89.3 | 72 | 93.7 | 90.3 | 92.2 | 94.9 | 92.3 | 98 |
| **CD56** | 5.25 | 32.8 | 1.08 | 1.48 | 4 | 0.498 | 0.724 | 0.644 | 0.828 | 6.1 |
| **CD57** | 29.3 | 35.7 | 24.2 | 47.4 | 26.3 | 27.4 | 73.8 | 41.6 | 51.4 | 68.2 |
| **CD58** | 97.7 | 90 | 95.7 | 72.9 | 91.9 | 60.9 | 83.1 | 87.8 | 88.8 | 53.3 |
| **CD59** | • | 100 | 66.7 | 99.4 | 100 | 99.2 | 100 | 100 | 60 | 98.2 |
| **CD61** | 43.7 | 71.2 | 13.9 | 59.8 | 49.8 | 19.2 | 66.9 | 56.9 | 53.9 | 25.9 |
| **CD62E** | 0.483 | 0.478 | 0.643 | 0.543 | 0.272 | 0.392 | 0.556 | 0.23 | 0.803 | 0.381 |
| **CD62L** | 0.787 | 0.726 | 0.593 | 0.504 | 0.257 | 0.547 | 0.312 | 0 | 0.391 | 0.328 |
| **CD62P** | 0.907 | 1.02 | 0.663 | 0.504 | 0.321 | 0.461 | 0.902 | 0.25 | 0.596 | 0.316 |
| **CD63** | 92.8 | 82.1 | 92.8 | 70.4 | 83.4 | 73.3 | 71.3 | 93 | 77.8 | 74 |
| **CD64** | 0.676 | 0.63 | 0.758 | 0.39 | 0.302 | 0.479 | 0.451 | 0.128 | 0.577 | 0.466 |
| **CD66(a.c.d.e)** | 7.13 | 1.64 | 4.3 | 1.13 | 0.561 | 5.97 | 0.286 | 0.38 | 1.28 | 0.592 |
| **CD66b** | 0.555 | 0.808 | 0.779 | 0.404 | 0.404 | 0.477 | 0.602 | 0.379 | 0.982 | 0.337 |
| **CD66f** | 0.792 | 0.947 | 0.929 | 0.472 | 0.323 | 0.449 | 0.275 | 0.11 | 0.409 | 0.395 |
| **CD69** | 0.331 | 0.257 | 0.726 | 0.39 | 0.302 | 0.598 | 0.414 | 0 | 0.377 | 0.194 |
| **CD70** | 6.98 | 5 | 6.52 | 2.1 | 1.62 | 2.79 | 0.594 | 3.68 | 31 | 1.78 |
| **CD71** | 90 | 84.8 | 96.5 | 98.4 | 99.4 | 95.5 | 88.9 | 93.8 | 93.2 | 92.4 |
| **CD72** | 0.909 | 0.86 | 0.833 | 0.572 | 0.438 | 0.636 | 1.56 | 0.245 | 0.621 | 0.529 |
| **CD73** | 98.8 | 96.5 | 100 | 84.9 | 99 | 80.4 | 100 | 96.1 | 97.3 | 97.5 |
| **CD74** | 0.472 | 0.768 | 0.523 | 0.813 | 0.241 | 0.565 | 0.958 | 0.475 | 0.223 | 1.62 |
| **CD75** | 0.18 | 0.579 | 0.591 | 0.735 | 0.159 | 0.574 | 0.611 | 0.255 | 0.607 | 0.365 |
| **CD77** | 0.375 | 0.524 | 0.712 | 0.788 | 0.926 | 0.757 | 0.868 | 0.503 | 1.13 | 22.1 |
| **CD79b** | 0.866 | 1.43 | 0.641 | 0.61 | 0.357 | 0.397 | 1.26 | 0.351 | 0.586 | 0.347 |
| **CD80** | 0.847 | 0.589 | 0.6 | 0.518 | 0.544 | 0.78 | 0.529 | 0.303 | 1.18 | 0.628 |
| **CD81** | 100 | 94.9 | 99.1 | 99.6 | 100 | 99.9 | 99.4 | 99.4 | 95.2 | 97 |
| **CD83** | 0.989 | 0.771 | 0.615 | 0.462 | 0.669 | 0.622 | 1.62 | 0.357 | 1.43 | 0.381 |

| | | | | | | | | | | |
|---|---|---|---|---|---|---|---|---|---|---|
| **CD84** | 0.483 | 0.608 | 0.885 | 0.509 | 0.597 | 0.439 | 0.798 | 0.363 | 1.28 | 0.458 |
| **CD85** | 0.757 | 0.835 | 0.83 | 0.256 | 0.469 | 0.725 | 1.05 | 0.49 | 0.395 | 0.403 |
| **CD86** | 1.22 | 0.456 | 0.544 | 0.463 | 0.444 | 0.284 | 0.287 | 0.444 | 1.13 | 0.285 |
| **CD87** | 2.14 | 1.22 | 1.46 | 0.674 | 0.572 | 0.625 | 2.31 | 0.307 | 1.12 | 0.869 |
| **CD88** | 1.13 | 0.786 | 1.09 | 0.505 | 0.4 | 0.685 | 1.1 | 0.218 | 0.415 | 0.56 |
| **CD89** | 0.938 | 0.447 | 0.968 | 0.551 | 0.455 | 0.497 | 0 | 0.188 | 0.363 | 0.521 |
| **CD90** | 33.1 | 59.6 | 32.1 | 26 | 49 | 47.3 | 52.2 | 13.5 | 69 | 83.8 |
| **CD91** | 87.2 | 77.8 | 90.3 | 72.5 | 80.9 | 62.9 | 51.8 | 73.5 | 48.7 | 65.5 |
| **CDw93** | 0.786 | 0.461 | 1.1 | 0.766 | 0.222 | 0.444 | 0.734 | 0.0494 | 0.372 | 0.577 |
| **CD94** | 0.668 | 0.357 | 0.776 | 0.578 | 0.412 | 0.596 | 0.541 | 0.0494 | 0.725 | 0.335 |
| **CD95** | 50.9 | 52 | 46.6 | 37 | 28 | 31.7 | 51.7 | 18.7 | 29.3 | 85.7 |
| **CD97** | 2.66 | 1.28 | 4.85 | 11.3 | 4.74 | 28.4 | 4.17 | 5.95 | 12.2 | 22.1 |
| **CD98** | 99.1 | 97.2 | 98.1 | 77 | 91.7 | 76.9 | 87.9 | 83.7 | 85.8 | 74.3 |
| **CD99** | 56 | 39.2 | 53 | 42.4 | 93 | 23.3 | 16.4 | 79 | 27.8 | 47.6 |
| **CD99R** | 1.17 | 0.962 | 1.23 | 1.82 | 36.3 | 0.608 | 0.358 | 12.7 | 1.64 | 1.88 |
| **CD100** | 1.35 | 1.06 | 1.08 | 0.334 | 0.302 | 0.322 | 0.513 | 0.161 | 0 | 0.237 |
| **CD102** | 1.47 | 0.743 | 1.94 | 0.708 | 0.411 | 1.2 | 0.889 | 0.278 | 0.632 | 5 |
| **CD103** | 1.1 | 0.962 | 0.91 | 0.366 | 0.153 | 0.455 | 0.436 | 0.111 | 0.409 | 0.576 |
| **CD105** | 97.3 | 91.2 | 99 | 67.7 | 97.5 | 55.7 | 95.1 | 91.2 | 94.6 | 92 |
| **CD106** | 26.7 | 4.96 | 5.75 | 5.49 | 9.89 | 0.929 | 2.09 | 15.5 | 5.97 | 1.44 |
| **CD107a** | 17.2 | 21.2 | 21.1 | 1.9 | 8.12 | 4.43 | 6.64 | 28.1 | 9.23 | 0.878 |
| **CD107b** | 5.44 | 6.09 | 5.95 | 0.999 | 3.21 | 2.8 | 3.71 | 10.9 | 4.59 | 0.488 |
| **CD108** | 58.4 | 86.4 | 83.7 | 67.2 | 78 | 29.8 | 81.8 | 63.4 | 69.7 | 70.7 |
| **CD109** | 1.3 | 0.479 | 1.28 | 0.371 | 0.698 | 0.524 | 0.881 | 0.475 | 1.19 | 0.378 |
| **CD112** | 2.91 | 11 | 14.9 | 1.18 | 2.03 | 0.928 | 0.622 | 1.68 | 1.26 | 0.198 |
| **CD114** | 0.708 | 0.93 | 0.906 | 0.603 | 0.278 | 0.289 | 0.673 | 0.297 | 0.694 | 0.745 |
| **CD116** | 53.4 | 13.4 | 44.6 | 26.5 | 8.06 | 30.7 | 24.6 | 7.9 | 28.4 | 20.6 |
| **CD117** | 0.913 | 0.908 | 1.04 | 0.331 | 0.466 | 0.24 | 0.278 | 0.214 | 0.187 | 0.533 |
| **CD118** | 1.05 | 1.02 | 0.709 | 0.483 | 0.194 | 0.519 | 0.407 | 0.157 | 0.537 | 0.59 |
| **CD119** | 6.5 | 3.72 | 7.41 | 2.74 | 3.43 | 2.86 | 1.71 | 5.64 | 6.03 | 0.95 |
| **CD120a** | 2.07 | 1.36 | 1.69 | 0.905 | 0.319 | 1.13 | 2.21 | 1.8 | 4.32 | 1.35 |
| **CD121a** | 1.07 | 0.849 | 0.62 | 0.445 | 0.212 | 0.258 | 0.374 | 0.161 | 0.187 | 0.61 |
| **CD121b** | 0.483 | 0.535 | 0.667 | 0.697 | 0.299 | 0.348 | 0.289 | 0.17 | 0.634 | 0.405 |
| **CD122** | 1.03 | 0.536 | 0.841 | 0.485 | 0.215 | 0.203 | 0.522 | 0.0528 | 0.552 | 0.41 |
| **CD123** | 0.798 | 0.656 | 0.834 | 0.879 | 38.8 | 0.443 | 49.1 | 30.6 | 40.7 | 0.486 |
| **CD124** | 0.573 | 0.297 | 0.287 | 0.37 | 0.567 | 0.412 | 0.136 | 0.225 | 0.758 | 0.29 |
| **CD126** | 0.558 | 0.424 | 0.327 | 0.542 | 0.41 | 0.413 | 1.52 | 0.272 | 1.06 | 0.323 |
| **CD127** | 1.48 | 1.13 | 1.14 | 0.412 | 0.342 | 0.385 | 0.492 | 0.0981 | 0.337 | 0.381 |
| **CD128b** | 0.906 | 0.354 | 0.678 | 0.632 | 0.303 | 0.418 | 0 | 0.278 | 0.394 | 0.495 |
| **CD130** | 27.2 | 3.92 | 6.03 | 3.38 | 2.46 | 1.16 | 5.59 | 5.37 | 4.25 | 6.22 |
| **CD134** | 0.927 | 0.76 | 0.639 | 0.598 | 0.126 | 0.725 | 0.557 | 0.0518 | 0.197 | 0.403 |
| **CD135** | 0.745 | 0.837 | 0.787 | 0.423 | 0.0952 | 0.477 | 0 | 0.37 | 0.189 | 0.229 |
| **CD137** | 0.929 | 6.84 | 3.24 | 1.48 | 0.947 | 0.467 | 2.08 | 1.28 | 0.533 | 2.05 |
| **CD137L** | 0.539 | 0.757 | 0.795 | 0.471 | 0.27 | 0.372 | 0.546 | 0.212 | 0.363 | 0.447 |
| **CD138** | 0.674 | 0.811 | 0.563 | 0.45 | 0.338 | 0.454 | 5.03 | 0.0532 | 4.8 | 0.612 |
| **CD140b** | 99 | 89.3 | 98.9 | 71.8 | 86.5 | 76.1 | 57.5 | 50.2 | 78.8 | 54.2 |
| **CD141** | 6.29 | 2.51 | 20.6 | 3.01 | 9.35 | 4.16 | 1.72 | 5.71 | 0.186 | 1.01 |
| **CD142** | 38.5 | 19.6 | 49.9 | 13.5 | 24.4 | 19 | 69.5 | 25.7 | 86.6 | 0.598 |
| **CD144** | 0.649 | 0.63 | 0.73 | 0.638 | 0.0874 | 0.512 | 0.313 | 0.21 | 0.208 | 0.362 |
| **CD146** | 83.9 | 78 | 85.5 | 66.9 | 95.7 | 62.9 | 74.9 | 88.2 | 79.5 | 89.6 |

| | | | | | | | | | | |
|---|---|---|---|---|---|---|---|---|---|---|
| **CD147** | 98.1 | 94.4 | 98.3 | 94.6 | 99.7 | 92.2 | 100 | 96.2 | 96.2 | 93.9 |
| **CD150** | 0.849 | 0.933 | 1.03 | 0.382 | 0.3 | 0.408 | 0.44 | 0.162 | 0.529 | 0.243 |
| **CD151** | 97.1 | 89.1 | 97.2 | 78.6 | 84.4 | 60.6 | 64.8 | 65.6 | 57.5 | 94.7 |
| **CD152** | 0.83 | 1.05 | 0.706 | 0.594 | 0.299 | 0.44 | 0 | 0.054 | 0.174 | 0.212 |
| **CD153** | 1.26 | 0.826 | 0.636 | 0.444 | 0.22 | 0.34 | 0.346 | 0.0571 | 0.949 | 0.337 |
| **CD154** | 0.607 | 0.556 | 0.751 | 0.43 | 0.246 | 0.609 | 0.162 | 0.104 | 0.189 | 0.317 |
| **CD158a** | 0.706 | 0.76 | 0.949 | 0.568 | 0.215 | 0.522 | 0.141 | 0.155 | 0.377 | 0.405 |
| **CD158b** | 0.404 | 0.49 | 0.409 | 0.403 | 0.214 | 0.377 | 0.48 | 0.346 | 0.375 | 0.178 |
| **CD161** | 0.347 | 0.434 | 0.668 | 0.224 | 0.206 | 0.387 | 0.404 | 0.0948 | 0.18 | 0.275 |
| **CD162** | 0.393 | 0.298 | 0.0931 | 0.532 | 0.212 | 0.482 | 0.162 | 0.259 | 0.19 | 0.51 |
| **CD163** | 0.665 | 0.714 | 1.2 | 0.625 | 0.147 | 0.514 | 0.39 | 0.0499 | 0 | 0.253 |
| **CD164** | 99 | 90.6 | 98.5 | 92.9 | 98.4 | 93.2 | 90.8 | 96.3 | 93.7 | 88.1 |
| **CD165** | 83.2 | 73.4 | 86 | 48.4 | 90.8 | 41.3 | 64.3 | 87.4 | 67.6 | 26.6 |
| **CD166** | 96.5 | 83.4 | 88.6 | 88.6 | 87.5 | 63.9 | 90 | 87.8 | 79.2 | 83.9 |
| **CD171** | 3.56 | 0.824 | 0.945 | 1.03 | 0.461 | 0.229 | 2.74 | 0.324 | 3.23 | 0.255 |
| **CD172b** | 0.881 | 0.882 | 0.597 | 0.218 | 0.0486 | 0.297 | 0.134 | 0.0525 | 0.182 | 0.176 |
| **CD177** | 0.901 | 1.21 | 0.988 | 0.448 | 0.1 | 0.356 | 0.432 | 0.165 | 0.178 | 0.431 |
| **CD178** | 0.715 | 0.497 | 0.526 | 0.523 | 0.195 | 0.363 | 0.161 | 0.102 | 0.37 | 0.369 |
| **CD180** | 0.454 | 0.947 | 0.665 | 0.563 | 0.247 | 0.409 | 0.136 | 0.225 | 0 | 0.403 |
| **CD181** | 0.7 | 0.452 | 0.627 | 0.672 | 0.362 | 0.378 | 0.92 | 0.106 | 0.372 | 0.51 |
| **CD183** | 0.909 | 0.366 | 0.742 | 0.829 | 0.186 | 0.487 | 0.308 | 0.154 | 0.187 | 0.219 |
| **CD184** | 0.464 | 0.504 | 0.54 | 0.522 | 0.375 | 0.325 | 0.462 | 0.197 | 0.375 | 0.388 |
| **CD193** | 1.02 | 0.863 | 0.709 | 0.878 | 0.218 | 0.45 | 0.415 | 0 | 0.187 | 0.535 |
| **CD195** | 1.13 | 1.4 | 1.42 | 0.586 | 0.166 | 0.521 | 0.524 | 0.0504 | 0.182 | 0.319 |
| **CD196** | 1.25 | 1.32 | 1.29 | 0.641 | 0.202 | 0.534 | 0.431 | 0.111 | 0.503 | 0.257 |
| **CD197** | 1.14 | 1.13 | 1.24 | 0.64 | 0.262 | 0.637 | 0.634 | 0 | 1.42 | 0.405 |
| **CD200** | 7.78 | 7.12 | 5.77 | 0.541 | 1.23 | 0.914 | 0.603 | 0.223 | 0.202 | 21.2 |
| **CD205** | 1.17 | 0.451 | 0.8 | 0.626 | 0.278 | 0.667 | 0.446 | 0.226 | 0.601 | 0.335 |
| **CD206** | 1.32 | 1.05 | 1.32 | 0.565 | 0.26 | 0.317 | 0.849 | 0.112 | 0.394 | 0.319 |
| **CD220** | 0.482 | 1.05 | 0.579 | 0.315 | 0.305 | 0.521 | 0.447 | 0.314 | 0.191 | 0.299 |
| **CD221** | 24.7 | 22.9 | 15.4 | 3.23 | 2.55 | 1.8 | 7.38 | 2.49 | 15.1 | 2.65 |
| **CD226** | 0.193 | 0.541 | 0.484 | 0.463 | 0.175 | 0.478 | 0.933 | 0.272 | 0.731 | 0.298 |
| **CD227** | 79.6 | 44.1 | 33.6 | 18.5 | 20.1 | 3.23 | 10.5 | 7.19 | 6.78 | 33.6 |
| **CD229** | 0.994 | 0.509 | 1.08 | 0.66 | 0.386 | 0.354 | 0.406 | 0.105 | 1.1 | 0.48 |
| **CD231** | 2.15 | 1.91 | 3.03 | 0.978 | 0.211 | 0.837 | 0.461 | 0.315 | 0.704 | 0.458 |
| **CD235a** | 7.31 | 1.33 | 4.79 | 6.03 | 5.98 | 3.03 | 9.34 | 4.67 | 13.8 | 0.769 |
| **CD243** | 1.82 | 2.47 | 2.02 | 0.737 | 0.384 | 0.282 | 0.558 | 0.218 | 0.536 | 0.256 |
| **CD244** | 1.03 | 1.3 | 0.968 | 0.618 | 0.175 | 0.496 | 0.591 | 0 | 0.563 | 0.324 |
| **CD255** | 1.15 | 2.95 | 1.29 | 1.91 | 0.207 | 0.639 | 1.13 | 0.161 | 0.427 | 2.97 |
| **CD268** | 0.718 | 0.52 | 0.792 | 0.659 | 0.29 | 0.38 | 0.525 | 0 | 0.419 | 0.222 |
| **CD271** | 2.85 | 1.24 | 1.13 | 0.756 | 0.255 | 0.625 | 0.696 | 0.271 | 3.11 | 0.765 |
| **CD273** | 7.11 | 14 | 13 | 7.56 | 7.01 | 10.5 | 24.4 | 17.3 | 42.3 | 15.6 |
| **CD274** | 20.8 | 28.9 | 19.8 | 18.4 | 20.5 | 17.5 | 62.2 | 47.3 | 57.3 | 5.84 |
| **CD275** | 0.433 | 0.447 | 0.535 | 0.654 | 0.336 | 0.737 | 0.467 | 0.161 | 0.735 | 0.357 |
| **CD278** | 0.423 | 0.349 | 0.271 | 0.545 | 0.274 | 0.525 | 0.602 | 0.107 | 1.08 | 0.252 |
| **CD279** | 0.796 | 0.775 | 0.701 | 0.53 | 0.184 | 0.526 | 0.591 | 0 | 0.362 | 0.326 |
| **CD282** | 1.51 | 0.993 | 0.983 | 0.699 | 0.348 | 0.528 | 0.562 | 0.0502 | 0 | 0.461 |
| **CD305** | 3.06 | 2.41 | 1.88 | 0.723 | 0.302 | 0.588 | 0.399 | 0.163 | 0.182 | 0.702 |
| **CD309** | 1.18 | 1.43 | 1.23 | 0.441 | 0.275 | 0.817 | 0.867 | 0.275 | 0 | 0.269 |
| **CD314** | 1.09 | 0.614 | 0.729 | 0.493 | 0.27 | 0.521 | 0.547 | 0.112 | 0.196 | 0.424 |

| | | | | | | | | | | |
|---|---|---|---|---|---|---|---|---|---|---|
| **CD321** | 46.9 | 7.95 | 43.6 | 7.4 | 8.83 | 19.2 | 19.3 | 4.76 | 21 | 0.644 |
| **CDw327** | 0.619 | 0.482 | 0.597 | 0.616 | 0.172 | 0.38 | 0.292 | 0.279 | 0 | 0.551 |
| **CDw328** | 1.35 | 0.887 | 1.36 | 0.539 | 0.272 | 0.37 | 0.764 | 0.251 | 0.344 | 0.354 |
| **CDw329** | 1.46 | 1.08 | 1.37 | 0.589 | 0.382 | 0.39 | 0.708 | 0.324 | 0.748 | 0.339 |
| **CD335** | 1.1 | 0.81 | 1.41 | 0.513 | 0.593 | 0.27 | 0.797 | 0.306 | 1.26 | 0.342 |
| **CD336** | 0.917 | 1.05 | 0.784 | 0.502 | 1.24 | 0.584 | 1.29 | 1.19 | 1.06 | 0.363 |
| **CD337** | 1.31 | 1.08 | 0.986 | 0.416 | 0.299 | 0.512 | 0.882 | 0.226 | 0 | 0.391 |
| **CD338** | 3.73 | 1.05 | 1.54 | 0.868 | 0.227 | 0.376 | 0 | 0.113 | 0 | 0.585 |
| **CD340** | 94.6 | 56.3 | 76.5 | 37.8 | 25.6 | 25.2 | 24.9 | 13.8 | 26 | 33.3 |
| **abTCR** | 1.06 | 0.95 | 0.749 | 0.699 | 0.258 | 0.448 | 0.311 | 0.171 | 0.203 | 0.345 |
| **B2-uGlob** | 95.7 | 93.3 | 98 | 88.6 | 85.5 | 68.7 | 90.6 | 81.2 | 79.4 | 90.2 |
| **BLTR-1** | 0.371 | 0.62 | 0.788 | 0.534 | 0.204 | 0.325 | 0.437 | 0 | 0.39 | 0.152 |
| **CLIP** | 0.915 | 0.618 | 0.951 | 0.657 | 0.124 | 0.432 | 0.273 | 0.16 | 0 | 0.236 |
| **CMRF-44** | 1.17 | 1.22 | 1.57 | 0.512 | 0.149 | 0.697 | 0.412 | 0.328 | 0.943 | 0.205 |
| **CMRF-56** | 1.78 | 0.862 | 0.914 | 1.37 | 0.149 | 0.292 | 0.259 | 0.326 | 0.548 | 0.497 |
| **Fmlp-r** | 0.835 | 0.853 | 0.875 | 0.492 | 0.293 | 0.55 | 0.43 | 0.331 | 0.755 | 0.435 |
| **gd TCR** | 1.16 | 0.724 | 0.813 | 0.295 | 0.612 | 0.583 | 1.62 | 0.102 | 0.361 | 0.394 |
| **Hem. Prog. Cell** | 8.4 | 1.56 | 0.88 | 1.28 | 0.253 | 0.389 | 1.11 | 0.277 | 0.185 | 0.615 |
| **HLA-A,B,C** | 98.6 | 98.4 | 99.4 | 99.6 | 81.8 | 98.1 | 92.3 | 74.8 | 81.9 | 96.9 |
| **HLA-A2** | 1.34 | 0.971 | 0.865 | 0.408 | 0.65 | 0.488 | 0.665 | 0.197 | 0.348 | 0.194 |
| **HLA-DQ** | 43.9 | 43.9 | 48.3 | 34 | 5.18 | 29.3 | 8.03 | 12.6 | 6.74 | 30.1 |
| **HLA-DR** | 0.564 | 0.487 | 0.508 | 0.62 | 0.159 | 0.467 | 0.27 | 0.203 | 0.697 | 10.1 |
| **HLA-DR,DP,DO** | 1.25 | 0.836 | 0.823 | 0.553 | 0.368 | 0.401 | 0.565 | 0.171 | 1 | 11 |
| **Invariant NKT** | 0.828 | 0.592 | 0.711 | 0.53 | 0.226 | 0.724 | 0.759 | 0.0509 | 0.174 | 0.327 |
| **Disialoganglioside GD2** | 3.21 | 5.09 | 1.73 | 2.82 | 8.96 | 0.873 | 0.675 | 1.07 | 0.71 | 26.3 |
| **MIC A/B** | 5 | 0.752 | 12.6 | 17.4 | 0.517 | 16.1 | 2.92 | 0.612 | 7.5 | 0.522 |
| **NKB1** | 1.31 | 0.626 | 1.09 | 0.588 | 0.276 | 0.276 | 1.33 | 0.212 | 1.02 | 0.457 |
| **SSEA-1** | 1.14 | 0.925 | 1.21 | 1.2 | 0.414 | 2.04 | 1.62 | 1.01 | 8.1 | 0.672 |
| **SSEA-4** | 75.4 | 84 | 80.5 | 66.9 | 87.4 | 52.7 | 10.6 | 45.5 | 6.43 | 80.3 |
| **TRA-1-60** | 0.809 | 0.964 | 0.825 | 0.295 | 0.263 | 0.563 | 0.57 | 0.22 | 1.15 | 0.428 |
| **TRA-1-81** | 0.707 | 0.474 | 0.597 | 0.555 | 0.412 | 0.649 | 0.462 | 0.345 | 0 | 0.403 |
| **Vb 23** | 0.777 | 0.515 | 0.884 | 0.451 | 0.264 | 0.303 | 0.153 | 0.162 | 0.201 | 0.239 |
| **Vb 8** | 0.656 | 1.01 | 0.688 | 0.508 | 0.293 | 0.484 | 0.408 | 0.104 | 0.36 | 0.37 |
| **CD326** | 3.55 | 1.55 | 1.35 | 1.33 | 0.413 | 0.684 | 0.388 | 0.201 | 0.484 | 0.363 |
| **mIgM** | 1 | 0.591 | 0.752 | 0.465 | 0.0241 | 0.404 | 0.255 | 0 | 0 | 0.294 |
| **mIgG1** | 0.994 | 1.22 | 0.931 | 0.387 | 0.0252 | 0.446 | 0 | 0 | 0 | 0.144 |
| **mIgG2a** | 0.787 | 0.758 | 0.869 | 0.346 | 0.125 | 0.266 | 0 | 0 | 0.183 | 0.208 |
| **mIgG2b** | 1.02 | 0.552 | 0.943 | 0.191 | 0.0224 | 0.355 | 0.125 | 0 | 0.167 | 0.292 |
| **mIgG3** | 0.894 | 0.864 | 0.788 | 0.627 | 0.0721 | 0.407 | 0.404 | 0.179 | 0 | 0.161 |
| **CD49f** | 73.7 | 70.5 | 75.4 | 91.5 | 75 | 89.1 | 79.1 | 84.4 | 49.2 | 88 |
| **CD104** | 3.42 | 1.23 | 1.77 | 0.803 | 0.271 | 0.319 | 0.826 | 0.27 | 0 | 0.382 |
| **CD120b** | 0.352 | 0.648 | 0.113 | 0.516 | 0.157 | 0.361 | 0.59 | 0.0511 | 0.521 | 1.73 |
| **CD132** | 0.336 | 0.269 | 0.594 | 0.86 | 0.417 | 0.756 | 1.33 | 0.207 | 0.898 | 0.596 |
| **CD201** | 94.5 | 79.1 | 95 | 96.5 | 77 | 93.8 | 50.3 | 53.4 | 39.7 | 85.3 |
| **CD210** | 0.312 | 0.389 | 0.214 | 0.677 | 0.184 | 0.539 | 0.485 | 0 | 0.173 | 0.283 |
| **CD212** | 0.12 | 0.249 | 0.292 | 0.645 | 0.0235 | 0.42 | 0.362 | 0.255 | 0.192 | 0.287 |
| **CD267** | 0.353 | 0.138 | 0.222 | 0.45 | 0.0463 | 0.455 | 0.528 | 0.108 | 0.366 | 0.319 |
| **CD294** | 0.515 | 0.414 | 0.495 | 0.526 | 0.146 | 0.695 | 0.214 | 0.0964 | 0 | 0.486 |
| **SSEA3** | 0.168 | 0.627 | 0.381 | 0.857 | 0.215 | 0.834 | 0.733 | 0.168 | 0.746 | 33.9 |

| | | | | | | | | | | |
|---|---|---|---|---|---|---|---|---|---|---|
| **Cut. Lymph. Ant.** | 0.464 | 1.3 | 2.17 | 1.03 | 0.972 | 4.53 | 0.84 | 1.93 | 0.18 | 0.57 |
| **INT B7** | 0.39 | 0.621 | 0.457 | 0.825 | 0.0665 | 0.751 | 0.46 | 0.158 | 0.5 | 1.32 |
| **rIgM** | 0.541 | 0.212 | 0.445 | 0.573 | 0.143 | 0.61 | 0.632 | 0.108 | 0 | 0.319 |
| **rIgG1** | 0.337 | 0.261 | 0.64 | 0.323 | 0.146 | 0.67 | 0.26 | 0.169 | 0.2 | 0.52 |
| **rIgG2a** | 0.403 | 0.192 | 0.111 | 0.364 | 0.26 | 0.448 | 0.535 | 0.218 | 0.358 | 0.214 |
| **rIgG2b** | 0.248 | 0.421 | 0.16 | 0.558 | 0.182 | 0.525 | 0.259 | 0.259 | 0.172 | 0.207 |

### *B.3.2 Stiffness-driven changes in iMSC morphology are consistent across multiple iMSC lines*

Hydrogels were formed by photocrosslinking Nor groups in HA macromers with thiols in DTT crosslinkers as previously reported.[167] The amount of macromer (3 wt%) was kept constant and Low (5.19 ± 1.04 kPa), Med (9.58 ± 0.98), and High (19.27 ± 2.41 kPa) matrix stiffness hydrogels were formed by varying the amount of crosslinker added (Figure B.5). It is important to maintain the amount of HA constant since MSCs interact with HA via surface receptors including CD44 and CD168.[296] To promote cell adhesion, thiolated RGD peptides were coupled to the macromer backbone using a procedure described in the supplemental methods section (Figure B.5), and $^1$H NMR was used to confirm HA modifications (Figure B.6).

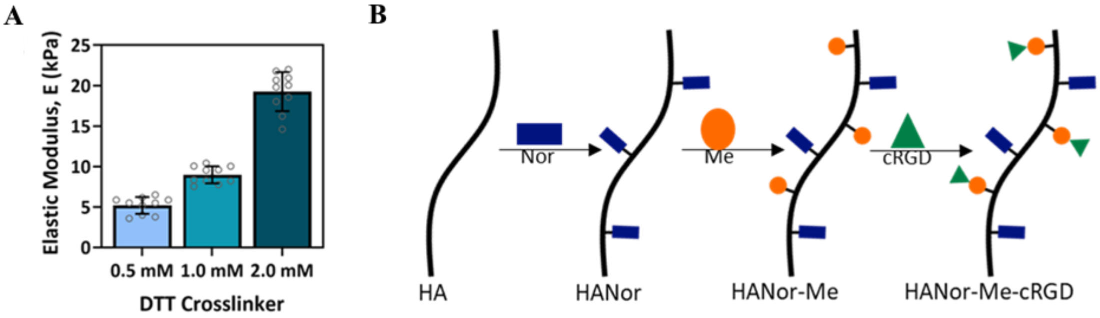

*Figure B. 5.* Hydrogel mechanics characterization and macromer design. **(A)** Click crosslinking reaction between norbornenes in HA macromer and dithiothreitol (DTT) was used to form hydrogels with a range in mechanics by varying crosslinker concentrations (Low, 0.5 mM; Med, 1.0 mM, High, 2.0 mM). **(B)** Scheme for forming HANor-Me-cRGD macromers from HA. Bar graphs represent the mean and error bars represent standard deviation.

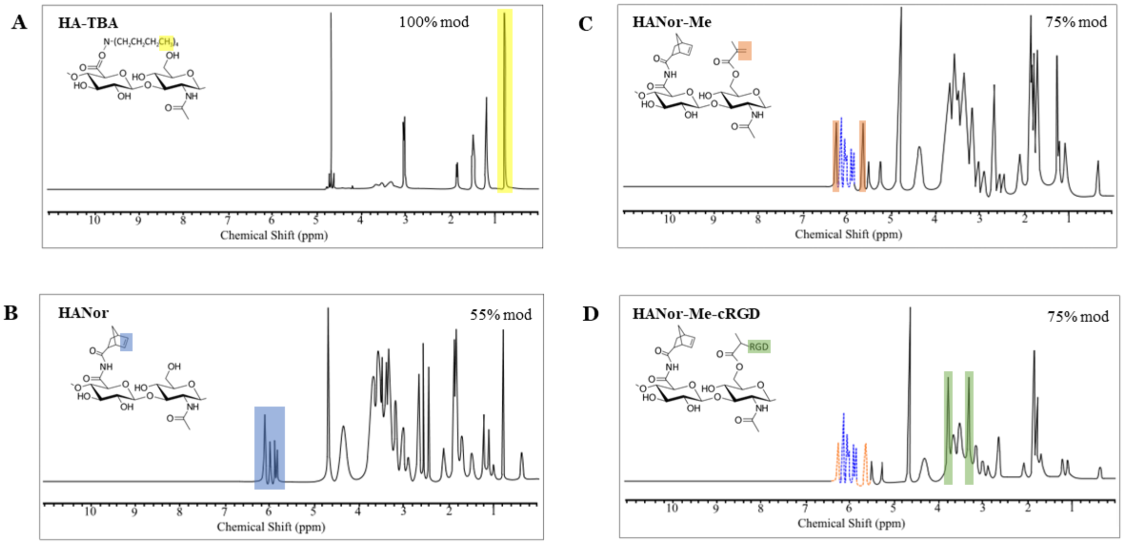

*Figure B. 6.* ${}^{1}$H-NMR spectra of hyaluronic acid with coupled functionalities. NMR of **(A)** Tetrabutylammonium salt of hyaluronic acid (HA-TBA) shows 100% modification with TBA (yellow peak), **(B)** Hyaluronic acid coupled with norbornene (HANor) shows 55% modification with Nor- (blue peaks), **(C)** HANor coupled with methacrylates (HANorMe) shows 75% modification with Me- (orange peaks), and **(D)** HANorMe coupled with thiolated RGD peptide (HANorMe-cRGD) shows 75% modification with cRGD peptide (green peaks).

To evaluate the effects of stiffness on iMSC morphology, three different iMSC lines were cultured atop Low, Med, and High stiffness hydrogels. After three days in culture, all iMSC lines displayed comparable stiffness-mediated changes in morphology. Cell area for iMSCs on Low, Med, and High stiffness hydrogels was 530 ± 141, 900 ± 360, and 1,400 ± 250 $\mu m^2$, respectively (Figure B.7A). Although average cell area values were consistent with data of MSCs cultured on hydrogels of comparable stiffness, there were significant differences in area across different MSC lines (Figure B.8A). In contrast, low heterogeneity was observed within and across iMSC lines for iMSCs cultured on Low, Med, and High stiffness hydrogels (Figure B.7A). Next, we evaluated circularity since MSC roundness decreases with increasing stiffness on 2D substrates.[187] Analogous to MSCs, iMSC circularity decreased with increasing stiffness, with circularity values ranging from 0.81 ± 0.14 for iMSCs on Low to 0.24 ± 0.12 for iMSCs on Stiff hydrogels (Figure B.7B).

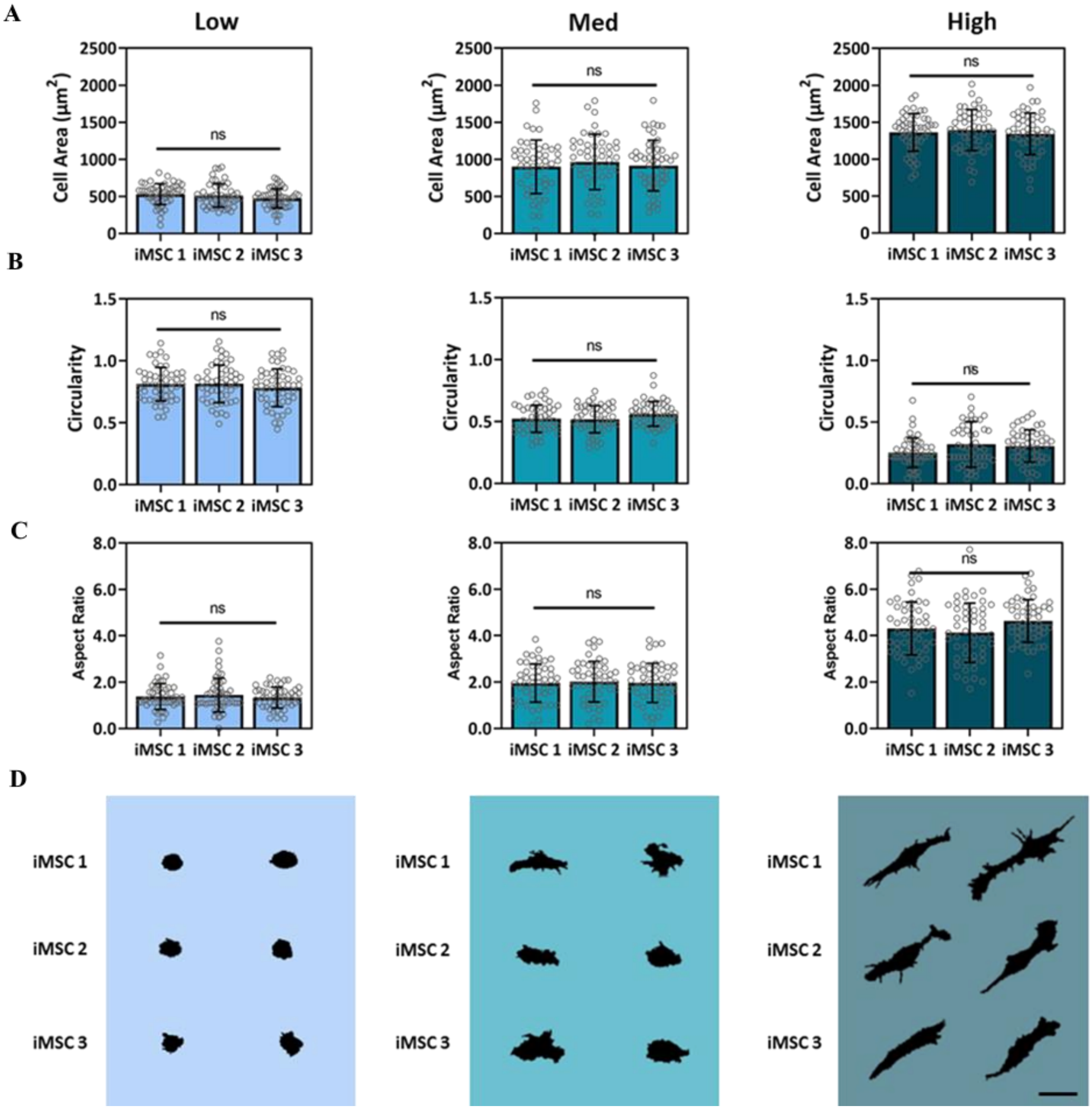

*Figure B. 7*. Effects of Matrix Stiffness on iMSC Morphology. Single-cell image analysis was performed to attain iMSC **(A)** cell Area, **(B)** circularity, and **(C)** aspect ratio for three iMSC lines cultured on Low, Med, and High stiffness hydrogels. **(D)** Representative single-cell silhouettes of iMSCs cultured atop Low, Med, and High hydrogels shown. Scale bar, 50 μm. Bar graphs represent the mean and error bars represent standard deviation; n > 50 cells per group, n.s. not significant.

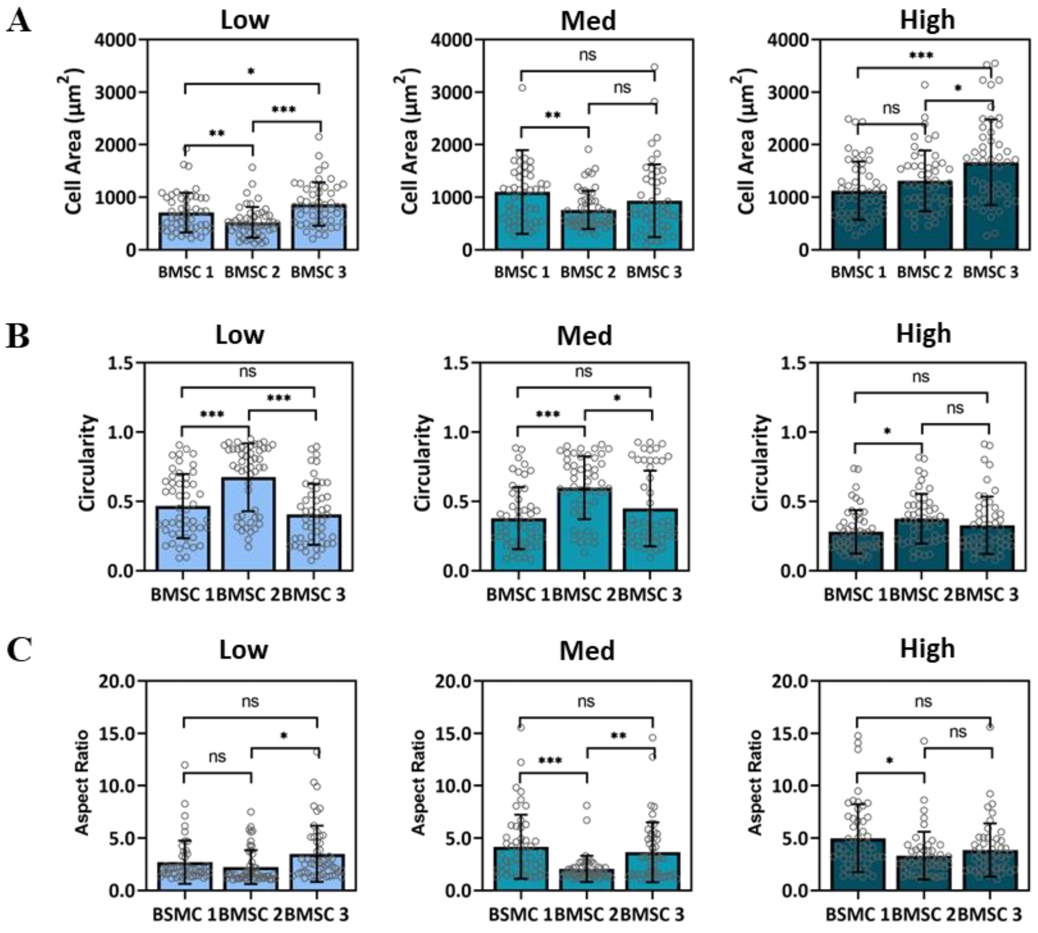

*Figure B. 8.* Cell morphology quantifications for MSCs cultured atop Low, Med, and High stiffness hydrogels. **(A)** Cell spread area. **(B)** Cell circularity. **(C)** Cell aspect ratio. n > 50 cells per group, bar graphs represent the mean and error bard represent standard deviation, *p < 0.1, **p < 0.01, ***p < 0.001, ns = no significant difference.

Aspect ratio indicates cellular elongation, and iMSC aspect ratio increased with increasing stiffness, with aspect ratio values ranging from 1.32 ± 0.51 for iMSCs on Low to 4.31 ± 0.81 on High stiffness hydrogels (Figure B.7C). Although iMSC and MSC stifness-mediated circularity and aspect ratio trends are consistent, there is significant variability in MSC circularity (Figure B.8B) and aspect ratio (Figure B.8C) values. Representative images of single-cell silhouettes show observable differences in morphology in different stiffness groups but show no discernable differences across iMSC lines cultured on Low, Med, and High stiffness hydrogels (Figure B.7D). These results show that although stiffness-driven changes in morphology for iMSCs follow the same trend as MSCs, iMSC morphology is more consistent and less heterogeneous across iMSC lines.

### *B.3.3 Mechanosensitive biomarkers of iMSCs are significantly impacted by matrix mechanics*

After demonstrating that iMSC morphology is highly consistent across donors and matrix stiffness groups, we evaluated stiffness-driven changes in iMSC mechanosensing. YAP acts as a nuclear relay of mechanical signals exerted by matrix stiffness and cell shape.[185,187,395] In MSCs, YAP is predominantly cytoplasmic in small and round cells and is nuclear in spread cells. After three days in culture, all iMSC lines displayed increasing nuclear YAP with increasing stiffness, with nuclear YAP values ranging from 1.22 ± 0.44 on Low to 2.76 ± 0.58 on High stiffness hydrogels (Figure B.9A). Although the stiffness-mediated trend in average nuclear YAP values is consistent with data of MSCs cultured on hydrogels of comparable stiffness[187], the range in nuclear YAP values across stiffness groups is much larger for iMSCs than for MSCs (Figure B.10A).

Besides nuclear YAP localization, focal adhesion morphology and actin anisotropy give an insight to MSC mechanosensing.[384,396] Phosphorylated focal adhesion kinase (pFAK) is known to initialize at least two signaling pathways of MSC mechanosensing and plays an important role in controlling several cellular processes including cell spreading and migration.[182] After three days in culture, all iMSC lines displayed an increase in focal adhesion maturation with increasing matrix stiffness. pFAK length for iMSCs on Low, Med, and High stiffness hydrogels was 3.94 ± 0.56, 5.98 ± 0.62, and 7.18 ± 0.56 μm, respectively (Figure B.9B). Number of adhesions per cell also increased with increasing stiffness, with an average of 6 ± 1 focal adhesions per cell on Low and 25 ± 3 on High stiffness hydrogels (Figure B.9C). Actin anisotropy is a measure of actin stress fiber alignment, and MSCs on stiff matrices (≥ 20 kPa) exhibit high cytoskeletal tension, resulting in anisotropic actin fibers.[397] Actin anisotropy of iMSCs also increased with increasing stiffness, and actin anisotropy values were consistent across all iMSC lines (Figure B.9D).

Average iMSC pFAK length values show low standard deviations within stiffness groups and a large range in pFAK lengths of iMSCs atop Low, Med, and High stiffness hydrogels. The average iMSC pFAK length is ~2 µm longer than for MSCs on the same stiffness conditions, and the standard deviations are lower for iMSCs on every stiffness group (Figure B.10B). Similarly, iMSC lines exhibit more adhesions per cell (~10 more adhesions) than MSCs for every stiffness group (Figure B.10C). The increase in actin anisotropy for iMSCs across the stiffness groups is consistent and highly significant, whereas for MSCs the increase between the Low to Med stiffness is greater than from Med to High stiffness (Figure B.10D). Representative quantifications of low (1.14) and high (3.26) nuclear YAP values (Figure B.9E) show brighter nuclear fluorescence for higher nuclear YAP values. The representative quantification of high (0.32) actin anisotropy (Figure B.9F) show actin fibers with prevailing directionality. Representative quantifications of low (Figure B.9G) and high (Figure B.9H) pFAK length feature the observable differences in focal adhesion maturation and number of adhesions in each cell. Taken together, these findings show that iMSC lines are highly homogeneous and mechanoresponsive to matrix stiffness.

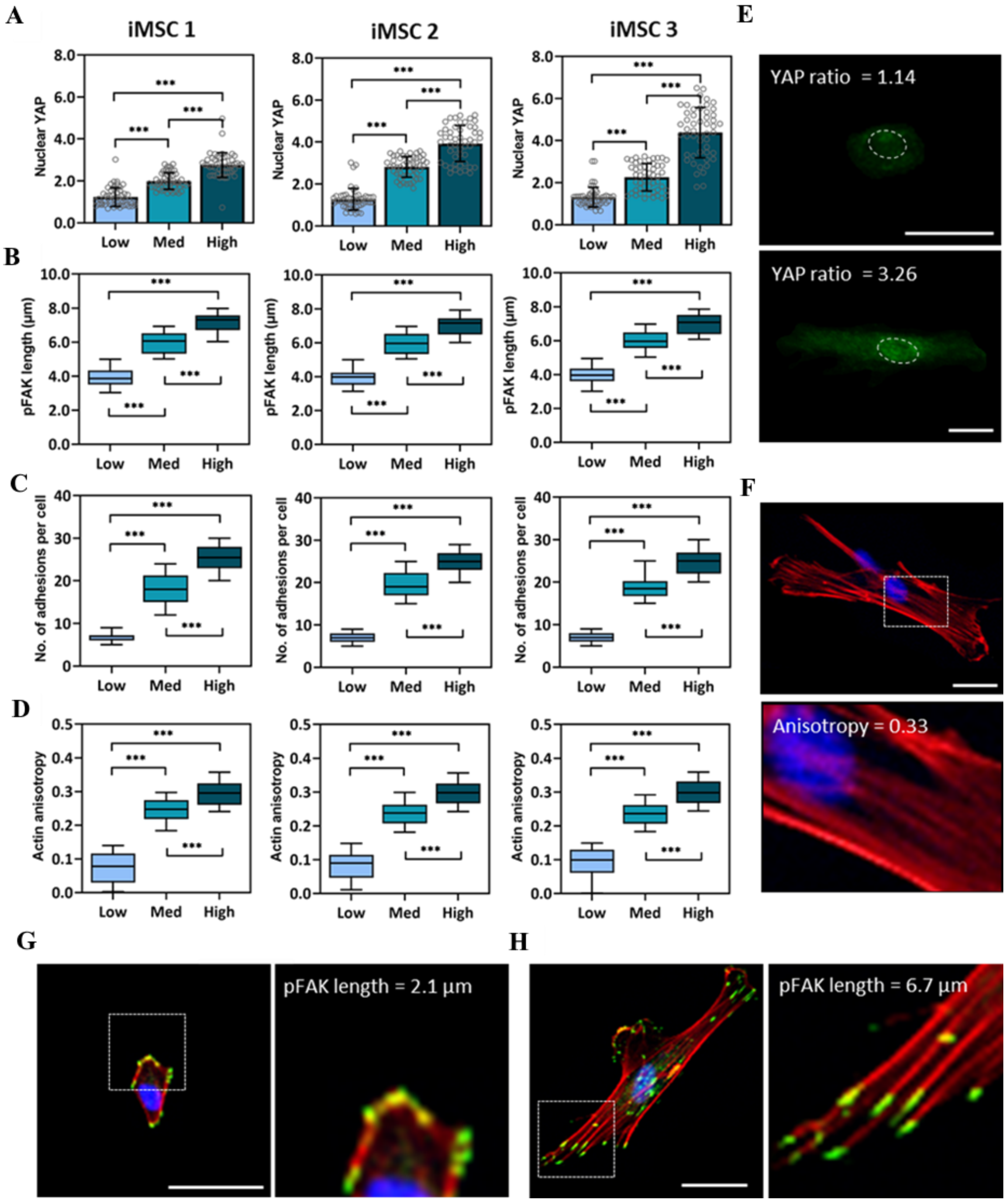

*Figure B. 9.* Mechanosensitivity of iMSC lines. Single-cell image analysis of **(A)** nuclear YAP localization, **(B)** pFAK length, **(C)** number of adhesions per cell, and **(D)** actin fiber anisotropy of iMSCs cultured atop Low, Med, and High stiffness hydrogels. **(E)** Representative quantifications of high and low nuclear YAP ratios (YAP, green; nucleus, white dashed oval). Scale bar, 50 µm. **(F)** Representative image and quantification of iMSC cultured atop Med stiffness hydrogel (red, actin; blue, nucleus). Scale bar, 50 µm. Representative image and quantification of iMSC cultured atop a **(G)** Low and **(H)** High stiffness hydrogel (green, pFAK; red, actin; blue, nucleus). Scale bar, 50 µm. Bar graphs represent the mean and error bars represent standard deviation. Box plots show 25/50/75th percentiles, whiskers show minimum/maximum; n > 50 cells per group, *** p < 0.001.

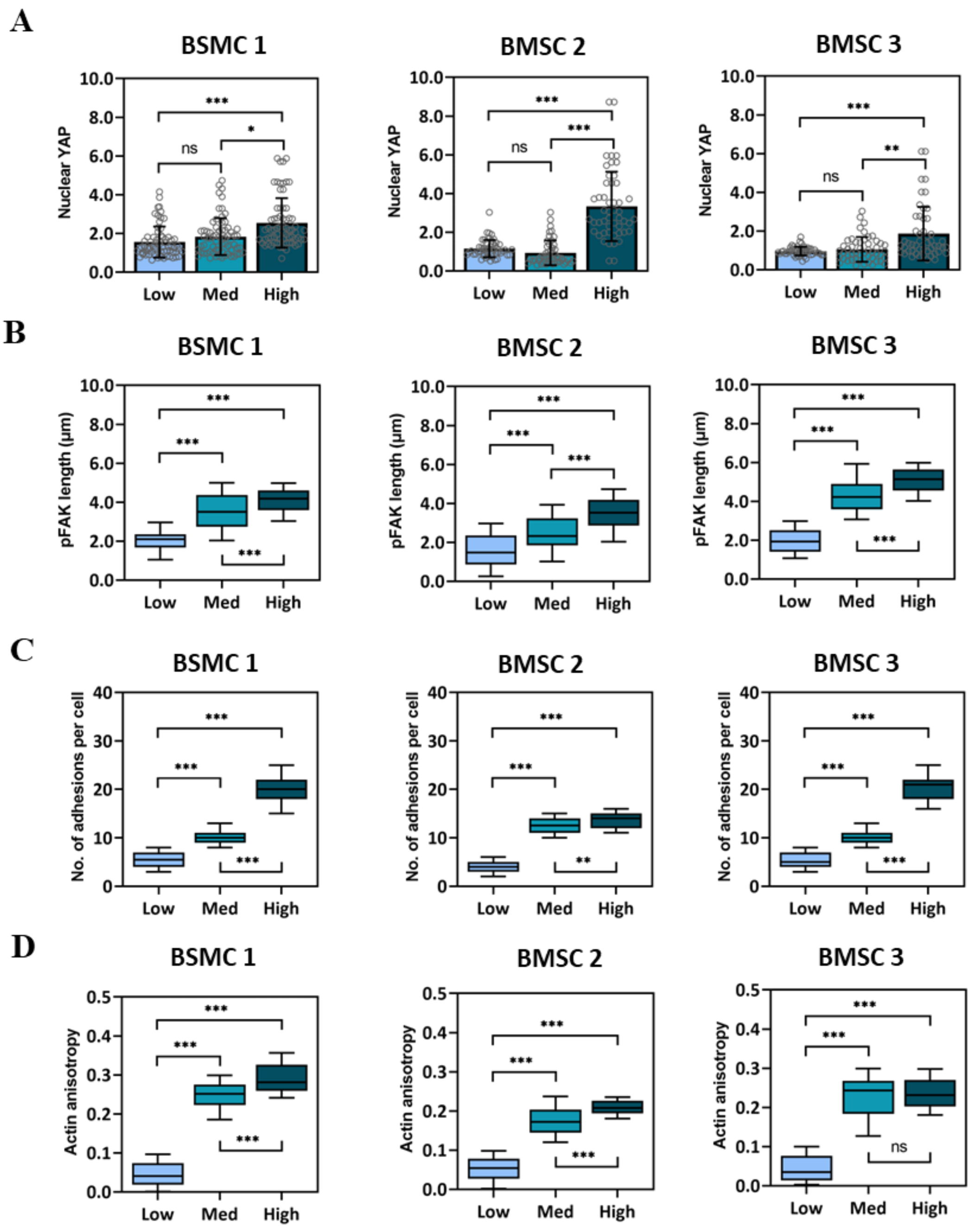

*Figure B. 10.* Mechanosensitivity quantifications for MSCs cultured atop Low, Med, and High stiffness hydrogels. **(A)** YAP nuclear localization. **(B)** Phosphorylated focal adhesion kinase (pFAK) length. **(C)** Number of pFAK adhesions per cell. **(D)** Actin fiber anisotropy. 50 cells per group, box plots show 25/50/75th percentiles, whiskers show minimum/maximum, *p < 0.1, **p < 0.01, ***p < 0.001, ns = no significant difference.

### *B.3.4 iMSCs are more homogeneous and mechanosensitive than MSCs*

Based on the findings above, we performed a direct comparison between iMSC and MSC morphology and cellular mechanosensing. On Med (~10 kPa) stiffness substrates, representative cell silhouettes of iMSCs (Figure B.11A, top) qualitatively show little variation in cell morphology across iMSC lines, whereas cell silhouettes of MSCs (Figure B.11A, bottom) show increased elongation and more variability in morphology across MSC lines. Cell area for iMSCs ranged from 904 ± 355 $\mu m^2$ to 983 ± 348 $\mu m^2$, which is a smaller range than for MSCs (758 ± 364 $\mu m^2$ to 1039 ± 561 $\mu m^2$) on Med stiffness hydrogels. Differences between iMSC and MSC morphology were not as pronounced on Low or High stiffness hydrogels (Figure B.12).

Histograms of cell area show a homogeneous distribution for iMSCs (Figure B.11B, top). In contrast, although MSC lines 2 and 3 had a homogeneous cell area distribution, there was significant heterogeneity observed in MSC line 1 (Figure B.11B, bottom). Histograms of nuclear YAP show that iMSC lines peak at a nuclear YAP ratio of ~2 (Figure B.11C, top), whereas there is significant heterogeneity observed in nuclear YAP values across MSC lines (Figure B.11C, bottom). In the Low and High stiffness groups there was consistent homogeneity (iMSCs) and heterogeneity (MSCs) observed for cell area (Figure B.13), circularity (Figure B.14A), aspect ratio (Figure B.14B), and nuclear YAP localization (Figure B.15).

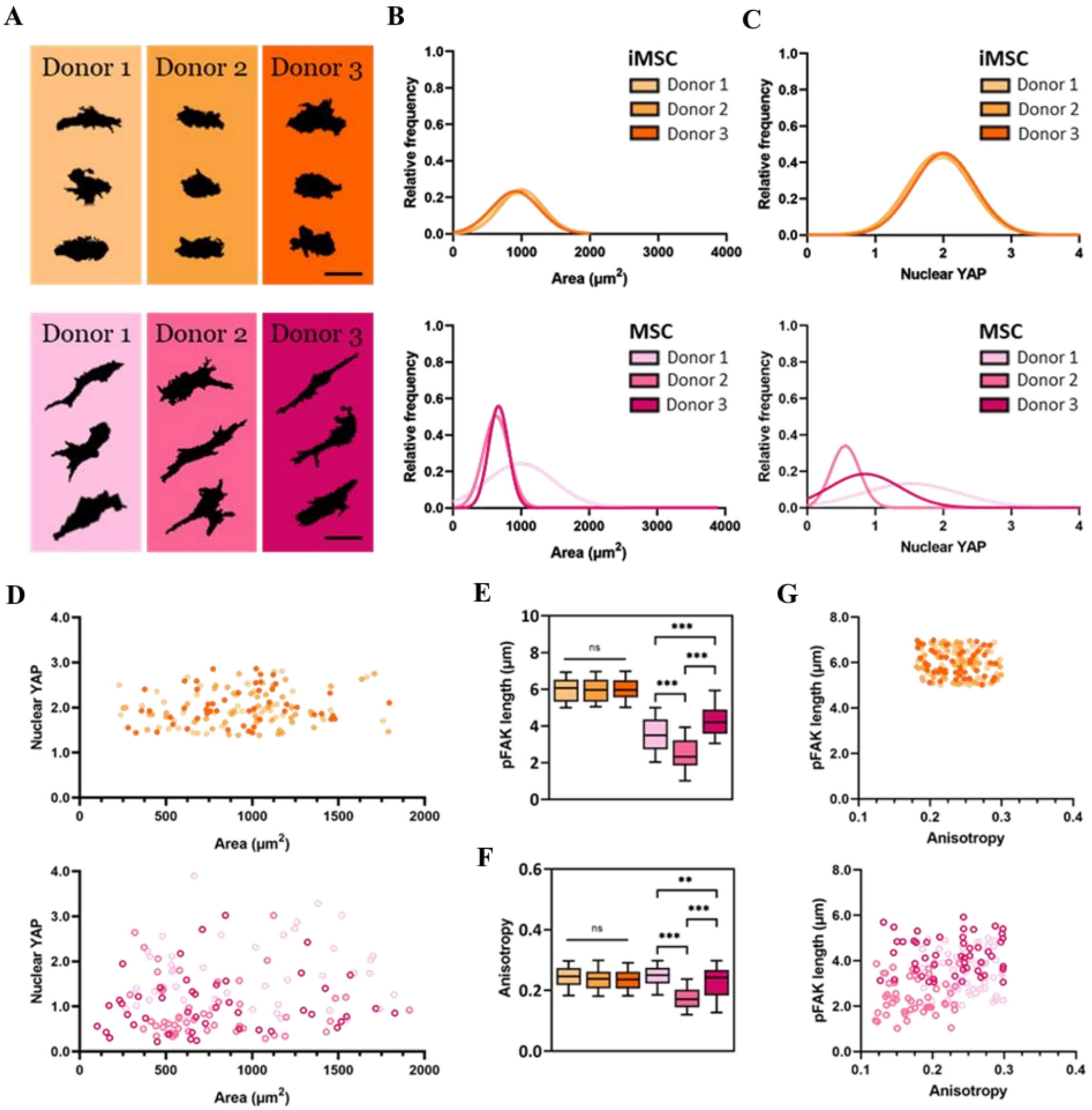

*Figure B. 11*. Morphological and cellular mechanosensing comparison between iMSCs and MSCs on Med stiffness hydrogels. **(A)** Representative cell silhouettes of 3 iMSC (top) and MSC (bottom) cell lines. Histograms of **(B)** cell area and **(C)** nuclear YAP of 3 iMSC (top) and MSC (bottom) cell lines. **(D)** Nuclear YAP versus area scatter plot of 3 iMSC (top) and MSC (bottom) cell lines. Whisker plots of **(E)** pFAK length and **(F)** actin anisotropy of iMSC (3 left whisker plots) and MSC (right whisker plots) cell lines. **(G)** Scatter plots of pFAK length versus actin anisotropy of 3 iMSC (top) and MSC (bottom) cell lines. Scale bars: 50 μm. Box plots show 25/50/75th percentiles, whiskers show minimum/maximum; n > 50 cells per group, * $p < 0.05$, ** $p < 0.01$, *** $p < 0.001$, n.s. not significant.

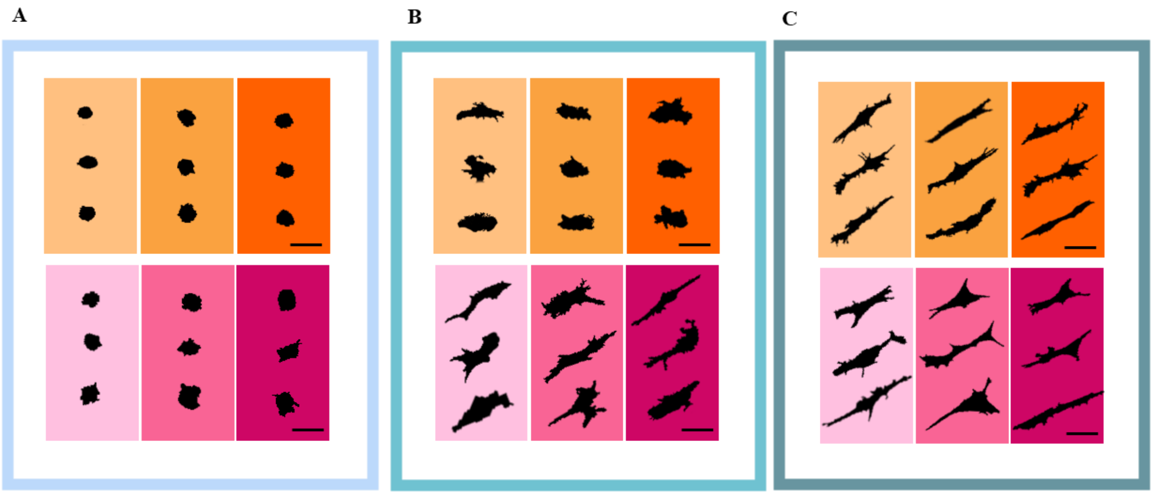

*Figure B. 12.* Representative silhouettes for all iMSC and MSC lines atop Low and High stiffness hydrogels. **(A)** Top: iMSC lines 1 to 3 (left to right), Bottom: BMSC lines 1 to 3 (left to right) on Low hydrogels. **(B)** Top: iMSC lines 1, 2, and 3 (left to right), Bottom: MSC lines 1, 2, and 3 (left to right) on Med hydrogels. **(C)** Top: iMSC lines 1, 2, and 3 (left to right), Bottom: MSC lines 1, 2, and 3 (left to right) on High hydrogels. Scale bars: 50 µm.

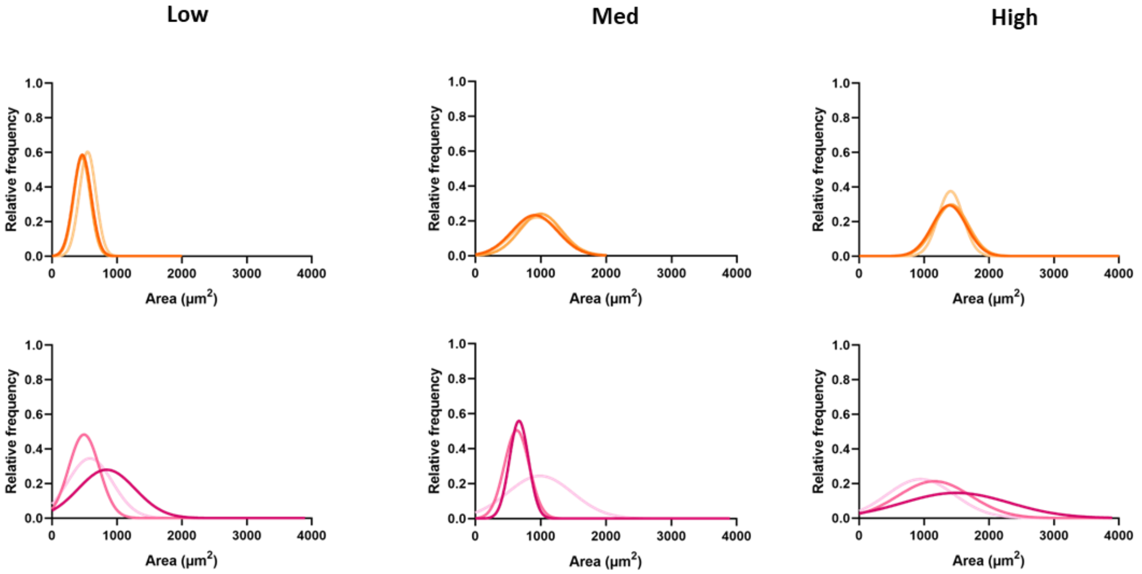

*Figure B. 13.* Frequency distribution of spread area for all iMSC and MSC lines atop Low, Med, and High stiffness hydrogels. Top: iMSC lines 1, 2, and 3, Bottom: MSC lines 1, 2, and 3.

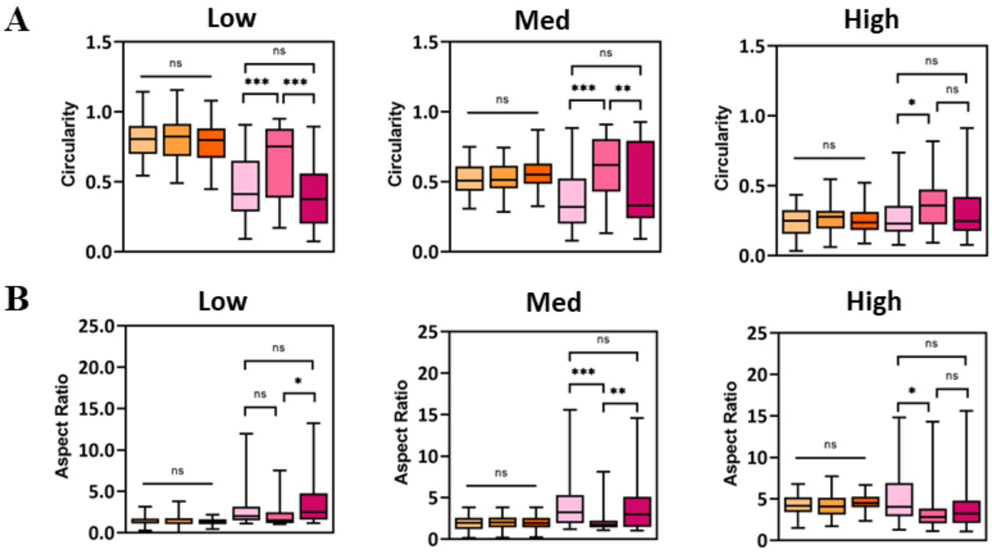

*Figure B. 14.* Morphology quantifications for all iMSC and MSC lines atop Low, Med, and High stiffness hydrogels. **(A)** Cell circularity. **(B)** Aspect ratio. n > 50 cells per group, box plots show 25/50/75th percentiles, whiskers show minimum/maximum, *p < 0.1, **p < 0.01, ***p < 0.001, ns = no significant difference.

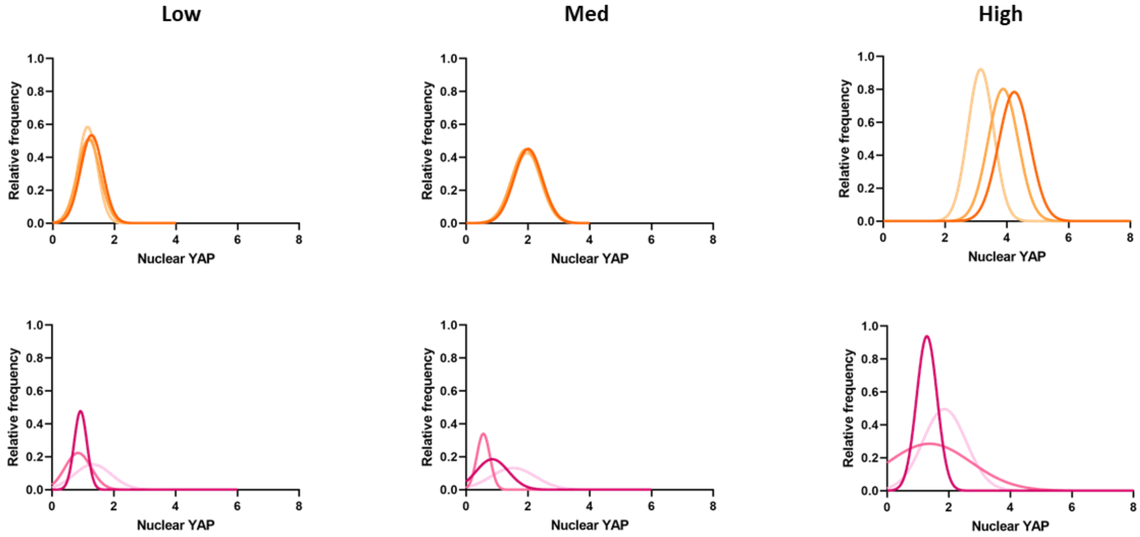

*Figure B. 15.* Frequency distribution of nuclear YAP for all iMSC and MSC lines atop Low, Med, and High stiffness hydrogels. Top: iMSC lines 1, 2, and 3, Bottom: MSC lines 1, 2, and 3.

Next, we examined scatter plots of nuclear YAP versus area of iMSC (Figure B.11D, top) and MSC (Figure B.11D, bottom) lines cultured on Med stiffness hydrogels.

Although there is a range in area for iMSC lines, the range in nuclear YAP values is lower for iMSCs than for MSCs. This observation was also seen between iMSC and MSC lines on Low and High stiffness groups (Figure B.16). An iMSC versus MSC comparison between pFAK length on Med stiffness hydrogels shows no significant difference in pFAK length (~6 µm) for iMSC lines, which contrasts the heterogeneity observed across MSC lines, with values ranging from 2.47 ± 0.82 µm to 4.27 ± 0.83 µm (Figure B.11E).

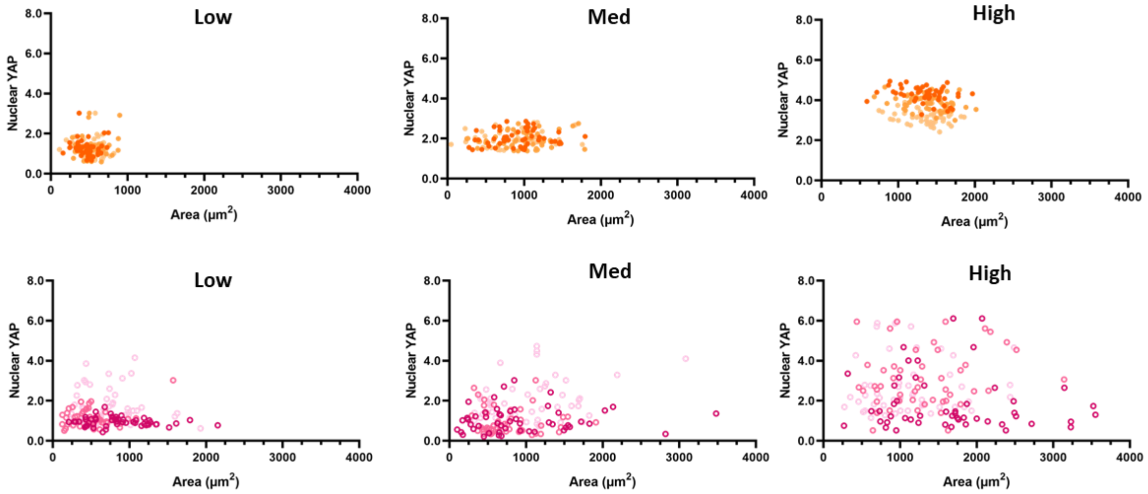

*Figure B. 16.* Scatter dot plot of nuclear YAP as a function of cell area for all iMSC and MSC lines atop Low, Med, and High stiffness hydrogels. Top: iMSC lines 1, 2, and 3, Bottom: MSC lines 1, 2, and 3.

Actin anisotropy values for iMSCs were also consistent across different lines while for MSCs actin anisotropy was significantly different across cell lines (Figure B.11F). These findings were consistent for pFAK length (Figure B.17A) and actin anisotropy (Figure B.17B) between iMSCs and MSCs cultured on Low and High stiffness hydrogels. Single cell scatter plots of pFAK length as a function of actin anisotropy for iMSCs and MSCs on Med stiffness hydrogels reveal tight clustering of data points for iMSC lines (Figure B.11G, top), whereas data points for MSCs were more scattered (Figure B.11G, bottom). This was also observed for iMSCs and MSCs cultured on Low and High stiffness hydrogels (Figure B.18).

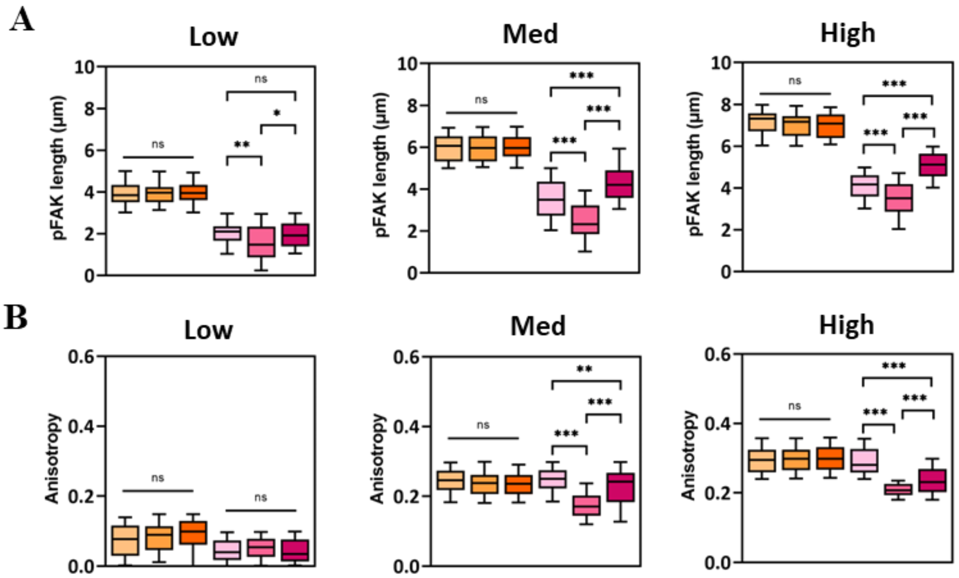

*Figure B. 17.* Mechanosensing quantifications for all iMSC and MSC lines atop Low, Med, and High stiffness hydrogels. **(A)** Phosphorylated focal adhesion kinase (pFAK) length. **(B)** Actin anisotropy. n > 50 cells per group, box plots show 25/50/75th percentiles, whiskers show minimum/maximum, *p < 0.1, **p < 0.01, ***p < 0.001, ns = no significant difference.

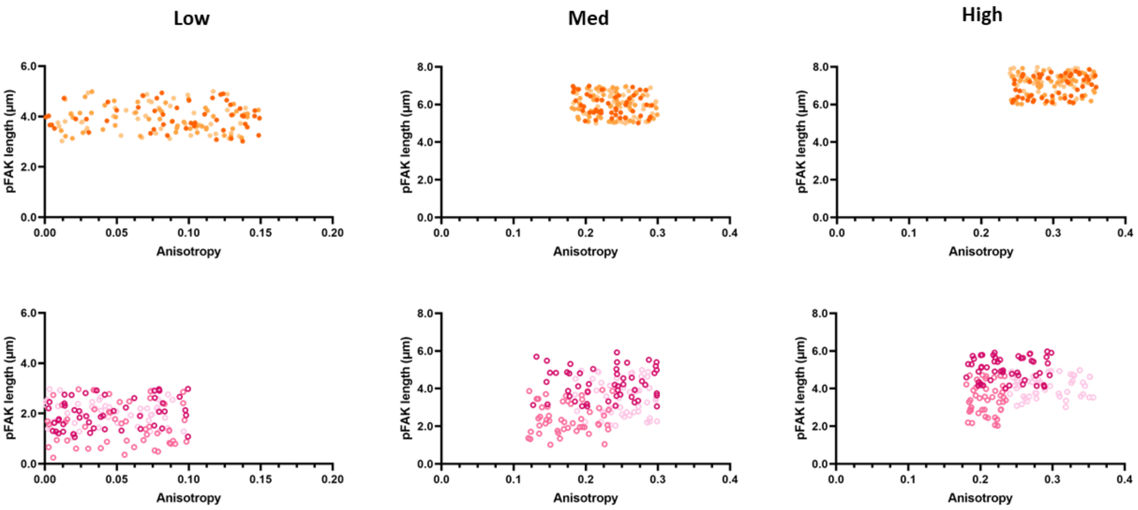

*Figure B. 18.* Scatter dot plot of pFAK length as a function of actin anisotropy for all iMSC and MSC lines on Low, Med, and High stiffness hydrogels. Top: iMSC lines 1, 2, and 3, Bottom: MSC lines 1, 2, and 3.

## B.4 Conclusions

In this study, we derive iMSCs from iPSCs and demonstrate that iMSCs are more homogeneous and mechanosensitive than MSCs isolated from adult tissues. This finding resulted from evaluating iMSC morphology and matrix mechanosensing on mechanically defined 2D hydrogels and motivates future studies that investigate iMSC-material interactions in more complex and physiologically relevant environments. To this end, the thiol-Nor chemistry used here can be easily adapted to form hydrogels that support 3D cell culture and spatial patterning of biophysical and biochemical signals.[196] Due to their remarkable sensitivity and homogeneity, iMSCs could be a viable source for large scale manufacturing of human stem cells for both autogenic and allogeneic cell therapies. As we continue to increase our understanding of iMSC-material interactions, we also believe that iMSCs will emerge as a new class of human stem cells for tissue engineering applications.

## B.5 Experimental Section

### *B.5.1 Derivation and Characterization of Human iMSC Lines*

Skin biopsies were collected from healthy individuals after written informed consent. Human iPSC lines were derived, quality controlled, expanded, and characterized using the Global Stem Cell Array® as previously reported.[390] Generated iPSC lines were expanded in StemFlex™ medium (Thermo Fisher Scientific) on Geltrex™-coated plasticware before mesenchymal induction (iPSC → iMSC). The expression of pluripotency makers was confirmed via immunofluorescence. Briefly, cells were fixed in 4% paraformaldehyde, permeabilized with 0.1% Triton X-100 in PBS, blocked with 5% (vol/vol) donkey serum (Jackson ImmunoResearch Laboratories Inc.) in PBS, and incubated overnight with primary antibodies against TRA-1-60 (2 µL/mL; Stemgent, 09-0010) and Oct-4 (2 µL/mL; Stemgent, 09-0023). Alexa Fluor secondary antibodies were used for detection (1 µL/mL; Invitrogen, A32795 and A32773). Colonies were counterstained with phalloidin (25 µL/mL; Invitrogen, A12379) and Hoechst 33342 (4 µL/mL; Invitrogen; H3570) to visualize the actin filaments and nuclei, respectively. Samples were imaged with an Olympus IX71 mounted with Q-Color 3 imaging camera and equipped with Olympus DP-BSW software.

For mesenchymal induction, confluent iPSC cultures were treated with induction medium consisting of KO-DMEM supplemented with 20% (vol/vol) HyClone FBS, 2 mM GlutaMAX, 0.1 mM nonessential amino acids, 0.1 mM β-mercaptoethanol, and 100 U/mL Anti-Anti (Gibco™) for 1 week. Following induction, cells were passaged using trypsin (0.25%) and cultured in gelatin-coated tissue culture flasks until they became homogenous for a fibroblastic-like morphology.[387] Cells were expanded under similar conditions for 10 passages to investigate their proliferation potential. Briefly, cells were seeded at a density of 5,000 cells/cm$^2$ and cultured in expansion medium for 5 days. At the end of each passage, cells were detached using trypsin (0.25%) and analyzed using a nucleocounter to count and measure the cell size. Results are expressed as cumulative growth.

Presence of pluripotency markers was confirmed for parental iPSC lines (Figure B.2) and absence of these markers was also evaluated for resultant iMSC lines (Figure B.3A). At passage 2, all iMSC lines were also karyotyped to assess genome integrity (Cell Line Genetics) (Figure B.3B). The global surface markers profile was probed using the BD Lyoplate$^{TM}$ Human Cell Surface Marker Screening Panel (BD Biosceinces). Briefly, cells at passage 2, 5, and 10 were detached using trypsin, washed with PBS, and barcoded with Live/Dead Fixable Dyes (Thermo Scientific; L34955, L34959, L23101, L10119) at 5x concentration. Cells were combined and incubated with BD Human Cell Surface Marker Screening Panel (BD Biosciences; 560747). Flow Cytometry data were acquired on a 4-laser Attune NxT (405nm, 488nm, 561nm) with Autosampler. Analysis of data was performed with Flowjo v9.

The mesodermal differentiation potential was evaluated in monolayer and micromass pellet cultures. For monolayer cultures, cells at passage 5 were plated into gelatin-coated cell culture plates and cultured for 4 weeks in OsteoLife™ and AdipoLife™ media (LifeLine). Osteogenesis was evaluated by von Kossa staining of calcium deposition following standard procedures. Adipogenesis was assessed by Oil Red O staining of accumulated lipids following standard procedures. For micromass pellet cultures, 500,000 cells at passage 5 were centrifuged at 300 × g for 5 minutes and cultured for 4 weeks in ChondroLife™ medium (LifeLine). Next, pellets were fixed in

4% paraformaldehyde, washed, cryopreserved in 30% w/v sucrose, and finally embedded in optimal cutting temperature (OCT) solution (Sakura) in isopentane. Thereafter, samples were sectioned using a cryostat at -21 °C and transferred to glass slides (Superfrost plus) for staining. The presence of glycosaminoglycans (GAG) was evaluated by Alcian blue (LifeLine) stain using standard procedures. Expansion medium was used as control for all differentiation experiments.

### *B.5.2 Macromer Synthesis*

Sodium hyaluronate (NaHA) was first converted to its tetrabutylammonium salt (HA-TBA). To synthesize HANor, the carboxylic acid residues of HA-TBA were modified with 5-norbornene-2-methylamine (~50% of repeat units were functionalized with Nor-). To synthesize HANorMe, the hydroxyl residues of HANor were modified with methacrylic anhydride (~75% of repeat units were functionalized with Me-). To biofunctionalize HANorMe with RGD, a Michael addition reaction between thiolated RGD (cRGD) peptide and methacrylates was performed (2 mM final cRGD concentration). Representative $^1$H NMR spectra used to calculate percent of HA repeat units functionalized with Nor- and Me- can be found in Figure B.6.

### *B.5.3 Hydrogel Synthesis and Mechanical Testing*

HANor was dissolved in phosphate buffer saline (PBS) at 3 wt% with varying amounts of DTT and 0.05 wt% I2959. The prepolymer solution (80 µL) was pipetted into a silicone mold (11 mm ⌀, 0.5 mm h) and irradiated with UV light (10 mins, 10 mW/cm$^2$). Individual hydrogels were removed from the molds and placed in 1 mL of PBS to swell overnight at 37 °C before mechanical testing. Compressive moduli were determined using a Shimadzu EZ-SX Mechanical Tester running at a constant strain rate of 10%/min. The modulus was calculated from the slope of the stress-strain curve between 10 and 20% strain ($n \geq 3$).

### B.5.4 Human MSC and iPSC Cell Culture

Stem cell lines from the New York Stem Cell Foundation (NSYCF) expanded to passage 4 in growth media (α-MEM supplemented with 10% (v/v) FBS (Gibco), 1% (v/v) penicillin-streptomycin (Invitrogen)) were used in all experiments. Human mesenchymal stem cell lines (Lonza) were expanded to passage 4 using the culture media described above. Cells were then cultured on top of Low, Medium, or High stiffness hydrogels (3,000 cells/cm$^2$).

### B.5.5 Immunofluorescence Staining, Imaging, and Image Analysis

After 3 days in culture, stem cell-laden hydrogels were fixed, permeabilized, and stained with appropriate antibodies (YAP, pFAK), phalloidin (actin), and/or Hoescht (nuclei). Samples were then imaged using a Nikon A1 confocal microscope and ImageJ software was used to calculate morphology (area, circularity, aspect ratio) and cellular mechanosensing (pFAK morphology, actin anisotropy, nuclear YAP) parameters.

### B.5.6 Statistical Analysis

All data are from three independent biological experiments. At least 50 cells per treatment and biological experiment were quantified. For three group comparisons, one way ANOVA between groups ($\alpha = 0.05$) was performed using GraphPad Prism. If the results of the ANOVA were found to be significant, post hoc analysis was performed using the Tukey multiple comparisons test to compare results among groups. Hierarchical clustering of surface marker data was generated using the analysis software Morpheus (Broad Institute) based on Euclidean distance.

# Appendix C

## Plant Tissue Parenchyma and Vascular Bundles Selectively Regulate Stem Cell Mechanosensing and Differentiation

**Note:** Sections of this chapter have been reproduced from the following publication with permissions:

**Driscoll, K., Butani, M.S., Gultian, K.A., McSweeny, A., Vega, S.L. (2022).** Plant tissue parenchyma and vascular bundles selectively regulate stem cell mechanosensing and differentiation, *Cellular and Molecular Bioengineering 2022 Young Innovators Special Issue*.

## C.1 Abstract

Plant tissues are plentiful, diverse, and due to convergent evolution are structurally similar to many animal tissues. Decellularized plant tissues feature microtopographies that resemble cancellous bone (porous parenchyma) and skeletal muscle (fibrous vascular bundles). However, the use of plant tissues as an inexpensive and abundant biomaterial for controlling stem cell behavior has not been widely explored. Celery plant tissues were cut cross-sectionally (porous parenchyma) or longitudinally (fibrous vascular bundles) and decellularized. Human MSCs were then cultured atop plant tissues and confocal imaging of single cells was used to evaluate the early effects of microtopography on MSC adhesion, morphology, cytoskeletal alignment, Yes-associated protein (YAP) signaling, and downstream lineage commitment to osteogenic or myogenic phenotypes. MSCs cultured on porous parenchyma spread isotropically along the periphery of plant tissue pores. In contrast, MSCs cultured on vascular bundles spread anisotropically and aligned in the direction of fibrous vascular bundles. Differences in microtopography also influenced MSC nuclear YAP localization and actin anisotropy, with higher values observed on fibrous tissues. When exposed to osteogenic or myogenic culture medium, MSCs on porous parenchyma had a higher percentage of cells stain positive for bone biomarker alkaline phosphatase, whereas myoblast determination protein 1 (MyoD) was significantly upregulated for MSCs on fibrous vascular bundles. Together, these results show that plant tissues are an abundant biomaterial with defined microarchitecture that can reproducibly regulate MSC morphology, mechanosensing, and differentiation.

## C.2 Introduction

Annually, an estimated 20 million animals are sacrificed in biomedical research in the United States, raising questions about ethics and sustainability.[398] Due to convergent evolution, nature has designed a wide dichotomy of natural biomaterials with a variety of biochemical and microarchitectural features.[399,400] The plant kingdom offers an inexpensive and bioethical source of natural and biocompatible scaffolds that can be used to control cell-material interactions of adherent cells.[401],[402] For example, Modulevsky and coworkers implanted decellularized plant material in mice and showed a typical foreign body reaction which dissipated within eight weeks, along with fibroblast migration, deposition of new collagen ECM, and blood vessel formation within the plant-based biomaterial.[403] On a microscopic level, decellularized plant tissue microarchitecture resembles the complexity of native Mammalian tissues,[404] and as such studies have reported their use as natural biomaterials for cell culture. The microarchitecture of apple hypanthium resembles cancellous bone, and these plant tissues have been shown to support adhesion and regulate the morphology of mouse NIH3T3 fibroblasts and C2C12 muscle myoblasts.[405] When C2C12 cells are cultured on highly aligned green-onion plant tissues, they align and differentiate into cohesive myotubular networks. [406] Gershlak et al. also showed that decellularized spinach leaves can be repopulated with functional pluripotent stem cell-derived cardiomyocytes and MSCs.[407] Although decellularized plant tissues support stem cell culture,[407],[408] decoupling the effects of topographical features of plant tissues on stem cell mechanosensing and differentiation has not been widely explored.

Stem cells are adherent cells that are highly responsive to physical properties of their surrounding environment.[181] Cell-material interactions regulate early changes in stem cell morphology and mechanosensing, leading to downstream lineage commitment.[340] To explore the role of morphology on MSC differentiation, McBeath and coworkers used microcontact printing to create adhesive islands of different sizes to control the area of single cell attachment.[409] They found that larger MSCs had increased levels of GTPase RhoA and Rho kinase (ROCK), a Rho effector involved in myosin-based cytoskeletal contractility.[410] Consequently, the cytoskeleton of MSCs was more aligned and contractile. If cells are confined to morphologies that enhance or reduce cytoskeletal alignment, MSCs preferentially differentiate into osteoblasts or adipocytes, respectively.[409,411] Stem cell shape is also closely related to the organization of mechanosensitive proteins including Yes-associated protein (YAP).[185] YAP is a transcriptional regulator that transmits mechanical signals to the nucleus.[185,395] YAP is ubiquitous, constantly shuttling between the cytoplasm and nucleus of small cells, and it accumulates in the nucleus of larger cells. The role of YAP on topography-guided stem cell differentiation has also been widely studied,[412] and the effects of microtopography on stem cell differentiation is also well documented.[413–417] For example, MSCs cultured on continuous patterns expressed increased bone biomarker (alkaline phosphatase, ALP) expression when compared to MSCs cultured on discontinuous patterns.[32]

While the effects of microtopography on early changes in stem cell morphology, mechanosensing, and ultimately, differentiation are highly understood, it remains unclear whether microtopography of plant tissues can be used to guide stem cells to distinct mechanosensitive states and phenotypes. Celery (*Apium graveolens* L.) is an inexpensive and highly available vegetable, consisting of a root that splits into leaf-topped stalks.[418,419] The stalks consist of parenchyma and collenchyma cells within highly aligned microfibrils and vascular bundles that contain xylem and phloem to facilitate nutrient and water transfer.[420–422] The microarchitecture of celery stalks has unique features depending on its orientation. A longitudinal cut of celery stalks exposes vascular bundles which highly resemble fibrous structures present in connective tissues including skeletal muscle.[423] In contrast, a cross-sectional cut of the stalk exposes a porous plane, with pore diameters and roundness concomitant with cancellous bone.[424]

The goal of this study is to leverage the ability to create two distinct natural biomaterials derived from the same plant tissue to evaluate cell-material interactions of MSCs. Celery stalks were cut cross-sectionally (porous parenchyma) or longitudinally (fibrous vascular bundles) prior to decellularization. Human MSCs were cultured atop porous and fibrous tissues, and MSCs adhered and proliferated on collagen-coated celery tissues. After 3 days, confocal images of labeled single cells were used to assess early changes in morphology (area, roundness, aspect ratio) and mechanosensing (actin alignment/anisotropy, nuclear YAP localization) due to porous and fibrous microarchitectures. Due to the porous and fibrous plant tissue resemblance to native human cancellous bone and muscle, preferential MSC lineage commitment to osteogenic (bone) or myogenic (muscle) was also studied. MSCs were cultured on porous or fibrous celery tissues in either osteogenic (OS) or myogenic (MYO) medium and stained with alkaline phosphatase (ALP, bone) and myoblast determination protein 1 (MyoD, muscle) biomarkers after 7 days in culture.

## C.3 Results and Discussion

### *C.3.1 MSC Morphology is Influenced by Plant Tissue Microtopography*

To evaluate the morphological behavior of MSCs on decellularized plant tissues, MSC were cultured atop porous and fibrous celery tissues for 3 days and microtopography-driven changes in morphological parameters (area, roundness, aspect ratio) were evaluated. Representative images of MSCs on porous (Figure C.1A) and fibrous (Figure C.1B) celery tissues show distinct differences in morphology. MSCs on porous tissues were significantly smaller (1,232 ± 407 $\mu m^2$) than MSCs on fibrous tissues (1,954 ± 601 $\mu m^2$) (Figure C.1C). MSCs were also significantly rounder on porous tissues (Figure C.1D) and had a larger aspect ratio on fibrous tissues (Figure C.1E). MSC morphology atop fibrous celery tissues were consistent with the morphology of MSCs atop GelMe hydrogels of comparable bulk stiffness. MSCs on GelMe hydrogels have an area of 1,950 ± 79 $\mu m^2$, roundness of 0.32 ± 0.17, and aspect ratio of 2.67 ± 1.80 (Figure S4).

These results show that the differences in topographical features between porous and fibrous celery tissues result in distinct morphologies of cultured MSCs, a critical finding given the established relationship between MSC morphology and downstream lineage commitment.[184,411] This finding supports the idea that the inherent physical properties of plant-derived tissue engineering scaffolds can independently influence the behavior of stem cells.

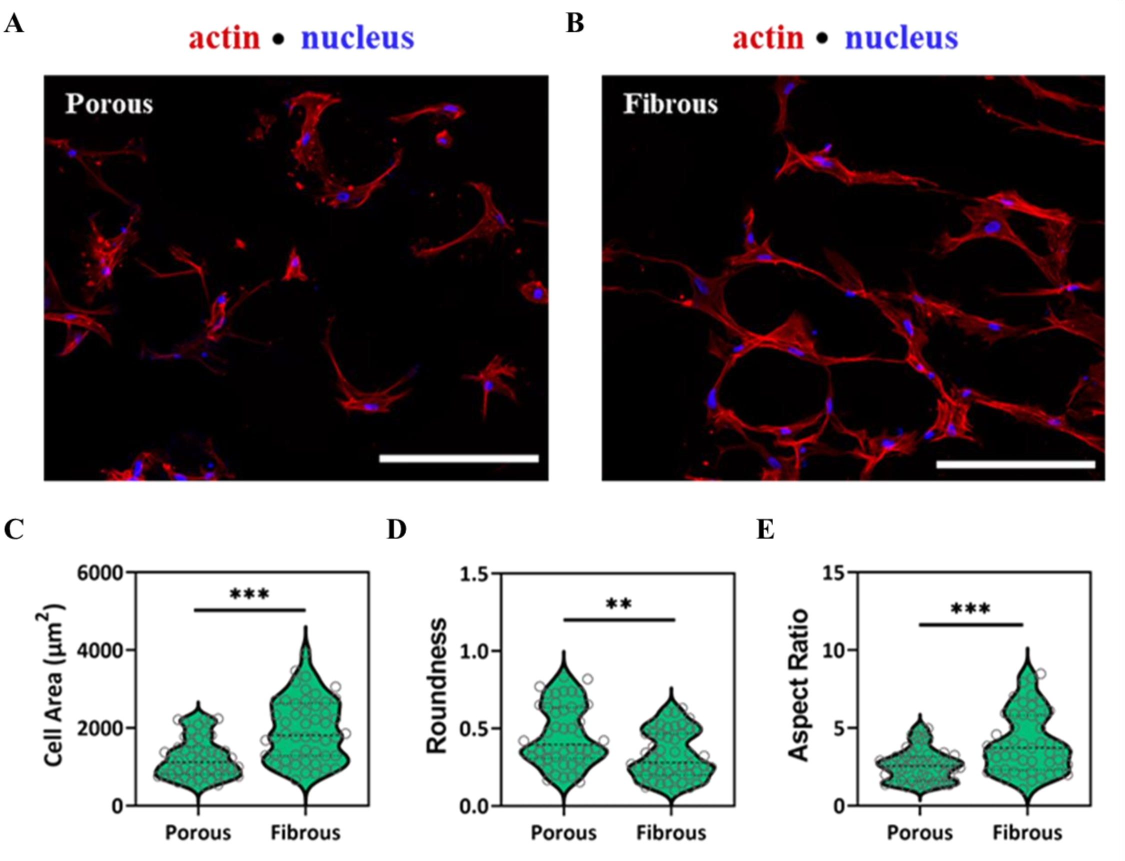

*Figure C. 1*. MSC morphology is influenced by plant tissue topography. Representative F-actin (red) and nuclear (blue) staining of MSCs seeded atop **(A)** porous and **(B)** fibrous celery tissues. Quantification of cell **(C)** area, **(D)** roundness, and **(E)** aspect ratio. Sample size is n ≥ 50 cells per condition with significant differences determined with ANOVA followed by Tukey's post hoc test where $**p < 0.01$, $***p < 0.001$. Scale bar: 200 µm.

### *C.3.2 MSC Mechanosensing on Fibrous Vascular Bundles is Higher than in Porous Parenchyma*

To further evaluate the extent to which 2D mechanical cues from distinct microtopography of celery tissues influence cellular mechanosensing, the presence and location of intracellular mechanosensitive proteins were assessed. The protein YAP is a key transducer of mechanical signals, and MSCs express and increase in nuclear YAP localization with increasing mechanical stimulation.[185]

After 3 days in culture atop celery tissues, nuclear YAP on the fibrous group was higher than the porous group (Figure C.2A), with values of 2.00 ± 0.41 on porous and 2.82 ± 0.89 on fibrous celery tissues (Figure C.2B). This is not surprising, since the fibrous microarchitecture also induced an increase in MSC area and aspect ratio, suggesting a more contractile, mechanoactive state (Figure C.1C, C.1E). Nuclear YAP values on soft GelMe hydrogels were lower than porous or fibrous (Figure C.3A), further demonstrating that plant microarchitecture can enhance nuclear YAP, and thus cellular mechanosensing. Actin anisotropy (actin fiber alignment) is a measure of the organization of actin stress fibers, and there was also a significant increase in actin anisotropy (0.18 ± 0.05 vs. 0.33 ± 0.05) between MSCs in porous and fibrous celery tissues (Figure C.2C, C.2D). Actin alignment on soft GelMe hydrogels was lower than on celery tissues with microarchitecture (Figure C.3B).

Taken together, these results show that topographies that cause an increase in cell area and aspect ratio also enhance MSC mechanosensing. Cellular mechanical activity has been shown to have important implications for stem cell differentiation and developing biomaterials with properties that encourage directed differentiation is of considerable scientific and clinical interest. These results indicate that physical properties beyond stiffness alone can be leveraged to drive stem cell mechanosensing and ultimately differentiation.

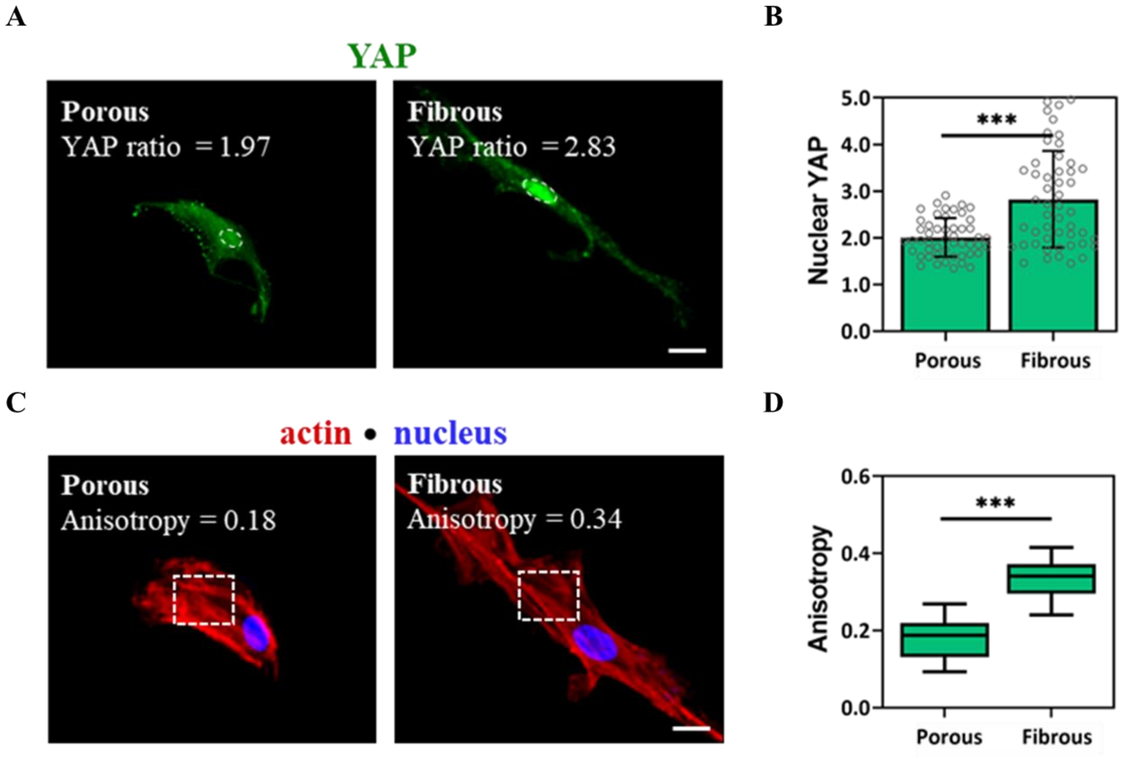

*Figure C. 2.* MSC mechanosensing on fibrous vascular bundles is higher than in porous parenchyma. **(A)** Representative YAP (green) staining with outlined nuclei (dashed oval) of MSCs on porous or fibrous celery tissues. **(B)** Quantification of nuclear YAP ratio. **(C)** Representative F-actin (red) and nuclear (blue) staining of MSCs with region of interest for actin anisotropy measurement (dashed rectangle). **(D)** Quantification of actin anisotropy. Error bars are shown as SD (n ≥ 50 cells per condition) with significant differences determined with ANOVA followed by Tukey's post hoc test where ***p < 0.001. Scale bar: 20 µm.

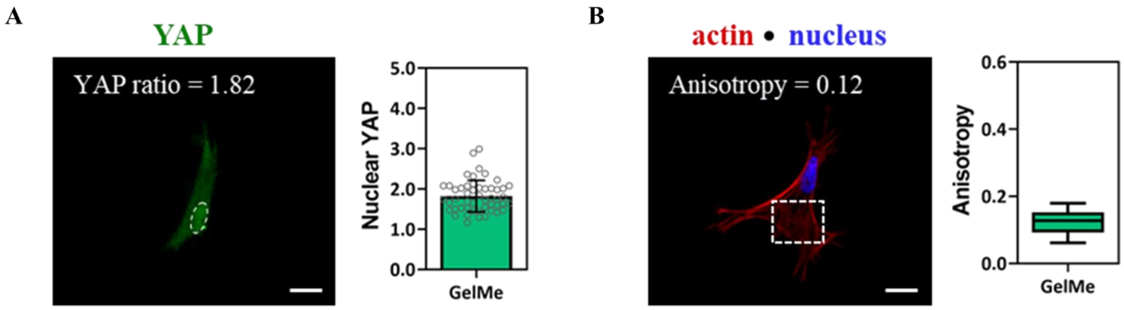

*Figure C. 3.* Representative mechanosensing staining. **(A)** YAP (green) staining with outlined nuclei (dashed line) and nuclear YAP quantification of MSCs on GelMe hydrogels. **(B)** F-actin (red) and nuclear (blue) staining and actin fiber anisotropy of MSCs on GelMe hydrogels. (n ≥ 50 cells per condition). Scale bar: 20 µm.

### *C.3.3 MSC Lineage Commitment Based on Plant Tissue Microtopography*

Cellular mechanosensing plays a large role in directing MSC differentiation.[415–417] On aligned microgrooves, the expression of myogenic biomarkers increases with MSC alignment.[417] In contrast, porosity of ceramic materials enhance MSC differentiation into osteoblasts *in vitro* and *in vivo*.[416] To assess the effects of the porous and fibrous topographical features of celery tissues on MSC lineage commitment, MSCs were seeded atop porous or fibrous celery tissues and cultured in growth, OS, or MYO medium. After 7 days in culture, samples were fixed and sequentially stained for bone and muscle biomarkers ALP and MyoD, respectively, then counterstained with phalloidin (cell body) and Hoescht (nuclei). To minimize bias in identifying MSCs as ALP or MyoD positive, MSCs were also cultured in Growth, OS, or MYO medium on flat GelMe hydrogels for 1 week and the mean fluorescence intensity (MFI) was plotted as Growth vs. OS (Figure C.4A) and Growth vs. MYO (Figure C.4B) histograms. The cutoff MFI for ALP was then determined by subtracting the mean OS MFI value by one standard deviation, shown as a vertical dashed line in Figure C.4A. A similar process was employed to determine the cutoff MFI for MyoD, and a threshold MFI of 19 and 38 were found for ALP and MyoD, respectively.

In osteogenic medium, MSCs on porous celery tissues had a stronger ALP expression in comparison to the fibrous group as seen by higher ALP fluorescence intensity (magenta) (Figure C.4C). Percentage of ALP-expressing cells using an MFI cutoff of 19 (MSCs are classified as ALP-positive if their MFI is greater than 19) was 98 ± 2% on porous celery tissues and significantly lower (70 ± 5%) on fibrous plant tissues (Figure C.4D). Remarkably, nearly every single MSC on porous celery tissues analyzed expressed ALP. Conversely, MSCs on fibrous tissues had a higher intensity of MyoD fluorescence (green) compared to MSCs on porous tissues (Figure C.4E), with positive cell response for MyoD of 24 ± 6% and 82 ± 5% on porous and fibrous tissues, respectively (Figure C.4G). Notably, there is a greater than threefold increase in MyoD expressing cells on the fibrous celery tissue when compared to the porous tissues. Further, certain groups exhibited heightened levels of ALP or MyoD expression on plant scaffolds in the absence of inductive media (Figure C.5). On porous celery tissues cultured in Growth medium, the positive cell response was determined to be 49 ± 2% and 6 ± 3% for ALP and MyoD, respectively (Figure C.5C). Similarly on fibrous tissues, the positive cell response was determined to be 39 ± 6% and 40 ± 7% for ALP and MyoD, respectively (Figure C.5C).

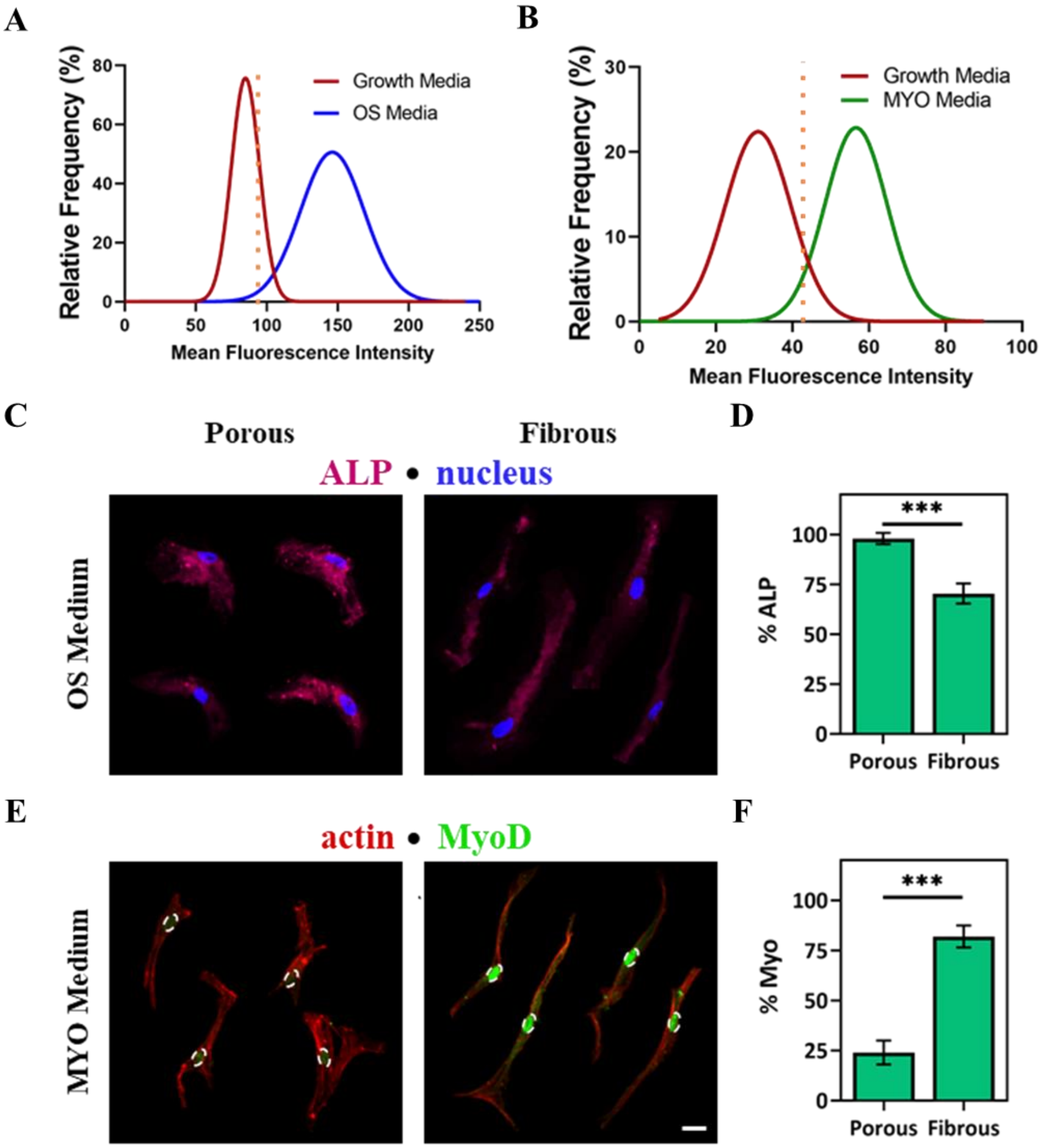

*Figure C. 4.* MSC lineage commitment based on plant tissue microtopography. Frequency distribution of mean fluorescence intensity (MFI) of MSCs seeded atop flat GelMe hydrogels for **(A)** ALP and **(B)** MyoD analysis. **(C)** Representative ALP (magenta) and nuclear (blue) staining of MSCs cultured on porous or fibrous celery tissues in OS medium. **(D)** Quantification of ALP positive MSCs on porous and fibrous celery tissues. **(E)** Representative MyoD (green) and F-actin (red) staining of MSCs cultured on porous or fibrous celery tissues in MYO medium. **(F)** Quantification of MSCs positive for MyoD expression. Bar graphs are shown as mean ± SD (n ≥ 50 cells per condition) with significant differences determined with ANOVA followed by Tukey's post hoc test where ***p < 0.001. Scale bar: 20 μm.

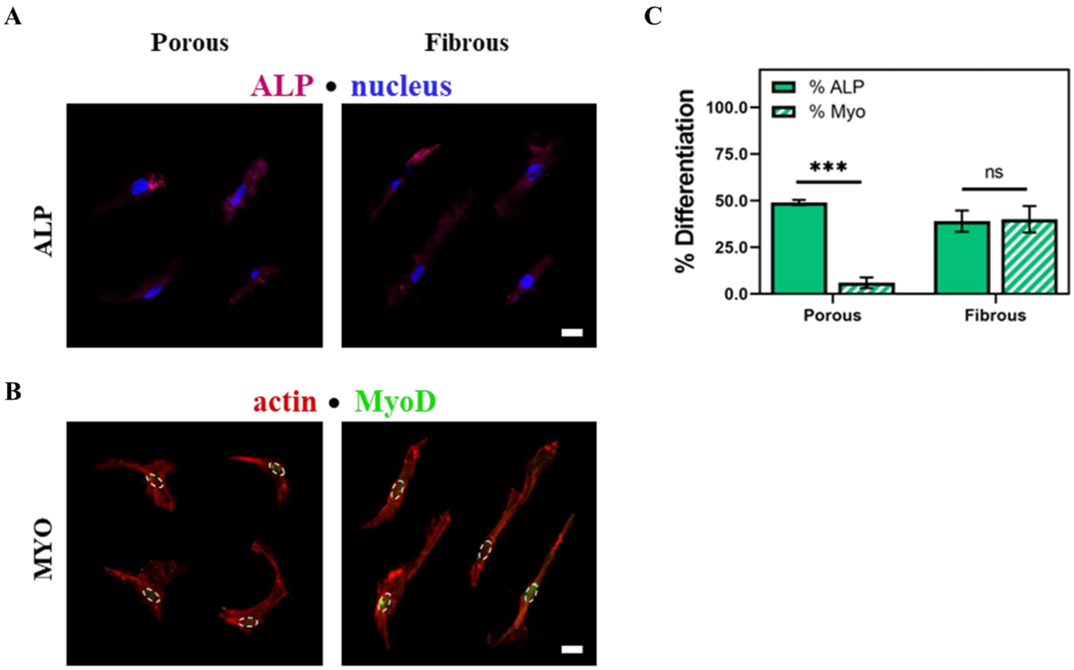

*Figure C. 5.* Quantification of osteogenic and myogenic differentiation in MSC Growth medium. **(A)** Representative ALP (magenta) and nuclear (blue) staining of MSCs in Growth medium. **(B)** Representative MyoD1 (green) and F-actin (red) staining of MSCs in Growth medium. **(C)** Quantification of MSCs positive for ALP and MyoD expression of MSCs cultured on decellularized porous or fibrous scaffolds in Growth medium. Bar graphs shown as mean ± SD ($n \geq 3$ samples per condition) with significant differences determined with ANOVA followed by Tukey's post hoc test where no significant differences (ns) and $^{***}p < 0.001$. Scale bars: 20 μm.

Taken together, these results indicate that the microtopography of plant scaffolds can be leveraged to enhance the differentiation potential of MSCs. The effects of soluble growth factors on MSC differentiation are particularly improved when the underlying microtopography of the plant tissue reflects that of the desired native tissue (porous parenchyma that mimic cancellous bone and fibrous bundles that to mimic skeletal muscle). When cultured in OS medium, nearly all MSCs cultured on porous parenchyma expressed the bone biomarker, ALP. Further, MyoD was expressed at significantly higher rates in MSCs on fibrous (muscle-mimicking) than on porous celery tissues. Surprisingly, the bulk and indentation moduli differences between the porous and fibrous materials were shown to be insignificant, decoupling substrate stiffness from the improved differentiation capacities from microtopographical features alone. Where these features are often difficult and costly to reproduce in synthetic materials, nature has provided us with a diverse array of plant scaffold materials with properties reflective of native human tissues to choose from.

## C.4 Conclusions

In this study, celery stalks were cut cross-sectionally or longitudinally to expose distinct microtopographies. These microtopographies were shown to influence MSC morphology, mechanosensing, and downstream differentiation in inductive media. Through these experiments, we have sought to demonstrate that given their biocompatibility, low-cost, and structural complexity, plant-derived biomaterials are uniquely suited for use as tissue engineering scaffolds.

Future work in this area should include an exploration of other microtopographies and structural elements inherent in nature, as well as a more in-depth analysis of the host immune reaction to and degradation kinetics of these biomaterials *in vivo*. Further functionalizing plant-derived tissue scaffolds with biofunctional molecules also offers a promising avenue for exploration. Ultimately, the potential future applications for plant-derived biomaterials are only limited by the diversity of the plant kingdom itself.

## C.5 Experimental Section

### *C.5.1 Celery Plant Tissue Decellularization*

Celery stalks were cut cross-sectionally or longitudinally using a mandolin slicer (2 mm thickness) and then cut into cylinders using a biopsy punch (8mm diameter). Cylindrical celery tissue samples were placed in a 5% bleach (v/v) and 3% sodium bicarbonate (w/v) solution in deionized water and warmed to 70 °C. The samples were stirred gently until cleared, as determined visually by the loss of tissue pigmentation. Unless otherwise noted, all samples were incubated in a 4% (v/v) rat tail collagen in phosphate-buffered saline (PBS) for 24 hours prior to cell seeding.

### *C.5.2 Hydrogel Polymerization*

Methacrylated gelatin (GelMe) was dissolved in PBS at 2 wt% with 0.05 wt% 2-hydroxy-4'-(2-hydroxyethoxy)-2-methylpropiophenone (I2959). The prepolymer solution (80 µL) was pipetted into a silicone mold (8 mm diameter, 2 mm height) and irradiated with UV light (10 mins, 10 mW/cm$^2$). Individual hydrogels were removed from the molds and placed in 1 mL of PBS overnight at 37 °C. Compressive moduli were then determined using a Shimadzu EZ-SX Mechanical Tester fitted with a compression clamp running at a constant strain rate of 10%/min in air at room temperature. The modulus was calculated from the slope of the stress-strain curve between 10 and 20% strain ($n \geq 3$).

### *C.5.3 MSC Culture and Seeding*

Human MSCs (Lonza) were cultured in MSC growth medium (formulation in Table C.1). Low passage MSCs (P3 to P4) were thawed and plated on tissue culture plastic and cultured in growth medium at 37 °C in a humidity-controlled incubation chamber (5% $CO_2$) until reaching 80% confluency. Upon reaching 80% confluency, MSCs were detached with trypsin-EDTA (0.25%, Gibco) and either passaged or seeded onto decellularized plant tissues. For differentiation studies, MSCs were cultured in osteogenic (OS) or myogenic (MYO) medium using formulations listed in Table C.1. Media changes were performed every other day unless cells were fixed on the day of a media change. MSCs were seeded on celery tissues at a concentration of 10,000 cells/cm$^2$ and cultured for 3 days for morphology and mechanosensing studies. For differentiation studies, MSCs acclimated for 12 hours in MSC growth medium before changing to appropriate inductive media.

**Table C. 1**

*MSC Growth, OS, and MYO Medium Formulations*

| **Media** | **Formulation** |
|---|---|
| MSC Growth Media | AMEM + 10% FBS + 1% Penicillin/Streptomycin |
| Osteoblast Induction Media (OS) | AMEM + 10% FBS + 0.5% Dexamethasone + 2% L-Glutamine + 1% β-Glycerophosphate + 0.5% Ascorbate + 1% Penicillin/Streptomycin |
| Myoblast Induction Media (MYO) | AMEM + 10% FBS + 50 uM hydrocortisone + .1uM dexamethasone + 1% Penicillin/Streptomycin |

### *C.5.4 Immunostaining and Image Analysis*

To evaluate MSC morphology and mechanosensing, MSCs were cultured on decellularized porous or fibrous plant tissues for 3 days and stained with actin, YAP (Santa Cruz Biotechnologies, 1:200, Alexa Fluor 488 secondary, 1:200), and Hoescht. Fluorescently labeled samples were imaged using a Nikon A1 confocal microscope. Cell shape descriptors (area, roundness, aspect ratio), actin alignment/anisotropy, and nuclear YAP localization were acquired from confocal images using ImageJ software. Nuclear YAP localization was determined by measuring the integrated density of YAP of five regions of interest (ROI) on the cytoplasm and nucleus of each cell, respectively. The ratio between the integrated density of the nuclear and cytoplasmic ROIs were defined as the nuclear YAP value.

To evaluate MSC differentiation, after 7 days in culture, samples were sequentially stained for MyoD (Santa Cruz Biotechnologies, 1:200, Alexa Fluor 488 secondary, 1:200) and alkaline phosphatase using Fast Blue (1.45 M Fast Blue RR Salt, 4% Naphthol AS-MX Phosphate, Sigma Aldrich, 1 hour). Fast blue fluoresces upon deep red (640 nm) excitation, and acquisition of all immunofluorescence images was performed with a Nikon A1 confocal microscope. For analysis, maximum intensity z-projection images of the nucleus (blue), cell body (red), MyoD (green), and ALP (magenta) channels were obtained and converted to 8-bit images. To evaluate myogenic differentiation, the mean fluorescence intensity (MFI) of MyoD in the nucleus was quantified using ImageJ software.

To evaluate osteogenic differentiation, an ROI mask was created to measure the fluorescence of ALP in the cytoplasm while excluding the nucleus. The mask is a ring with an outer diameter determined by a 4x dilation of the nucleus and inner diameter of the original nucleus. This mask was overlaid onto the ALP channel to generate rings of ALP fluorescence. The 3D Objects Counter tool on ImageJ was then used to calculate the area of the rings, and the Measurement tool was used to quantify the integrated density of the ALP rings. The corresponding MFI of every cell was calculated by taking the ratio between the integrated density and the area of the ring.

To determine the minimal MFI for an MSC to be classified as ALP or MyoD positive, MFI frequency distribution curves were used.[203] MSCs were cultured on flat GelMe hydrogels in Growth, OS, or MYO medium for 7 days followed by staining and imaging to acquire and plot MFI frequency distribution curves. The MFI values which were one standard deviation from the mean MFI (mean minus SD) of the OS or MYO cell curves were selected as thresholds for classifying an ALP or MyoD positive cell. Based on the minimal MFI (MFI > 38 for positive MyoD; MFI > 19 for positive ALP), the percentage of cells positive for MyoD and ALP was determined.

### *C.5.5 Statistical Analysis*

Statistical analyses were performed using GraphPad Prism 9.3.1 software. All experiments were carried out in triplicates and single cell analysis was done with at least 50 cells per group. All graphs represent mean ± standard deviation (SD). For comparisons of three or more groups, normally distributed populations were analyzed via analysis of variance (ANOVA) with a Tukey's post hoc test to correct for multiple comparisons. Differences among groups are stated as $p < 0.05$ (*), $p < 0.01$ (**), or $p < 0.001$ (***). Differences between groups that are not statistically significant are denoted as (ns). Box plots show 25/50/75th percentiles, whiskers show minimum/maximum.